

# UC San Diego

## UC San Diego Electronic Theses and Dissertations

### Title

Investigations of Atmospheric Sulfur Cycle Oxidation Using Stable and Radioactive Isotopes /

### Permalink

<https://escholarship.org/uc/item/0wg0780n>

### Author

Hill-Falkenthal, Jason

### Publication Date

2014

Peer reviewed|Thesis/dissertation

**UNIVERSITY OF CALIFORNIA, SAN DIEGO**

Investigations of Atmospheric Sulfur Cycle Oxidation Using Stable and Radioactive Isotopes

A dissertation submitted in partial satisfaction of the requirements for the degree

Doctor of Philosophy

in

Chemistry

by

Jason Hill-Falkenthal

Committee in charge:

Professor Mark H. Thiemens, Chair  
Professor Tim Bertram  
Professor Kim Prather  
Professor Jeff Severinghaus  
Professor William Trogler

2014



The dissertation of Jason Hill-Falkenthal is approved, and it is acceptable in quality and form for publication on microfilm and electronically:

---

---

---

---

---

**Chair**

University of California, San Diego

2014

## **DEDICATION**

Dedicated to my family as proof that the last 5 years can almost constitute as a real job.

## TABLE OF CONTENTS

Signature Page.....	iii
Dedication.....	iv
Table of Contents.....	v
List of Figures.....	x
List of Tables.....	xii
Acknowledgements.....	xiii
Vita.....	xv
Abstract of the Dissertation.....	xvii
Chapter 1 Sulfur Cycle.....	1
1.1 Introduction.....	1
1.2 Natural Sources.....	2
1.2.1 Biogenic Emissions.....	2
1.2.2 Volcanic Emissions.....	3
1.2.3 Sea Spray.....	3
1.3 Anthropogenic Sources.....	5
1.4 Sinks.....	5
1.5 Chemical Transformation of Sulfur Species.....	6
1.5.1 Reduced Sulfur Species.....	6
1.5.2 Oxidation of SO <sub>2</sub> .....	8
1.5.2.1 Gas Phase Oxidation.....	9
1.5.2.2 Dissolution of SO <sub>2</sub> into the Aqueous Phase.....	9
1.5.2.3 Aqueous Phase Oxidation by Dissolved O <sub>3</sub> .....	9
1.5.2.4 Aqueous Phase Oxidation via H <sub>2</sub> O <sub>2</sub> .....	10
1.5.2.5 Metal Catalyzed O <sub>2</sub> Oxidation of S(IV).....	10
1.5.2.6 Oxidation of S(IV) on Sea Salt Aerosols.....	11

1.6.1 Size Segregation.....	11
1.6.2 Nanoparticles.....	12
1.7 Climatic Impact: Direct and Indirect Effects.....	13
1.8 References.....	23
Chapter 2 Isotope Theory.....	32
2.1 Nuclear Stability.....	32
2.2 Stable Isotopes.....	32
2.2.1 Isotopic Measurement through IRMS.....	33
2.2.2 The Delta Notation and Isotopic Standard.....	34
2.2.3 Mass Dependent Fractionation Effects.....	34
2.2.3.1 Kinetic Fractionation.....	36
2.2.3.2 Equilibrium Fractionation.....	37
2.2.4 Mass Independent Fractionation.....	40
2.2.5 Mass independent Fractionation in Sulfate.....	42
2.2.6 Previous Measurements.....	44
2.3 Radioactive Isotopes.....	44
2.3.1 Radioactive Decay.....	44
2.3.2 Beta Decay.....	45
2.3.3 Measurement of $\beta$ Decay through Scintillation Spectroscopy.....	47
2.3.3.1 Liquid Scintillation Gel.....	47
2.3.3.2 Minimizing Background Contributions through Shielding.....	48
2.3.4 Measurement Units.....	49
2.3.5 Galactic Cosmic Rays.....	49
2.3.5.1 Interaction with Earth's Magnetic Fields.....	50
2.3.5.2 Solar Modulation.....	52
2.3.5.3 Cosmic Ray Propagation.....	54

2.3.5.4 Rate of Cosmogenic Nuclide Production in the Atmosphere .....	55
2.3.6 Applications of Radionuclides to Atmospheric Processes.....	56
2.3.6.1 <sup>35</sup> S as a Tracer for Atmospheric Processes.....	58
2.3.6.2 Previous Measurements.....	59
2.4 References.....	79
Chapter 3 Differentiating Sulfate Aerosol Oxidation Pathways for Varying Source	
Altitudes Using <sup>35</sup> S and Δ <sup>17</sup> O Tracers.....	88
3.1 Abstract.....	88
3.2 Introduction.....	88
3.3 Methods.....	91
3.4 Results and Discussion.....	93
3.4.1 Coastal Climate Samples.....	93
3.4.2 Santa Ana Samples.....	95
3.4.3 STE Samples.....	97
3.5 Conclusions.....	99
3.6 Acknowledgements.....	99
3.7 References.....	103
Chapter 4 Seasonal Variations in <sup>35</sup> S and Δ <sup>17</sup> O of Sulfate Aerosols on the Antarctic	
Plateau.....	109
4.1 Abstract.....	109
4.2 Introduction.....	109
4.3 Methods.....	112
4.4 Antarctic Meteorology.....	113
4.5 Sources of Sulfate in Antarctica.....	114
4.5.1 Biogenic Sulfate Source.....	114



4.5.2 Stratospheric Sulfate Source.....	115
4.5.3 Continental Sulfate Source.....	117
4.6 Results and Discussion.....	119
4.6.1 Sulfate Concentrations.....	119
4.6.2 Seasonality of $^{35}\text{S}$ Activity.....	119
4.6.3 Seasonal Variation of $\Delta^{17}\text{O}$ in Sulfate.....	122
4.6.3.1 Summer/Autumn and Spring/Summer.....	122
4.6.3.2 Winter.....	124
4.6.4 Constraints on Stratospheric Flux.....	127
4.7 Conclusions.....	128
4.8 Acknowledgements.....	129
4.9 References.....	136
Chapter 5 Detection of Radioactive $^{35}\text{S}$ at Fukushima and other Japanese Sites.....	146
5.1 Abstract.....	146
5.2 Introduction.....	146
5.3 Methods.....	148
5.4 Results and Discussion.....	149
5.5 Conclusions.....	153
5.6 Acknowledgements.....	153
5.7 References.....	164
Chapter 6 Future Applications to Heterogeneous Chemistry.....	167
6.1 Abstract.....	167
6.2 Introduction.....	167
6.3 Experimental.....	169
6.3.1 Flow Tube Apparatus.....	169

6.3.2 Determination of Uptake Coefficients.....	170
6.3.3 Radioactivity Measurements.....	171
6.3.4 Formation and Calibration of $^{35}\text{SO}_2$ Bulb.....	171
6.4 Results and Discussion.....	172
6.5 Conclusions.....	177
6.6 References.....	185

## LIST OF FIGURES

Figure 1.1 Sulfur Flux Between Reservoirs.....	16
Figure 1.2 Major Components of Stratospheric Sulfur.....	17
Figure 1.3 Conceptual Map of Wet Deposition.....	18
Figure 1.4 DMS Oxidation.....	19
Figure 1.5 pH Dependence of SO <sub>2</sub> Oxidation Pathways.....	20
Figure 1.6 Aerosol Size Segregation.....	21
Figure 2.1 Nuclear Stability.....	61
Figure 2.2 Triple Isotope Plot.....	62
Figure 2.3 Babikov Zero Point Energy Effect.....	63
Figure 2.4 Mass Independent Atmospheric Species.....	64
Figure 2.5 Beta Decay Spectra.....	65
Figure 2.6 Scintillation Process.....	65
Figure 2.7 Scintillation Counter Depiction.....	66
Figure 2.8 Primary Cosmic Flux.....	67
Figure 2.9 Earth's Magnetic Field.....	68
Figure 2.10 Variation in Cosmic Ray Intensity.....	69
Figure 2.11 Latitude Dependence of Cutoff Rigidity.....	70
Figure 2.12 Rigidity/Kinetic Energy of Incoming Cosmic Particles.....	71
Figure 2.13 Solar Modulation.....	72
Figure 2.14 Cosmic Ray Dependence on Sunspot Strength.....	73
Figure 2.15 Nuclear Cascade.....	74
Figure 2.16 Energy Spectra for Cosmic Ray Flux at Various Atmospheric Depths.....	75
Figure 2.17 Calculated Production Rates.....	76
Figure 3.1 Specific Activity vs. $\Delta^{17}\text{O}$ .....	100
Figure 3.2 $\Delta^{17}\text{O}$ vs. Concentration.....	101
Figure 4.1 Seasonality of Sulfate Concentration, <sup>35</sup> S Activity, and Specific Activity.....	131

Figure 4.2 Seasonality of $\Delta^{17}\text{O}$ .....	132
Figure 4.3 Specific Activity vs. $\Delta^{17}\text{O}$ .....	133
Figure 5.1 Japanese Sampling Locations.....	154
Figure 5.2 Measured $^{35}\text{SO}_4^{2-}$ Activity.....	155
Figure 5.3 $^{35}\text{SO}_4^{2-}$ Activity in Different Size Fractions.....	156
Figure 5.4 Modeled Back Trajectories for AORI Sampling Site.....	157
Figure 6.1 Depiction of Flow Tube Setup.....	178
Figure 6.2 Measured Uptake Ratios.....	179

## LIST OF TABLES

Table 1.1 Atmospheric Sulfur Compounds.....	22
Table 2.1 Production Rates and Concentrations of Radiogenic Nuclides.....	77
Table 2.2 Calculated <sup>35</sup> S Production Rates.....	78
Table 3.1 Summary of Sulfate Concentrations, Specific Activity, and $\Delta^{17}\text{O}$ .....	102
Table 4.1 $\Delta^{17}\text{O}$ of Sulfate Oxidation Pathways.....	134
Table 4.2 Sulfate Concentrations, <sup>35</sup> S Activity, and $\Delta^{17}\text{O}$ Measurements.....	135
Table 5.1 Radioactive <sup>35</sup> S Measurements near Fukushima.....	158
Table 5.2 <sup>35</sup> S Measurements at Different Size Fractions.....	161
Table 5.3 <sup>35</sup> S in Rain Water Samples.....	163
Table 6.1 Published SO <sub>2</sub> Uptake Ratios.....	180
Table 6.2 Shielding Tests.....	181
Table 6.3 Measurement Blanks.....	182
Table 6.4 Bulb Calibration.....	183
Table 6.5 Measured Uptake Ratios at Various Linear Velocities.....	184

## ACKNOWLEDGEMENTS

I would like to acknowledge many people whose assistance made this dissertation possible. First of all, I would like to thank my thesis advisor Mark Thiemens for his support and guidance through the ups and downs of this five year project. Antra Priyadarshi served as an invaluable mentor through the entire process and was instrumental in my growth throughout the years. Terri Jackson's scientific experience and magical ability to fix most instrumental problems by just walking into the room is vital to the success of the whole lab. Thoughtful scientific discussions and unyielding support from current lab research scientists Subrata Chakraborty and Robina Shaheen and graduate students Morgan Nunn and Mang Lin are also gratefully acknowledged.

I would like to thank my committee members, Dr. Tim Bertram, Dr. Kim Prather, Dr. William Trogler, and Dr. Jeff Severinghaus for their guidance and helpful scientific discussions along the way. Special thanks goes to Dr. Tim Bertram for the extra time he spent with me discussing my scientific progress and for his generosity in allowing me to borrow laboratory equipment for some of the work in this thesis.

I need to also thank those collaborators outside UCSD for their generosity. I graciously thank Joel Savarino for his help with acquiring the Antarctic samples and his insightful comments in the data analysis process. Scientific discussions and guidance from Gerardo Dominguez of Cal State San Marcos were both insightful and rewarding. Collaborators Naohiro Yoshida and Sakae Toyoda from Japan are graciously acknowledged for their helpful discussions on the radioactive release from Fukushima Daiichi.

I would like to thank the undergraduates that worked under me throughout the years for their assistance in sample processing. Their relaxed demeanor always made them a joy to work with. They include Victoria Azzi, Farris Serio, and Hayley Johnson. And last but not least, all of the family members who provided support throughout the years, especially those who told me exactly what I needed to hear when times got difficult.

Chapter 3, in full, is a reprint of material as it appears in Journal of Geophysical Research- Atmospheres, Hill-Falkenthal, J., A. Priyadarshi, and M. Thiemens, Differentiating Sulfate Aerosol Oxidation Pathways for Varying Source Altitudes Using  $^{35}\text{S}$  and  $\Delta^{17}\text{O}$  Tracers, volume 117, 2012. The

dissertation author was the primary author of this paper. The authors thank S. Chakraborty, G. Dominguez, R. Shaheen, and T. Jackson for beneficial scientific discussions which improved the manuscript significantly.

Chapter 4, in full, is a reprint of material from Journal of Geophysical Research-Atmospheres, Hill-Falkenthal, J., A. Priyadarshi, J. Savarino, and M. Thiemens, Seasonal variations in  $^{35}\text{S}$  and  $\Delta^{17}\text{O}$  of sulfate aerosols on the Antarctic plateau, volume 118, 2013. The dissertation author was the primary author of this paper.

Chapter 5, in full, is a reprint of material from Journal of Geophysical Research-Atmospheres, Priyadarshi, A., J. Hill-Falkenthal, M. Thiemens, N. Yoshida, S. Toyoda, K. Yamada, A. Mukotaka, A. Fujii, M. Uematsu, S. Hatakeyama, I. Noguchi, Y. Nojiri, and H. Tanimoto, Detection of radioactive  $^{35}\text{S}$  at Fukushima and other Japanese sites, volume 118, 2013. The dissertation author was one of two primary investigators and authors of this paper.

## VITA

- 2009 B.S., Chemistry and Biochemistry, University of California, San Diego
- 2012 M.S., Chemistry and Biochemistry, University of California, San Diego
- 2014 Ph.D., Chemistry, University of California, San Diego

## PUBLICATIONS

Hill-Falkenthal, J., A. Priyadarshi, and M. Thiemens (2012), Differentiating sulfate aerosol oxidation pathways for varying source altitudes using  $^{35}\text{S}$  and  $\Delta^{17}\text{O}$  tracers, *J. Geophys. Res.*, *117*, D18302, doi: 10.1029/2012JD018242.

Priyadarshi, A., J. Hill-Falkenthal, E. Coupal, G. Dominguez, and M. H. Thiemens (2012), Measurements of  $^{35}\text{S}$  in the marine boundary layer at La Jolla, California: A new technique for tracing air mass mixing during Santa Ana events, *J. Geophys. Res.* *117*, D08301, doi: 10.1029/2011JD016878.

Hill-Falkenthal, J., A. Priyadarshi, J. Savarino, and M. Thiemens (2013), Seasonal variations in  $^{35}\text{S}$  and  $\Delta^{17}\text{O}$  of sulfate aerosols on the Antarctic plateau, *J. Geophys. Res. Atmos.*, *118*, 9444-9455, doi: 10.1002/jgrd.50716.

Priyadarshi, A., J. Hill-Falkenthal, M. Thiemens, N. Yoshida, S. Toyoda, K. Yamada, A. Mukotaka, A. Fujii, M. Uematsu, S. Hatakeyama, I. Noguchi, Y. Nojiri, H. Tanimoto. (2013). Detection of radioactive  $^{35}\text{S}$  at Fukushima and other Japanese sites, *J. Geophys. Res., Atmos.*, *118*, 1020–1027, doi: 10.1029/2012JD018485.

Priyadarshi, A. J. Hill-Falkenthal, M. Thiemens, A. Zhang, M. Lin, J. Chuen-Yu Chan, S. Kang (2014), Cosmogenic  $^{35}\text{S}$  measurements in the Tibetan Plateau to quantify glacier snowmelt, *J. Geophys. Res. Atmos.*, *119*, 4125-4135, doi: 10.1002/2013JD019801.

Hill-Falkenthal, J., Pandey, A., Coupal, E. Kim, S, Dominguez, G., Thiemens, M.H., Investigating atmospheric transport processes using cosmogenic  $^{35}\text{S}$  and oxygen isotopic anomaly ( $\Delta^{17}\text{O}$ ) in sulfate, (abstract), *EOS Trans, AGU*, 2010.

Hill-Falkenthal, J., Priyadarshi, A., Savarino, J.P, Thiemens, M.H., Understanding Antarctic sulfur cycle chemistry using cosmogenic  $^{35}\text{S}$ , (abstract), *EOS Trans, AGU*, 2011.



## **FIELDS OF STUDY**

Major Field: Chemistry

Studies in Isotope Geochemistry

Professor Mark H. Thiemens

Studies in Atmospheric Chemistry

Professor Mark. H. Thiemens

## ABSTRACT OF THE DISSERTATION

### Investigations of Atmospheric Sulfur Cycle Oxidation Using Stable and Radioactive Isotopes

by

Jason Hill-Falkenthal

Doctor of Philosophy in Chemistry

University of California, San Diego, 2014

Professor Mark H. Thiemens, Chair

The studies presented here provide new means to assess sulfur cycle chemistry in the atmosphere. Sulfate aerosols play an important role in global radiative forcing through their inherent ability to scatter light and ability to serve as cloud condensation nuclei. Mass independent fractionation in oxygen isotopes of sulfate aerosols provides constraints on atmospheric oxidation processes from SO<sub>2</sub> to SO<sub>4</sub>. Cosmogenically produced <sup>35</sup>S offers a unique way to trace sulfur cycling in the atmosphere and enables enhanced understanding of boundary layer chemistry, air mass transfer, and stratospheric-tropospheric exchange (STE). <sup>35</sup>S has a short life time (87.2 days) and is advantageous over other radioactive tracers due to its continuous presence in gas, liquid, and aerosol phases. Combining Δ<sup>17</sup>O and <sup>35</sup>S measurements offers a new way to quantify how sulfate formation is influenced by atmospheric variability since both chemical (Δ<sup>17</sup>O) and chronological (<sup>35</sup>S) information is available.

Simultaneous measurements of Δ<sup>17</sup>O and <sup>35</sup>S in sulfate aerosols from La Jolla, California (Chapter 3) and Dome C, Antarctica (Chapter 4) are presented. Chapter 3 reveals strong correlation between specific activity (<sup>35</sup>S atoms/sulfate concentration) and Δ<sup>17</sup>O during Santa Ana wind events. This simultaneous increase is linked to enhanced free tropospheric flux descending into Southern California as a result of the

strong pressure gradient that develops during this weather phenomenon. Chapter 4 presents the first yearlong study of  $\Delta^{17}\text{O}$  and  $^{35}\text{S}$  in sulfate aerosols on the Antarctic plateau.  $^{35}\text{S}$  activity is directly related to the seasonal STE cycle and the oxidative capacity of the atmosphere. The  $\Delta^{17}\text{O}$  anomaly suggests a relative increase in ozone oxidation during spring/autumn relative to summer. An unexpected decline in  $\Delta^{17}\text{O}$  occurs during winter potentially related to decreased vertical mixing due to the lack of radiative heating.

Chapter 5 studies the release of  $^{35}\text{S}$  radiation from the Fukushima Daiichi Power Plant during the aftermath of the March, 11, 2011 earthquake at 6 different Japanese sites. Even after 6 months,  $^{35}\text{S}$  activity remains above cosmogenic levels. Chapter 6 looks at the future application of  $^{35}\text{S}$  to heterogeneous chemistry. Preliminary test results are presented to determine the feasibility of applying  $^{35}\text{S}$  to chemical flow studies.

## Chapter 1

### Sulfur Cycle

#### 1.1 Introduction

The sulfur cycle is highly complex, with compounds existing in solid, liquid, and gaseous forms and ranging in oxidation states from -2 to 6 (Table 1.1). Complicating matters more, sulfur species in the lithosphere, hydrosphere, and atmosphere transport from one reservoir to another through biological and chemical interactions, forming new compounds in varying chemical states [Charlson *et al.*, 1992]. For example, the reduction of oceanic sulfate by phytoplankton creates gaseous dimethyl sulfide which is then transported to the atmospheric reservoir. These reduced sulfur species are then oxidized in the atmosphere and deposited back to the hydrosphere or the lithosphere. The vast majority of sulfur exists in the lithosphere and most transfer between reservoirs occurs through the hydrosphere and atmosphere (Figure 1.1).

Here, we focus our studies on the chemical processes of sulfur species that affect the atmospheric reservoir. The amount of sulfur in the atmosphere at any given time is small relative to the hydrosphere and lithosphere as a result of the short lifetimes (days to weeks) of most atmospheric species. In contrast, sulfur species are cycled much slower in the hydrosphere and lithosphere, resulting in greater sulfur burdens [Charlson *et al.*, 1992]. The short lifetimes and quick chemical processing of atmospheric species make it a challenge to constrain the chemical and physical transformations of atmospheric sulfur. In addition, human activities have greatly perturbed the biogeochemical cycles by adding to the complexity. On a global scale, anthropogenic species dominant the total anthropogenic sulfur budget and account for 2 to 3 times the amount of sulfur compared to natural sources [Rodhe, 1999]. In a clean marine environment where anthropogenic sources are minimal, natural emissions become the dominant sulfur species [De Bruyn *et al.*, 1995]. DMS is considered the only relevant source of sulfur species during summer at coastal Antarctic sites, accounting for over 90% of the sulfate budget [Minikin *et al.*, 1998; Preunkert *et al.*, 2007]. Natural sources of sulfur include biogenic, volcanic, and sea spray emissions, whereas anthropogenic sources are generally related to the combustion and refining of fossil fuels.

## 1.2 Natural Sources

### 1.2.1 Biogenic Emissions

Natural sulfur emissions are primarily biologically produced and emitted as H<sub>2</sub>S or as organic sulfur gases, DMS (dimethyl sulfide), OCS (carbonyl sulfide), and CS<sub>2</sub> (carbon disulfide), predominantly over oceans, wetlands, salt marshes, and estuaries by algae and bacteria [De Kok *et al.*, 2007; Watts, 2000]. DMS is the principal volatile sulfur compound released from oceans and is thought to originate from the decomposition of dimethyl sulfoniopropionate (DMSP) produced by marine organisms such as phytoplankton and zooplankton [Andreae, 1990]. Global annual emissions of DMS are estimated to be 27.6 Tg/yr [Kloster *et al.*, 2006]. DMS mixing ratios in the marine boundary layer (MBL) only range from 80-110 ppt due to its short atmospheric lifetime, (1 day [Kloster *et al.*, 2006]), reaching as high as 1 ppb over coastal, upwelling waters [Seinfeld and Pandis, 2006].

Hydrogen sulfide production is largely the by-product of sulfate reducing bacteria which obtain energy by breaking down SO<sub>4</sub><sup>2-</sup> to H<sub>2</sub>S. Elevated H<sub>2</sub>S mixing ratios have been observed over anaerobic swamps, salt marshes, tidal flats, and the open ocean. Over the open ocean, the biochemical sources must be located in near-surface waters, as H<sub>2</sub>S from deeper waters is oxidized before escape to the atmosphere [Warneck, 1999]. Oceanic emissions of H<sub>2</sub>S have been estimated to be less than 0.3 Tg/year globally [Andreae *et al.*, 1991].

The oceans provide a source of CS<sub>2</sub>, however, abundances in the atmosphere are low. The main sources of CS<sub>2</sub> are thought to be rotting organic matter, oceans, soils, or marshes [Khalil and Rasmussen, 1984]. An ocean to atmosphere flux has been estimated to release about 0.18 Tg of CS<sub>2</sub> per year [Chin and Davis, 1993; Xie and Moore, 1997].

OCS is the most abundant sulfur species in the atmosphere and is fairly evenly distributed throughout the troposphere with a mixing ratio of about 500 ppt. The main source of OCS is through photochemical production of dissolved organosulfur species in the ocean [Zepp and Andreae, 1994]. Due to its long residence time of about 7 years, OCS is the only sulfur compound that reaches the stratosphere with

the exception of volcanic injection of SO<sub>2</sub>. The total quantity of OCS in the troposphere and stratosphere is estimated to be 5.2 Tg and 4.63 Tg, respectively, with an estimated global source strength of 0.86 Tg/yr [Chin and Davis, 1995]. OCS is one of the main contributors to stratospheric sulfate aerosols and plays an important role in the Earth's radiation budget.

### 1.2.2 Volcanic Emissions

Sulfur gases are emitted to the atmosphere from both erupting and non-erupting volcanoes. The major sulfur compound emitted is SO<sub>2</sub>, with SO<sub>4</sub> and H<sub>2</sub>S comprising less than 1%, and OCS less than 0.1% of total sulfur emissions [Belviso *et al.*, 1986; Khalil and Rasmussen, 1984; Stoiber *et al.*, 1987]. Recent modeling studies have suggested that emissions from volcanic activity represent about 10% of the present-day global SO<sub>2</sub> budget in the atmosphere [Stevenson *et al.*, 2003]. Violent eruptions inject SO<sub>2</sub> into the stratosphere leading to an increase in stratospheric sulfate aerosols (SSA). SSA reflect sunlight back to space resulting in a net cooling effect for 1 to 2 years until these particles deposit back into the troposphere. For example, satellite observations indicated a global mean decrease of about 5 W/m<sup>2</sup> in the absorbed solar radiation following the Mt. Pinatubo eruption in 1991 [Seinfeld and Pandis, 2006]. Recently, there have been no eruptions approaching the magnitude of Mt. Pinatubo, however, smaller volcanic events contribute minimally to the reduction in radiative forcing, about 0.1 W/m<sup>2</sup> [Solomon *et al.*, 2011; Trenberth and Fasullo, 2013]. Figure 1.2 depicts the fluxes of sulfur species to the stratosphere. The volcanic contribution is included in the natural SO<sub>2</sub> flux to the stratosphere, second largest after OCS.

### 1.2.3 Sea Spray

Sea salt aerosols (SSA) represent one of the largest fluxes of aerosol particles into the atmosphere and are formed at the sea surface mainly by breaking waves via bubble bursting and by tearing of wave crests [Ault *et al.*, 2013; Barthel *et al.*, 2014]. SSA often dominates the mass concentration of marine aerosol, and along with mineral dust, is the dominant aerosol globally emitted to the atmosphere [de Leeuw *et al.*, 2011]. When a wave breaks, air is entrained into the water and dispersed into a cloud of bubbles which rise to the surface and burst [Thorpe, 1992]. The near-surface wind speed, at a height of 10 meters and below, plays a dual role in influencing the flux of SSA: first, by being the dominant factor controlling

wave generation and the subsequent wave breaking, and second, through upward turbulent transport of the newly formed particles [*de Leeuw et al.*, 2011]. Two types of primary aerosols are formed during the bubble bursting process, small film and larger jet droplets [*Blanchard*, 1964]. During the collapse of a bubble from the water film, several hundred film droplets are formed with typical radii of 1  $\mu\text{m}$  or less [*Lewis and Schwartz*, 2004]. Jet droplets are emitted from a vertical jet emerging from the bottom of a bubble with radii distributions of 4  $\mu\text{m}$  and below [*Mårtensson et al.*, 2003; *O'Dowd and Smith*, 1993]. The dislocation of water droplets from the wave crest due to wind stress produces the largest sea spray particles known as spume droplets with a minimum diameter of 40  $\mu\text{m}$  and no defined maximum [*Andreas*, 1998; *Monahan et al.*, 1983]. The atmospheric residence times vary from seconds to minutes for larger particles where gravitational sedimentation is the principal removal mechanism, to days for smaller particles, which are removed primarily by precipitation [*de Leeuw et al.*, 2011].

The sea salt aerosol is an important contributor to the sulfate budget near coastal sites and is often the dominant component of sulfate in the undisturbed marine environment isolated from continental and anthropogenic sources [*Lewis and Schwartz*, 2004]. The concentration of sulfate associated with sea salt is determined by using a marker ion for sea salt and assuming the ratio in the aerosol is consistent with those in seawater [*Millero*, 1974]. Sodium, chlorine, and magnesium have all been used as sea salt tracers. Typically, sodium is the tracer of choice, and can be estimated by using the molar ratio of  $\text{SO}_4^{2-}/\text{Na}^+$ , 0.0604, in sea water [*Lide*, 2004]. However, at some sampling sites, the use of sodium can be problematic due to the influence of non-marine sources of sodium, such as crustal material through soil runoff and erosion. This alters the ratio of sulfate to sodium in sea water leading to negative values for the calculation of non-sea salt sulfate [*Arimoto et al.*, 1992; *Caine et al.*, 1999; *Martens et al.*, 1973]. This effect was prevalent in samples measured in La Jolla, California, requiring a separate tracer to estimate sea salt sulfate. Attachment of  $\text{HNO}_3$  vapor to sea salt droplets lowers the pH of the particle causing the release of HCl to the atmosphere [*Martens et al.*, 1973]. Therefore, the use of chlorine leads to an underestimation of the total concentration of sea salt aerosol. Magnesium was selected in preference to sodium and chlorine as the tracer that best marked sea salt sulfate by *Ayers et al.*, (1986), *Caine et al.*, (1999), and *Sievering et al.*,

(2004) due to the problems with sodium and chlorine. The  $\text{SO}_4^{2-}/\text{Mg}^+$  molar ratio of 0.5369 [Lide, 2004] is used to correct for sea salt sulfate in the proceeding chapters.

### 1.3 Anthropogenic Sources

Human activities have had a major effect on the cycling of sulfur compounds throughout the atmosphere resulting in enhanced sulfur deposition and sulfate concentrations near most industrialized areas. It is estimated that about 70% of global emissions of sulfur to the atmosphere are from anthropogenic sources [Chin and Jacob, 1996; Stern, 2005] with the largest contribution coming from the combustion of coal, largely from coal-fired power plants. Other significant contributors include the combustion and refinement of fossil fuels and biomass burning. Although biomass burning can be a natural phenomenon, recent human activities related to forest deforestation significantly outweigh natural fires, which only account for about 10% of total biomass burning [Innes *et al.*, 2000]. Sulfur dioxide is the primary pollutant released from anthropogenic sources and is subsequently oxidized to sulfate. Intercontinental transport of aerosol species averages about 1-2 weeks permitting regional pollutant emissions the ability to affect distant environments. Pollution from Eurasia transports across the Pacific and affects local atmospheres of the Western United States [Ault *et al.*, 2011; Creamean *et al.*, 2013; Yu *et al.*, 2012]. Dust from African deserts has also been shown to travel across the Atlantic Ocean and deposit in South America [Ben-Ami *et al.*, 2009; Formenti *et al.*, 2001]. Thus, perturbations to the sulfur cycle through human activities pose a threat to the global environment due to the complex roles that sulfur species play in atmospheric processes.

### 1.4 Sinks

Sulfur species are removed from the atmosphere through several processes: chemical transformation/oxidation, dry and wet deposition. In the atmosphere, reduced sulfur species are oxidized to  $\text{SO}_2$ , and subsequently to  $\text{SO}_4^{2-}$ . Once sulfate is formed, chemical transformation is negligible due to the strong chemical stability of the  $\text{SO}_4^{2-}$  molecule. Wet deposition refers to the natural processes by which a particle is brought into the presence of condensed water through scavenging and dissolved in clouds, rain, fog, or snow [Finlayson-Pitts and Pitts, 2000; Seinfeld and Pandis, 2006]. Figure 1.3 depicts the various wet deposition processes. This includes the rainout of particles, an in-cloud scavenging process, where a



compound becomes involved in precipitation formation processes within the cloud and is removed from the atmosphere via the resultant precipitation. In addition, wash out can occur where a compound is removed from the atmosphere through entrainment by falling precipitation, resulting in below-cloud scavenging. Dry deposition, on the other hand, represents the transport of gaseous and particulate species from the atmosphere to the Earth's surface without the aid of precipitation [Seinfeld and Pandis, 2006].

The importance of wet and dry deposition to an existing species depends on many parameters including the solubility, size, and density of an existing particle [Seinfeld and Pandis, 2006]. In addition, the amount of precipitation a region receives and the type of terrain that covers the surface play roles as well. Tanaka and Turekian, (1995) determined the dry deposition rate of sulfur compared to total deposition varied from 0.05 to 0.75 throughout the year in New Haven, Connecticut with a weighted average of 0.22. Additional studies have calculated dry/wet deposition ratios ranging from 0.3-2 at various locations in the United States including Tennessee, Pennsylvania, New York, and Illinois [Hicks *et al.*, 1989]. The amount of wet deposition is highly dependent on the occurrence of precipitation events, likely creating the large variations in the calculated ratios.

## 1.5 Chemical Transformation of Sulfur Species

### 1.5.1 Reduced Sulfur Species

Reduced sulfur species mainly react in the gas phase. The main process that removes H<sub>2</sub>S from the atmosphere is via reaction with the OH<sup>•</sup> radical:



Reactions of H<sub>2</sub>S with O<sub>3</sub> and NO<sub>2</sub> are slow. The rate coefficient for the direct reaction of O<sub>3</sub> with H<sub>2</sub>S in the gas phase is less than 2\*10<sup>-20</sup> cm<sup>3</sup> molecule<sup>-1</sup> s<sup>-1</sup> at 298K, an atmospheric conversion time greater than 100 days for H<sub>2</sub>S [Becker *et al.*, 1975]. The reaction between OH<sup>•</sup> and H<sub>2</sub>S has a rate coefficient of 4.8\*10<sup>-12</sup> cm<sup>3</sup> molecule<sup>-1</sup> s<sup>-1</sup> and removes H<sub>2</sub>S in a few days [Becker *et al.*, 1975; Dlugokencky and Howard, 1988; Tyndall and Ravishankara, 1991; Warneck, 1999]. The HS<sup>•</sup> radical, formed from the reaction between H<sub>2</sub>S and OH, is highly reactive and converts to HSO in the troposphere via reaction with O<sub>2</sub>, O<sub>3</sub>, and NO<sub>2</sub> to

form HSO. The rate coefficients for the oxidation of HS<sup>·</sup> by O<sub>2</sub>, O<sub>3</sub>, and NO<sub>2</sub> are equal to 4\*10<sup>-19</sup>, 3.7\*10<sup>-12</sup>, and 5.8\*10<sup>-11</sup> cm<sup>3</sup> molecules<sup>-1</sup> s<sup>-1</sup>, respectively, resulting in a lifetime for HS<sup>·</sup> of a few seconds [Atkinson *et al.*, 1997; Finlayson-Pitts and Pitts, 2000; Stachnik and Molina, 1987]. HSO ultimately oxidizes to SO<sub>2</sub> via atmospheric oxygen [Warneck, 1999].

The lifetime for DMS is typically on the order of days, predominantly via reaction with the hydroxyl radical. One exception is in polar regions where the UV flux substantially declines during winter leading to a significant decline in OH<sup>·</sup> radical production. Oxidation via OH<sup>·</sup> is believed to proceed by two channels, abstraction of hydrogen from a methyl group and addition of OH<sup>·</sup> to the sulfur atom. The oxidative fates of the CH<sub>3</sub>SCH<sub>2</sub><sup>·</sup> radical and the CH<sub>3</sub>S(OH)CH<sub>3</sub> molecule are under considerable debate, but it is known that subsequent reaction leads to the formation of SO<sub>2</sub> and methanesulfonic acid (MSA), the two major reaction products of DMS oxidation [Hewitt and Jackson, 2009]. The nitrate radical, and possibly BrO, also play a role in the oxidation of DMS to SO<sub>2</sub> [Read *et al.*, 2008; Seinfeld and Pandis, 2006; Warneck, 2000]. Potential pathways leading to SO<sub>2</sub> and MSA are shown in Figure 1.4.

OH-induced oxidation of CS<sub>2</sub> results in relatively equal amounts of SO<sub>2</sub> and OCS as products [Barnes *et al.*, 1983; Hynes *et al.*, 1988; Jones *et al.*, 1982]. An intermediate adduct is formed that reacts with O<sub>2</sub> [Atkinson *et al.*, 1997; Shallcross *et al.*, 2003]:



Both OCS and SO<sub>2</sub> are produced rapidly, suggesting they are either formed directly from reactions 1.3 and 1.4, or formed from a very fast secondary reaction [Finlayson-Pitts and Pitts, 2000].

The oceans are the main source of OCS from direct outgassing and via oxidation of DMS and CS<sub>2</sub> as mentioned [Kettle *et al.*, 2002]. Oxidation of OCS via the OH radical in the troposphere is extremely slow with a rate coefficient of 1.96 \* 10<sup>-15</sup> cm<sup>3</sup> molecules<sup>-1</sup> s<sup>-1</sup> [DeMore *et al.*, 1987]. Owing to its long

tropospheric lifetime, 2-7 years, OCS is transported to the stratosphere where it undergoes reaction [Xu *et al.*, 2002]. OCS has a lifetime of about 10 years in the stratosphere [Chin and Davis, 1995] although recent satellite measurements have estimated a much longer stratospheric lifetime of  $64 \pm 21$  years [Barkley *et al.*, 2008]. OCS is photolyzed at a wavelength of 290 nm and shorter in the stratosphere or reacts with O atoms oxidizing to SO<sub>2</sub> [Shallcross *et al.*, 2003; Suzuki *et al.*, 1998]:



Newly formed stratospheric SO<sub>2</sub> oxidizes to SO<sub>4</sub><sup>2-</sup> via mechanisms described in the following sections, and forms a steady concentration of stratospheric sulfate aerosols (SSA) around 20 km known as the Junge layer [Junge, 1963; Whitten *et al.*, 1980]. Typical SSA concentrations are about 1-10 particles/cm<sup>3</sup> [Finlayson-Pitts and Pitts, 2000]. Large volcanic eruptions which input SO<sub>2</sub> directly into the stratosphere have been shown to increase sulfate concentration inside the Junge layer by 1-2 orders of magnitude, leading to enhanced cooling of the planet [Russell *et al.*, 1996]. However, these increased concentrations usually only last for 2-3 years before depositing back to the troposphere.

### 1.5.2 Oxidation of SO<sub>2</sub>

Most anthropogenic sulfur species produced through human activities are as SO<sub>2</sub>. Thus, constraining the oxidation pathways of SO<sub>2</sub> to SO<sub>4</sub><sup>2-</sup> are pertinent to understanding the atmospheric implications of sulfur chemistry. There are three main pathways of SO<sub>2</sub> oxidation to SO<sub>4</sub><sup>2-</sup>, homogeneous gas phase oxidation via the OH radical and heterogeneous aqueous phase oxidation via ozone and hydrogen peroxide.

### 1.5.2.1 Gas Phase Oxidation

Reaction via OH<sup>·</sup> to produce sulfate proceeds according to the following mechanism:



where M is a third body consisting of either N<sub>2</sub> or O<sub>2</sub> [Seinfeld and Pandis, 2006]. At typical atmospheric levels of OH, the lifetime of SO<sub>2</sub> is about one week.

### 1.5.2.2 Dissolution of SO<sub>2</sub> into the Aqueous Phase

Dissolution of SO<sub>2</sub> into aqueous solution is the initial step of heterogeneous oxidation to SO<sub>4</sub><sup>2-</sup>. The dissolution is pH dependent and follows the equilibrium steps [Eriksen, 1972; Harris et al., 2012; Moore et al., 2005]:



At a pH lower than 2, SO<sub>2</sub>·H<sub>2</sub>O is the dominant S(IV) form. Between pH of 3 and 6, S(IV) is mainly in the HSO<sub>3</sub><sup>-</sup> phase and above pH of 7, SO<sub>3</sub><sup>2-</sup> is the chief species. Cloud and water droplets exist at a pH of about 5.5, making HSO<sub>3</sub><sup>-</sup> the predominant sulfur species.

### 1.5.2.3 Aqueous Phase Oxidation by Dissolved O<sub>3</sub>

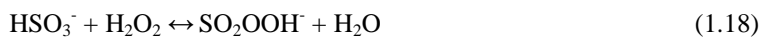
Oxidation by ozone occurs by the electrophilic displacement of O<sub>3</sub> [Savarino et al., 2000]:



The rate of S(IV) reaction with ozone in the gas phase is slow, yet rapid in aqueous phase and highly pH dependent. Ozone oxidation is the dominant mechanism at high pH, and decreases rapidly as solutions become acidic (Figure 1.5) [Lee and Thiemens, 2001]. Investigations of the reaction between S(IV) and ozone in aqueous solutions have determined that ozone reacts more rapidly with  $\text{SO}_3^{2-}$  than either  $\text{HSO}_3^-$  or  $\text{SO}_2\cdot\text{H}_2\text{O}$  [Botha et al., 1994; Hoffman and Calvert, 1985]. Hence, ozone oxidation rates are consistent with the pH dependence of  $\text{SO}_3^{2-}$  concentrations and is only relevant at pH's above typical rain and cloud droplets.

#### 1.5.2.4 Aqueous Phase Oxidation via $\text{H}_2\text{O}_2$

Atmospheric oxidation via  $\text{H}_2\text{O}_2$  is believed to proceed through nucleophilic displacement forming peroxymonosulfurous acid as an intermediate and then undergoing proton-assisted rearrangement to form sulfuric acid [Halperin and Taube, 1952; McArdle and Hoffmann, 1983]:



The rate of  $\text{H}_2\text{O}_2$  oxidation is nearly independent of pH (Figure 1.5) [Lee and Thiemens, 2001]. The rate of equation 1.19 becomes faster as the solution becomes more acidic, however, the effective Henry's Law constant for  $\text{SO}_2$  increases as pH rises. These competing variables nearly cancel each other creating a negligible dependence on pH [Seinfeld and Pandis, 2006].  $\text{H}_2\text{O}_2$  concentrations are up to six orders of magnitude higher than dissolved ozone under typical ambient conditions. Hence, aqueous oxidation of S(IV) via  $\text{H}_2\text{O}_2$  is thought to be the dominant aqueous phase oxidation pathway of S(IV) as  $\text{HSO}_3^-$  is the dominant S(IV) species in ambient atmospheric conditions.

#### 1.5.2.5 Metal Catalyzed $\text{O}_2$ oxidation of S(IV)

S(IV) can be oxidized in the aqueous phase by oxygen when catalyzed by metals such as Fe(III) and Mn(II). Studies of transition metals have been performed on cobalt, copper, and nickel, however, Fe and Mn are thought to be the most efficient transition metal catalysts for S(IV) oxidation [Bengtsson and

*Bjerles, 1975; Berglund et al., 1993; Graedel and Weschler, 1981; Grgić et al., 1991*].  $O_2$  oxidation increases with pH, but requires significant metal concentrations of  $Fe(III) = 1.0 \mu\text{molar}$  and  $Mn(II) = 0.1 \mu\text{molar}$  [*Ibusuki and Takeuchi, 1987*]. This reaction is thought to be of little importance on a global scale and is often omitted in global atmospheric chemistry models because of the large uncertainties in the atmospheric concentrations of  $Fe(III)$  and  $Mn(II)$  [*Alexander et al., 2009*]. On a regional scale, metal catalyzed oxidation of  $S(IV)$  can become significant in heavily polluted environments. For example, this oxidation pathway has been shown to contribute between 10% and 18% of the sulfate produced in Alert, Canada during the Arctic winter likely influenced by distant pollution sources from Eurasia and possibly North America [*McCabe et al., 2006*].

#### **1.5.2.6 Oxidation of S(IV) on Sea Salt Aerosols**

Deliquescent sea-salt and dust particles have been suggested as important sites for aqueous phase sulfate production [*Chameides and Stelson, 1992; Song and Carmichael, 2001*]. Due to the high  $CO_3^{2-}/HCO_3^-$  content of seawater, sea salt aerosols have a high alkalinity relative to clouds and atmospheric water. Uptake of  $SO_2$  and  $HNO_3$  are important for titrating sea-salt aerosol alkalinity. Titration by  $SO_2$  is most important at extratropical northern latitudes where anthropogenic emissions are high, while titration by  $HNO_3$  is more important in the tropics where  $NO_x$  emissions from soils, biomass burning, and lightning dominate  $SO_2$  emissions [*Alexander et al., 2005*]. Due to the high pH, uptake of  $SO_2$  by sea salt aerosols is driven by the  $SO_3^{2-} + O_3$  aqueous phase reaction. Once the alkalinity is consumed, the pH of the aerosols drops and effectively shuts off the ozone oxidation mechanism [*Chameides and Stelson, 1992*].

#### **1.6.1 Size Segregation**

Atmospheric aerosols consist of particles ranging in size, from tens of angstroms to several hundred micrometers. Particle size affects the physical and chemical properties of each aerosol and plays an important role in the deposition lifetime. The distribution of particles, Figure 1.6, results in three distinct size ranges including the nuclei mode, diameter less than  $0.1 \mu\text{m}$ , accumulation mode, diameter between  $0.1\text{-}1 \mu\text{m}$ , and coarse mode, consisting of particles with a diameter greater than  $1 \mu\text{m}$ . The nuclei mode is the largest mode by number, however, due to their small size, make up only a few percent of the total aerosol

mass budget. The nuclei mode consists primary of combustion particles emitted directly to the atmosphere and particles formed by gas-to-particle conversion. The accumulation mode accounts for the highest aerosol surface area of any mode. Sources include combustion particles, and coagulation of nuclei particles. The sizes of accumulation particles are most effective at scattering visible light and account for most visibility effects associated with aerosols. The combination of nuclei and accumulation size ranges collectively constitute the fine particle mode. Coarse particles represent the largest mode by volume and arise from mechanical processes, usually from anthropogenic sources or natural dust and sea spray emissions [Finlayson-Pitts and Pitts, 2000].

The size of a particle affects its lifetime in the atmosphere [Seinfeld and Pandis, 2006]. Coarse particles are large enough to be effected by gravitational forces and settle out of the atmosphere with lifetimes on the order of days. Large coarse particles ( $>10\ \mu\text{m}$ ) rapidly fall out of the air and can have lifetimes on the order of minutes to hours [Webb *et al.*, 2008]. Gravity exerts minimal force on small particles resulting in a slow sedimentation velocity allowing atmospheric mixing processes to become dominant. Even though nuclei mode particles aren't strongly affected by gravity, they have a relatively short lifetime of minutes to days due to their chemical reactivity and physical mobility. These particles grow larger through the condensation of low-volatility gases such as  $\text{H}_2\text{SO}_4$ ,  $\text{HNO}_3$ , and  $\text{NH}_3$ . This process is most effective when the production rate of low-volatility gases is high and the total surface area of the particles is low [Pierce and Adams, 2007]. Additionally, growth through Brownian coagulation occurs in the nuclei mode where particles combine together to form a single, larger particle. Over a series of reactions, these particles grow in size and are incorporated into the accumulation mode. Accumulation particles are largely lost by wet and dry deposition as both gravitational settling and coagulation are slow [Saltzman, 2013]. This results in a longer lifetime relative to nuclei and coarse particles, ranging on the order of a week or two.

### **1.6.2 Nanoparticles**

Over the last few decades, nanosized particles ( $\leq 100\ \text{nm}$  diameters) have received attention from the scientific community. These particles constitute a special class within the nuclei size range known as

the ultrafine particle mode. Their small sizes and large reactive surface areas have led to increased use in fields such as medicine, materials science, electronics, and energy storage [Aguar Fernandez and Hullmann, 2007; Helland et al., 2006]. As with other particles in the nuclei size mode, nanoparticles can be produced through both natural and anthropogenic sources such as volcanic eruptions, biological processes, and combustion. Many studies have detected large concentrations of these small nanosized particles near clouds and close to the tropopause [Keil and Wendisch, 2001; Twohy et al., 2002]. Frequent observations have shown the presence of 1-3 nm sized particles followed by subsequent growth to about 100 nm over the course of a few days [Creamean et al., 2011; Kulmala et al., 2004]. Nanoparticles are important precursors to the formation of larger particles that strongly influence global climate. Constraints on the formation and growth patterns of these small particles are important to developing a complete understanding of aerosol chemistry and cloud formation processes.

Atmospheric nanoparticles also represent an area of growing health concern. Their small size allows them to be breathed deeply into the lungs and enter the blood stream [Terzano et al., 2010]. They may also translocate within the body to the central nervous system, the brain, and into organs such as the liver [Helland et al., 2008]. Nanoparticles are more reactive and toxic than larger particles due to their enhanced surface areas, potentially leading to detrimental health effects [Buseck and Adachi, 2008; Nel et al., 2006; Slezakova et al., 2013]. Unlike fine and coarse particles, regulatory laws regarding nanoparticles have not been created. Reliable characterization of airborne nanoparticles is thus vital for developing the framework necessary to properly address regulatory issues in an effort to prevent public exposures [Kulmala et al., 2004].

### **1.7 Climatic Impact: Direct and Indirect Effects**

Sulfate particles affect the radiation budget of the planet through their ability to scatter light. Particles most effective at scattering light at visible wavelengths back to space (direct effect) include the size ranges of 0.2 to about 4  $\mu\text{m}$  and exhibit a negative net radiative forcing. Larger particles can absorb at infrared wavelengths and warm the surrounding air directly. The amount of total scattering is measured by the single scattering albedo which is equivalent to the fraction of radiation reflected by a particle surface.



Particles with a single scattering albedo above 0.85 usually lead to a net cooling, while those below 0.85, a net warming [Penner *et al.*, 2001]. The IPCC suggests that aerosol scattering constituents about a  $-0.5 \text{ W/m}^2$  forcing on the planet's radiation budget, though this value comes with significant uncertainty.

Sulfate particles are a dominant component of clouds and serve as cloud condensation nuclei (CCN) for water droplet formation (indirect effect). The indirect effect of aerosols is one of the largest uncertainties in predicting future climate changes [Ramanathan *et al.*, 2001]. Increases in sulfate aerosols will likely increase the number of cloud droplets, however, assuming constant atmospheric water content, this will decrease the overall size of each droplet affecting light scattering properties, overall lifetime, and precipitation patterns. Formation of sulfate in the gas phase results in the formation of new particles, thus increasing the amount of CCN available for cloud formation [Alexander *et al.*, 2005; Andronache *et al.*, 1997]. However, sulfate aerosols formed via aqueous phase oxidation do not form new particles as this mechanism of oxidation occurs on existing particles [Kulmala *et al.*, 2000; Stockwell and Calvert, 1983]. Therefore, the amount of indirect forcing from sulfate aerosols is highly sensitive not only to overall concentrations, but also to their formation pathways. Improved understanding of sulfate oxidation pathways and transport through the atmosphere can lead better estimations of future climate change.

Isotopic measurements have been used to constrain mechanistic pathways of aerosol formation and are the basis of this thesis. Here, we utilize oxygen isotopic ratio measurements and take advantage of mass independent fractionation theory to quantify formation pathways of  $\text{SO}_2$  oxidation to  $\text{SO}_4^{2-}$ . These measurements allow one to estimate the importance of  $\text{SO}_2$  oxidation pathways via OH,  $\text{H}_2\text{O}_2$ , and  $\text{O}_3$ . Knowledge of the formation pathways can help predict the formation of new CCN particles. In addition, radioactive  $^{35}\text{S}$  is studied in combination with oxygen isotopes as an additional constraint on sulfate formation.  $^{35}\text{S}$  is a unique tracer that can be used to trace the sulfur cycle through both gas and particle phases.  $^{35}\text{S}$  is formed from cosmogenic spallation, thus its production rate in the atmosphere is dependent on altitude and latitude. Therefore,  $^{35}\text{S}$  can be taken advantage of as a chronological clock tracing past locations of the collected air mass. The combination of these tracers can lead to a better understanding of how sulfate formation pathways vary due to changes in atmospheric circulation patterns. This ability is extremely important when trying to predict how future weather patterns and climate change will affect

aerosol production and down the road, can potentially be used to improve future model estimates of CCN production.

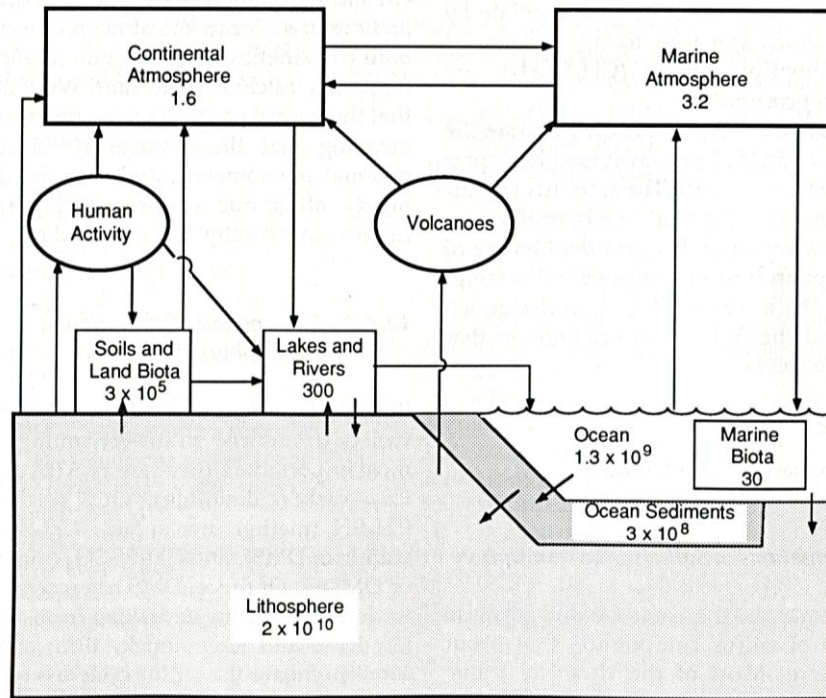


Figure 1.1

Burdens of sulfur for the lithosphere, hydrosphere, and atmosphere including the estimated transport fluxes between each reservoir. Units are in Tg ( $10^{12}$  g). [Charlson *et al.*, 1992]

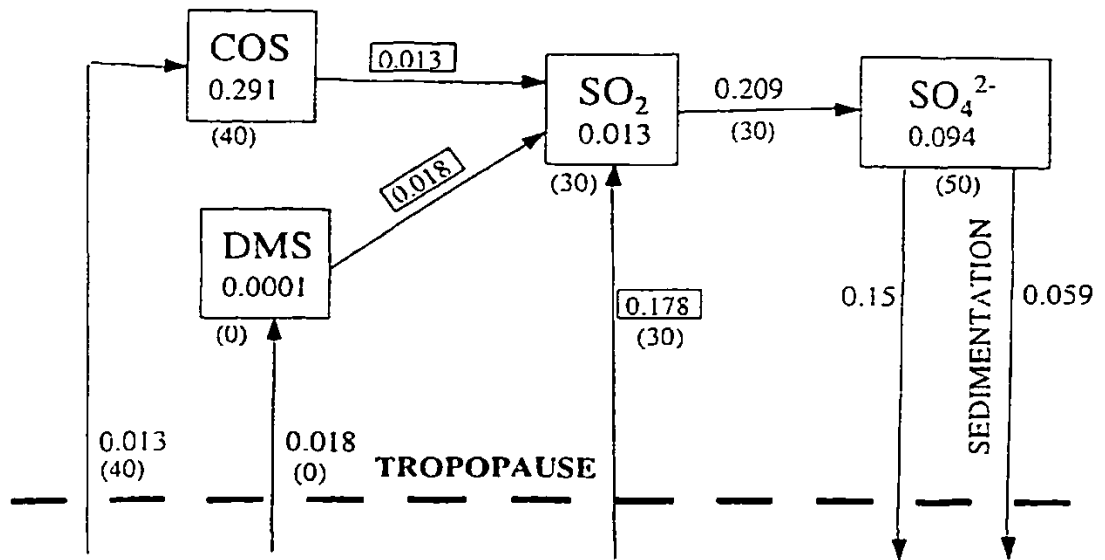


Figure 1.2

Global burdens (Tg S) and fluxes (Tg/yr) of stratospheric sulfur during non-volcanic periods. Numbers in brackets represent the percent of anthropogenic contribution [Rodhe, 1999].

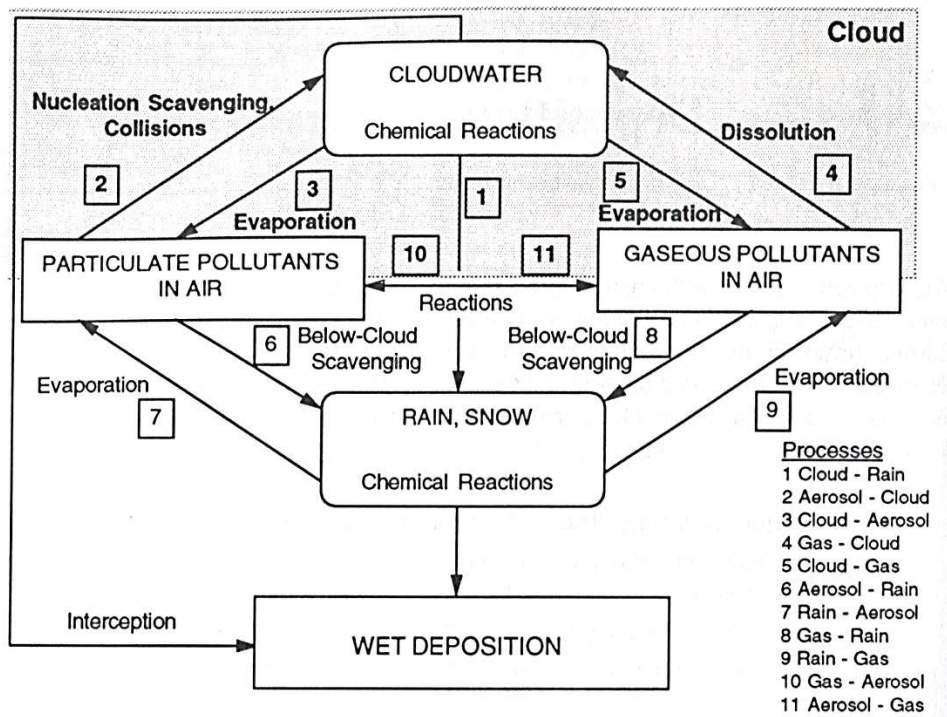


Figure 1.3

Conceptual framework of the wet deposition process. Image obtained from Seinfeld and Pandis, (2006).



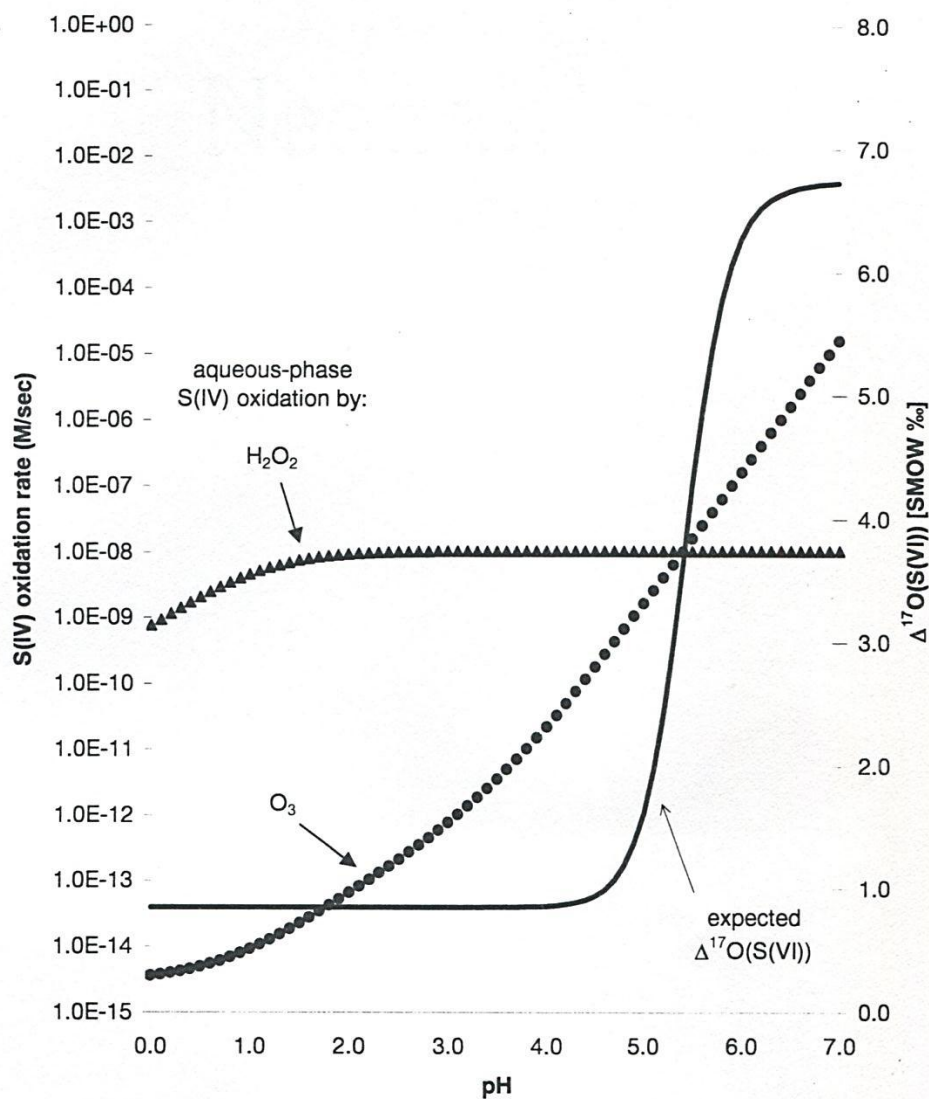
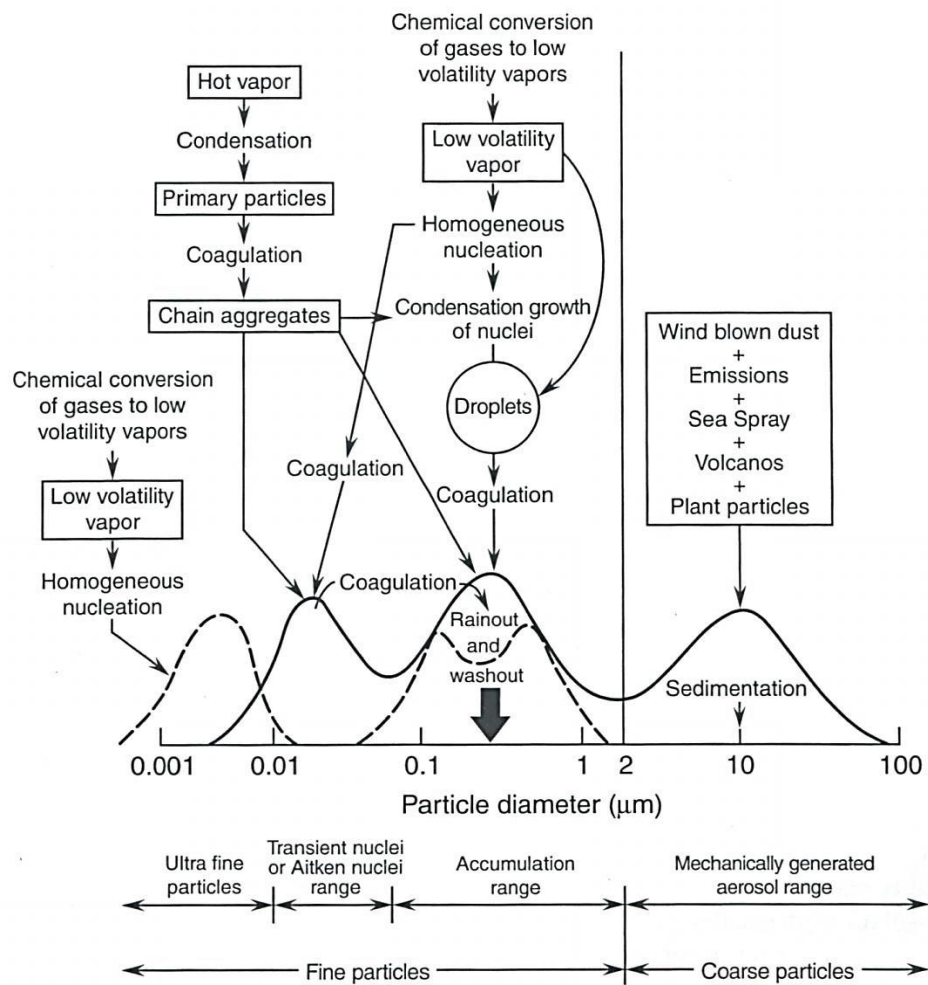


Figure 1.5

Depiction of the pH dependence on the rate of reaction for the main aqueous oxidative pathways of  $\text{SO}_2$  to  $\text{SO}_4^{2-}$ . Ozone oxidation is highly pH dependent, whereas hydrogen peroxide oxidation is relatively constant. As a result, ozone is the main oxidant at a high pH and hydrogen peroxide is the main oxidant at a lower pH. The estimated  $\Delta^{17}\text{O}$  values are also shown which are discussed in detail in chapter 2 of this thesis. Image obtained from *Lee and Thiemens, (2001)*.



**Figure 1.6**

Schematic of the main modes of atmospheric aerosol size distributions. Fine particles are broken down into nuclei and accumulation and coarse modes. Ultra-fine particles are usually blended with the nuclei particle mode. Image obtained from *Finlayson-Pitts and Pitts, (2000)*.



Table 1.1:

Atmospheric Sulfur Compounds [Lee, 2000]

Oxidation State	Compound Name	Chemical Formula	Chemical Structure	Phase
-2	Hydrogen sulfide	H <sub>2</sub> S	H-S-H	Gas
	Dimethyl sulfide	CH <sub>3</sub> SCH <sub>3</sub>	CH <sub>3</sub> -S-CH <sub>3</sub>	Gas
	Carbon disulfide	CS <sub>2</sub>	S=C=S	Gas
	Carbon sulfide	OCS	O=C=S	Gas
	Methyl mercaptan	CH <sub>3</sub> SH	CH <sub>3</sub> -S-H	Gas
-1	Dimethyl disulfide (DMS)	CH <sub>3</sub> SSCH <sub>3</sub>	CH <sub>3</sub> -S-S-CH <sub>3</sub>	Gas
0	Dimethyl sulfoxide	CH <sub>3</sub> SOCH <sub>3</sub>	$\begin{array}{c} \text{O} \\    \\ \text{CH}_3\text{-S-CH}_3 \end{array}$	Gas
2	Dimethyl sulfone	CH <sub>3</sub> SO <sub>2</sub> CH <sub>3</sub>	$\begin{array}{c} \text{O} \\    \\ \text{CH}_3\text{-S-CH}_3 \\    \\ \text{O} \end{array}$	Gas
	Hydroxymethane sulfonic acid (HMSA)	HOCH <sub>2</sub> SO <sub>3</sub> H	$\begin{array}{c} \text{O} \\    \\ \text{HOCH}_2\text{-S-CH}_3 \\    \\ \text{O} \end{array}$	Aqueous
4	Sulfur dioxide	SO <sub>2</sub> SO <sub>2</sub> ·H <sub>2</sub> O	O=S=O	Gas Aqueous
	Bisulfite ion	HSO <sub>3</sub> <sup>-</sup>		Aqueous
	Sulfite ion	SO <sub>3</sub> <sup>2-</sup>		Aqueous
	Methane sulfonic acid (MSA)	CH <sub>3</sub> SO <sub>3</sub> H	$\begin{array}{c} \text{O} \\    \\ \text{CH}_3\text{-S-OH} \\    \\ \text{O} \end{array}$	Gas/aqueous
6	Sulfuric acid	H <sub>2</sub> SO <sub>4</sub>	$\begin{array}{c} \text{O} \\    \\ \text{HO-S-OH} \\    \\ \text{O} \end{array}$	Gas, Aqueous/aerosol
	Bisulfate ion	HSO <sub>4</sub> <sup>-</sup>	$\begin{array}{c} \text{O} \\    \\ \text{HO-S-O}^- \\    \\ \text{O} \end{array}$	Aqueous/aerosol
	Sulfate ion	SO <sub>4</sub> <sup>2-</sup>	$\begin{array}{c} \text{O} \\    \\ \text{}^- \text{O-S-O}^- \\    \\ \text{O} \end{array}$	Aqueous/aerosol

## 1.8 References

Aguar Fernandez, M. P., and A. Hullmann (2007), A boost for safer nanotechnology, *Nano Today*, 2(1), 56.

Alexander, B. (2002), Mass-independent isotopic compositions in oxygen containing molecules as a tool to investigate present and past changes in the Earth's oxidation capacity, University of California, San Diego (Thesis).

Alexander, B., R. J. Park, D. J. Jacob, and S. Gong (2009), Transition metal-catalyzed oxidation of atmospheric sulfur: Global implications for the sulfur budget, *J. Geophys. Res.*, 114, D02309, doi: 10.1029/2008JD010486.

Alexander, B., R. J. Park, D. J. Jacob, Q. B. Li, R. M. Yantosca, J. Savarino, C. C. W. Lee, and M. H. Thiemens (2005a), Sulfate formation in sea-salt aerosols: Constraints from oxygen isotopes, *J. Geophys. Res.-Atmos.*, 110, D10307, doi: 10.1029/2004JD005659.

Alexander, B., R. J. Park, D. J. Jacob, Q. B. Li, R. M. Yantosca, J. Savarino, C. C. W. Lee, and M. H. Thiemens (2005b), Sulfate formation in sea-salt aerosols: Constraints from oxygen isotopes, *Journal of Geophysical Research: Atmospheres*, 110(D10), D10307.

Andreae, M. O. (1990), Ocean-atmosphere interactions in the global biogeochemical sulfur cycle, *Marine Chemistry*, 30, 1-29.

Andreae, T., G. Cutter, N. Hussain, J. Radford-knoery, and M. Andreae (1991), Hydrogen sulfide and radon in and over the western North Atlantic Ocean, *Journal of Geophysical Research: Atmospheres (1984–2012)*, 96(D10), 18753-18760.

Andreas, E. L. (1998), A new sea spray generation function for wind speeds up to 32 m s<sup>-1</sup>, *Journal of Physical Oceanography*, 28(11), 2175-2184.

Andronache, C., W. L. Chameides, D. D. Davis, B. E. Anderson, R. F. Pueschel, A. R. Bandy, D. C. Thornton, R. W. Talbot, P. Kasibhatla, and C. S. Kiang (1997), Gas-to-particle conversion of tropospheric sulfur as estimated from observations in the western North Pacific during PEM-West B, *Journal of Geophysical Research: Atmospheres*, 102(D23), 28511-28538.

Arimoto, R., R. Duce, D. Savoie, and J. Prospero (1992), Trace elements in aerosol particles from Bermuda and Barbados: Concentrations, sources and relationships to aerosol sulfate, *Journal of Atmospheric Chemistry*, 14(1-4), 439-457.

Atkinson, R., D. Baulch, R. Cox, R. Hampson Jr, J. Kerr, M. Rossi, and J. Troe (1997), Evaluated kinetic and photochemical data for atmospheric chemistry: supplement VI. IUPAC subcommittee on gas kinetic data evaluation for atmospheric chemistry, *Journal of Physical and Chemical Reference Data*, 26(6), 1329-1499.

Ault, A. P., C. R. Williams, A. B. White, P. J. Neiman, J. M. Creamean, C. J. Gaston, F. M. Ralph, and K. A. Prather (2011), Detection of Asian dust in California orographic precipitation, *Journal of Geophysical Research: Atmospheres (1984–2012)*, 116(D16).

Ault, A. P., R. C. Moffet, J. Baltrusaitis, D. B. Collins, M. J. Ruppel, L. A. Cuadra-Rodriguez, D. Zhao, T. L. Guasco, C. J. Ebben, and F. M. Geiger (2013), Size-dependent changes in sea spray aerosol composition and properties with different seawater conditions, *Environmental Science & Technology*, 47(11), 5603-5612.

Ayers, G. P., J. M. Caine, R. W. Gillett, and J. P. Ivey (1997), Atmospheric sulphur and cloud condensation nuclei in marine air in the Southern Hemisphere, *Philosophical Transactions of the Royal Society of London Series B-Biological Sciences*, 352(1350), 203-211.

Barkley, M. P., P. I. Palmer, C. D. Boone, P. F. Bernath, and P. Suntharalingam (2008), Global distributions of carbonyl sulfide in the upper troposphere and stratosphere, *Geophysical Research Letters*, 35(14).

Barnes, I., K. Becker, E. Fink, A. Reimer, F. Zabel, and H. Niki (1983), Rate constant and products of the reaction  $\text{CS}_2 + \text{OH}$  in the presence of  $\text{O}_2$ , *International Journal of Chemical Kinetics*, 15(7), 631-645.

Barthel, S., I. Tegen, R. Wolke, and M. van Pinxteren (2014), Model study on the dependence of primary marine aerosol emission on the sea surface temperature, *Atmospheric Chemistry & Physics Discussions*, 14(1).

Becker, K. H., M. A. Inocencio, and U. Schurath (1975), Reaction of Ozone with Hydrogen-Sulfide and its Organic Derivatives, *International Journal of Chemical Kinetics*, 1, 205-220.

Belviso, S., B. C. Nguyen, and P. Allard (1986), Estimate of carbonyl sulfide (OCS) volcanic source strength deduced from OCS/ $\text{CO}_2$  ratios in volcanic gases, *Geophysical Research Letters*, 13(2), 133-136.

Ben-Ami, Y., I. Koren, and O. Altaratz (2009), Patterns of North African dust transport over the Atlantic: winter vs. summer, based on CALIPSO first year data, *Atmospheric Chemistry and Physics*, 9(20), 7867-7875.

Bengtsson, S., and I. Bjerles (1975), Catalytic oxidation of sulphite in diluted aqueous solutions, *Chemical Engineering Science*, 30(11), 1429-1435.

Berglund, J., S. Fronaeus, and L. I. Elding (1993), Kinetics and mechanism for manganese-catalyzed oxidation of sulfur (IV) by oxygen in aqueous solution, *Inorg Chem*, 32(21), 4527-4538.

Blanchard, D. C. (1964), Sea-to-air transport of surface active material, *Science*, 146(3642), 396-397.

- Botha, C. F., J. Hahn, J. J. Pienaar, and R. Van Eldik (1994), Kinetics and mechanism of the oxidation of sulfur (IV) by ozone in aqueous solutions, *Atmos Environ*, 28(20), 3207-3212.
- Buseck, P. R., and K. Adachi (2008), Nanoparticles in the atmosphere, *Elements*, 4(6), 389-394.
- Cainey, J. M., G. P. Ayers, H. Sievering, R. W. Gillett, and M. A. Hooper (1999), The use of magnesium as a marker for sea salt at Cape Grim, *Baseline Atmospheric Program-1996*.
- Chameides, W. L., and A. W. Stelson (1992), Aqueous-Phase Chemical Processes in Deliquescent Sea-Salt Aerosols - a Mechanism That Couples the Atmospheric Cycles of S and Sea Salt, *J Geophys Res-Atmos*, 97(D18), 20565-20580.
- Charlson, R. J., T. L. Anderson, and R. E. McDuff (1992), *The Sulfur Cycle, Global Biogeochemical Cycles*, Academic Press.
- Chin, M., and D. Davis (1993), Global sources and sinks of OCS and CS<sub>2</sub> and their distributions, *Global Biogeochemical Cycles*, 7(2), 321-337.
- Chin, M., and D. Davis (1995), A reanalysis of carbonyl sulfide as a source of stratospheric background sulfur aerosol, *Journal of geophysical research*, 100(D5), 8993-9005.
- Chin, M., and D. J. Jacob (1996), Anthropogenic and natural contributions to tropospheric sulfate: A global model analysis, *J. Geophys. Res.*, 101(D13), 18691-18699.
- Creamean, J. M., A. P. Ault, J. E. Ten Hoeve, M. Z. Jacobson, G. C. Roberts, and K. A. Prather (2011), Measurements of Aerosol Chemistry during New Particle Formation Events at a Remote Rural Mountain Site, *Environmental Science & Technology*, 45(19), 8208-8216.
- Creamean, J. M., et al. (2013), Dust and Biological Aerosols from the Sahara and Asia Influence Precipitation in the Western U.S., *Science*, 339(6127), 1572-1578.
- De Bruyn, W. J., E. Swartz, J. H. Hu, J. A. Shorter, P. Davidovits, D. R. Worsnop, M. S. Zahniser, and C. E. Kolb (1995), Henry's law solubilities and Setchenow coefficients for biogenic reduced sulfur species obtained from gas-liquid uptake measurements, *Journal of Geophysical Research: Atmospheres*, 100(D4), 7245-7251.
- De Kok, L. J., M. Durenkamp, L. Yang, and I. Stulen (2007), Atmospheric sulfur, in *Sulfur in Plants An Ecological Perspective*, edited, pp. 91-106, Springer.
- de Leeuw, G., E. L. Andreas, M. D. Anguelova, C. W. Fairall, E. R. Lewis, C. O'Dowd, M. Schulz, and S. E. Schwartz (2011), Production flux of sea spray aerosol, *Reviews of Geophysics*, 49(2), RG2001.

- DeMore, W. B., M. Molina, S. Sander, D. Golden, R. Hampson, M. Kurylo, C. Howard, and A. R. Ravishankara (1987), Chemical kinetics and photochemical data for use in stratospheric modeling evaluation Number 8.
- Dlugokencky, E. J., and C. J. Howard (1988), Laboratory studies of nitrate radical reactions with some atmospheric sulfur compounds, *The Journal of Physical Chemistry*, 92(5), 1188-1193.
- Eriksen, T. E. (1972), Sulfur isotope effects, *Acta Chem. Scand*, 26(2), 11.
- Finlayson-Pitts, B., and J. Pitts (2000), Chemistry of the upper and lower atmosphere: Theory, Experiments, and Applications, edited, Academic Press: New York.
- Formenti, P., M. Andreae, L. Lange, G. Roberts, J. Cafmeyer, I. Rajta, W. Maenhaut, B. Holben, P. Artaxo, and J. Lelieveld (2001), Saharan dust in Brazil and Suriname during the Large-Scale Biosphere-Atmosphere Experiment in Amazonia (LBA)-Cooperative LBA Regional Experiment (CLAIRE) in March 1998, *Journal of Geophysical Research: Atmospheres (1984–2012)*, 106(D14), 14919-14934.
- Graedel, T., and C. Weschler (1981), Chemistry within aqueous atmospheric aerosols and raindrops, *Reviews of Geophysics*, 19(4), 505-539.
- Grgić, I., V. Hudnik, M. Bizjak, and J. Levec (1991), Aqueous S (IV) oxidation—I. Catalytic effects of some metal ions, *Atmospheric Environment. Part A. General Topics*, 25(8), 1591-1597.
- Halperin, J., and H. Taube (1952), The Transfer of Oxygen Atoms in Oxidation—Reduction Reactions. IV. The Reaction of Hydrogen Peroxide with Sulfite and Thiosulfate, and of Oxygen, Manganese Dioxide and of Permanganate with Sulfite, *Journal of the American Chemical Society*, 74(2), 380-382.
- Harris, E., B. Sinha, P. Hoppe, J. Crowley, S. Ono, and S. Foley (2012), Sulfur isotope fractionation during oxidation of sulfur dioxide: gas-phase oxidation by OH radicals and aqueous oxidation by H<sub>2</sub>O<sub>2</sub>, O<sub>3</sub> and iron catalysis, *Atmospheric Chemistry and Physics*, 12(1), 407-423.
- Helland, A., H. Kastenholz, A. Thidell, P. Arnfalk, and K. Deppert (2006), Nanoparticulate materials and regulatory policy in Europe: an analysis of stakeholder perspectives, *Journal of Nanoparticle Research*, 8(5), 709-719.
- Helland, A., P. Wick, A. Koehler, K. Schmid, and C. Som (2008), Reviewing the environmental and human health knowledge base of carbon nanotubes, *Ciência & Saúde Coletiva*, 13(2), 441-452.
- Hewitt, C. N., and A. V. Jackson (2009), *Atmospheric science for environmental scientists*, John Wiley & Sons.

Hicks, B. B., T. P. Meyers, C. W. Fairall, V. A. Mohnen, and D. A. Dolske (1989), Ratios of dry to wet deposition of sulfur as derived from preliminary field data, *Global Biogeochemical Cycles*, 3(2), 155-162.

Hoffman, M., and J. Calvert (1985), Chemical transformation modules for eulerian acid deposition models, *The Aqueous Phase Chemistry*, 2, 3-85.

Hynes, A. J., P. H. Wine, and J. M. Nicovich (1988), Kinetics and Mechanism of the Reaction of OH with CS<sub>2</sub> under Atmospheric Conditions, *Journal of Physical Chemistry*, 92(13), 3846-3852.

Ibusuki, T., and K. Takeuchi (1987), Sulfur dioxide oxidation by oxygen catalyzed by mixtures of manganese (II) and iron (III) in aqueous solutions at environmental reaction conditions, *Atmospheric Environment (1967)*, 21(7), 1555-1560.

Innes, J. L., M. Beniston, and M. M. Verstraete (2000), *Biomass burning and its inter-relationships with the climate system*, Springer.

Jones, B. M. R., J. P. Burrows, R. A. Cox, and S. A. Penkett (1982), OCS Formation in the Reaction of OH with CS<sub>2</sub>, *Chemical Physics Letters*, 88(4), 372-376.

Junge, C. E. (1963), *Air chemistry and radioactivity*, Academic, New York.

Keil, A., and M. Wendisch (2001), Bursts of Aitken mode and ultrafine particles observed at the top of continental boundary layer clouds, *Journal of aerosol science*, 32(5), 649-660.

Kettle, A., U. Kuhn, M. Von Hobe, J. Kesselmeier, and M. Andreae (2002), Global budget of atmospheric carbonyl sulfide: Temporal and spatial variations of the dominant sources and sinks, *Journal of Geophysical Research: Atmospheres (1984-2012)*, 107(D22), ACH 25-21-ACH 25-16.

Khalil, M., and R. Rasmussen (1984), Global sources, lifetimes and mass balances of carbonyl sulfide (OCS) and carbon disulfide (CS<sub>2</sub>) in the earth's atmosphere, *Atmospheric Environment*, 18(9), 1805-1813.

Kloster, S., J. Feichter, E. M. Reimer, K. D. Six, P. Stier, and P. Wetzal (2006), DMS cycle in the marine ocean-atmosphere system - a global model study, *Biogeosciences*, 3(1), 29-51.

Kulmala, M., L. Pirjola, and J. M. Mäkelä (2000), Stable sulphate clusters as a source of new atmospheric particles, *Nature*, 404(6773), 66-69.

Kulmala, M., H. Vehkamäki, T. Petäjä, M. Dal Maso, A. Lauri, V.-M. Kerminen, W. Birmili, and P. H. McMurry (2004), Formation and growth rates of ultrafine atmospheric particles: a review of observations, *Journal of aerosol science*, 35(2), 143-176.

Lee, C. C.-W. (2000), Multiple stable oxygen isotopic studies of atmospheric sulfate: A new quantitative way to understand sulfate formation processes in the atmosphere, University of California, San Diego (Thesis).

Lee, C. C.-W., and M. H. Thiemens (2001), The  $\delta^{17}\text{O}$  and  $\delta^{18}\text{O}$  measurements of atmospheric sulfate from a coastal and high alpine region: A mass-independent isotopic anomaly, *Journal of geophysical research*, 106(D15), 17359-17317,17373.

Lewis, R., and E. Schwartz (2004), Sea Salt Aerosol Production: Mechanisms, Methods, Measurements and Models- A Critical Review, *Geophys. Monoge. Ser.*, vol. 152, 413 pp., AGU, Washington, D.C., doi:10.1029/GM152.

Lide, D. R. (2004), *CRC Handbook of Chemistry and Physics*, CRC press.

Martens, C. S., J. J. Wesolowski, R. C. Harriss, and R. Kaifer (1973), Chlorine Loss from Puerto-Rican and San-Francisco Bay Area Marine Aerosols, *Eos. T. Am. Geophys. Un.*, 54(4), 283-283.

Mårtensson, E., E. Nilsson, G. de Leeuw, L. Cohen, and H. C. Hansson (2003), Laboratory simulations and parameterization of the primary marine aerosol production, *Journal of Geophysical Research: Atmospheres (1984–2012)*, 108(D9).

McArdle, J. V., and M. R. Hoffmann (1983), Kinetics and mechanism of the oxidation of aquated sulfur dioxide by hydrogen peroxide at low pH, *The Journal of Physical Chemistry*, 87(26), 5425-5429.

McCabe, J. R., J. Savarino, B. Alexander, S. L. Gong, and M. H. Thiemens (2006), Isotopic constraints on non-photochemical sulfate production in the Arctic winter, *Geophys. Res. Lett.*, 33, L05810, doi: 10.1029/2005GL025164.

Millero, F. J. (1974), The physical chemistry of seawater, *Annual Review of Earth and Planetary Sciences*, 2, 101.

Minikin, A., M. Legrand, J. Hall, D. Wagenbach, C. Kleefeld, E. Wolff, E. C. Pasteur, and F. Ducroz (1998), Sulfur-containing species (sulfate and methanesulfonate) in coastal Antarctic aerosol and precipitation, *Journal of Geophysical Research: Atmospheres (1984–2012)*, 103(D9), 10975-10990.

Monahan, E. C., C. W. Fairall, K. L. Davidson, and P. J. Boyle (1983), Observed inter-relations between 10m winds, ocean whitecaps and marine aerosols, *Quarterly Journal of the Royal Meteorological Society*, 109(460), 379-392.

Moore, J., C. Stanitski, and P. Jurs (2005), *Chemistry: The Molecular Science*, Brooks/Cole, Thompson Learning, USA. A31-A32.

Nel, A., T. Xia, L. Mädler, and N. Li (2006), Toxic potential of materials at the nanolevel, *Science*, 311(5761), 622-627.

O'Dowd, C. D., and M. H. Smith (1993), Physicochemical properties of aerosols over the northeast Atlantic: Evidence for wind-speed-related submicron sea-salt aerosol production, *Journal of Geophysical Research: Atmospheres (1984–2012)*, 98(D1), 1137-1149.

Penner, J. E., D. Hegg, and R. Leaitch (2001), Unraveling the role of aerosols in climate change, *Environ Sci Technol*, 35(15), 332A-340A.

Pierce, J., and P. Adams (2007), Efficiency of cloud condensation nuclei formation from ultrafine particles, *Atmospheric Chemistry and Physics*, 7(5), 1367-1379.

Preunkert, S., M. Legrand, B. Jourdain, C. Moulin, S. Belviso, N. Kasamatsu, M. Fukuchi, and T. Hirawake (2007), Interannual variability of dimethylsulfide in air and seawater and its atmospheric oxidation by-products (methanesulfonate and sulfate) at Dumont d'Urville, coastal Antarctica (1999–2003), *Journal of geophysical research*, 112(D6), D06306.

Ramanathan, V., P. J. Crutzen, J. T. Kiehl, and D. Rosenfeld (2001), Aerosols, Climate, and the Hydrological Cycle, *Science*, 294(5549), 2119-2124.

Read, K. A., et al. (2008), DMS and MSA measurements in the Antarctic Boundary Layer: Impact of BrO on MSA production, *Atmospheric Chemistry and Physics*, 8(11), 2985-2997, doi: 10.5194/acp-8-2985-2008.

Rodhe, H. (1999), Human impact on the atmospheric sulfur balance, *Tellus A*, 51(1), 110-122.

Russell, P., J. Livingston, R. Pueschel, J. Bauman, J. Pollack, S. Brooks, P. Hamill, L. Thomason, L. Stowe, and T. Deshler (1996), Global to microscale evolution of the Pinatubo volcanic aerosol derived from diverse measurements and analyses, *Journal of Geophysical Research: Atmospheres (1984–2012)*, 101(D13), 18745-18763.

Saltzman, E. S. (2013), Marine Aerosols, in *Surface Ocean–Lower Atmosphere Processes*, edited, pp. 17-35, American Geophysical Union.

Savarino, J., C. C. W. Lee, and M. H. Thiemens (2000), Laboratory oxygen isotopic study of sulfur (IV) oxidation: Origin of the mass-independent oxygen isotopic anomaly in atmospheric sulfates and sulfate mineral deposits on Earth, *J. Geophys. Res.-Atmos.*, 105(D23), 29079-29088, doi: 10.1029/2000JD900456.

Seinfeld, J. H., and S. N. Pandis (1998), *Atmospheric Chemistry and Physics: From Air Pollution to Climate Change*, Wiley-Interscience, New York.



Seinfeld, J. H., and S. N. Pandis (2006), *Atmospheric Chemistry and Physics: From Air Pollution to Climate Change*, 2nd ed., Wiley, New York.

Shallcross, D., K.-Y. Wang, and C. H. Dimmer (2003), Biogeochemical Cycles and Residence Times, *Handbook of Atmospheric Science: Principles and Applications*, 90-123.

Sievering, H., J. Caine, M. Harvey, J. McGregor, S. Nichol, and P. Quinn (2004), Aerosol non-sea-salt sulfate in the remote marine boundary layer under clear-sky and normal cloudiness conditions: Ocean-derived biogenic alkalinity enhances sea-salt sulfate production by ozone oxidation, *J. Geophys. Res.-Atmos.*, 109(D19).

Slezakova, K., S. Morais, and M. do Carmo Pereira (2013), Atmospheric Nanoparticles and Their Impacts on Public Health.

Solomon, S., J. S. Daniel, R. R. Neely, J.-P. Vernier, E. G. Dutton, and L. W. Thomason (2011), The Persistently Variable "Background" Stratospheric Aerosol Layer and Global Climate Change, *Science*, 333(6044), 866-870.

Song, C. H., and G. R. Carmichael (2001), A three-dimensional modeling investigation of the evolution processes of dust and sea-salt particles in east Asia, *J Geophys Res-Atmos*, 106(D16), 18131-18154.

Stachnik, R., and M. Molina (1987), Kinetics of the reactions of mercapto radicals with nitrogen dioxide and oxygen, *Journal of Physical Chemistry*, 91(17), 4603-4606.

Stern, D. I. (2005), Global sulfur emissions from 1850 to 2000, *Chemosphere*, 58(2), 163-175.

Stevenson, D., C. Johnson, W. Collins, and R. Derwent (2003), The tropospheric sulphur cycle and the role of volcanic SO<sub>2</sub>, *Geological Society, London, Special Publications*, 213(1), 295-305.

Stockwell, W. R., and J. G. Calvert (1983), The mechanism of the HO-SO<sub>2</sub> reaction, *Atmospheric Environment*, 17(11), 2231-2235.

Stoiber, R. E., S. N. Williams, and B. Huebert (1987), Annual contribution of sulfur dioxide to the atmosphere by volcanoes, *Journal of Volcanology and Geothermal Research*, 33(1), 1-8.

Suzuki, T., H. Katayanagi, S. Nanbu, and M. Aoyagi (1998), Nonadiabatic bending dissociation in 16 valence electron system OCS, *The Journal of chemical physics*, 109(14), 5778-5794.

Tanaka, N., and K. Turekian (1995), Determination of the dry deposition flux of SO<sub>2</sub> using cosmogenic <sup>35</sup>S and <sup>7</sup>Be measurements, *Journal of Geophysical Research*, 100(D2), 2841-2848.

- Terzano, C., F. Di Stefano, V. Conti, E. Graziani, and A. Petroianni (2010), Air pollution ultrafine particles: toxicity beyond the lung, *Eur Rev Med Pharmacol Sci*, 14(10), 809-821.
- Thorpe, S. A. (1992), Bubble clouds and the dynamics of the upper ocean, *Quarterly Journal of the Royal Meteorological Society*, 118(503), 1-22.
- Trenberth, K. E., and J. T. Fasullo (2013), An apparent hiatus in global warming?, *Earth's Future*, 1(1), 19-32.
- Twohy, C. H., et al. (2002), Deep convection as a source of new particles in the midlatitude upper troposphere, *Journal of Geophysical Research: Atmospheres*, 107(D21), 4560.
- Tyndall, G. S., and A. Ravishankara (1991), Atmospheric oxidation of reduced sulfur species, *International Journal of Chemical Kinetics*, 23(6), 483-527.
- Warneck, P. (1999), *Chemistry of the Natural Atmosphere*, 2nd ed., Academic Press, San Diego, CA.
- Watts, S. F. (2000), The mass budgets of carbonyl sulfide, dimethyl sulfide, carbon disulfide and hydrogen sulfide, *Atmospheric Environment*, 34(5), 761-779.
- Webb, S., P. D. Whitefield, R. C. Miale-Lye, M. T. Timko, and T. G. Thrasher (2008), *ACRP Report 6: Research Needs Associated with Particulate Emissions at Airports*, The National Academies Press.
- Whitten, R. C., O. B. Toon, and R. P. Rurco (1980), The stratospheric sulfate aerosol layer: Processes, models, observations, and simulations, *PAGEOPH*, 118(1), 86-127.
- Xu, X., H. G. Bingemer, and U. Schmidt (2002), An empirical model for estimating the concentration of carbonyl sulfide in surface seawater from satellite measurements, *Geophysical Research Letters*, 29(9), 30-31-30-34.
- Yu, H., L. A. Remer, M. Chin, H. Bian, Q. Tan, T. Yuan, and Y. Zhang (2012), Aerosols from Overseas Rival Domestic Emissions over North America, *Science*, 337(6094), 566-569.
- Zepp, R. G., and M. O. Andreae (1994), Factors affecting the photochemical production of carbonyl sulfide in seawater, *Geophys Res Lett*, 21(25), 2813-2816.

## Chapter 2

### Isotope Theory

#### 2.1 Nuclear Stability

Isotopes are categorized as either stable or radioactive based on the nuclear stability of the atom. Stable isotopes retain their nuclear structure without alteration, however, radioactive isotopes, due to their unstable nucleus, decay by emitting high energy particles from the nucleus at a constant rate over time. Of the approximately 275 different stable nuclei, about 60% have an even number of protons and neutrons, while the remaining 40% are divided between an even/odd or odd/even ratio. Only 4 stable isotopes have an odd-odd configuration:  $^2\text{H}$ ,  $^6\text{Li}$ ,  $^{10}\text{B}$ , and  $^{14}\text{N}$ . The nucleus of an atom is more stable when two protons or two neutrons have paired spins (opposite signs). A nucleus with an odd configuration has a  $\frac{1}{2}$  integer spin number resulting in lower stability relative to even configurations, which have whole integer spin numbers [Suess and Urey, 1956].

The ratio of neutrons to protons also plays a role in the stability of the nucleus. In light elements, the neutron to proton ratio is approximately 1:1 (Figure 2.1). With increasing atomic number, the neutron to proton ratio increases to about 1.5:1. In an attempt to reach a more stable arrangement, an unstable nucleus will spontaneously emit particles and/or adjust its neutron/proton ratio to achieve a lower internal energy.

#### 2.2 Stable Isotopes

It was the discovery of deuterium by Harold Urey in 1931 that enriched the field of isotopic science. From Urey's work, it was determined that large differences existed in the physical and chemical properties between the hydrogen isotopes,  $^2\text{H}$  and  $^3\text{H}$ . In the subsequent years, additional isotopic studies producing smaller variations in physical and chemical properties were extended to carbon, nitrogen, and oxygen isotopes. The first accurate measurements of the isotopologues of  $\text{H}_2$ ,  $\text{N}_2$ , and  $\text{CO}_2$  were obtained in 1947 [Nier, 1947]. By measuring the electric current produced by the ionized molecules traveling through a magnetic field, variations in the angular momentum associated with the relative mass differences of each isotopic species were seen. Using these early studies in isotope chemistry as a cornerstone, advanced mass

spectrometric instrumentation has been developed to measure small isotopic abundances and is now an effective tool to elucidate transport processes and mechanisms of chemical and physical reactions.

### 2.2.1 Isotopic Measurement with Isotope Ratio Mass Spectrometry

Isotopic measurements are performed using a gas source isotope ratio mass spectrometer (IRMS). The spectrometer consists of four main parts including an inlet system, ion source, mass analyzer, and ion detector. Gas in the inlet system is maintained in the viscous flow regime where the mean free path of molecules is short, leading to frequent collisions and a well-mixed reservoir. This eliminates the possibility of mass fractionation between light and heavy isotopes during the initial sample introduction stage. The ion source is a heated tungsten filament which emits a beam of electrons focused in a narrow beam. Through bombardment, positive ions of sample gases are produced. The energy of the electrons used to bombard the sample gas is typically between 50-70 V to maximize the production of charged ions. At this range, single ionization is maximized as the energy is too low to produce a significant amount of multiple charged ions [Hoefs, 1997]. The positively produced ions are subsequently accelerated to 10 kV and focused into a narrow beam in an electric field and all have the same kinetic energy ( $\frac{1}{2}mv^2=10\text{kV}$ ) as they enter the magnetic field. The magnetic field deflects the beam of ions into circular paths with radii proportional to the square root of the mass to charge ratio as follows:

$$\frac{m}{e} = \frac{B^2 r^2}{2V} \rightarrow r = \frac{\sqrt{2Vm}}{B} \quad (2.1)$$

where B is the magnetic field, e is the ion charge (+1), m is the ion mass, V is the accelerating voltage ( $\approx 10,000\text{V}$ ), and r is the radius of curvature. Therefore, assuming e is equal to 1, ions are separated into different curves based on mass with the lightest isotope having the smallest radius of curvature. This allows the collection of each beam into its own individual Faraday cup detector, allowing for simultaneous measurement of all three stable oxygen isotopes at one time. The faraday cup consists of a metal container grounded through a high ohmic resistor. As the ion current passes to the ground, the potential drop in the resistor acts as a measure converting the signal to an electric current. These electrical impulses are fed into an amplifier and sent to a computer programmed to convert the electrical signals into the corresponding

numerical isotopic values. The working standard and subsequent sample are measured simultaneously through 10 cycles of alternating measurements. With simultaneous measurement, the standard and sample are compared in nearly identical conditions. In addition, isotopic compositions are measured relative to one another instead of as absolute abundances. This increases the precision of the measurement as errors associated with the measurement of each isotope are cancelled out. The uncertainty for such measurements is typically  $\pm 0.1\text{‰}$  for both  $\delta^{18}\text{O}$  and  $\delta^{17}\text{O}$ . Oxygen isotopic measurements reported in this thesis are all performed using a Finnigan MAT 253 dual inlet IRMS.

### 2.2.2 The Delta Notation and Isotopic Standard

Natural isotopic abundances for stable oxygen isotopes are as follows:

$$^{16}\text{O} = 99.763\%, \quad ^{17}\text{O} = 0.0375\%, \quad ^{18}\text{O} = 0.1995\%$$

Isotope ratios are presented in the delta ( $\delta$ ) notation by expressing the relative difference with the least abundant isotope relative to the more abundant isotope as shown here:

$$\delta(\text{‰}) = \left( \frac{R_{\text{sample}}}{R_{\text{standard}}} - 1 \right) * 1000 \quad (2.2)$$

where  $R = ^{17}\text{O}/^{16}\text{O}$  or  $^{18}\text{O}/^{16}\text{O}$ . Due to the relatively small differences in isotopic compositions resulting from physical/chemical processes, isotopic ratios are expressed in units of “per mil” or parts per thousand. Isotopes are measured against a known standard to allow for inter-laboratory comparison. The primary reference standard used for the measurement of oxygen isotopes is Standard Mean Ocean Water (SMOW), which by definition is normalized to  $\delta^{17}\text{O} = 0$  and  $\delta^{18}\text{O} = 0$ .

### 2.2.3 Mass Dependent Fractionation Effects

Isotopic fractionation refers to the partitioning of isotopes between two or more components of a system. Most isotopic fractionation processes proceed in a manner termed mass dependent fractionation, where isotopes fractionate in a relative proportion to their reduced masses. A triple isotope plot, Figure 2.2, displays  $\delta^{17}\text{O}$  on the y-axis and  $\delta^{18}\text{O}$  on the x-axis with a mass dependent fractionation slope approximately equal to 0.5, where:

$$\delta^{17}\text{O} \approx 0.5 * \delta^{18}\text{O} \quad (2.3)$$

The 1/2 ratio between  $\delta^{17}\text{O}$  and  $\delta^{18}\text{O}$  arises from the mass differences between  $^{18}\text{O}$ ,  $^{17}\text{O}$ , and  $^{16}\text{O}$ . The mass difference between  $^{17}\text{O}$  and  $^{16}\text{O}$  is 1 amu, whereas the mass difference between  $^{18}\text{O}$  and  $^{16}\text{O}$  is 2 amu, thus taking the ratio of these mass units yields a value of 1/2.

The partitioning of isotopes is represented by the fractionation factor ( $\alpha$ ) and is related to the equilibrium constant, where

$$\alpha_{A-B} = \frac{R_A}{R_B} = K^{\frac{1}{n}} \quad (2.4)$$

A and B are the two separate components of the system and n refers to the number of isotopes exchanged. The fractionation factor predicts the isotopic enrichment or depletion for a particular process. Here, A refers to the products of the system and B refers to the reactants. If only one isotope is exchanged in the system, the fractionation factor is equivalent to the equilibrium constant.

In an open system process with the progressive removal of a trace substance from a larger reservoir, the Rayleigh equation applies [Criss, 1999]:

$$\frac{R}{R_o} = f^{\alpha-1} \quad (2.5)$$

Rayleigh's equation allows the calculation of an instantaneous isotope ratio between two reservoirs where  $R_o$  is the initial isotope ratio of the bulk material, R is the instantaneous isotope ratio of the product and f is the fractional loss from the system. Rayleigh's equation can be applied to isotopic fractionation processes such as evaporation and condensation, along with photo-oxidation and photo-decomposition processes. For example, rain produced at high latitudes is isotopically lighter than rain produced near the equator. Most evaporation occurs in the tropics and travels poleward. As water vapor is condensed during its journey to higher latitudes,  $^{18}\text{O}$  preferentially condenses to the water phase relative to  $^{16}\text{O}$  resulting in isotopically lighter water vapor.

Fractionation factors vary widely depending on the element and its mass. In general, light masses are more susceptible to fractionation effects due to the larger relative mass difference between the isotopes in question. The largest isotopic fractionation effects occur in the hydrogen/deuterium system as a result of the large relative mass difference between the two isotopes. For example, D/H ratios of meteoric waters, including precipitation and groundwater, span a range of more than 400 ‰ depending on latitude, altitude, moisture source regions, storm track patterns, and evaporative regimes [Schimmelmann *et al.*, 2006; Sheppard, 1986]. The isotopic fractionation of heavier elements pales in comparison to the H/D system. Isotopic fractionation of  $^{238}\text{U}/^{235}\text{U}$  between low temperature and high temperature uranium deposits have been found to only fractionate by about 0.4 ‰ [Brennecka *et al.*, 2010].

### 2.2.3.1 Kinetic Fractionation

Kinetic fractionation processes, for example: diffusion, evaporation, and condensation, arise from the difference in mass between isotopomers. At a given temperature, each isotopomer has the same kinetic energy:

$$KE = \frac{3}{2}kt = \frac{1}{2}\mu v^2 \quad (2.6)$$

where  $k$  is the Boltzmann constant,  $t$  is temperature,  $\mu$  is the reduced mass and  $v$  is velocity. When discussing diatomic molecules, the reduced mass is defined by:

$$\mu = \frac{m_1 m_2}{m_1 + m_2} \quad (2.7)$$

as  $m$  refers to the mass of each atom of the molecule. The reduced masses and velocities are related through the following equation:

$$\frac{v_{light}}{v_{heavy}} = \sqrt{\frac{\mu_{heavy}}{\mu_{light}}} \quad (2.8)$$

Therefore, the isotopomer with the lighter mass travels slightly faster than the heavier isotopomer producing a preferential enrichment of the light isotope in the reaction product.

A kinetic isotope fractionation factor can be equated to the velocities of each isotopologue for the system in question. In a three isotope system, the relative fractionation factors for oxygen isotopes are equivalent to:

$$\frac{\ln(\alpha_{17})}{\ln(\alpha_{18})} = \frac{\ln\left(\frac{v_{17}}{v_{16}}\right)}{\ln\left(\frac{v_{18}}{v_{16}}\right)} = \frac{\ln\left(\frac{m_{16}}{m_{17}}\right)}{\ln\left(\frac{m_{16}}{m_{18}}\right)} \quad (2.9)$$

Equating the two fractionation factors gives:

$$\alpha_{17} = \alpha_{18}^{\beta} \quad (2.10)$$

where

$$\beta = \frac{\ln\left(\frac{m_{16}}{m_{17}}\right)}{\ln\left(\frac{m_{16}}{m_{18}}\right)} \quad (2.11)$$

Here,  $m_{16}$ ,  $m_{17}$ , and  $m_{18}$  are equivalent to the molecular masses of each isotopologue [Young *et al.*, 2002]. Because kinetic fractionation is dependent on the molecular mass,  $\beta$  will vary slightly depending on the molecule of interest with heavier molecules resulting in a slope closer to 0.5.

### 2.2.3.2 Equilibrium Fractionation

Equilibrium isotopic fractionation does not solely depend on classical mechanics such as kinetic fractionation, but arises due to quantum mechanical effects such as rotational/vibrational energy differences between isotopes and zero point energies. Consider an isotope exchange reaction between  $aX$  and  $bX$  such that:



where  $X_1$  and  $X_2$  represent the light and heavy isotopes, respectively. The equilibrium constant ( $K_{eq}$ ) for this reaction is expressed as:

$$K_{eq} = \frac{Q(aX_2) Q(bX_1)}{Q(aX_1) Q(bX_2)} \quad (2.13)$$



where the terms in parentheses represent molar concentrations and  $Q$  is the reduced isotopic partition function for the various species. The partition function represents the free energy of the isotopologues and includes electronic, translational, vibrational, rotational, and symmetry components. Using the Born-Oppenheimer approximation, electronic motion and nuclear motion can be treated as separate entities. Thus, the electronic energy structure should not be affected by isotopic substitution in the nucleus and has a negligible effect on isotope fractionation. The translational partition function is equal to the classical function at all temperatures and therefore contributes nothing to equilibrium fractionation. Rotational energies are small relative to the vibrational energy structure of diatomic molecules and are often ignored as, with the exception of hydrogen, the rotational partition function is classical at room temperature [Bigeleisen and Mayer, 1947]. Symmetry parameters cancel when the ratio of partition functions are taken [Young *et al.*, 2002]. Therefore, vibrational energy quantum effects are the predominant source of equilibrium isotope fractionation while the rest of the terms are considered negligible. There are some exceptions to these rules, however they usually only apply when considering hydrogen isotopes or extremely low temperatures.

$Q$  is defined by the vibrational partition function as:

$$Q = \sum \left( g_i * e^{\frac{E_i}{kT}} \right) \quad (2.14)$$

where  $E_i$  represents the allowed energy levels,  $g_i$  is the degeneracy,  $k$  is the Boltzmann constant and  $T$  is the temperature. Vibrational energy differences between isotopomers can be expressed through a discussion of the simple harmonic oscillator. Energy levels are discrete:

$$E_{vib} = \left( n + \frac{1}{2} \right) h\nu \quad (2.15)$$

where  $h$  is Plank's constant,  $\nu$  the vibrational frequency, and  $n$  represents the quantum number of the vibrational energy level. The vibrational frequency is given by:

$$\nu = \frac{1}{2\pi} \sqrt{\frac{k}{\mu}} \quad (2.16)$$

where  $k$  is the force constant, not the Boltzmann constant as noted previously. Vibrational energies are essential to describing the bond strength of each isotopomer. In its ground state ( $n=0$ ), each isotopomer still has a fundamental frequency at which it vibrates that is directly proportional to its reduced mass. Hence, the heavier isotopically substituted molecule will induce a lower zero point energy creating a stronger bond than that of the lighter isotopically substituted molecule. The lighter isotopomer will more readily react, producing isotopic fractionations. By treating the vibrations in equation 2.14 as harmonic oscillators, the relative isotope equilibrium exchange factor for the three isotope oxygen system reduces to:

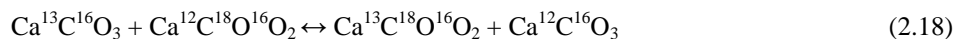
$$\beta = \frac{\frac{1}{m_{16}} - \frac{1}{m_{17}}}{\frac{1}{m_{16}} - \frac{1}{m_{18}}} = 0.529 \quad (2.17)$$

Here,  $m_{16}$ ,  $m_{17}$ , and  $m_{18}$  are equivalent to the atomic masses of the isotopes in question, not molecular masses like that seen in kinetic fractionation. This results in a unique value of  $\beta$  for oxygen bearing species, unlike that seen in kinetic fractionation.

Exponents for kinetic and equilibrium fractionation laws derive from the mass difference of different aspects of the partition functions, and therefore, are not identical [Young *et al.*, 2002]. The kinetic fractionation factor is derived purely from classical mechanics, whereas the equilibrium fractionation factor from quantum mechanics. As a result, the actual slope of mass-dependent fractionation will vary depending on the molecule and will lie somewhere between the kinetic and equilibrium slopes discussed above. Mass dependent fractionation actually varies between 0.50 and 0.53 depending on the mass of the oxygen bearing species and the relative amount of kinetic and equilibrium fractionation involved. The slight differences in kinetic and equilibrium fractionation are usually ignored as the difference between the two slopes is within the noise of the measurements for modest changes in delta values [Matsuhisa *et al.*, 1978]. These differences may become important over a large fractionation extent where the non-linearity of the mass fractionation is significant.

A relatively new application to isotope chemistry is the study of clumped isotopic formations where one measures the abundance of multiply-substituted isotopologues with two or more rare isotopes, such as  $^{13}\text{C}^{16}\text{O}^{18}\text{O}$ . Clumped isotope geochemistry examines the extent to which rare isotopes bond with or

near each other among all the possible isotopologues, independent of bulk isotopic composition. Deviations from a random distribution arise from the same physical and chemical processes that fractionate bulk isotopic compositions such as diffusion, exchange equilibrium, and evaporation [Eiler, 2007]. One of the most recognized areas of clumped isotope geochemistry is its application to paleothermometry through the measurement of mass 47 ( $^{13}\text{C}^{18}\text{O}^{16}\text{O}$ ) in carbonates. Conventional carbonate-water paleothermometry is based on a heterogeneous equilibrium isotope exchange that fractionates  $^{18}\text{O}$  between carbonate and water, thus the  $\delta^{18}\text{O}$  of both the carbonate rock and water at the time of formation must be known to determine the temperature [Criss, 1999]. In contrast, the carbonate clumped isotope thermometer is based on a homogeneous equilibrium among the carbonate crystal lattice and constrains temperatures based on the isotopic composition of carbonate alone, independent of the isotopic composition of the water from which it grew [Ghosh *et al.*, 2006]. The temperature dependent equilibrium constant for:



approaches one at high temperatures and decreases relatively monotonically with decreasing temperature [Schauble *et al.*, 2006]. Thermodynamic models indicate that the equilibrium constant controlling “clumping” in carbonates is equal to  $\approx 1.0005$  at earth-surface temperatures and decreases by  $\approx 0.000003$ - $0.000004$  per  $1^\circ\text{C}$  increase in temperature [Guo *et al.*, 2009; Schauble *et al.*, 2006]. Measurements of  $^{13}\text{C}^{18}\text{O}^{16}\text{O}$  in carbonate rocks have been used to estimate temperature profiles for the early Silurian and late Carboniferous seawater [Came *et al.*, 2007].

#### 2.2.4 Mass Independent Fractionation

Isotopic fractionations that do not obey mass dependent fractionation laws are termed mass independent fractionations (MIF), where  $\delta^{17}\text{O} \neq 0.5 \delta^{18}\text{O}$ . MIF is defined as:

$$\Delta^{17}\text{O} = \delta^{17}\text{O} - 0.5 \delta^{18}\text{O} \quad (2.19)$$

These fractionations were first observed in calcium–aluminum rich inclusions (CAI) in the Allende meteorite [Clayton *et al.*, 1973] with a depletion in the heavy oxygen isotope resulting in a ratio of  $\delta^{17}\text{O}/\delta^{18}\text{O} \approx 1$  instead of the traditional 0.5. This was initially interpreted to be a result of a nucleosynthetic

process as it was thought that no chemical process could produce a non-mass dependent fractionation. However, laboratory experiments demonstrated that the production of ozone via electrical discharge gives rise to a  $\delta^{17}\text{O}/\delta^{18}\text{O} \approx 1$  and were subsequently followed by studies that produced the same isotope effect in ozone via UV photolysis [Thiemens and Heidenreich, 1983; Thiemens and Jackson, 1985; 1987]. This showed that mass independent fractionation can indeed be caused by a chemical process.

Despite the simple isotopic fractionation pattern in the ozone formation process, defining the basic mechanism responsible for the process remains elusive [Thiemens, 2013; Thiemens et al., 2012]. The most accurate theory describing the mass independent isotope effect in ozone relies on Rice-Ramsperger-Kassel-Marcus (RRKM) theory for recombination reactions and introduces a non-statistical element that allows the density of states,  $\rho$ , to be less than the canonical statistical value [Gao and Marcus, 2001; 2002; Hathorn and Marcus, 1999; 2000]. After the excited ozone molecule is formed, redistribution of the energy between its vibrational-rotational modes proceeds at some finite rate and may result in incomplete distribution during the lifetime of the molecule [Gao and Marcus, 2001]. Half of the vibrational-rotational quantum states are forbidden in symmetric isotopologues due to the Pauli Exclusion Principle, resulting in less energy sharing and a reduction in the density of quantum states relative to the asymmetric species [Marcus, 2013]. Thus, the non-statistical effect is larger in symmetric molecules than asymmetric molecules resulting in a lower probability of stabilization and greater likelihood of dissociation back to the reactants [Marcus, 2008]. The magnitude of this effect is given by the parameter,  $\eta$ , which is chosen to match empirical rate constant data. Calculations of isotopic enrichments for scrambled systems match well with experimental data, though a value for  $\eta$  has not yet been determined theoretically.

An alternate mechanism has been proposed based on potential energy surfaces of the ozone molecule [Babikov et al., 2003b; Ivanov and Babikov, 2013]. Strong non-statistical features in the  $\text{O}_3^*$  lifetime spectrum were discovered using full quantum reactive scattering calculations and are attributed to differences in zero-point energies ( $\Delta\text{ZPE}$ ) of the various  $\text{O}_2$  molecules (e.g.  $^{16}\text{O}^{16}\text{O}$ ,  $^{16}\text{O}^{18}\text{O}$ ,  $^{18}\text{O}^{18}\text{O}$ ). Many long lived metastable states occur within the narrow  $\Delta\text{ZPE}$  range, whereas very few are located above the  $\Delta\text{ZPE}$  [Babikov et al., 2003a]. Metastable states formed above the  $\Delta\text{ZPE}$  can be formed from both channels, whereas metastable states in the  $\Delta\text{ZPE}$  part of the spectrum can only be formed from the lower

channel (Figure 2.3). The metastable states within the  $\Delta ZPE$  are stabilized more efficiently by collisions with a third body because they are energetically close to the bound  $O_3$  states [Babikov *et al.*, 2003b]. This significantly enhances the formation of  $O_3$  through the lowered channel resulting in an anomalous difference in the rates between the two entrance channels. When taking all resonances into account, the variations between the rates of the upper and lower channels lead to a mass independent effect [Babikov *et al.*, 2003b].

Basic questions remain, including the nature and origin of the symmetry effect (the  $\eta$ -effect) and whether it affects the relative isotope-specific  $O_3^*$  lifetimes prior to collisional stabilization, the collisional stabilization step, or both [Feilberg *et al.*, 2012]. Ivanov and Babikov (2013) consider the source of the  $\eta$ -effect to lie within the lifetime of the metastable  $O_3^*$  states due to differences in tunneling rates in/out of the reaction channels caused by the distortion of vibrational wave functions by isotopic substitution. However, the exact cause is still highly debated in the scientific community, and is not agreed upon.

### 2.2.5 Mass Independent Fractionation in Sulfate

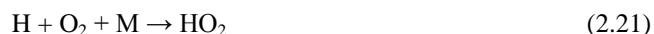
The measurement of MIF has become an important diagnostic tool in distinguishing chemical transformation processes. Many atmospheric species have been shown to possess MIF characteristics including  $CO_2$ ,  $CO$ ,  $SO_4^{2-}$ ,  $NO_3^-$ ,  $H_2O_2$ ,  $N_2O$ , and  $O_2$ , Figure 2.4. Here, we focus on the transformation of the  $O_3$  isotopic property to  $SO_4^{2-}$ . The first  $\Delta^{17}O$  anomaly in aerosol sulfate was observed from samples collected in La Jolla and White Mountain Research Station in Barcroft, California [Lee and Thiemens, 2001]. Laboratory studies revealed that the MIF characteristics in sulfate derive from aqueous oxidation via ozone and hydrogen peroxide, while gas phase oxidation via  $OH$  is a mass dependent process [Savarino *et al.*, 2000]. Oxygen isotopes in  $SO_2$  exchange rapidly with atmospheric water vapor reaching an equilibrium state [Holt *et al.*, 1981]. Therefore, any MIF characteristic found in sulfate is a direct result of  $SO_2$  oxidation to  $SO_4^{2-}$ . During aqueous phase oxidation, Savarino *et al.* (2000) determined that one oxygen atom is transferred from ozone to sulfate during ozone oxidation, whereas two oxygen atoms are transferred to sulfate during oxidation via  $H_2O_2$ . The remaining oxygen atoms in the sulfate molecule are equivalent to water. Studies have shown that ozone possesses a  $\Delta^{17}O$  value of about 27-35‰ [Johnston and

*Thiemens, 1997; Lyons, 2001*], while  $\text{H}_2\text{O}_2$  possesses a  $\Delta^{17}\text{O}$  value between 1.3 and 1.7‰ [*Savarino and Thiemens, 1999a*]. This results in a MIF transfer of about 8‰ from ozone and a MIF transfer of about 0.8‰ from  $\text{H}_2\text{O}_2$  to the sulfate molecule.

$\text{H}_2\text{O}_2$  forms via the combination of  $\text{HO}_2$  radicals:



Laboratory studies suggested the MIF characteristics of  $\text{H}_2\text{O}_2$  are a result of the  $\text{HO}_2$  formation reaction [*Savarino and Thiemens, 1999b*]:



which may show similar asymmetric characteristics to that of the ozone formation mechanism.  $\Delta^{17}\text{O}$  enrichment in these experiments varied greatly, limiting mechanistic resolution. The work did show that this reaction was mass independent. Other formation reactions such as the formation of  $\text{HO}_2$  via  $\text{OH}$  and  $\text{O}_3$  along with the photolysis of VOC's are likely additional sources of the MIF in  $\text{HO}_2$ , however, constraining the MIF budgets for each reaction is restricted. Even though the budget for each MIF formation mechanism in  $\text{H}_2\text{O}_2$  is not completely constrained, this does not limit the interpretation of the MIF characteristics in sulfate. As documented, the  $\Delta^{17}\text{O}$  value of  $\text{H}_2\text{O}_2$  is constrained at 1.3-1.7‰.

The homogeneous gas phase oxidation of  $\text{SO}_2$  via  $\text{OH}$  has been shown to be a mass dependent process [*Savarino et al., 2000*]. There are several processes that can contribute to a MIF anomaly in  $\text{OH}$  including that of formation via photolysis of ozone and nitrous acid, or reaction of  $\text{HO}_2$  radicals with  $\text{NO}$  [*Morin et al., 2007*]. However, the fast equilibrium exchange between water and  $\text{OH}$  in the atmosphere is faster than all  $\text{OH}$  sinks [*Michalski et al., 2003*], removing any MIF presence in  $\text{OH}$  radicals. It should be noted that in polar regions, the low temperatures and low water vapor levels greatly reduce the exchange reaction between  $\text{OH}$  and  $\text{H}_2\text{O}$ , potentially allowing  $\text{OH}$  radicals to competitively react with other species before equilibrium exchange has been obtained [*Morin et al., 2007*], though laboratory experiments have yet to confirm this hypothesis.

## 2.2.6 Previous Measurements

Measurements of  $\Delta^{17}\text{O}$  in  $\text{SO}_4^{2-}$  have not only provided detailed information on current oxidation pathways to aerosols and precipitation, but have also offered insight into the oxidation capacity of past atmospheres through ice core analysis [Alexander *et al.*, 2002; Alexander *et al.*, 2003; Kunasek *et al.*, 2010]. For example, using an ice core from Vostok, Antarctica, Alexander *et al.* (2002) demonstrated that the  $\Delta^{17}\text{O}$  anomaly in sulfate is considerably depleted in the last glacial period relative to isotopic compositions during past and present inter-glacial periods and attributed this to a reduction in atmospheric water vapor levels. Measurements in dry valley soils led to the interpretation that significant dry deposition from the atmosphere occurs in Antarctica and is linked to sources other than sea salt [Bao *et al.*, 2000]. In addition, the analysis of  $\Delta^{17}\text{O}$  in sulfate led to a quantitative constraint on maritime ship emissions in Southern California to the overall anthropogenic sulfate budget [Dominguez *et al.*, 2008] and determined that  $\text{O}_2$  oxidation via transition metal catalysis is an important oxidation pathway during the Arctic winter [McCabe *et al.*, 2006]. A recent snow pit study also linked the oxidation pathways of sulfate aerosols to the El Nino/La Nina cycle and documented hemispheric transport from the equator to the South Pole [Shaheen *et al.*, 2013]. Future studies will better constrain sulfate oxidation pathways and lead to better predictions of aerosol forcing in climate models.

## 2.3 Radioactive Isotopes

Radioactivity was discovered by Henri Becquerel in 1896 through the investigation of radiation emitted by uranium minerals. He found that photographic plates blackened when exposed to potassium uranyl sulfate with or without the presence of sunlight and determined that it must be due to an intrinsic property of the uranium salt itself. Marie Curie encountered similar properties in Thorium two years later. This discovery opened up new fields of study including that of natural radioactive dating techniques, fission technology, and the subsequent development of nuclear power reactors. Here in this thesis, the focus is on the use of the radioactive isotope  $^{35}\text{S}$  Sulfur ( $^{35}\text{S}$ ) and its use as a natural tracer for the atmospheric sulfur cycle.

### 2.3.1 Radioactive Decay

Radioactive decay is a spontaneous nuclear transformation that is insensitive to extranuclear conditions like pressure and temperature and follows the laws of statistics [Choppin *et al.*, 2002]. This decay process is expressed in terms of half-life ( $\tau_{1/2}$ ), which is the amount of time required for half of a radioactive sample to decay. The decay rate (A) is a measure of the number of disintegrations (decays) per unit time and is proportional to the number of atoms (N) available:

$$A = -dN/dt \quad (2.22)$$

Therefore, A is equal to a proportionality decay constant,  $\lambda$ , multiplied by the total amount of atoms:

$$A = -dN/dt = \lambda N \quad (2.23)$$

Integration of equation 2.23 leads to the general equation for radioactive decay:

$$N = N_0 e^{-\lambda t} \quad (2.24)$$

where  $N_0$  is the amount of radioactive nuclei at time zero. Solving for the half-life ( $\tau_{1/2}$ ) by plugging in  $N_0/2$  for N, equation 2.24 becomes:

$$N/N_0 = \frac{1}{2} = e^{-\lambda \tau_{1/2}} \quad (2.25)$$

$$\tau_{1/2} = \frac{\ln 2}{\lambda} = \frac{.693}{\lambda} \quad (2.26)$$

Hence, radioactive decay follows a kinetic exponential loss pattern.

### 2.3.2 Beta Decay

Beta decay occurs when the ratio of neutrons to protons (N/P ratio) is not stable inside the nucleus. To achieve a lower energy state, the nucleus spontaneously shifts the N/P ratio with the emission of either an electron ( ${}_{-1}^0e$ ) or positron ( ${}_{+1}^0e$ ). There are three types of  $\beta$  decay:  $\beta^-$  decay,  $\beta^+$  decay, and electron capture. An atom below the line of stability (Figure 2.1) is neutron rich, resulting in a high neutron to proton ratio. This atom will decay via a  $\beta^-$  reaction ( $n \rightarrow p + e^-$ ) to decrease its N/P ratio. An example of  $\beta^-$  decay is the decay of  ${}^{137}\text{Cs}$  to  ${}^{137}\text{Ba}$  as shown below:





where  $e^{-}$  represents an electron and  $\tilde{\nu}$  represents an antineutrino. An atom above the line of stability has a low N/P ratio and will decay via a  $\beta^{+}$  reaction ( $p \rightarrow n + e^{+}$ ) to increase its ratio.  ${}^{40}\text{Potassium}$  decays via a  $\beta^{+}$  reaction to  ${}^{40}\text{Calcium}$ :



where  $e^{+}$  represents a positron and  $\nu$  represents a neutrino. Neutrino interaction with matter is so unlikely, there is a high probability the neutrino passes through the entire earth without reacting [Choppin *et al.*, 2002]. However, they are necessary to conserve angular momentum and the nuclear quantum spin during the decay process [Perkins, 1987]. The change in nuclear spin quantum number ( $\Delta I$ ) must be an integral value. For the  $\beta^{-}$  decay reaction shown in equation 2.28, the spin value of ground state  ${}^{137}\text{Cs}$  is 7/2 and that of  ${}^{137}\text{Ba}$  is 11/2 [Choppin *et al.*, 2002]. An emitted electron has a spin number of 1/2. Without the additional emission of a neutrino particle (spin number of 1/2),  $\Delta I$  would not be a whole integral, thus violating the conservation of angular momentum.

Electron capture (EC) is an additional form of decay for proton-rich atoms where an inner atomic electron (K or L shell) is absorbed into the nucleus changing a proton into a neutron ( $p + e^{-} \rightarrow n + \nu$ ). EC is usually followed by the emission of a gamma particle because the capture process can leave the daughter nucleus in an excited state. There is no beta particle lost during EC making this process more energetically favorable than  $\beta^{+}$  decay [Choppin *et al.*, 2002; Kónya and Nagy, 2012; Lieser, 2008].

Beta decay shows a continuous energy distribution up to a maximum energy ( $E_{\text{max}}$ ), Figure 2.5.

$E_{\text{max}}$  is determined from the equation:

$$\Delta E = \Delta mc^2 = 931.5 \Delta m \quad (2.29)$$

where  $\Delta m$  is the difference between the initial and final nuclear mass energies of the parent and daughter nuclides. The beta decay of  ${}^{35}\text{Sulfur}$  to  ${}^{35}\text{Chlorine}$  is:



The atomic weight of  $^{35}\text{S}$  and  $^{35}\text{Cl}$  are equal to 34.969 amu and 34.968 amu [Lide, 2004] respectively, equating to an  $E_{\text{max}}$  energy release of 0.167 MeV. The values do not match perfectly here due to rounding factors. The released energy is distributed between the emitted neutrino and electron, and the recoil of the daughter nucleus. The recoil energy is much smaller relative to the emitted particles and is negligible. Only the energy of the  $\beta$  particle can be measured in scintillation spectroscopy as neutrinos don't interact with the scintillation gel. In general, the average value of a  $\beta^-$  particle is about  $0.3E_{\text{max}}$ , whereas the average value for a  $\beta^+$  particle is about  $0.4E_{\text{max}}$  [Choppin *et al.*, 2002].

### 2.3.3 Measurement of $\beta$ Decay through Scintillation Spectroscopy

Radioactivity measurements for this thesis have been determined using a Wallac 1220 Quantulus Ultra Low Level Liquid Scintillation Spectrometer. A scintillation gel cocktail is added to an aqueous solution of  $^{35}\text{SO}_4^{2-}$  salts to be measured. The emitted  $\beta^-$  decay is absorbed by the scintillation gel and results in a fluorescence detected by photomultipliers in the spectrometer.

#### 2.3.3.1 Liquid Scintillation Gel

The scintillation cocktail is composed of two basic components, the solvent and scintillator. The solvent absorbs energy released from the emitted  $\beta$  decay while the scintillator molecules convert this absorbed energy into light. About 99% of the cocktail solution consists of solvent molecules making it highly likely that the emitted  $\beta$  particle will only interact with the solvent upon decay. Solvent molecules use a conjugated  $\pi$  bond system to capture and transfer the released energy. This energy is transferred back and forth between solvent molecules until finally transferring to a scintillator (Figure 2.6). It is imperative that solvent molecules do not dissipate the absorbed energy during transfer. Typical solvents include toluene, phenyl xylylene, and di-isopropylnaphthalene, though toluene has problems with toxicity and flammability.

Linked benzene rings make a superior scintillator molecule and are divided into two classes: primary and secondary. Primary scintillators absorb the energy released by the solvent and re-emit this energy as visible light. Common primary scintillators include 2,5-diphenyloxazole (PPO) and butyl PBD.

Primaries generally emit the absorbed energy at wavelengths below 390 nm. This was a problem for early photomultipliers as sensitivity below wavelengths of 400 nm was low. To combat this problem, secondary scintillators were introduced to absorb the fluorescence released by the primary and re-emit it at a longer wavelength, although the actual mechanism of this process is unclear. With increased technology, photomultipliers have become more adept at collecting wavelengths below 400 nm, but secondary scintillators have been found to improve efficiency in the collection process and are still used in modern day scintillation gels. Common secondary phosphors include Bis-MSB and POPOP.

Most chemical extraction techniques used to isolate radioactive species for liquid scintillation measurement are done in an aqueous environment. This poses a problem as most aqueous species are insoluble in the organic solvents and scintillators. Surfactants are added to enable the mixture of aqueous and organic layers. Two types of surfactants exist in scintillation cocktails, non-ionic and ionic. The polar aqueous species bind to one side of the surfactant while the nonpolar organic species bind to the other creating a stable emulsion necessary for accurate counting [Fox, 1976; L'Annunziata, 2012; Ross *et al.*, 1991].

### **2.3.3.2 Minimizing Background Contributions through Shielding**

Instrument background sources include natural radiation produced from the outside environment and from internal components that contain small amounts of radioactive material. To minimize the influence of these effects, two types of shielding are used. A lead shield, shown in Figure 2.7, surrounds the measurement chamber and absorbs radiation from Earth's environment. The shell is at least 7-11 cm of lead in thickness throughout, sufficient for the attenuation of gamma radiation. X-rays emitted from the lead shell as a result of the absorption of this radiation are partially removed by the copper wall between the lead shell and the measurement chamber. However, the lead shell cannot stop high energy cosmic particles from penetrating into the measurement chamber and a second shielding element is needed to limit the background from these high energy sources.

A liquid scintillator guard completely surrounds the sample chamber. Two photomultiplier tubes are used to detect radiation in the scintillation guard, separate from the photomultiplier tubes used to

measure counts in the sample chamber itself. Any event that is simultaneously detected by both the sample detector and the guard detector is not considered an acceptable count and is eliminated. Thus, the sample detector operates in anticoincidence with the guard detector to reduce background counts from outside sources. The beta energy coming from the sample itself is too weak to penetrate the scintillation guard negating the possibility of a coincidence count coming from the sample itself.

### 2.3.4 Measurement Units

The SI unit for radioactivity is the Becquerel (Bq), which is equivalent to one disintegration per second. Measured count rates are typically given in counts per minute (CPM). In scintillation counting, especially for low energy beta particles, the counting efficiency is never 100%. To compensate, a known standard of the molecule of choice is measured to determine the counting efficiency of the apparatus. This ratio is then applied to the measured CPM to obtain the total disintegrations per minute (DPM). For example, if the counting efficiency is 90% for  $^{35}\text{S}$  and a measured value of 9 CPM is obtained, the actual amount of disintegrations that occurred during the measurement is 10 DPM. For the scintillation counter used in this thesis, the counting efficiency remained at 94.6% and was checked intermittently by a  $^{35}\text{S}$  standard purchased from Perkin Elmer. Most measurements are reported in units of atoms/m<sup>3</sup> due to the low concentration of natural  $^{35}\text{S}$  in the atmosphere and to normalize counts for sampling time. Atmospheric samples were collected continuously on Whatman filter papers using high-volume aerosol samplers. Normalization by cubic meters offset the fact that sampling time periods were not always equivalent.

### 2.3.5 Galactic Cosmic Rays

The major components of galactic cosmic rays (GCR) are protons and alpha particles, which constitute about 87% and 12% of the total cosmic ray budget entering Earth's atmosphere, respectively (Figure 2.8). GCR are thought to originate from supernova explosions occurring about once every 50 years in our galaxy and the resultant shockwaves produced from these explosions are generally accepted as the main source of acceleration for GCR up to about  $10^{15}$  eV. However, those GCR of larger energies, upwards of  $10^{21}$  eV, are likely of extragalactic origin [Dorman, 2004]. The intensity (I) of primary nucleons up to 100 TeV can be estimated by the power law:

$$I \approx 1.8 \cdot 10^4 \left( \frac{E}{1 \text{ GeV}} \right)^{-\alpha} \text{ nucleons/ m}^2 \text{ sec steradian} \quad (2.31)$$

where  $E$  is the kinetic energy of the incoming cosmic ray and  $\alpha$  is approximately 2.7 [Eidelman *et al.*, 2004]. Over 99% of the cosmic radiation that reaches Earth has an energy less than 100 GeV as the flux of high energetic cosmic rays is very small. While the cosmic ray intensity for a 100 GeV particle is 1 particle/(m<sup>2</sup>\*sec), the intensity of a particle near 10<sup>10</sup> GeV is only 1 particle/(km<sup>2</sup>\*yr) [Beer *et al.*, 2012]. GCR flux with energies in excess of 1 GeV decrease by about a factor of 50 for every tenfold increase in energy [Dunai, 2010]. GCR typically have energies between 100 MeV and 10 GeV, sufficiently energetic to penetrate Earth's magnetic field.

### 2.3.5.1 Interaction with Earth's Magnetic Fields

Due to its dipole component, Earth's geomagnetic field acts as a shield and deflects incoming cosmic rays. The force ( $F_L$ ) acting on a particle is given by the vector product

$$F_L = qv \times B \quad (2.32)$$

where  $q$  is the charge of the particle,  $v$  is the velocity vector, and  $B$  is the strength of the magnetic field. If the angle between  $v$  and  $B$  is  $\Theta$ , the magnitude of the deflection force is:

$$F_L = qvB\sin(\Theta) \quad (2.33)$$

The force applied by earth's magnetic field causes an incoming particle to follow a curved path and is equivalent to the centripetal force ( $F_c$ ):

$$F_L = F_c = \frac{mv^2}{r} \quad (2.34)$$

where  $m$  is the mass of the particle and  $r$  is the radius of curvature (gyroradius). The momentum ( $p$ ) of a cosmic ray is related to its kinetic energy through Einstein's relativistic energy-momentum equation:

$$p^2 c^2 = T^2 - (m_0 c^2)^2 \quad (2.35)$$

where  $c$  is the speed of light,  $T$  is the total energy (rest + kinetic) and  $m_0c^2$  is the rest energy. A particle's magnetic rigidity ( $R$ ) is defined as the momentum per unit charge (units of volts) and refers to a particle's ability to resist deflection by a magnetic field:

$$R = pc/q \quad (2.36)$$

where  $q$  is the electric charge of the incoming particle. Figure 2.9 represents a simple model of Earth's magnetic field which is perpendicular to the surface near the equator and approximately parallel to the surface near the poles. The angle between  $v$  and  $B$ , equation 2.33, is larger at low latitudes resulting in stronger deflection of incoming cosmic ray particles relative to high latitudes. A particle with a larger momentum resists the Earth's magnetic field better than a particle at a lower momentum, thus is not as significantly deflected from its original path. This results in greater penetration ability for particles approaching the Earth at high latitudes and with larger kinetic energies.

For a particle to penetrate the magnetic field and reach the top of the atmosphere, a minimum rigidity is needed, usually referred to as the cut-off rigidity. The cut-off rigidity is expressed as:

$$R_c(\lambda) = \frac{M}{D^2} \frac{\cos^4 \lambda}{[(1 + \cos \Theta \cos^3 \lambda)^{1/2} + 1]^2} \quad (2.37)$$

where  $M$  is the magnetic dipole moment of the earth,  $D$  is the radius of the Earth,  $\Theta$  is the angle of incident for the incoming cosmic ray particle,  $\lambda$  is the geomagnetic latitude in question, and  $M/D^2 \approx 59.6$  gigavolts (GV) [Beer *et al.*, 2012; Störmer, 1955]. Equation 2.37 simplifies to

$$R_c = 14.9 \cos^4 \lambda \quad (2.38)$$

when only taking into account cosmic rays arriving at the top of the atmosphere from the vertical direction,  $\Theta = 90^\circ$ . This approximation is commonly used as the greatest cosmic ray flux entering the atmosphere approaches from the zenith. The cosmic ray flux approaching the Earth is known to be roughly isotropic, having been randomized by interstellar magnetic fields [Nagashima *et al.*, 1998]. However, the atmospheric depth through which incoming cosmic rays must pass is thickest for rays penetrating close to

the horizon and thinnest for rays approaching at the zenith, thus resulting in a greater flux from the vertical [Gosse and Phillips, 2001]. The variation in cosmic flux with inclination angle is given by:

$$F(\Theta) = F_0 \cos^m(\Theta) \quad (2.39)$$

where  $F_0$  is the maximum intensity coming from the vertical, and  $\Theta$  is the inclination angle (Figure 2.10). Measurements of the value of  $m$  vary from 2.3 [Lal et al., 1958] to 3.5 [Heidbreder et al., 1971]. 2.3 is generally cited for cosmogenic nuclide applications. The cut-off rigidity near the equator is upwards of 15 GV and steadily decreases as one moves to higher latitudes, where almost all rigidities are permitted at the poles (Figure 2.11). This creates a gradient in the cosmic ray flux entering Earth's atmosphere with the largest flux near the poles and lower fluxes near the equator.

Relationships between rigidity and kinetic energy per nucleon of an incoming particle are given by:

$$R = \frac{A}{Z} \sqrt{(E_o + E_k)^2 - E_o^2} \quad (2.40)$$

$$E_k = \sqrt{\left(\frac{ZR}{A}\right)^2 + E_o^2} - E_o \quad (2.41)$$

where  $E_k$  is the kinetic energy,  $E_o$  is the nuclear rest energy, and  $Z$ ,  $A$  are the atomic number and mass, respectively, of the incoming cosmic particle [Beer et al., 2012]. Figure 2.12 plots the conversion from kinetic energy to rigidity for protons, electrons and alpha particles. Alpha particles have twice the rigidity of a proton with the same kinetic energy and are deflected less from their original vector course, therefore allowing lower energetic particles to further penetrate Earth's magnetic field relative to protons.

### 2.3.5.2 Solar Modulation

The sun emits particles at energies much lower than that of typical GCR. Solar cosmic rays (SCR) have energies around 1-100 MeV [Dunai, 2010] and consist mainly of protons ( $\approx 98\%$ ) [Michel et al., 1996]. SCRs can only cause nuclear reactions at the very top of Earth's atmosphere and are restricted to

high latitudes (above  $60^\circ$ ). Because of this, they do not contribute significantly to cosmogenic nuclide production [Lal and Peters, 1967; Masarik and Beer, 1999].

The solar particle stream, known as the solar wind, forms the heliosphere in outer space. Interaction between GCR and the solar wind result in scattering, diffusion, and energy losses for incoming GCR as they travel towards Earth [Masarik and Beer, 1999]. This modulation has a profound influence on cosmic rays below 20 GeV and is the dominant cause of the observed variability in the galactic cosmic ray flux approaching Earth [Mcdonald, 1998]. The solar modulation potential ( $\phi$ ) is defined as:

$$\phi = \int \frac{J}{3k_{(r)}} dr \quad (2.42)$$

$$k_{(r)} = \frac{v\lambda}{3} \quad (2.43)$$

where the integral is from the orbit of Earth to infinity,  $J$  is the speed of the solar wind and  $k_{(r)}$  is a scalar cosmic ray diffusion coefficient that includes  $\lambda$ , the mean free path for the galactic ray particle, and  $v$ , the speed of the galactic cosmic ray [Gleeson and Axford, 1967; 1968]. Solar activity follows an 11 year cycle, oscillating between periods of low and high material outflow with the number of sunspots reflecting the amount of solar activity during a given period. The GCR flux entering the Earth's atmosphere is anti-correlated with solar intensity, Figure 2.13. Large material outflow as a consequence of increased solar activity leads to greater solar wind speeds and a decrease in the mean free path of approaching cosmic rays, resulting in more energy loss. The solar modulation parameter ranges from 0.3-1.2 GV depending on the strength of solar activity [Usoskin et al., 2005]. Galactic cosmic rays with rigidities less than the solar modulation parameter cannot approach Earth. Solar modulation effects are greatest at high latitudes as a large proportion of low-energy particles are emitted in these regions, and minimal at low latitudes where low-energy particles are excluded due to larger cut-off energies [Bachelet et al., 1967; Stoker and Moraal, 1995]. The flux of low-energy GCR (less than 1 GeV) varies by an order of magnitude between the solar minimum/maximum, whereas high-energy particles are hardly effected (Figure 2.14) [Masarik and Beer, 1999]. As a result, variations in the nucleon flux at high latitudes generally range from 15-25% between solar minimum and maxima, whereas the flux at low latitudes shifts by less than 7% [Lifton et al., 2005]



### 2.3.5.3 Cosmic Ray Propagation

High energy GR particles entering the Earth's atmosphere are typically in large excess of the binding energies in atomic nuclei ( $\approx 7\text{-}9$  MeV per nucleon). Consequently, once primary cosmic rays collide with another particle, spallation reactions occur resulting in the ejection of nucleons from the target atom. The secondary sputtered nucleons continue to interact with other molecules in the atmosphere and initiate a nuclear cascade process (Figure 2.15). Secondary cosmic rays formed during this cascade process are broken down into three groups, electromagnetic, mesonic, and nucleonic. The electromagnetic sector, electrons ( $e^-$ ), positrons ( $e^+$ ), and gamma photons ( $\gamma$ ), do not induce nuclear transmutations in the atmosphere [Lal and Peters, 1967]. The mesonic component is only important to cosmogenic nuclide production in the Earth's subsurface. Pions ( $\pi^\pm$ ) decay in  $1.8 \times 10^{-8}$  seconds to muons ( $\mu$ ), which interact weakly with matter [Eidelman *et al.*, 2004]. Due to their weak interaction, muons penetrate into the Earth's crust and are responsible for almost all cosmogenic nuclide production below a few centimeters of the surface. Neutral pions ( $\pi^0$ ) disintegrate into gamma rays contributing to the electromagnetic sector. Therefore, the nucleonic component, protons and neutrons, is the only significant contributor to cosmogenic nuclide production in the atmosphere [Lal *et al.*, 1958].

In the upper atmosphere (atmospheric depth of  $30 \text{ g/cm}^2$ ), protons dominate the nucleonic component. Over the course of the cascade, the cosmic ray flux shifts from proton to neutron dominated where neutrons constitute 98% of the overall flux at sea level. Low energy protons (below 500 MeV) are removed from the atmosphere due to high rates of ionization loss, whereas neutrons are unaffected by this loss mechanism. The flux of low-energy nucleons is over an order of magnitude greater than the flux of high energy nucleons everywhere except the very top of the atmosphere (Figure 2.16). Hence, the production yield of cosmogenic isotopes peaks in the low energy region, where the overwhelming majority are produced via neutron reactions [Beer *et al.*, 2012; Masarik and Beer, 1999].

Cosmic ray intensity is also dependent on the mass of the atmosphere traversed by an incident particle, characterized by the attenuation length ( $\Lambda$ ):

$$\Lambda = \frac{X_1 - X_2}{\ln(I_2) - \ln(I_1)} \quad (2.44)$$

where  $I_1$  and  $I_2$  are the cosmic ray intensities measured at atmospheric depths  $X_1$  and  $X_2$ . Cosmic ray fluxes reach a maximum between 80 and 200 g/cm<sup>2</sup> in the atmosphere (roughly 15 km). Between atmospheric depths 200 g/cm<sup>2</sup> ( $\approx$ 12 km) and 1033 g/cm<sup>2</sup> (sea level), intensities exhibit an approximately exponential absorption with increasing depth [Lifton *et al.*, 2005]. At shallow atmospheric depths, there is an insufficient target density to collide with and promote nuclear reactions. In addition, secondary particles produced at low depths tend to diffuse out of the atmosphere, back into space. Above depths of 200 g/cm<sup>2</sup>, the cosmic ray flux is rapidly attenuated and consumed by reactions with atmospheric nuclei [Gosse and Phillips, 2001]. As an approximation, the nucleonic flux doubles with every 1500 meter increase in altitude up to  $\approx$  200g/cm<sup>2</sup> [Dunai, 2010]. Thus, the flux of cosmic rays is largest in the stratosphere and decreases swiftly upon reaching the troposphere.

#### 2.3.5.4 Rate of Cosmogenic Nuclide Production in the Atmosphere

To use cosmogenic nuclides as tracers of meteorological circulation patterns, it is necessary to determine the isotope production rate at all latitudes and altitudes.

The production rate (P) of cosmogenic nuclide j at atmospheric depth D is found to be:

$$P_j(D) = \sum_i N_i \sum_k \int_0^\infty \sigma_{ijk}(E_k) * J_k(E_k, D, M, \phi) dE_k \quad (2.45)$$

where the production is summed over all interactions with all the target nuclei i (e.g., O, N, or Ar). For <sup>35</sup>S production, the target nuclei are Argon atoms.  $N_i$  represents the concentration of the target atom.  $J_k(E_k, D, M, \phi)$  is the cosmic ray particle flux of a given energy ( $E_k$ ) at atmospheric depth D taking into account the magnetic field strength M, and the solar modulation parameter  $\phi$ .  $\sigma_{ijk}(E_k)$  is the cross section for the given reaction at energy  $E_k$  [Masarik and Beer, 2009]. Particle fluxes can be calculated with sophisticated models using Monte Carlo algorithms which run millions of simulations to calculate probable outcomes. These programs contain over 200,000 lines of code depicting all the necessary physics to simulate electromagnetic, mesonic, and nucleonic interactions in the atmosphere including ionization, elastic and

inelastic collisions, decay, and energy loss related to cosmogenic particle production [Beer *et al.*, 2012]. Details of the coding systems (e.g., GEANT and MCNP codes) applied to calculate cosmic particle fluxes are beyond the scope of this thesis, but may be obtained from Masarik and Beer, (1999; 2009); Reedy, (2011) and references within.

The interaction of a particle with a nucleus is complex and no nuclear models exist that provide accurate cross-sections over all relevant energies. Most models for estimating cross-sections are approximations with uncertainties up to 100% [Beer *et al.*, 2012; Rudstam, 1966]. The only reliable method is to determine cross-sections experimentally, and limits applications to cosmogenic nuclides with extensively studied cross sections.

The first extensive undertaking to calculate production rates of various cosmogenic nuclides was done by Lal and Peters, (1967). Lacking reliable cross section data and cascade models, their findings were based solely on experimental data. Direct observation through the use of photographic emulsions and ionization chambers at various sampling locations were used to determine the production rates of cosmic rays as a function of altitude and latitude. Yield functions for the formation of the cosmogenic nuclides  $^7\text{Be}$ ,  $^{32}\text{P}$ ,  $^{33}\text{P}$ , and  $^{35}\text{S}$  were determined experimentally by exposing water and argon to cosmic rays at different altitudes for 2-4 month durations [Lal *et al.*, 1960]. Although lacking the sophisticated modeling techniques of present day calculations, the relative latitude/altitude variations are thought to be accurate to within  $\pm 10\%$  [Lal, 1991]. Figure 2.17 depicts the production rates of various cosmogenic nuclides calculated by Lal and Peters, (1967). A steady rise in the overall flux is evident with increasing latitude and altitude. The flattening of the production rate between  $60^\circ$  and  $90^\circ$  latitudes corresponds to the fact that the additional primary cosmic ray particle flux that enter the atmosphere at  $\lambda > 60^\circ$  have little energy and are usually brought to rest by ionization before resulting in a nuclear collision [Lal and Peters, 1967]. Production rates of various cosmogenically produced radionuclides are depicted in Table 2.1. Radionuclide production occurs mostly in the stratosphere,  $\approx 70\%$ , and only a fraction of the total inventory is present in the troposphere.

### 2.3.6 Applications of Radionuclides to Atmospheric Processes

Cosmogenic nuclides have long been used to trace atmospheric transport and exchange processes. Common radionuclides applied to atmospheric studies include  $^{14}\text{C}$ ,  $^3\text{H}$ ,  $^7\text{Be}$ , and  $^{10}\text{Be}$ .  $^{14}\text{C}$ , produced via absorption of thermal neutrons by nitrogen, is widely recognized for its chronological applications and was instrumental in proving that anthropogenic activity and fossil fuel consumption was increasing atmospheric  $\text{CO}_2$  concentrations. [Keeling, 1979; Revelle and Suess, 1957]. Having formed millions of years ago, fossil fuels do not contain  $^{14}\text{C}$ , thus emission of these carbon products reduces atmospheric  $^{14}\text{C}/^{12}\text{C}$  ratios. This phenomenon is known as the Suess effect.  $^{14}\text{C}$  is a key tool in elucidating the global ocean circulation patterns. The long half-life (5,730 years) enables  $^{14}\text{C}$  to become fully incorporated in thermohaline oceanic circulation [Lynch-Stieglitz, 2006], which has a mixing time scale of about 100-1000 years. This long half-life limits the use of  $^{14}\text{C}$  as an atmospheric aerosol tracer since aerosol lifetimes in the troposphere are on 1-2 week timescales.  $^{14}\text{C}$  is generally constrained to time resolutions greater than 100 years due to the combination of its long half-life, low isotopic abundance, and the limited experimental precision attainable for natural  $^{14}\text{C}$  measurements [Froehlich, 2009].

The predominant form of tritium in the atmosphere resides in heavy water (HTO). Tropospheric  $^3\text{H}$  concentrations are controlled by the seasonal downward flux of stratospheric air masses and has been used as a tracer to study stratospheric-tropospheric exchange (STE) [Gaggeler, 1995]. However, the half-life of  $^3\text{H}$  (12.36 years) is still too long to adequately trace the shorter time scales of aerosol chemistry.

Beryllium has two radioisotopes used in atmospheric tracer studies and, in combination, are used to study air mass exchange between the stratosphere and the troposphere. The half-lives vary markedly in  $^7\text{Be}$  (53 days) and  $^{10}\text{Be}$  (1.5 million years), however, the production ratio of  $^{10}\text{Be}/^7\text{Be}$  is consistent at 0.52 [Masarik and Beer, 2009]. Due to the difference in resident lifetimes,  $^7\text{Be}$  decays substantially in the stratosphere relative to the troposphere, whereas  $^{10}\text{Be}$  is unaffected. This results in a much larger  $^{10}\text{Be}/^7\text{Be}$  ratio in the stratosphere. Therefore, long-term sampling campaigns studying the variation in the  $^{10}\text{Be}/^7\text{Be}$  ratio can be used to study seasonal shifts of downward stratospheric flux into the troposphere at a specific site [Jordan et al., 2003; Koch and Rind, 1998].

$^7\text{Be}$  appears to be a perfect candidate for studying aerosol processes in the atmosphere for two reasons: 1) the half-life (53 days) of  $^7\text{Be}$  allows for high resolution on aerosol depositional timescales, unlike  $^{14}\text{C}$  and  $^3\text{H}$ , and 2) beryllium isotopes readily attach to aerosol surfaces subsequent to their formation [Feely *et al.*, 1989]. However, beryllium isotopes are not scavenged by atmospheric aerosols irreversibly resulting in desorption from one particle and absorption on another [Su and Huh, 2006]. Rapid desorption of  $^7\text{Be}$  from air particulates has been observed upon contact with water and their sorption behaviors and concentrations in cloud and rain water are strongly dependent on pH [Bloom and Crecelius, 1983; Su and Huh, 2006; Taylor *et al.*, 2013]. Also, beryllium isotopes may only behave as solids with their lifetimes controlled by the carrier aerosol. These limitations complicate the use of  $^7\text{Be}$  as a tracer for atmospheric chemistry in the atmosphere especially when studying the sulfur cycle as all sulfur constituents are in the gas phase until  $\text{SO}_2$  is oxidized. A tracer is needed that offers the same timescale resolution as  $^7\text{Be}$ , but exists in both gas and aerosol phases to allow for simultaneous interpretation of both sulfur gases and particulates.

### 2.3.6.1 $^{35}\text{S}$ as a Tracer for Atmospheric Processes

$^{35}\text{S}$  is produced by the cosmic ray spallation of  $^{40}\text{Ar}$  and decays to  $^{35}\text{Cl}$  with a half-life of 87.2 days.  $^{35}\text{S}$  is advantageous over other radionuclide tracers as it is simultaneously present in gas, solid, and liquid phases.  $^{35}\text{S}$  quickly oxidizes to  $^{35}\text{SO}$  in about 1 ms and into  $^{35}\text{SO}_2$  in about 1 second [Black *et al.*, 1982; Robertshaw and Smith, 1980].  $^{35}\text{SO}_2$  is then incorporated into the global sulfur cycle and can be removed from the atmosphere via wet and dry deposition, radioactive decay, and oxidation to  $^{35}\text{SO}_4^{2-}$ . With a half-life similar to that of  $^7\text{Be}$ ,  $^{35}\text{S}$  has the unique ability to trace both gas and aerosol phases of the sulfur cycle with a resolution timescale adequate for tropospheric aerosol lifetimes.  $^{35}\text{S}$  also has the ability to be used as a tracer for stratospheric-tropospheric exchange (STE) events. Most  $^{35}\text{S}$  decays to  $^{35}\text{Cl}$  in the stratosphere before reaching the troposphere due to the long residence time of stratospheric constituents. However, STE events result in a shorter lifetime for the stratospheric component relative to that of typical mixing dynamics between the stratosphere and troposphere. Consequently, excess  $^{35}\text{S}$  is injected into the troposphere during STE events and large spikes in tropospheric activity measurements can potentially be linked to a stratospheric influence.

### 2.3.6.2 Previous Measurements

Previous attempts to use  $^{35}\text{S}$  as an atmospheric tracer are scarce, although studies have provided information regarding the kinetics of  $\text{SO}_2$  oxidation and its removal from the atmosphere. Measurements of  $\text{SO}_2$ ,  $^{35}\text{SO}_2$ ,  $\text{SO}_4^{2-}$ , and  $^{35}\text{SO}_4^{2-}$  made in aerosol and precipitation samples in New Haven, Connecticut determined the  $\text{SO}_2$  oxidation lifetime, aerosol mean residence time, and in-cloud scavenging time to be 7, 12, and 18 days, respectively [Tanaka and Turekian, 1991]. Combined with a two-box model and subsequent measurements of  $^7\text{Be}$ , scavenging coefficients and mean lifetimes for  $\text{SO}_2$  and  $\text{SO}_4^{2-}$  were estimated for both the free troposphere and marine boundary layer. A value of 0.26 was also determined for the ratio of dry to wet deposition with the highest fraction of dry deposition occurring during the fall and winter months [Tanaka and Turekian, 1995; Turekian and Tanaka, 1992].

Recently, a new method has been developed to measure low-level activity samples of  $^{35}\text{S}$  using an aqueous sample preparation technique resulting in an improvement in background activity levels. Previous preparation methods converted sulfate into its barium salt to remove impurities. However, the use of barium sulfate results in high background activities due to the contribution from radiogenic barium which appears to have a large variability depending on the chemical source (0.86-559 dpm/mol of Ba) [Brothers *et al.*, 2010], minimizing the sensitivity of the measurement. Similar measurements to those of Tanaka and Turekian were reported in Southern California measuring  $\text{SO}_2$  lifetimes at coastal and inland sites. At Scripps Pier in La Jolla,  $\text{SO}_2$  lifetimes ranged from 0.2 – 4.5 days, whereas, in the polluted San Fernando Valley,  $\text{SO}_2$  lifetimes ranged from 10.6 – 22.3 days. The stark variation in the measurements between coastal and inland sites likely reflects differences in the predominant mechanisms affecting the  $\text{SO}_2$  lifetime [Brothers *et al.*, 2010].

A 4-box model describing the marine boundary layer, buffer layer, free troposphere, and lower stratosphere has been developed to calculate the production rates of  $^{35}\text{SO}_2$  and  $^{35}\text{SO}_4^{2-}$  [Priyadarshi *et al.*, 2011]. Parameters taken into account include the production rate of  $^{35}\text{S}$  at the latitude and altitude in question, wet and dry deposition, cloud scavenging, mixing lifetimes of particles, and the oxidation from  $\text{SO}_2$  to  $\text{SO}_4^{2-}$ . The model was run for 400 days to determine steady state concentrations for  $^{35}\text{SO}_2$  and  $^{35}\text{SO}_4^{2-}$  in each reservoir box (Table 2.2).  $^{35}\text{SO}_2$  and  $^{35}\text{SO}_4^{2-}$  concentrations in the stratosphere are calculated

to be about a magnitude greater than those in the troposphere. These model calculations are used as the basis for estimation of stratospheric and free tropospheric fluxes into the boundary layer throughout this thesis.

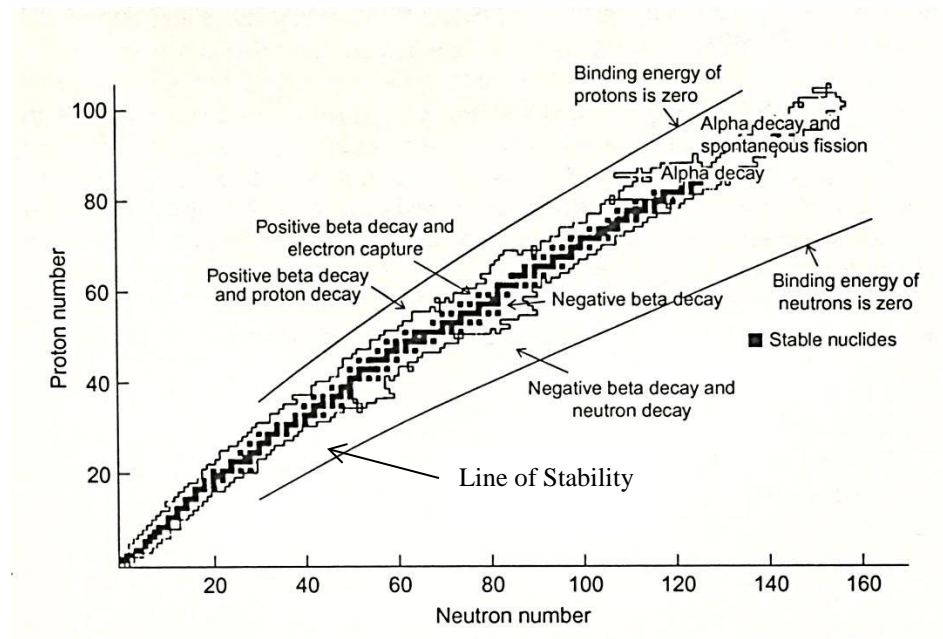


Figure 2.1

Nuclear stability as a function of an atom's proton and neutron numbers.  $\beta^-$  decay occurs in atoms with an excess number of neutrons, whereas  $\beta^+$  decay occurs in atoms with an excess number of protons [Kónya and Nagy, 2012].



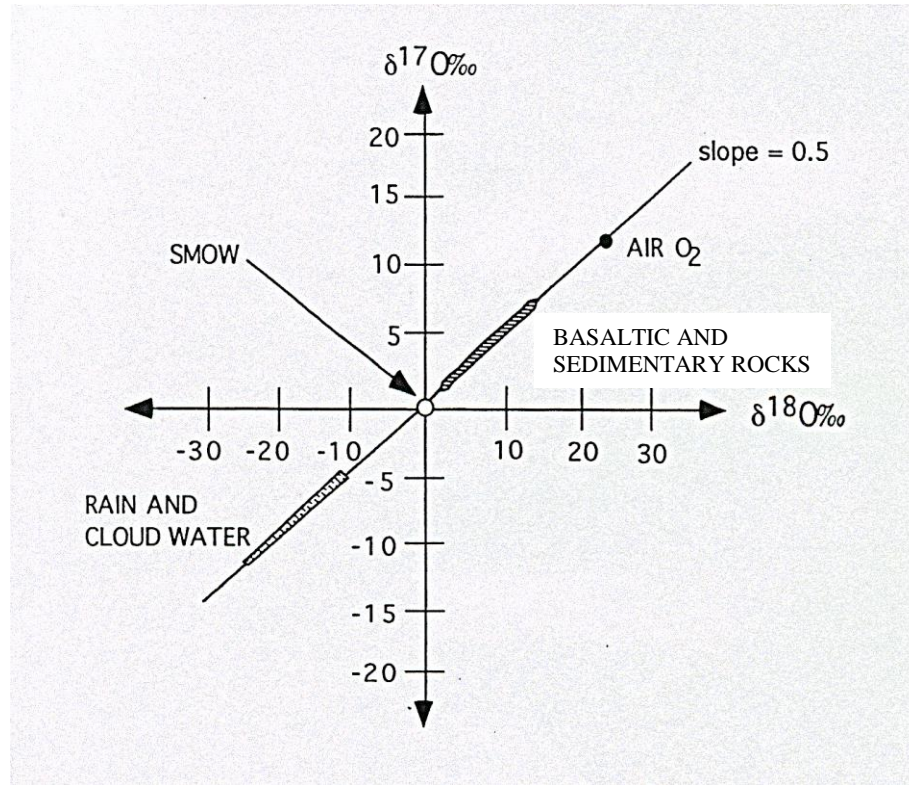


Figure 2.2

Oxygen triple isotope plot with  $\delta^{18}\text{O}$  plotted on the x-axis and  $\delta^{17}\text{O}$  plotted on the y-axis. SMOW, Standard Mean Ocean Water, is placed at the origin by definition. The line represents the mass-dependent fractionation line with a slope of  $\approx 0.5$ . Several mass dependent species are shown including atmospheric oxygen, rain and cloud water, and basaltic and sedimentary rocks [Thiemens, 1992].

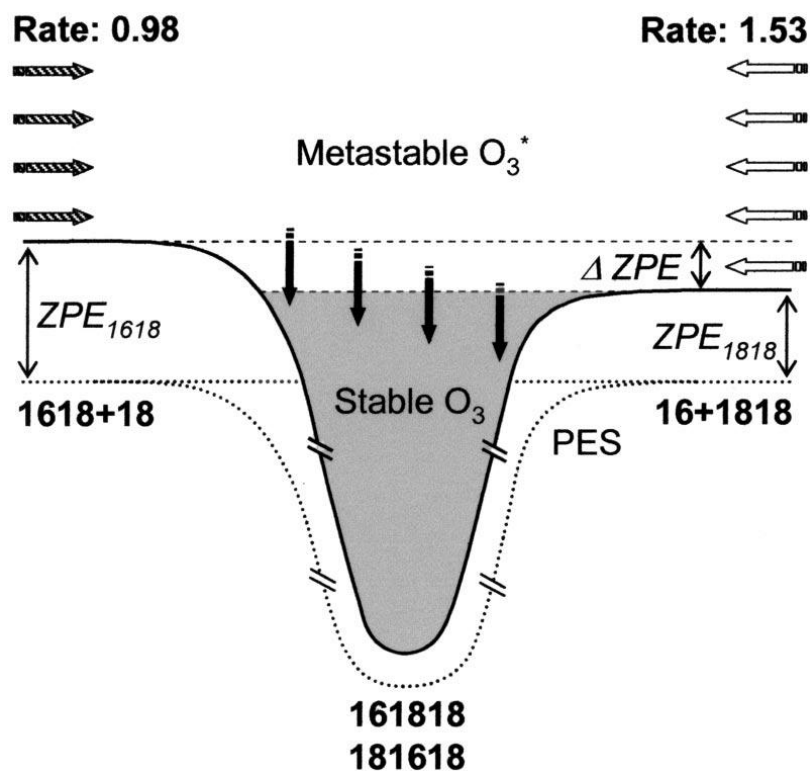
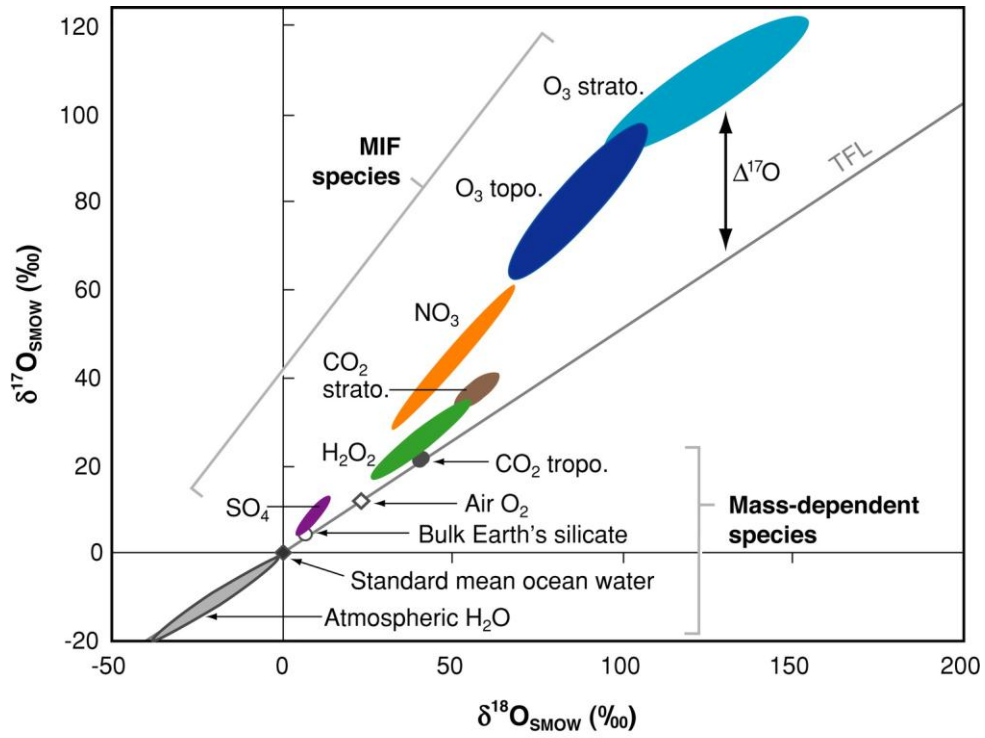


Figure 2.3

Diagram depicting the theory behind the  $\Delta ZPE$  effect. Metastable states above the  $\Delta ZPE$  can be formed from both entrance channels, whereas metastable states in the  $\Delta ZPE$  are exclusively formed from the  $^{16}O^{18}O^{18}O$  entrance channel on the right. The stabilization process to the ozone molecule is shown with descending black arrows into the well. The relative difference between the rates of ozone formation for each channel can be seen at the top [Babikov *et al.*, 2003b].




 Thiemens MH. 2006.  
 Annu. Rev. Earth Planet. Sci. 34:217–62

Figure 2.4

Triple isotope plot of atmospheric species containing mass-independent and mass-dependent constituents [Thiemens, 2006].

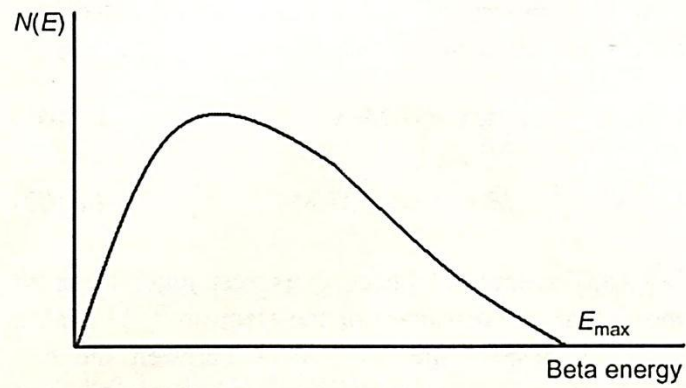


Figure 2.5

General shape of a beta spectra: the number of beta particles ( $N(E)$ ) vs. beta energy ( $E$ ) [Kónya and Nagy, 2012].

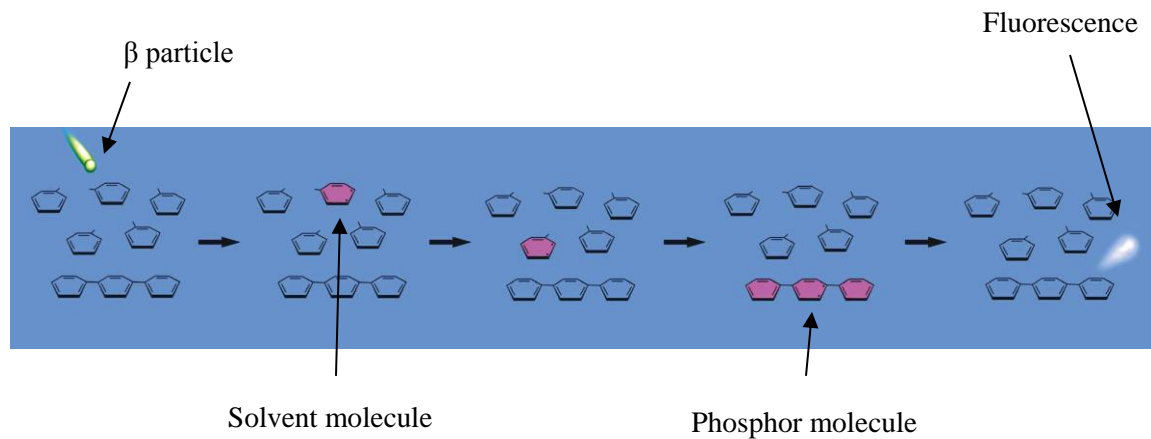


Figure 2.6

Depiction of the scintillation measurement process. The emitted  $\beta$  particle is absorbed by solvent molecules. The energy is transferred between solvent molecules and then to a scintillator molecule which absorbs the energy releases the energy and releases it as a fluorescence when de-exciting [National Diagnostics, 2002].

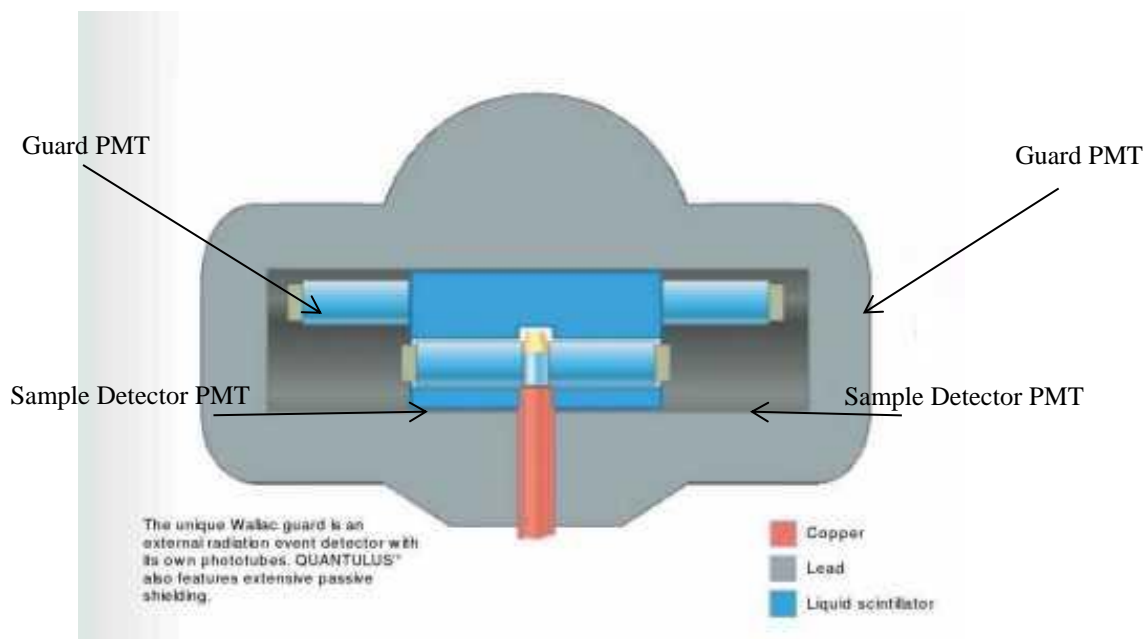


Figure 2.7

A depiction of the Wallac 1120 Quantulus Ultra Low Level Liquid Scintillation Spectrometer used to measure radioactive  $^{35}\text{S}$  throughout this thesis. PMT is short for photomultiplier. (Diagram modified from Wallac 1220 Quantulus instruction manual)

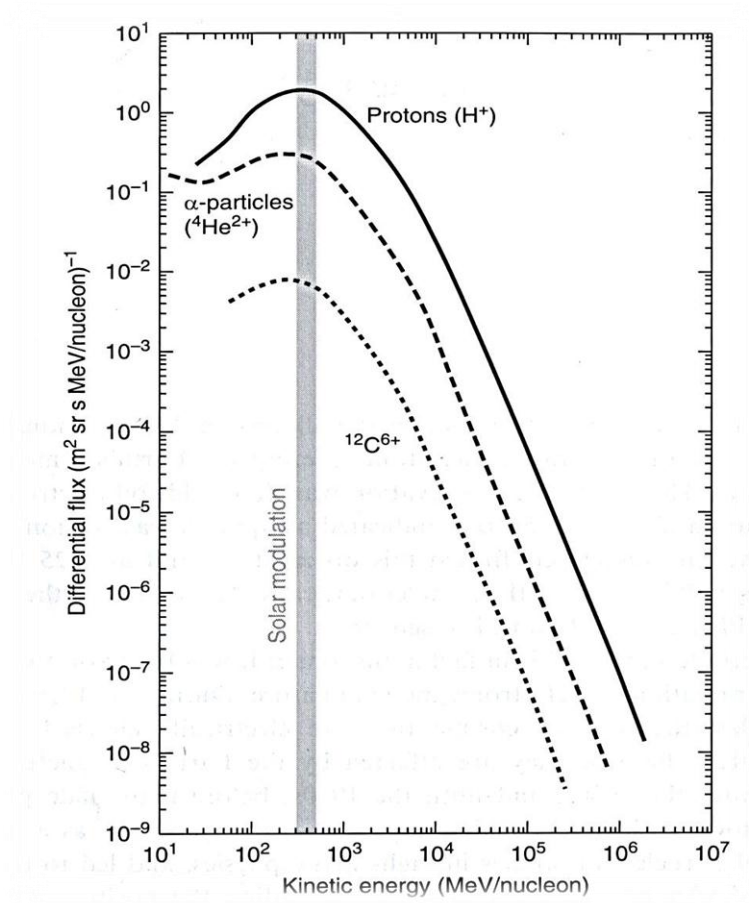


Figure 2.8

The major components of the primary cosmic ray flux entering the top of the atmosphere consist of protons and alpha particles. Heavier nuclei are rare. The flux of each nuclei is plotted against its kinetic energy. Particles with energies lower than the solar modulation parameter do not have enough energy to reach Earth's atmosphere [*Dunai*, 2010].

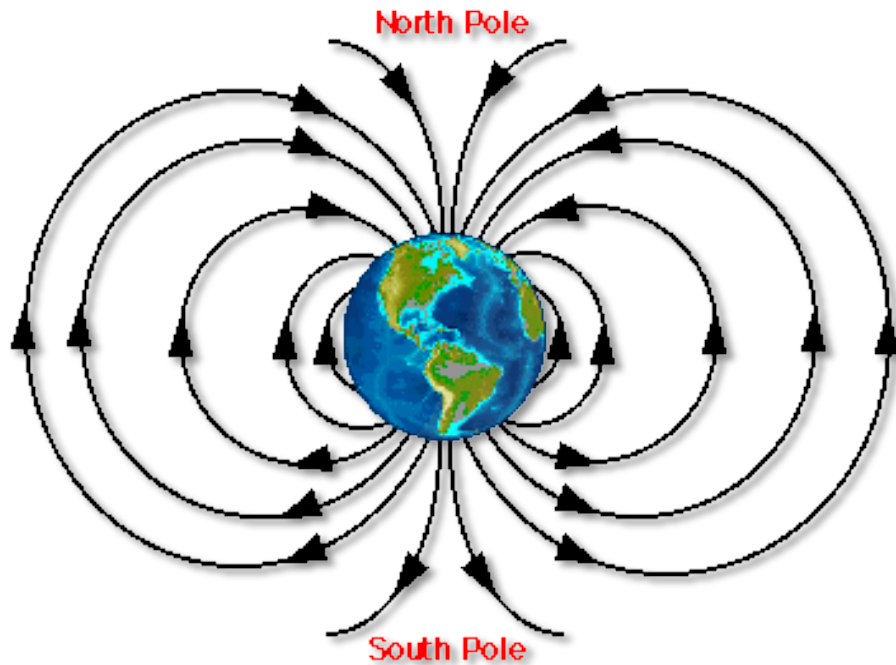


Figure 2.9

Earth's magnetic field is perpendicular to the surface at low latitudes and parallel to the surface at high latitudes resulting in stronger deflection of incoming cosmic rays near the equator relative to the poles. This creates a gradient in the cosmic ray flux entering the Earth's atmosphere. (Image was obtained from [www.unc.edu/depts/oceanweb/turtles/geomag.html](http://www.unc.edu/depts/oceanweb/turtles/geomag.html))

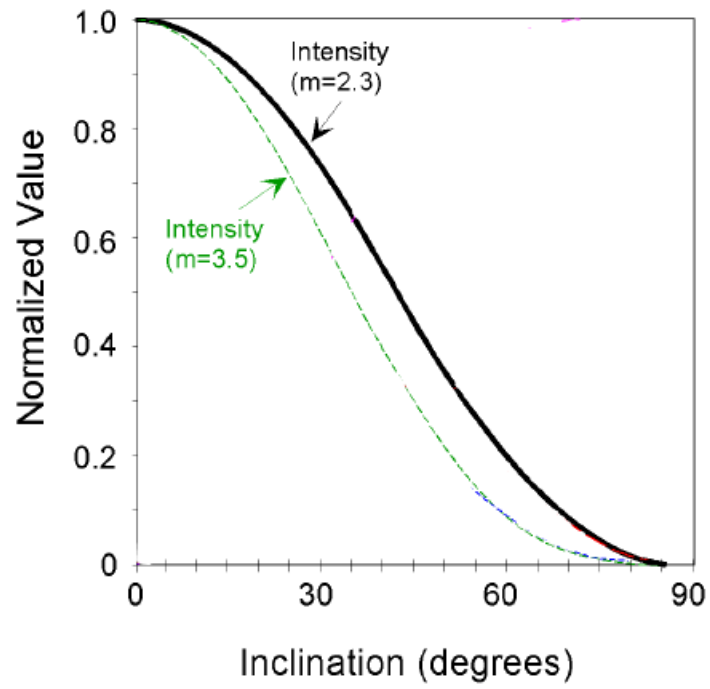


Figure 2.10

Variation of the cosmic ray intensity with inclination angle for  $m=2.3$  and  $m=3.5$  [Gosse and Phillips, 2001].



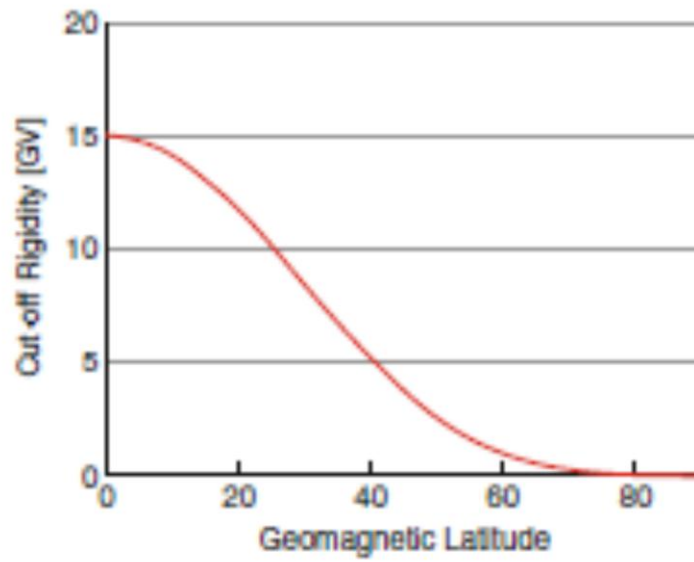


Figure 2.11

The cutoff rigidity for incoming cosmic rays approaching the Earth from the vertical estimated from equation 2.42 [Beer *et al.*, 2012].

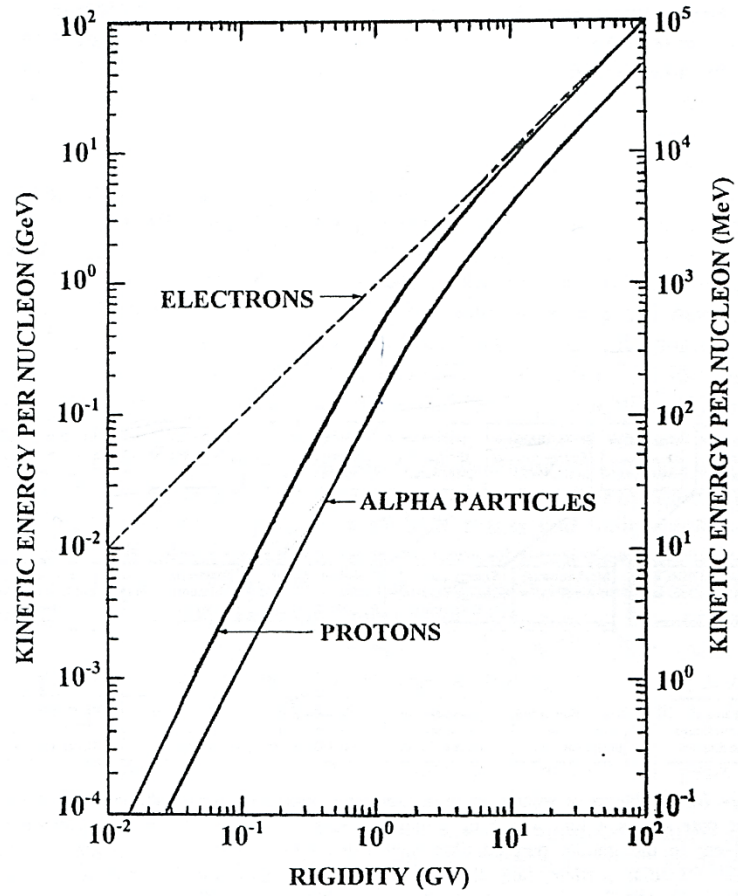


Figure 2.12

Conversion from rigidity to kinetic energy per nucleon for electrons, protons, and alpha particles [Shea, 1993].

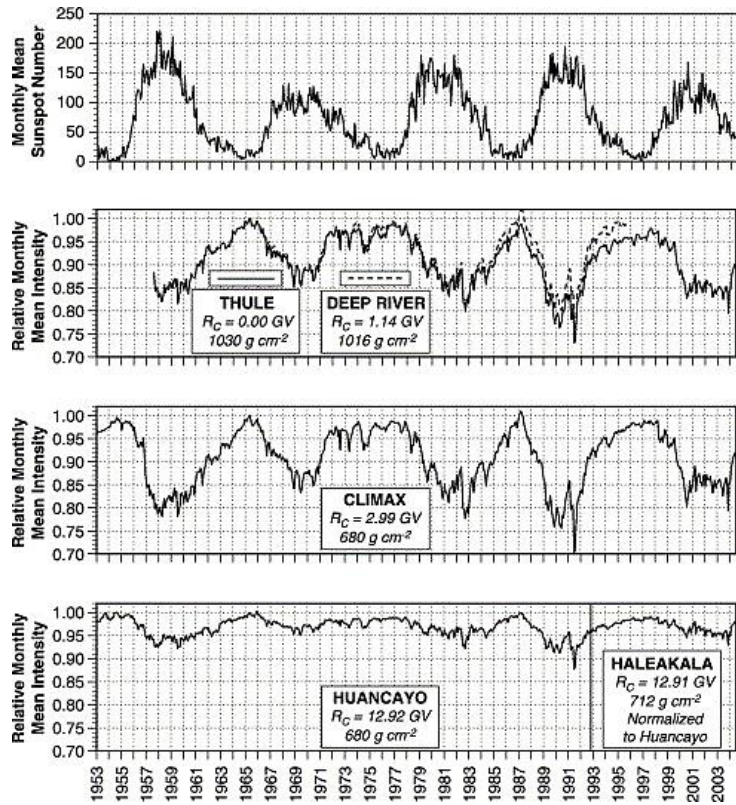


Figure 2.13

Monthly mean sunspot numbers plotted against the relative intensities of different neutron monitor systems from 1953 to 2004. Neutron monitor records have been normalized to the monthly mean of May 1965. Thule is located near sea level and Climax is located at an altitude of 3.4 km. No altitude information is given for the Huancayo/Haleakala site. Strong anticorrelation between the sunspot number and the cosmic ray flux is evident [Lifton *et al.*, 2005].

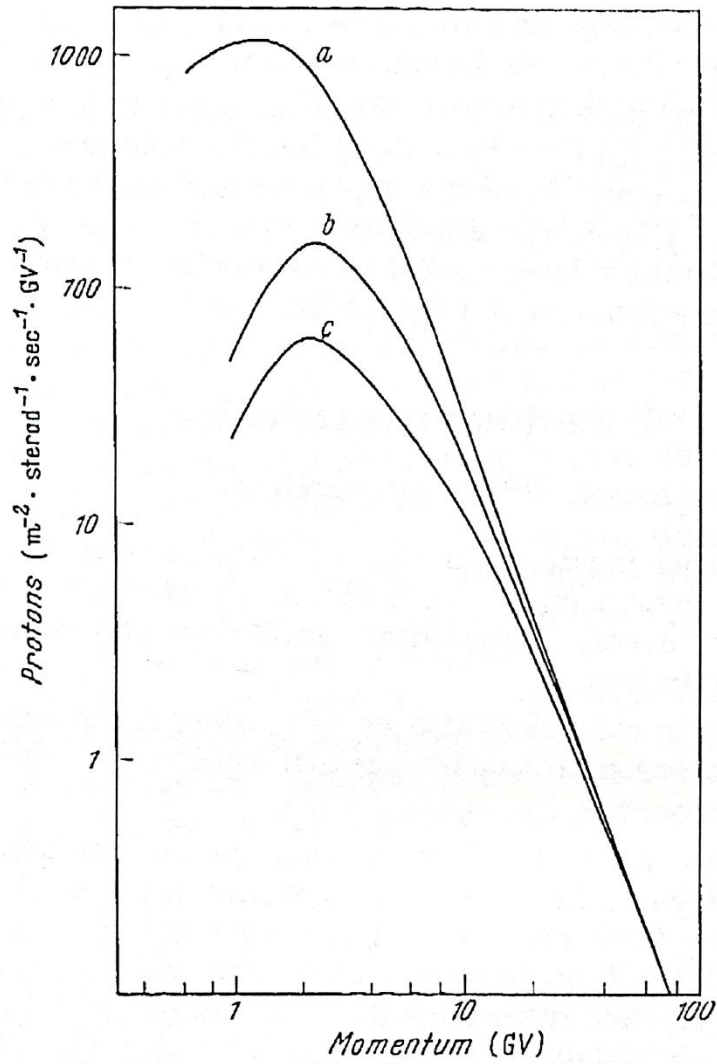
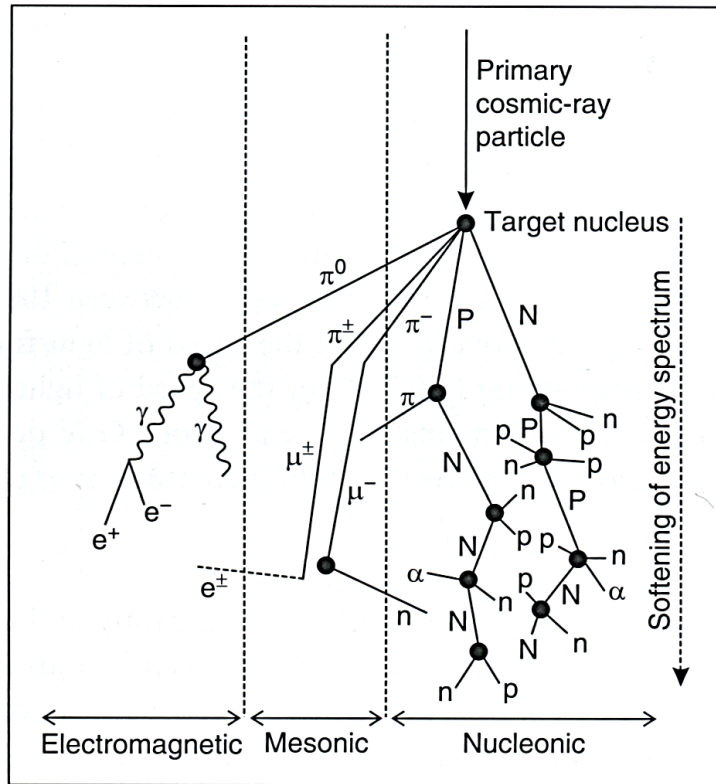


Figure 2.14

Flux of incoming protons at three different periods during a solar cycle. a) sunspot minimum during 1954, b) sunspot maximum during 1958/1959, c) lowest observed flux during a Forbush in July 1959. A forbush refers to a rapid decrease in the observed galactic cosmic ray flux following a coronal mass ejection (CME) which strengthens the magnetic field of the plasma solar wind. Time scales of these events are usually a few hours [Lal and Peters, 1967].



**Figure 2.15**

The cosmic ray cascade in the atmosphere. Abbreviations include: neutron (n), proton (p), alpha particle ( $\alpha$ ), electron/positron ( $e^\pm$ ), gamma ray photon ( $\gamma$ ), pion ( $\pi$ ), and muon ( $\mu$ ). Capital letters indicate particles carrying the nuclear cascade [Dunai, 2010].

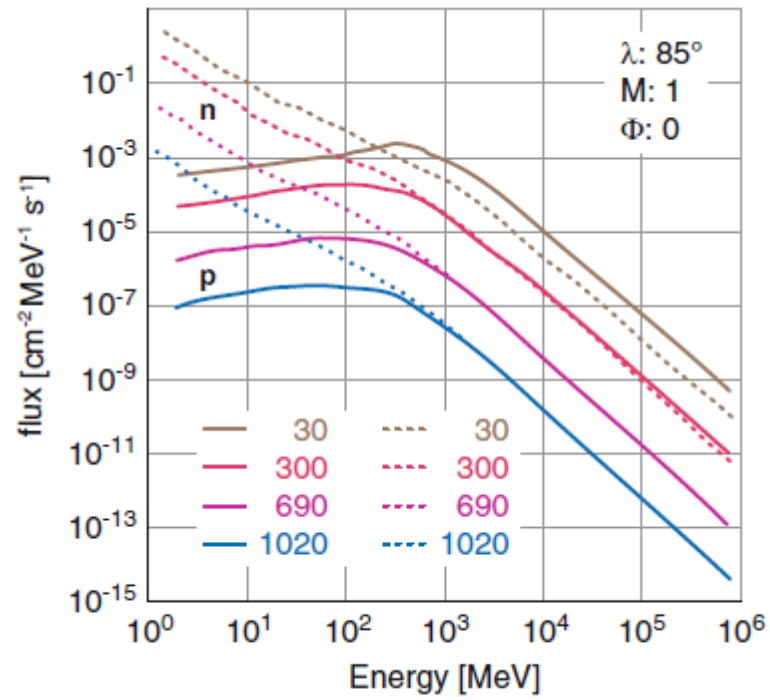


Figure 2.16

Energy spectra for protons (solid lines) and neutrons (dotted lines) for different atmospheric depths assuming no solar modulation and a geomagnetic latitude of  $85^\circ$  [Beer *et al.*, 2012].

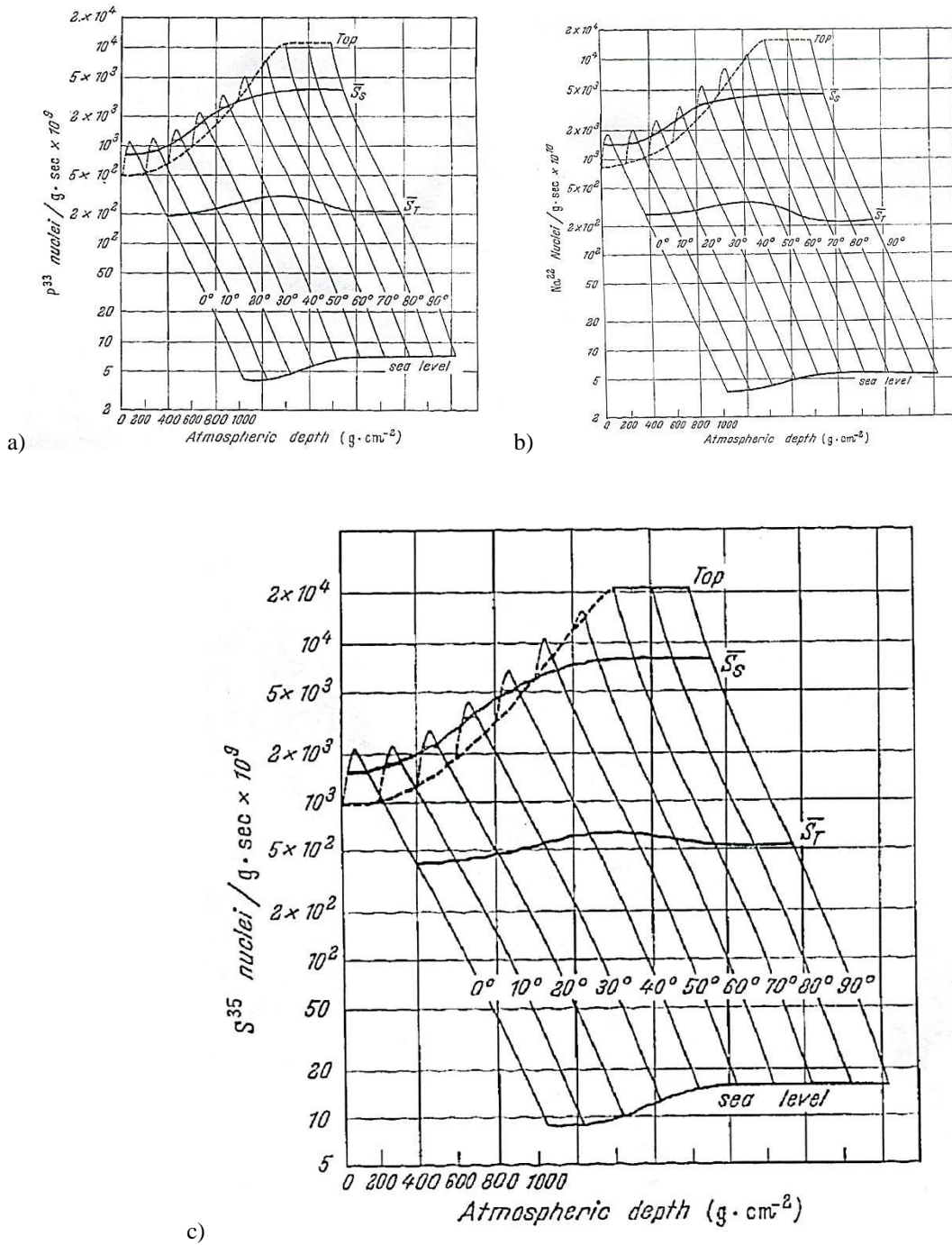


Figure 2.17

Calculated production rates of radionuclides a)  $^{33}\text{P}$ , b)  $^{22}\text{Na}$ , and c)  $^{35}\text{S}$  per gram of air, per second plotted as a function of atmospheric pressure at various latitudes [Lal and Peters, 1967]

Table 2.1

Production Rates and Concentrations of Cosmogenic Radionuclides in the Atmosphere

Radionuclide	Production rate		Global Inventory (PBq)	Fractional amount in troposphere	Concentration <sup>b</sup> in troposphere (mBq/m <sup>3</sup> )
	Per Unit Area <sup>a</sup> (atoms/m <sup>2</sup> *s)	Annual Amount <sup>c</sup> (PBq/year)			
<sup>3</sup> H	2500	72	1275	0.004	1.4
<sup>7</sup> Be	810	1960	413	0.11	12.5
<sup>10</sup> Be	450	6.4*10 <sup>-5</sup>	230	0.0023	0.15
<sup>14</sup> C	25000	1.54	12750	0.016	56.3
<sup>22</sup> Na	0.86	0.12	0.44	0.017	0.0021
<sup>26</sup> Al	1.4	1.0*10 <sup>-6</sup>	0.71	7.7*10 <sup>-8</sup>	1.5*10 <sup>-8</sup>
<sup>32</sup> Si	1.6	8.7*10 <sup>-4</sup>	0.82	1.1*10 <sup>-4</sup>	2.5*10 <sup>-5</sup>
<sup>32</sup> P	8.1	73	4.1	0.24	0.27
<sup>33</sup> P	6.8	35	3.5	0.16	0.15
<sup>35</sup> S	14	21	7.1	0.08	0.16
<sup>36</sup> Cl	11	1.3*10 <sup>-5</sup>	5.6	6*10 <sup>-8</sup>	9.3*10 <sup>-8</sup>
<sup>37</sup> Al	8.3	31	4.2	0.37	0.43
<sup>39</sup> Ar	56	0.074	28.6	0.83	6.5
<sup>81</sup> Kr	0.01	1.7*10 <sup>-8</sup>	0.005	0.82	0.0012

Table obtained from [UNSCEAR, 2000].

<sup>a</sup> Values obtained from [Lal and Peters, 1967; Lal and Suess, 1968].<sup>b</sup> Assumes tropospheric volume of 3.62275\*10<sup>18</sup> m<sup>3</sup>; inferred from [Lal and Peters, 1967].<sup>c</sup> Assumes surface area of world equal to 5.1005\*10<sup>14</sup> m<sup>2</sup> [Lide, 1992].



Table 2.2

Calculated production rates for  $^{35}\text{S}$  radionuclide and steady state concentrations of  $^{35}\text{SO}_4^{2-}$  at Dome C, Antarctica and La Jolla, CA.

Location	Antarctica <sup>(a)</sup>	La Jolla <sup>(b)</sup>
Latitude	74.3° S	32.85° N
<b><math>^{35}\text{S}</math> Production Rate (atoms/cm<sup>3</sup>*day)</b>		
MBL	$5.3 \times 10^{-6}$	$2.8 \times 10^{-6}$
BL	$5.3 \times 10^{-6}$	$2.8 \times 10^{-6}$
FT	$7.1 \times 10^{-5}$	$6.5 \times 10^{-5}$
LS	$2.1 \times 10^{-4}$	$1.1 \times 10^{-4}$
<b>Steady State <math>^{35}\text{SO}_4^{2-}</math> Concentrations (atoms/m<sup>3</sup>)</b>		
MBL	728	545
BL	932	673
FT	1160	913
LS	13383	6316

\*Abbreviations used include: marine boundary layer (MBL), buffer layer (BL), free troposphere (FT), and lower stratosphere (LS). For details regarding calculations and model parameters, refer to the following references: <sup>(a)</sup> [Priyadarshi et al., 2011] and <sup>(b)</sup> [Priyadarshi et al., 2012].

## 2.4 References

- Alexander, B., J. Savarino, N. Barkov, R. Delmas, and M. Thiemens (2002), Climate driven changes in the oxidation pathways of atmospheric sulfur, *Geophysical Research Letters*, 29(14), 1685.
- Alexander, B., M. Thiemens, J. Farquhar, A. Kaufman, J. Savarino, and R. Delmas (2003), East Antarctic ice core sulfur isotope measurements over a complete glacial-interglacial cycle, *Journal of geophysical research*, 108(D24), 4786.
- Babikov, D., B. K. Kendrick, R. B. Walker, R. T. Pack, P. Fleurat-Lesard, and R. Schinke (2003a), Metastable states of ozone calculated on an accurate potential energy surface, *The Journal of Chemical Physics*, 118(14), 6298-6308.
- Babikov, D., B. K. Kendrick, R. B. Walker, R. T. Pack, P. Fleurat-Lesard, and R. Schinke (2003b), Formation of ozone: Metastable states and anomalous isotope effect, *The Journal of Chemical Physics*, 119, 2577.
- Bachelet, F., E. Dyring, N. Iucci, and G. Villorosi (1967), Synoptic study of the attenuation coefficients for the cosmic-ray neutron monitors of the IGY network from 1957 to 1965, *Il Nuovo Cimento B Series 10*, 52.1, 106-123.
- Bao, H., D. A. Campbell, J. G. Bockheim, and M. H. Thiemens (2000), Origins of sulphate in Antarctic dry-valley soils as deduced from anomalous  $^{17}\text{O}$  compositions, *Nature*, 407(6803), 499-502.
- Beer, J., K. McCracken, and R. Von Steiger (2012), *Cosmogenic radionuclides: theory and applications in the terrestrial and space environments*, Springer.
- Bigeleisen, J., and M. G. Mayer (1947), Calculation of equilibrium constants for isotopic exchange reactions, *The Journal of Chemical Physics*, 15, 261.
- Black, G., R. Sharpless, and T. Slanger (1982), Rate coefficients at 298 K for SO reactions with  $\text{O}_2$ ,  $\text{O}_3$ , and  $\text{NO}_2$ , *Chemical Physics Letters*, 90(1), 55-58.
- Bloom, N., and E. A. Crecelius (1983), Solubility behavior of atmospheric  $^7\text{Be}$  in the marine environment, *Marine Chemistry*, 12(4), 323-331.
- Brennecka, G. A., L. E. Borg, I. D. Hutcheon, M. A. Sharp, and A. D. Anbar (2010), Natural variations in uranium isotope ratios of uranium ore concentrates: Understanding the  $^{238}\text{U}/^{235}\text{U}$  fractionation mechanism, *Earth and Planetary Science Letters*, 291(1-4), 228-233.

Brothers, L. A., G. Dominguez, A. Abramian, A. Corbin, B. Bluen, and M. H. Thiemens (2010), Optimized low-level liquid scintillation spectroscopy of  $^{35}\text{S}$  for atmospheric and biogeochemical chemistry applications, *Proceedings of the National Academy of Sciences*, 107(12), 5311-5316.

Came, R. E., J. M. Eiler, J. Veizer, K. Azmy, U. Brand, and C. R. Weidman (2007), Coupling of surface temperatures and atmospheric  $\text{CO}_2$  concentrations during the Palaeozoic era, *Nature*, 449(7159), 198-201.

Choppin, G. R., J.-O. Liljenzin, and J. Rydberg (2002), *Radiochemistry and Nuclear Chemistry*, 3rd ed., Butterworth-Heinemann.

Clayton, R. N., L. Grossman, and T. K. Mayeda (1973), A component of primitive nuclear composition in carbonaceous meteorites, *Science (New York, NY)*, 182(4111), 485.

Criss, R. E. (1999), *Principles of stable isotope distribution*, Oxford University Press, USA.

Dominguez, G., T. Jackson, L. Brothers, B. Barnett, B. Nguyen, and M. H. Thiemens (2008), Discovery and measurement of an isotopically distinct source of sulfate in Earth's atmosphere, *Proceedings of the National Academy of Sciences*, 105(35), 12769-12773.

Dorman, L. I. (2004), *Cosmic rays in the Earth's Atmosphere and Underground*, Kluwer Academic Publishers, Dordrecht, Netherlands.

Dunai, T. (2010), *Cosmogenic Nuclides: Principles, Concepts and Applications in the Earth*, Cambridge University Press, United Kingdom.

Eidelman, S., K. Hayes, K. e. Olive, M. Aguilar-Benitez, C. Amsler, D. Asner, K. Babu, R. Barnett, J. Beringer, and P. Burchat (2004), Review of Particle Physics, *Physics Letters B*, 592(1), 1-5.

Eiler, J. M. (2007), "Clumped-isotope" geochemistry—The study of naturally-occurring, multiply-substituted isotopologues, *Earth and Planetary Science Letters*, 262(3), 309-327.

Feely, H. W., R. J. Larsen, and C. G. Sanderson (1989), Factors that cause seasonal variations in Beryllium-7 concentrations in surface air, *Journal of Environmental Radioactivity*, 9(3), 223-249.

Feilberg, K., A. Wiegel, and K. Boering (2012), Probing the unusual isotope effects in ozone formation: Bath gas and pressure dependence of the non-mass-dependent isotope enrichments in ozone, *Chemical Physics Letters*.

Fox, B. W. (1976), *Techniques of Sample Preparation for Liquid Scintillation Counting in "Laboratory Techniques in Biochemistry and Molecular Biology"*, North-Holland Publishing Company.

- Froehlich, K. (2009), *Environmental radionuclides: tracers and timers of terrestrial processes*, Elsevier, Oxford, UK.
- Gaggeler, H. W. (1995), Radioactivity in the atmosphere, *Radiochimica Acta*, 70-1, 345-353.
- Gao, Y. Q., and R. A. Marcus (2001), Strange and Unconventional Isotope Effects in Ozone Formation, *Science*, 293(5528), 259-263.
- Gao, Y. Q., and R. A. Marcus (2002), On the theory of the strange and unconventional isotopic effects in ozone formation, *The Journal of Chemical Physics*, 116(1), 137-154.
- Ghosh, P., J. Adkins, H. Affek, B. Balta, W. Guo, E. A. Schauble, D. Schrag, and J. M. Eiler (2006),  $^{13}\text{C}$ – $^{18}\text{O}$  bonds in carbonate minerals: A new kind of paleothermometer, *Geochimica et Cosmochimica Acta*, 70(6), 1439-1456.
- Gleeson, L., and W. Axford (1967), Cosmic Rays in the Interplanetary Medium, *Astrophys. J.*, 149: L115-8.
- Gleeson, L., and W. Axford (1968), Solar modulation of galactic cosmic rays, *The Astrophysical Journal*, 154, 1011.
- Gosse, J. C., and F. M. Phillips (2001), Terrestrial in situ cosmogenic nuclides: theory and application, *Quaternary Science Reviews*, 20(14), 1475-1560.
- Guo, W., J. L. Mosenfelder, W. A. Goddard Iii, and J. M. Eiler (2009), Isotopic fractionations associated with phosphoric acid digestion of carbonate minerals: Insights from first-principles theoretical modeling and clumped isotope measurements, *Geochimica et Cosmochimica Acta*, 73(24), 7203-7225.
- Hathorn, B. C., and R. A. Marcus (1999), An intramolecular theory of the mass-independent isotope effect for ozone. I, *The Journal of Chemical Physics*, 111(9), 4087-4100.
- Hathorn, B. C., and R. A. Marcus (2000), An intramolecular theory of the mass-independent isotope effect for ozone. II. Numerical implementation at low pressures using a loose transition state, *The Journal of Chemical Physics*, 113(21), 9497-9509.
- Heidbreder, E., K. Pinkau, C. Reppin, and V. Schönfelder (1971), Measurements of the distribution in energy and angle of high-energy neutrons in the lower atmosphere, *Journal of geophysical research*, 76(13), 2905-2916.
- Hoefs, J. (1997), *Stable Isotope Geochemistry*. Springer-Verlag, Berlin.

Holt, B., R. Kumar, and P. Cunningham (1981), Oxygen-18 study of the aqueous-phase oxidation of sulfur dioxide, *Atmospheric Environment* (1967), 15(4), 557-566.

Ivanov, M. V., and D. Babikov (2013), On molecular origin of mass-independent fractionation of oxygen isotopes in the ozone forming recombination reaction, *Proceedings of the National Academy of Sciences*, 110(44), 17708-17713.

Johnston, J. C., and M. H. Thiemens (1997), The isotopic composition of tropospheric ozone in three environments, *Journal of Geophysical Research-Atmospheres*, 102(D21), 25395-25404.

Jordan, C., J. Dibb, and R. Finkel (2003),  $^{10}\text{Be}/^{7}\text{Be}$  tracer of atmospheric transport and stratosphere-troposphere exchange, *Journal of geophysical research*, 108(D8), 4234.

Keeling, C. D. (1979), The Suess effect:  $^{13}\text{C}$ - $^{14}\text{C}$  interrelations, *Environment International*, 2(4-6), 229-300.

Koch, D., and D. Rind (1998), Beryllium 10/beryllium 7 as a tracer of stratospheric transport, *Journal of Geophysical Research: Atmospheres* (1984-2012), 103(D4), 3907-3917.

Kónya, J., and N. M. Nagy (2012), *Nuclear and radiochemistry*, Elsevier, London, UK.

Kunasek, S., B. Alexander, E. Steig, E. Sofen, T. Jackson, M. Thiemens, J. McConnell, D. Gleason, and H. Amos (2010), Sulfate sources and oxidation chemistry over the past 230 years from sulfur and oxygen isotopes of sulfate in a West Antarctic ice core, *Journal of Geophysical Research: Atmospheres* (1984-2012), 115(D18).

L'Annunziata, M. F. (2012), *Handbook of Radioactivity Analysis, 2nd ed.*, Elsevier, Great Britain.

Lal, D. (1991), Cosmic ray labeling of erosion surfaces: *in situ* nuclide production rates and erosion models, *Earth and Planetary Science Letters*, 104(2), 424-439.

Lal, D., and B. Peters (1967), Cosmic ray produced radioactivity on the earth, *Handb. Phys.*(46), 551-612.

Lal, D., and H. Suess (1968), The radioactivity of the atmosphere and hydrosphere, *Annual Review of Nuclear Science*, 18(1), 407-434.

Lal, D., P. Malhotra, and B. Peters (1958), On the production of radioisotopes in the atmosphere by cosmic radiation and their application to meteorology, *Journal of Atmospheric and Terrestrial Physics*, 12(4), 306-328.

Lal, D., J. R. Arnold, and M. Honda (1960), Cosmic-Ray Production Rates of  $\text{Be}^7$  in Oxygen, and  $\text{P}^{32}$ ,  $\text{P}^{33}$ ,  $\text{S}^{35}$  in Argon at Mountain Altitudes, *Physical Review*, 118(6), 1626.

Lee, C. C.-W., and M. H. Thiemens (2001), The  $\delta^{17}\text{O}$  and  $\delta^{18}\text{O}$  measurements of atmospheric sulfate from a coastal and high alpine region: A mass-independent isotopic anomaly, *Journal of geophysical research*, 106(D15), 17359-17317,17373.

Lide, D. R. (1992), *CRC Handbook of Chemistry and Physics*, 73rd edition, CRC Press, Boca Raton.

Lide, D. R. (2004), *CRC Handbook of Chemistry and Physics*, CRC press.

Lieser, K. H. (2008), *Nuclear and Radiochemistry: Fundamentals and Applications*, 2nd ed., Wiley-VCH, Germany.

Lifton, N. A., J. W. Bieber, J. M. Clem, M. L. Duldig, P. Evenson, J. E. Humble, and R. Pyle (2005), Addressing solar modulation and long-term uncertainties in scaling secondary cosmic rays for in situ cosmogenic nuclide applications, *Earth and Planetary Science Letters*, 239(1–2), 140-161.

Lynch-Stieglitz, J. (2006), Tracers of past ocean circulation, *Treatise on geochemistry*, 6, 433-451.

Lyons, J. R. (2001), Transfer of mass-independent fractionation in ozone to other oxygen-containing radicals in the atmosphere, *Geophysical Research Letters*, 28(17), 3231-3234.

Marcus, R. A. (2008), Mass-Independent Oxygen Isotope Fractionation in Selected Systems. Mechanistic Considerations, *Advances in Quantum Chemistry*, 55, doi:10.1016/S0065-3276(07)00202-X.

Marcus, R. A. (2013), Theory of mass-independent fractionation of isotopes, phase space accessibility, and a role of isotopic symmetry, *Proceedings of the National Academy of Sciences*, 110(44), 17703-17707.

Masarik, J., and J. Beer (1999), Simulation of particle fluxes and cosmogenic nuclide production in the Earth's atmosphere, *Journal of Geophysical Research: Atmospheres*, 104(D10), 12099-12111.

Masarik, J., and J. Beer (2009), An updated simulation of particle fluxes and cosmogenic nuclide production in the Earth's atmosphere, *Journal of Geophysical Research: Atmospheres (1984–2012)*, 114(D11).

Matsuhisa, Y., J. R. Goldsmith, and R. N. Clayton (1978), Mechanisms of hydrothermal crystallization of quartz at 250 C and 15 kbar, *Geochimica et Cosmochimica Acta*, 42(2), 173-182.

McCabe, J. R., J. Savarino, B. Alexander, S. Gong, and M. H. Thiemens (2006), Isotopic constraints on non-photochemical sulfate production in the Arctic winter, *Geophysical Research Letters*, 33(5).

McDonald, F. B. (1998), Cosmic-ray modulation in the heliosphere a phenomenological study, *Space Science Reviews*, 83(1-2), 33-50.

Michalski, G., Z. Scott, M. Kabling, and M. H. Thiemens (2003), First measurements and modeling of  $\Delta^{17}\text{O}$  in atmospheric nitrate, *Geophysical Research Letters*, 30(16).

Michel, R., I. Leya, and L. Borges (1996), Production of cosmogenic nuclides in meteoroids: accelerator experiments and model calculations to decipher the cosmic ray record in extraterrestrial matter, *Nuclear Instruments and Methods in Physics Research Section B: Beam Interactions with Materials and Atoms*, 113(1-4), 434-444.

Morin, S., J. Savarino, S. Bekki, S. Gong, and J. Bottenheim (2007), Signature of Arctic surface ozone depletion events in the isotope anomaly ( $\Delta^{17}\text{O}$ ) of atmospheric nitrate, *Atmospheric Chemistry and Physics*, 7(5), 1451-1469.

Nagashima, K., K. Fujimoto, and R. M. Jacklyn (1998), Galactic and heliotail-in anisotropies of cosmic rays as the origin of sidereal daily variation in the energy region  $< 104$  GeV, *Journal of Geophysical Research: Space Physics*, 103(A8), 17429-17440.

National Diagnostics (2002), Principles and Applications of Liquid Scintillation Counting, A Primer for Orientation, [http://www.ehs.psu.edu/radprot/LSC\\_Theory2.pdf](http://www.ehs.psu.edu/radprot/LSC_Theory2.pdf).

Nier, A. O. (1947), A mass spectrometer for isotope and gas analysis, *Review of Scientific Instruments*, 18(6), 398-411.

Perkins, D. H. (1987), *Introduction to high energy physics*, Addison-Wesley Reading, Massachusetts.

Priyadarshi, A., G. Dominguez, J. Savarino, and M. Thiemens (2011), Cosmogenic  $^{35}\text{S}$ : A unique tracer to Antarctic atmospheric chemistry and the polar vortex, *Geophysical Research Letters*, 38(13), L13808.

Priyadarshi, A., J. Hill-Falkenthal, E. Coupal, G. Dominguez, and M. H. Thiemens (2012), Measurements of  $^{35}\text{S}$  in the marine boundary layer at La Jolla, California: A new technique for tracing air mass mixing during Santa Ana events, *Journal of Geophysical Research: Atmospheres (1984-2012)*, 117(D8).

Reedy, R. (2011), Cosmogenic-nuclide production rates: Reaction cross section update, *Nuclear Instruments and Methods in Physics Research Section B: Beam Interactions with Materials and Atoms*.

Revelle, R., and H. E. Suess (1957), Carbon Dioxide Exchange Between Atmosphere and Ocean and the Question of an Increase of Atmospheric CO<sub>2</sub> during the Past Decades, *Tellus*, 9(1), 18-27.

Robertshaw, J. S., and I. W. Smith (1980), Rate data for  $O + OCS \rightarrow SO + CO$  and  $SO + O_3 \rightarrow SO_2 + O_2$  by a new time-resolved technique, *International Journal of Chemical Kinetics*, 12(10), 729-739.

Ross, H. H., J. E. Noakes, and J. D. Spaulding (1991), *Liquid scintillation counting and organic scintillators*, Lewis Publishers, INC, USA.

Rudstam, G. (1966), Systematics of Spallation Yields, *Z Naturforsch 21a*:1027-1041.

Savarino, J., and M. H. Thiemens (1999a), Mass-independent oxygen isotope (O-16, O-17, O-18) fractionation found in H-x, O-x reactions, *Journal of Physical Chemistry A*, 103(46), 9221-9229.

Savarino, J., and M. H. Thiemens (1999b), Analytical procedure to determine both delta O-18 and delta O-17 of H<sub>2</sub>O<sub>2</sub> in natural water and first measurements, *Atmospheric Environment*, 33(22), 3683-3690.

Savarino, J., C. C. Lee, and M. H. Thiemens (2000), Laboratory oxygen isotopic study of sulfur (IV) oxidation: Origin of the mass-independent oxygen isotopic anomaly in atmospheric sulfates and sulfate mineral deposits on Earth, *Journal of Geophysical Research: Atmospheres (1984–2012)*, 105(D23), 29079-29088.

Schauble, E. A., P. Ghosh, and J. M. Eiler (2006), Preferential formation of <sup>13</sup>C–<sup>18</sup>O bonds in carbonate minerals, estimated using first-principles lattice dynamics, *Geochimica et Cosmochimica Acta*, 70(10), 2510-2529.

Schimmelmann, A., A. L. Sessions, and M. Mastalerz (2006), Hydrogen isotopic (D/H) composition of organic matter during diagenesis and thermal maturation, *Annu. Rev. Earth Planet. Sci.*, 34, 501-533.

Shaheen, R., M. Abauanza, T. L. Jackson, J. McCabe, J. Savarino, and M. H. Thiemens (2013), Tales of volcanoes and El-Niño southern oscillations with the oxygen isotope anomaly of sulfate aerosol, *Proceedings of the National Academy of Sciences*.

Shea, M. A. a. S., D.F. (1993), Solar proton events: History, statistics and predictions, In: *Solar-Terrestrial Prediction-IV. Proc. of a Workshop at Ottawa, Canada, May 18-22, 1992*. Vol 2. NOAA, Environmental Research Laboratories, Boulder, Co., USA.

Sheppard, S. M. (1986), Characterization and isotopic variations in natural waters, *Reviews in Mineralogy and Geochemistry*, 16(1), 165-183.



Stoker, P. H., and H. Moraal (1995), Neutron monitor latitude surveys at aircraft altitudes, *Astrophysics and Space Science*, 230.1-2, 365-373.

Störmer, C. (1955), *The Polar Aurora*, Oxford University Press, London.

Su, C.-C., and C.-A. Huh (2006), Measurements of  $^7\text{Be}$  and  $^{210}\text{Pb}$  in cloudwaters: Toward a better understanding of aerosol transport and scavenging, *Geophysical Research Letters*, 33(4), L04807.

Suess, H. E., and H. C. Urey (1956), Abundances of the Elements, *Reviews of Modern Physics*, 28(1), 53-74.

Tanaka, N., and K. Turekian (1991), Use of cosmogenic  $^{35}\text{S}$  to determine the rates of removal of atmospheric  $\text{SO}_2$ .

Tanaka, N., and K. Turekian (1995), Determination of the dry deposition flux of  $\text{SO}_2$  using cosmogenic  $^{35}\text{S}$  and  $^7\text{Be}$  measurements, *Journal of Geophysical Research*, 100(D2), 2841-2848.

Taylor, A., W. H. Blake, H. G. Smith, L. Mabit, and M. J. Keith-Roach (2013), Assumptions and challenges in the use of fallout beryllium-7 as a soil and sediment tracer in river basins, *Earth-Science Reviews*, 126(0), 85-95.

Thiemens, M. (1992), Mass-independent isotopic fractionations and their applications, in *Isotope Effects in Gas-Phase Chemistry*, edited by J. A. Kaye, pp. 138-154, American Chemical Society, Washington, D.C.

Thiemens, M. H. (2006), History and applications of mass-independent isotope effects, *Annu. Rev. Earth Planet. Sci.*, 34, 217-262.

Thiemens, M. H. (2013), Introduction to Chemistry and Applications in Nature of Mass Independent Isotope Effects Special Feature, *Proceedings of the National Academy of Sciences*, 110(44), 17631-17637.

Thiemens, M. H., and J. E. Heidenreich (1983), The Mass-Independent fractionation of Oxygen - A Novel Isotope Effect and its Possible Cosmochemical Implications, *Science*, 219(4588), 1073-1075.

Thiemens, M. H., and T. Jackson (1985), Production of Mass Independently Fractionated Oxygen Isotopic Components by ultra-Violet Light, *Meteoritics*, 20(4), 775-776.

Thiemens, M. H., and T. Jackson (1987), Production of Isotopically Heavy Ozone by Ultraviolet-Light Photolysis of  $\text{O}_2$ , *Geophysical Research Letters*, 14(6), 624-627.

Thiemens, M. H., S. Chakraborty, and G. Dominguez (2012), The Physical Chemistry of Mass-Independent Isotope Effects and Their Observation in Nature, *Annual Review of Physical Chemistry*, 63, 155-177.

Turekian, K. K., and N. Tanaka (1992), The use of atmospheric cosmogenic  $^{35}\text{S}$  and  $^7\text{Be}$  in determining depositional fluxes of  $\text{SO}_2$ , *Geophysical Research Letters*, 19(17), 1767-1770.

UNSCEAR (2000), *United Nations Scientific Committee on the Effects of Ionizing Radiation. Sources and Effects of Ionizing Radiation*, United Nations, New York.

Usoskin, I. G., K. Alanko-Huotari, G. A. Kovaltsov, and K. Mursula (2005), Heliospheric modulation of cosmic rays: Monthly reconstruction for 1951–2004, *Journal of Geophysical Research: Space Physics* (1978–2012), 110(A12).

Young, E. D., A. Galy, and H. Nagahara (2002), Kinetic and equilibrium mass-dependent isotope fractionation laws in nature and their geochemical and cosmochemical significance, *Geochimica et Cosmochimica Acta*, 66(6), 1095-1104.

## Chapter 3

### Differentiating Sulfate Aerosol Oxidation Pathways for Varying Source Altitudes

#### Using $^{35}\text{S}$ and $\Delta^{17}\text{O}$ Tracers

##### 3.1 Abstract

Due to the complex nature of the sulfur cycle, uncertainties remain in the transport rate and chemical transformation mechanisms of sulfur species, including sulfate aerosols. Here, we report oxygen isotopic anomaly and radioactive  $^{35}\text{S}$  measurements in sulfate aerosols collected at La Jolla, California during 2009-2010. A strong correlation results from increased levels of specific activity (up to 195 atoms of  $^{35}\text{S}/\text{nmol}$  non sea salt (nss)- $\text{SO}_4$ ) and  $\Delta^{17}\text{O}$  (up to 1.50‰) in sulfate aerosol (fine fraction) samples during Santa Ana wind events compared to background levels. This is possibly due to an increase in mixing of free tropospheric air mass, containing higher levels of  $^{35}\text{S}$  specific activity and higher  $\Delta^{17}\text{O}$ , into the boundary layer. These tracers show the ability to detect changes in oxidation chemistry during high altitude air mixing events and have the potential to trace the changes in oxidation pathways of sulfur species during Stratospheric-Tropospheric exchange events. Sampling at higher latitudes where deep stratospheric intrusions are more prominent can help further parameterize how stratospheric-tropospheric exchange events (STE) affect oxidation chemistry in the boundary layer.

##### 3.2 Introduction

Sulfate represents a major chemical constituent of atmospheric aerosols, and is of particular importance due to its potential to serve as a cloud condensation nuclei as well as its enhancement of the Earth's albedo by reflecting sunlight back to space [Kumala *et al.*, 2000; Alexander *et al.*, 2012]. Our knowledge of chemical and photochemical processes that govern the chemical transformations and transport of sulfur compounds in the atmosphere is incomplete due to the complex nature of the sulfur cycle and uncertainties in understanding aerosol chemistry [Brothers *et al.*, 2010]. Gaining a better understanding of the chemical transformations and transport of sulfur compounds in the atmosphere is essential to improve our knowledge of sulfur chemistry and predict future climate change.

Sulfur-35( $^{35}\text{S}$ ) is a unique tracer in that it can be used to follow the sulfur cycle through both gas, as  $\text{SO}_2$ , and particle phases, as aerosol sulfate, and has been used to study  $\text{SO}_2$  oxidation and transport

between the boundary layer and the free troposphere [Tanaka and Turekian, 1995].  $^{35}\text{S}$  is a naturally occurring radionuclide (half life: 87 days) produced from cosmic ray spallation of Argon. Once produced,  $^{35}\text{S}$  rapidly oxidizes to  $^{35}\text{SO}$  (lifetime~1 ms) via  $\text{O}_2/\text{O}_3$  reaction and subsequently to  $^{35}\text{SO}_2$  (lifetime~1 s) in the presence of  $\text{O}_2$ ,  $\text{O}_3$ ,  $\text{N}_2\text{O}$ , or  $\text{OCIO}$  [Black et al., 1982; Brothers et al., 2010; Priyadarshi et al., 2012; Robertshaw and Smith, 1980]. On a global average, only about 50% of  $\text{SO}_2$  is oxidized to  $\text{SO}_4^{2-}$  via homogenous (OH) or heterogeneous ( $\text{H}_2\text{O}_2$ ,  $\text{O}_3$ ) oxidation with the remainder of  $\text{SO}_2$  lost through dry and wet deposition [Chin et al., 1996]. The production rate of  $^{35}\text{S}$  increases exponentially with altitude, attaining a maximum in the stratosphere [Lal et al., 1960]. Priyadarshi, (2012) calculated steady state concentrations of  $2.8 \times 10^{-6}$  atoms  $\text{cm}^{-3} \text{ day}^{-1}$ ,  $6.5 \times 10^{-5}$  atoms  $\text{cm}^{-3} \text{ day}^{-1}$ , and  $1.1 \times 10^{-4}$  atoms  $\text{cm}^{-3} \text{ day}^{-1}$  in the boundary layer, free troposphere, and lower stratosphere, respectively, for La Jolla, California.  $^{35}\text{S}$  activities of sulfate aerosols are a result of the equilibrium between  $^{35}\text{S}$  production rates, radioactive decay, oxidation of  $^{35}\text{SO}_2$  to  $^{35}\text{SO}_4^{2-}$ , wet and dry deposition, and air mass mixing between the troposphere and stratosphere [Priyadarshi et al., 2012]. Due to the long residence time of gases and aerosols,  $^{35}\text{SO}_2$  and  $^{35}\text{SO}_4^{2-}$  produced in the stratosphere mostly decays to  $^{35}\text{Cl}$  before reaching the troposphere, except during STE. STE may have a significant impact on the chemical composition of both the lower stratosphere and troposphere as these events can alter water vapor content, ozone concentration, and affects the oxidizing capacity of the atmosphere, thus changing the lifetime of many gases. Since  $^{35}\text{SO}_4^{2-}$  possesses identical chemical properties as bulk  $\text{SO}_4^{2-}$ , and the concentration of  $^{35}\text{SO}_4^{2-}$  is expected to vary significantly in the troposphere and stratosphere,  $^{35}\text{S}$  has the potential to be an effective tracer for understanding boundary layer chemistry and STE [Brothers et al., 2010; Cho et al., 2011; Lal and Peters, 1968; Lee and Thiemens, 2001; Osaki et al., 1999; Priyadarshi et al., 2011; Priyadarshi et al., 2012; Tanaka and Turekian, 1991; 1995; Turekian and Tanaka, 1992].

Combined with stable oxygen isotopic measurements,  $^{35}\text{S}$  has the potential to study how sulfate oxidation varies in the boundary layer due to mixing with high altitude air. Lee and Thiemens, (2001) were the first to show a correlation between specific activity ( $^{35}\text{S}$  abundance normalized to the amount of sulfate in a sample) and oxygen isotopes. Most atmospheric processes obey a mass dependent isotopic fractionation, as  $\delta^{17}\text{O}$  and  $\delta^{18}\text{O}$  vary in relative proportion to their reduced masses. Any process that

deviates from this relationship is termed mass independent fractionation and is quantified by  $\Delta^{17}\text{O}$ , where  $\Delta^{17}\text{O} \approx \delta^{17}\text{O} - 0.515 \delta^{18}\text{O}$ ,  $\delta = (R_{\text{sample}}/R_{\text{standard}} - 1) * 1000$  and  $R = {}^{17}\text{O}/{}^{16}\text{O}$  or  ${}^{18}\text{O}/{}^{16}\text{O}$ . In the troposphere,  $\text{SO}_2$  is presumed to be mass dependent due to equilibrium isotope exchange with water [Holt *et al.*, 1981] as the isotopic composition of water in the troposphere is dominated by mass dependent isotope effects such as meteorological evaporation and condensation [Franz and Röckmann, 2005]. Therefore, any observed mass independent compositions found in sulfate aerosols derive from the oxidation of  $\text{SO}_2$  to  $\text{SO}_4^{2-}$  [Savarino *et al.*, 2000]. OH radicals are mass dependent even though there exist several processes that contribute non-zero MIF anomalies [Morin *et al.*, 2007] including formation via photolysis of ozone and nitrous acid, or reaction of  $\text{HO}_2$  radicals with NO [Seinfeld and Pandis, 1998]. The fast equilibrium isotope exchange between water and OH, which is faster than all OH sinks [Michalski *et al.*, 2003], eliminates any  $\Delta^{17}\text{O}$  anomaly originally produced in OH radicals.  $\text{H}_2\text{O}_2$  and  $\text{O}_3$  have been experimentally determined to possess  $\Delta^{17}\text{O}$  values of  $\sim 1.7\text{‰}$  and  $27\text{‰}$ , respectively [Johnston and Thiemens, 1997; Savarino and Thiemens, 1999; Thiemens and Heidenreich, 1983]. Recently, ambient measurements of  $\Delta^{17}\text{O}(\text{O}_3)_{\text{bulk}}$  have yielded a value of  $22.9 \pm 1.9\text{‰}$  using nitrite coated filters [Vicars *et al.*, 2012]. Although slightly lower than previous measurements, the reported value is within the error of previous studies which used cryogenic trapping to collect ozone. These laboratory measurements have been applied to field observations and include the recognition that wintertime Arctic  $\text{SO}_2$  oxidation processes are dominated by  $\text{O}_2$  via transition metal catalysis on aerosol surfaces, rather than OH and  $\text{H}_2\text{O}_2$  [Alexander *et al.*, 2009; McCabe *et al.*, 2006]. Quantitative definition of the contributions from maritime shipping to the primary anthropogenic sulfate budget has also been reported [Dominguez *et al.*, 2008]. Modeling efforts of  $\Delta^{17}\text{O}$  has been employed to identify specific reaction characteristics such as the role of aerosol particle surfaces above the Indian Ocean as well as show the variation in tropospheric  $\text{O}_3$  and OH oxidation from pre-industrial to industrial times in ice cores [Alexander *et al.*, 2005; Kunasek *et al.*, 2010].

In the stratosphere, both  $\text{SO}_2$  and OH are expected to contain larger  $\Delta^{17}\text{O}$  anomalies compared to their tropospheric counterparts. Stratospheric water is mostly photochemical in origin, suggesting stratospheric water may have a mass independent composition [Franz and Röckmann, 2005]. At parts per million water vapor levels in the stratosphere, the equilibrium isotope exchange between  $\text{SO}_2$ , OH, and

water vapor is likely a minor, or restricted process. A stratospheric ozone anomaly ( $\Delta^{17}\text{O}$ ) has been measured up to 40 ‰ [Krankowsky *et al.*, 2000; Krankowsky *et al.*, 2007; Lämmerzahl *et al.*, 2002; Mauersberger *et al.*, 2001] while the isotopic composition of OH in the stratosphere has been estimated to be as large as 30‰-40‰ [Lyons, 2001; Zahn *et al.*, 2006]. Because  $\text{H}_2\text{O}_2$  is produced from  $\text{HO}_2$  radicals, which are formed through the reaction of OH and  $\text{O}_3$ , stratospheric  $\text{H}_2\text{O}_2$  is also expected to contain elevated  $\Delta^{17}\text{O}$  values as compared to tropospheric  $\text{H}_2\text{O}_2$  [Morin *et al.*, 2011]. These findings indicate that stratospheric sulfate should contain larger  $\Delta^{17}\text{O}$  anomalies than tropospheric sulfate. It may be anticipated that STE can affect boundary layer  $\Delta^{17}\text{O}$  chemistry in two ways; first, increased transport of stratospheric sulfate with high  $\Delta^{17}\text{O}$  values to the boundary layer, and secondly, increased oxidation of  $\text{SO}_2$  in the troposphere due to increased levels of ozone from a stratospheric source. Therefore, the oxygen anomaly is expected to correlate with  $^{35}\text{S}$  activity in stratosphere sulfate. Combining radioactive sulfur measurements and  $\Delta^{17}\text{O}$  in sulfate has the potential to enhance understanding of the extent of STE events into the troposphere and how these events affect the oxidation of sulfur oxides to sulfate aerosols.

In this paper, we show the variations in  $^{35}\text{S}$  and  $\Delta^{17}\text{O}$  in sulfate aerosols collected during three Santa Ana wind events and three STE events and compare them to normal coastal climate samples in Southern California. STE events are not a common occurrence at low latitudes, but are sporadically seen during late winter and early spring. Santa Ana events occur in Southern California between September and March and are a result of a high pressure system building over the Great Basin in the southern Sierra Nevada Mountains simultaneously with a low pressure system offshore. The result is the creation of strong, dry winds from the east which lowers the relative humidity and increases the risk of forest fires [Guazzotti *et al.*, 2001; Miller and Schlegel, 2006; Raphael, 2003; Westerling *et al.*, 2004]. Even though Santa Ana events are not linked to STE, through the use of  $^{35}\text{S}$  measurements, Priyadarshi *et al.*, (2012) showed that these events lead to an increase in the mixing of free tropospheric air into the boundary layer, and consequently may affect oxidation chemistry in the boundary layer.

### 3.3 Methods

Samples were collected at the Scripps Pier in La Jolla, California (32.7° N, 117.2° W) using a standard high volume (Thermo-Electron), five-stage slotted impact collector with glass-fiber filter papers.

This site is located on the Pacific Ocean, 10 miles north of downtown San Diego. Depending on meteorological patterns, this site collects on-shore oceanic as well as off-shore air masses with possible anthropogenic sulfate sources from the Los Angeles urban environment. From September to March, this site experiences occasional strong Santa Ana winds as air pressure builds over the Great Basin in Nevada leading to off-shore high altitude air masses pouring into the Southern California basin.

Samples were collected from February, 2009 to August, 2010 and previously measured for  $^{35}\text{S}$  activity in *Priyadarshi et al.*, (2012) following the procedure of *Brothers et al.*, (2010) with a background error of less than 5 atoms/m<sup>3</sup>. Fine particle mode samples (PM< 1.5  $\mu\text{m}$ ) were analyzed for oxygen isotopes to observe the potential relation between  $^{35}\text{S}$  and  $\Delta^{17}\text{O}$  during different climatic events in Southern California including Santa Ana and STE events. Santa Ana events were determined to occur when the relative humidity dropped below 30% and strong easterly winds prevailed. NOAA Hysplit back trajectory models [*Draxler and Rolph*, 2011] confirm that air masses during these events originated from the Great Basin of Nevada before descending into Southern California. STE events were determined in *Priyadarshi et al.*, (2012) where the  $^{35}\text{S}$  activity in the fine particle mode was higher than 2 sigma deviations from annual averages, at least 769 atoms/m<sup>3</sup>. Samples which did not experience a Santa Ana or STE event were also measured for background oxygen isotopic levels and are referred to as coastal climate samples. Oxygen isotope measurements were performed by separating sulfate through ion chromatography and converting to  $\text{Ag}_2\text{SO}_4$ .  $\text{O}_2$  gas was collected from pyrolysis of  $\text{Ag}_2\text{SO}_4$  at a temperature of 1030° C and measured for  $\delta^{18}\text{O}$  and  $\delta^{17}\text{O}$  values on a MAT 251 mass-spectrometer. The value of the oxygen anomaly ( $\Delta^{17}\text{O}$ ) was determined with an error of  $\pm 0.1\%$  [*Savarino et al.*, 2001].

Oxygen isotopic compositions are corrected for sea salt content in each sample using magnesium as a sea salt tracer and assuming the molar ratio of  $\text{SO}_4^{2-}:\text{Mg}^{2+}$  in sea water to be 0.5369 and sea salt sulfate to have a  $\Delta^{17}\text{O}$  of 0‰ and a  $\delta^{18}\text{O}$  value of 10‰. Sodium is frequently used as a sea salt marker, but at some sampling sites, the use of sodium may be problematic due to the influence of non-marine sources of sodium, such as crustal material [*Cainey et al.*, 1999; *Martens et al.*, 1973; *Sievering et al.*, 2004]. In our samples, the average ratio of Na:Mg and Cl:Mg was 16.7 and 19.8 respectively, compared to the expected

sea water ratios of 8.9 and 10.4, leading to overestimation of sea salt sulfate when using sodium as a sea salt proxy.

### 3.4 Results and Discussion

The average sulfate concentration of bulk fine sulfate, reported in Table 1, is 21 nmol/m<sup>3</sup>, with a maximum of 63 nmol/m<sup>3</sup>, and nss sulfate concentrations averaging 20 nmol/m<sup>3</sup>, with a maximum of 62 nmol/m<sup>3</sup>. Specific activity averages 54 atoms/[nmol nss-sulfate] with a maximum of 195 atoms/[nmol nss-sulfate], whereas  $\Delta^{17}\text{O}$  anomalies in nss-sulfate range from 0.47‰ to 1.50‰ with an average value of 0.92‰. Figure 1 shows the relationship between specific activity and  $\Delta^{17}\text{O}$ . Santa Ana samples show enhanced levels of specific activity (138-195 atoms/nmol nss-sulfate) and  $\Delta^{17}\text{O}$  (1.42‰-1.50‰) relative to coastal climate samples. STE events, defined as samples where <sup>35</sup>S activity is higher than 2 sigma deviations from annual averages in *Priyadarshi et al.*, (2012), show specific activity and  $\Delta^{17}\text{O}$  levels which agree with coastal climate samples. These results suggest that Santa Ana events have a larger effect on boundary layer chemistry than STE events in Southern California.  $\Delta^{17}\text{O}$  shows a strong correlation with specific activity, but not with <sup>35</sup>S activity (<sup>35</sup>S atoms/m<sup>3</sup>) likely because specific activity normalizes the radioactivity count to the sulfate concentration, thus accounting for non-radioactively produced sulfate such as those derived from anthropogenic fossil fuel production. As  $\Delta^{17}\text{O}$  is a measurement of total atmospheric sulfate, including anthropogenic and natural sources, it is expected that  $\Delta^{17}\text{O}$  would compare more favorably to specific activity than <sup>35</sup>S activity. It is possible that specific activity better traces atmospheric chemical (oxidation) processes compared to <sup>35</sup>S activity due to the inclusion of non-radioactive production processes.

The question of whether coarse mode sulfate follows the same patterns as fine mode sulfate remains unanswered. Due to the close proximity of the sampling site to the ocean, coarse samples consisted of sea salt sulfate compositions reaching excesses of 90%. This result magnifies the error in the sea salt correction immensely and can lead to a few per mil error in  $\Delta^{17}\text{O}$  making it difficult to determine if a relationship between specific activity and  $\Delta^{17}\text{O}$  exists in coarse mode sulfate [*Patris et al.*, 2007].

#### 3.4.1 Coastal Climate Samples



Specific activity in coastal climate samples (referred to as samples C1-C13 in Table 1) range from 4-73 atoms/[nmol nss-sulfate] with an average value of 33 atoms/[nmol].  $\Delta^{17}\text{O}$  ranges from 0.47‰ to 1.09‰ and agree relatively well with previous sulfate isotopic measurements taken at Scripps Pier [Dominguez *et al.*, 2008; Lee and Thiemens, 2001].  $\Delta^{17}\text{O}$  is negatively correlated with nss-sulfate, as seen in Figure 2. From analysis of Table 1, specific activity can also be seen to decrease with sulfate concentrations suggesting the influence of a non-radioactive, mass dependent sulfate component. Anthropogenic emissions contribute 70-80% of the total sulfate burden in the northern hemisphere [Rasch *et al.*, 2000], potentially more in urban settings. NOAA Hysplit back trajectory models show the five most concentrated fine mode samples; C-1 to C-5; trace back to the Los Angeles region, which is known for high pollution levels [Su *et al.*, 2009].  $\delta^{18}\text{O}$  values do not correlate with  $\Delta^{17}\text{O}$ , suggesting multiple sources, not one distinct source. It's possible that the mixing line is composed of mass dependent sulfate sources including land based primary diesel sulfate ( $\delta^{18}\text{O}\approx 5\text{‰}-7\text{‰}$ ,  $\Delta^{17}\text{O}\approx 0\text{‰}$ ) [Lee *et al.*, 2002] and primary sulfate from ship emissions ( $\delta^{18}\text{O}\approx 20\text{‰}$ ,  $\Delta^{17}\text{O}\approx 0\text{‰}$ ) [Dominguez *et al.*, 2008]. On a global scale, primary sulfate emissions are small, however, proximal to these sources, combustion sulfate can locally contribute a significant portion of atmospheric sulfate [Holt *et al.*, 1982]. Dominguez *et al.*, (2008) calculated that ships can contribute up to 44% of the nss-sulfate found in fine particulate matter within Southern California. As vehicle and ship sulfate emissions are derived from fossil fuel, they possess a  $^{35}\text{S}$  activity of zero, thus diluting specific activity along with  $\Delta^{17}\text{O}$ .

Biomass burning ( $\delta^{18}\text{O}\approx 6\text{‰}-11\text{‰}$ ,  $\Delta^{17}\text{O}\approx 0\text{‰}$ ) [Lee *et al.*, 2002] is another possible source of mass dependent sulfate. Southern California is highly susceptible to wildfires due to its dry climate with wildfire season typically running from mid-May to early December. It is unknown how these biomass burning events affect radioactive sulfur activity in the atmosphere. Cho *et al.*, (2011) has suggested a  $^{35}\text{S}$  turnover process in plants and soil of 66 days caused by the deposition of  $^{35}\text{SO}_4^{2-}$  in soil and the release of  $\text{H}_2\text{S}$  by plants, which subsequently oxidizes to  $\text{SO}_4$  in the atmosphere. It is plausible that biomass burning can lead to a release of  $^{35}\text{S}$  into the atmosphere. However, constraining the amount of  $^{35}\text{S}$  discharge from biomass burning during a distinct event is difficult. Dead biomass will not uptake  $^{35}\text{S}$  from the soil and thus is not suspected to release  $^{35}\text{S}$  upon burning. However, as the half life of  $^{35}\text{S}$  is 87 days, it is possible that a plant

which has recently died might still possess trace amounts of  $^{35}\text{S}$  which will be released to the atmosphere upon burning. Therefore, the release of  $^{35}\text{S}$  is not constrained to just live plant matter. Samples (C-8 to C-10) collected during the Station Fire, which burned 160,577 acres from August 26<sup>th</sup> to October 16<sup>th</sup>, 2009 in Los Angeles County, making it the largest fire in Los Angeles County recorded history [NOAA, 2009], do not show variation in specific activity relative to other coastal climate samples suggesting that biomass burning events have only minor effects on  $^{35}\text{S}$  radioactivity in the atmosphere. This assumption agrees with calculations from *Priyadarshi et al.*, (2012), who estimated the contribution of this turnover process to account for only 2-5% of the measured  $^{35}\text{S}$  in the atmosphere. Therefore, the negative correlation seen in Figure 2 implies a heavy influence from fossil fuel emissions, not biomass burning.

### 3.4.2 Santa Ana Samples

Santa Ana samples (A1-A3) possess low levels of  $^{35}\text{S}$  activity in the fine mode, ranging from 336 to 471 atoms/m<sup>3</sup> with an average of 415 atoms/m<sup>3</sup>. Depositional rates are thought to increase on ocean surfaces and vegetation due to the prevailing strong gravity produced winds [*Priyadarshi et al.*, 2012] and may account for the low observed  $^{35}\text{S}$  activity measurements. This is consistent with findings by *Guazzotti et al.*, (2001), who observed a stark decrease in fine particle concentration at the onset of a Santa Ana event. It is interesting to note that although total sulfate concentrations dropped during Santa Ana events, sea salt sulfate concentrations stayed fairly constant relative to coastal climate and STE samples, resulting in an increase in the relative proportion of sea salt sulfate to the overall sulfate budget. *Guazzotti et al.*, (2001) noticed a decrease in sea salt sulfate while sampling during Santa Ana events in Riverside, California. This variation could be due to the differences in sampling locations as data collected here was taken directly on the ocean, whereas Riverside, California is about 50 miles inland. The change from offshore winds to onshore winds typical of Santa Ana wind events probably has minimal effect on the sea salt concentrations seen here since the ocean was in such close proximity to the sampler.

Specific activity measurements display large increases as compared to coastal climate samples, ranging from 139 to 195 atoms/[nmol]. Since the chemical properties of  $^{35}\text{SO}_4^{2-}$  are thought to be essentially identical to bulk  $\text{SO}_4^{2-}$ , specific activity is likely unaffected by increased deposition rates as it is assumed that  $^{35}\text{SO}_4^{2-}$  deposits concomitantly with bulk sulfate. During Santa Ana events,  $\Delta^{17}\text{O}$  values vary

from 1.42-1.50‰. The concurrent rise of specific activity and  $\Delta^{17}\text{O}$  suggests an increase in sulfate (high in  $\Delta^{17}\text{O}$ ) which is oxidized at a higher altitude, thus implying the presence of high altitude air mixing with the boundary layer. A similar correlation between specific activity and  $\Delta^{17}\text{O}$  was observed by *Lee and Thiemens*, (2001) at White Mountain Research Station, which is located at the remote site of Mount Barcroft (37.5° N, 118.2° S), northeast of Bishop, California and above the planetary boundary layer at an altitude of 3.8 km. Santa Ana events are thought to result in mid and upper tropospheric air mixing with the boundary layer, not stratospheric intrusions [*Fosberg*, 1966; *Huang et al.*, 2009]. Also, *Priyadarshi et al.*, (2012) estimated that up to 41% of total air mass sampled in the boundary layer during Santa Ana events in Southern California originated from the free troposphere. Therefore, the source of STE as a cause for the observed increases in specific activity and  $\Delta^{17}\text{O}$  is ruled out as the main source of mixing during Santa Ana events.

Aqueous oxidation of sulfur dioxide via ozone is the predominant source of  $\Delta^{17}\text{O}$  anomalies in sulfate compared to oxidation by hydrogen peroxide ( $\Delta^{17}\text{O O}_3 \approx 27\text{‰}$ ,  $\Delta^{17}\text{O H}_2\text{O}_2 \approx 1.7\text{‰}$ ) suggesting that the increase in  $\Delta^{17}\text{O}$  is a direct relation to an increase in ozone oxidation. However, at typical cloud pH levels of around 3-5 [*Faloon et al.*, 2009], the rate of aqueous phase oxidation of S(IV) is dominated by  $\text{H}_2\text{O}_2$  rather than ozone oxidation;  $10^{-8}$  M/sec compared to  $10^{-11}$  M/sec [*Lee and Thiemens*, 2001]. The ozone mixing ratio in the free troposphere would have to be much greater relative to the boundary layer to produce large changes in  $\Delta^{17}\text{O}$  sulfate anomalies. Increases in ozone oxidation of S(IV) should lead to larger  $\delta^{18}\text{O}$  values as  $\delta^{18}\text{O}$  of tropospheric ozone have been measured to be above 80‰ [*Johnston and Thiemens*, 1997]. A substantial increase in  $\delta^{18}\text{O}$  in Santa Ana samples relative to coastal climate samples is not observed, suggesting this is a minor process, and not the dominant mechanism driving the increase of  $\Delta^{17}\text{O}$  in free tropospheric sulfate.

It is possible that the difference in observed  $\Delta^{17}\text{O}$  values arises from a dilution effect in the boundary layer. The boundary layer, in general, possesses larger concentrations of mass dependent sulfate due to anthropogenic emissions and ocean derived sulfate, which lower the  $\Delta^{17}\text{O}$  anomaly in bulk sulfate. This may account for the difference in  $\Delta^{17}\text{O}$  between free tropospheric sulfate and boundary layer sulfate rather than a change in aqueous oxidation pathways. Thermally convective transport of boundary layer air

to the free troposphere is possible, however, it is expected that upward mixing is significantly decreased during Santa Ana events as large levels of high altitude air spill into the boundary layer [Priyadarshi *et al.*, 2012]. As amplified anomalous concentrations of free tropospheric sulfate flow into the boundary layer, the resultant mixing increases the  $\Delta^{17}\text{O}$  of the bulk sample.

Another mechanism to potentially account for the correlation between specific activity and  $\Delta^{17}\text{O}$  of sulfate is the transfer of free tropospheric  $\text{SO}_2$  to the boundary layer with subsequent oxidation to sulfate. To result in increased  $\Delta^{17}\text{O}$  anomalies, this mechanism requires a relative change in oxidative formation pathways of S(IV) in the boundary layer due to the prevailing Santa Ana winds. Increased wind speeds can boost mineral dust concentrations in the atmosphere, which can lead to an increase in the pH of the boundary layer. Guazzotti *et al.*, (2001) found an increase in the concentration of mineral dust during Santa Ana events compared to normal weather conditions in Riverside, CA. Uptake of  $\text{SO}_2$  in the presence of mineral dust is thought to occur via aqueous phase oxidation of  $\text{SO}_3^{2-}$  by  $\text{O}_3$  due to the increased alkalinity of mineral dust. Hydrogen peroxide oxidation is the primary oxidant at low pH values, but above a pH of  $\sim 5.6$ ,  $\text{O}_3$  oxidation dominates [Alexander *et al.*, 2002]. However, nss-calcium concentrations in the fine particle mode remain consistent with coastal climate sample measurements. As nss-calcium is used as a tracer for mineral dust, this suggests that  $\text{SO}_2$  uptake via mineral dust is not a dominant mechanism in fine modal sulfate [Athanasopoulou *et al.*, 2010; Virkkula *et al.*, 2006]. The observations suggest the increase in  $\Delta^{17}\text{O}$  is a result of increased sulfate levels from the free troposphere and not a change in oxidative pathway of the boundary layer.

### 3.4.3 STE Samples

Although STE samples (E1-E3) contain larger  $^{35}\text{S}$  activity values, ranging from 819-868 atoms/ $\text{m}^3$ , the specific activity (average value of 31 atoms/[nmol]) of these samples are comparable to coastal climate samples. Deep STE intrusion events, where stratospheric air mixes directly into the boundary layer, typically occur at high altitudes, but are rarely detected at sea level. The STE event considered here is a shallow type of stratospheric-tropospheric mixing, where stratospheric air masses are mixed into the free troposphere and subsequently mixed into the boundary layer [Priyadarshi *et al.*, 2012]. Although Priyadarshi *et al.*, (2012) calculated 5-6% mixing of lower stratospheric air with the boundary

layer, specific activity measurements suggest that this mixing had minimal compositional effect on the boundary layer.  $\Delta^{17}\text{O}$  measurements, ranging from 0.53‰ to 0.76‰, agree with this hypothesis as no increase is seen relative to coastal climate samples. Stratospheric mixing events are expected to lead to changes in the oxidation chemistry of the troposphere due to an increase in ozone levels, thus effecting the  $\Delta^{17}\text{O}$  measurements. Nevertheless, no spikes were observed in ozone concentrations relative to the average during the sampling periods, suggesting only weak interaction with the boundary layer. Even with admixture of anomalous stratospheric sulfate into the boundary layer, it is likely that the percentage of stratospheric sulfate to the total sulfate budget was negligibly small such that any large  $\Delta^{17}\text{O}$  signal from these particles was diluted by a predominant boundary layer sulfate component.

We note that as cosmogenic nuclide production increases with latitude, there is a possibility that the large increases in  $^{35}\text{S}$  concentrations seen in STE samples arise due to a contribution of tropospheric air from high latitudes ( $>60^\circ\text{N}$ ) and is not necessary due to an STE event. To quantify the likelihood of this scenario, the steady state model described in detail in *Priyadarshi et al., (2011) and Priyadarshi et al., (2012)* was used to determine steady state concentrations for  $^{35}\text{S}$  at the  $60^\circ\text{N}$  latitude.  $^{35}\text{SO}_4^{2-}$  concentrations were determined to be 716, 886, 1062, and 11925 atoms/ $\text{m}^3$  in the marine boundary layer, buffer layer, free troposphere, and lower stratosphere, respectively. Assuming the transport of air from higher latitudes as a result of free tropospheric air mixing into the boundary layer in La Jolla, CA., a simple mass balance can be used to estimate the percentage of free tropospheric air from  $60^\circ\text{N}$  necessary to replicate the measured  $^{35}\text{SO}_4^{2-}$  values seen in the STE samples. Upon calculation, the collected air mass must contain 53%, 53%, and 63% of free tropospheric air from  $60^\circ\text{N}$  for samples E1, E2, and E3, respectively, to match the measured  $^{35}\text{SO}_4^{2-}$  values. High latitude air masses mix with air from lower latitudes as they travel south, thus diluting the  $^{35}\text{S}$  concentration, meaning this calculation can be considered a lower limit to the amount of high latitude air required. As stated earlier, *Priyadarshi et al., (2012)* estimated up to a 41% influx of upper altitude air mass from the free troposphere during Santa Ana events. This influx is aided by a large pressure gradient forcing upper altitude air into the boundary layer. Pressure gradients of this magnitude were not seen during the sampling periods that E1, E2, and E3 were taken suggesting that the increase in  $^{35}\text{S}$  is unlikely to occur due from free tropospheric air masses above  $60^\circ\text{N}$  latitudes. Measurements of  $^7\text{Be}$

and  $^{210}\text{Pb}$  have been used to study air mass mixing between the upper altitudes and the boundary layer, and in the future, can be used in support of  $^{35}\text{S}$  measurements to determine the extent of stratospheric mixing [Graustein and Turekian, 1996]. To resolve the stratospheric source, sampling should also be done at locations where strong stratospheric intrusions are thought to periodically occur, such as near the poles. For example, Priyadarshi *et al.*, (2011) measured  $^{35}\text{S}$  activities at Dome C, Antarctica and estimated up to a 10% mixing of stratospheric air mass with the boundary layer.

### 3.5 Conclusions

Concurrent measurements of  $^{35}\text{S}$  and  $\Delta^{17}\text{O}$  of sulfate along the San Diego coastline are reported and reveal sulfate oxygen isotopic anomalies during Santa Ana wind events. It is observed that during Santa Ana events  $^{35}\text{S}$  specific activities of fine sulfate aerosols strongly correlates with the oxygen anomaly ( $\Delta^{17}\text{O}$ ), indicating increased levels of mixing between the free troposphere and the boundary layer. From data presented here, it is apparent that free tropospheric sulfate may contain increased  $\Delta^{17}\text{O}$  anomalies relative to boundary layer sulfate. This results from increased levels of anthropogenic sulfate at ground level, diluting the  $\Delta^{17}\text{O}$  of boundary layer sulfate. In addition, the possibility of increased ozone oxidation of  $\text{SO}_2$  in the free troposphere may produce a potential change in the oxidation chemistry of the free troposphere compared to the boundary layer. The combination of these tracers has the potential of studying variations in oxidative pathways arising from deep stratospheric intrusions, as well as tracing sulfur-oxygen chemical processes during transport.

### 3.6 Acknowledgements

Chapter 3, in full, is a reprint of material as it appears in Journal of Geophysical Research-Atmospheres, Hill-Falkenthal, J., A. Priyadarshi, and M. Thiemens, Differentiating Sulfate Aerosol Oxidation Pathways for Varying Source Altitudes Using  $^{35}\text{S}$  and  $\Delta^{17}\text{O}$  Tracers, volume 117, 2012. The dissertation author was the primary author of this paper. The authors thank S. Chakraborty, G. Dominguez, R. Shaheen, and T. Jackson for beneficial scientific discussions which improved the manuscript significantly.

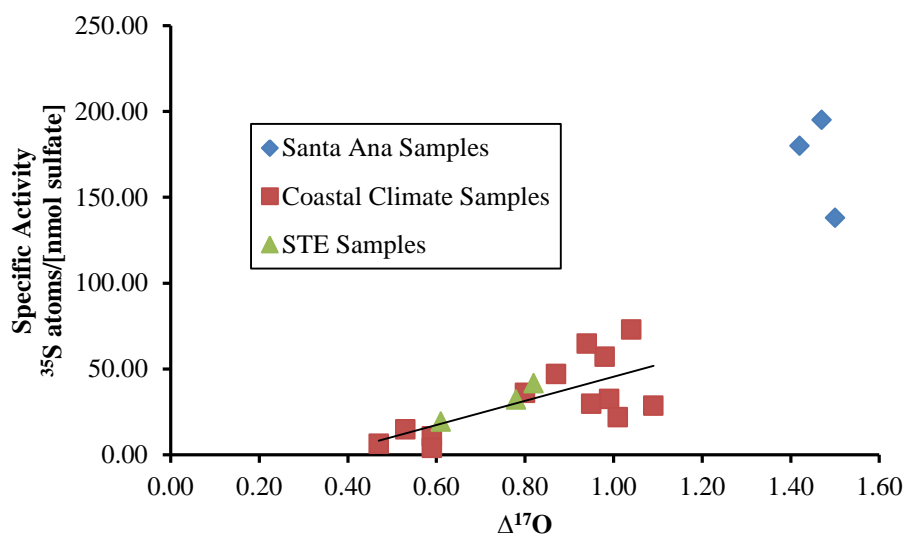


Figure 3.1

Specific activity plotted against  $\Delta^{17}\text{O}$  in the fine particle fraction ( $<1.5\mu\text{m}$ ). During Santa Ana events, enhanced specific activity shows strong correlation with increased  $\Delta^{17}\text{O}$  anomalies.

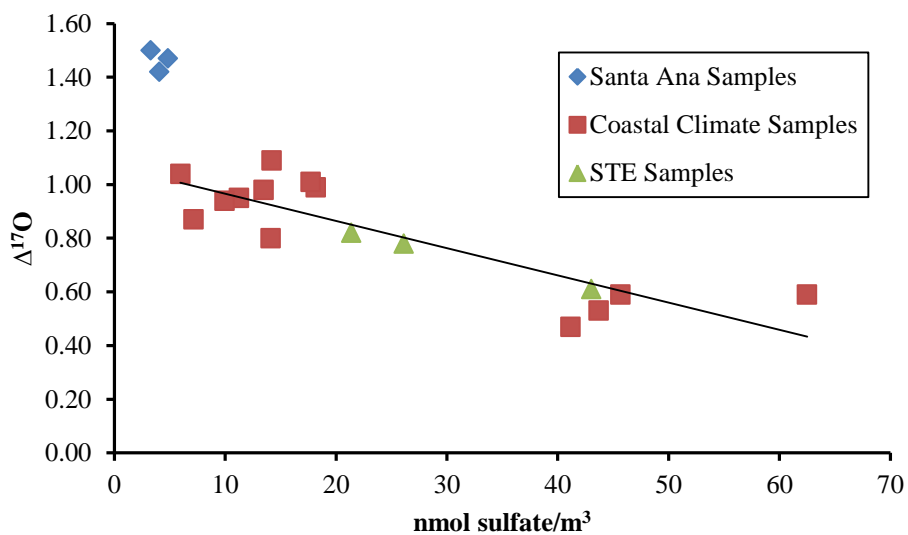


Figure 3.2

The correlation between  $\Delta^{17}\text{O}$  and sulfate concentrations in the fine particle fraction ( $<1.5\mu\text{m}$ ). Santa Ana samples suggest mixing of a high altitude air source containing fewer aerosols into the boundary layer. The negative trend line seen in coastal climate samples suggests a mixing source of anthropogenic primary sulfate decreasing the  $\Delta^{17}\text{O}$  anomaly, yet increasing the sulfate concentration.



Table 3.1

Summary of sulfate concentration, specific activity, and  $\Delta^{17}\text{O}$  in fine particles. Uncorrected  $\delta$  values refer to measurements before the sea salt correction is applied, whereas NSS- $\delta$  values refer to measurement values after the sea salt correction.

Sample ID	Start Date	End Date	[SO <sub>4</sub> ]; nmol/m <sup>3</sup>	NSS-[SO <sub>4</sub> ]; nmol/m <sup>3</sup>	<sup>35</sup> S (atoms/m <sup>3</sup> )	SA ( <sup>35</sup> S atoms/nmol nss SO <sub>4</sub> )	Uncorrected $\delta^{18}\text{O}$ (‰)	Uncorrected $\delta^{17}\text{O}$ (‰)	NSS- $\delta^{18}\text{O}$ (‰)	NSS- $\Delta^{17}\text{O}$ (‰)
Coastal Climate Samples										
C-1	4/28/09	5/1/09	62.50	61.63	664	10.77	11.32	6.41	11.34	0.59
C-2	5/5/09	5/8/09	45.65	43.59	175	4.01	8.97	5.15	8.92	0.59
C-3	5/15/09	5/19/09	41.16	40.68	263	6.47	8.46	4.82	8.44	0.47
C-4	5/26/09	5/29/09	43.69	43.44	646	14.87	10.49	5.93	10.49	0.53
C-5	7/9/09	7/14/09	14.20	13.62	390	28.64	9.86	6.14	9.86	1.09
C-6	8/4/09	8/7/09	7.14	6.95	327	47.06	17.23	9.72	17.42	0.87
C-7	8/28/09	9/1/09	18.19	16.65	541	32.50	8.51	5.29	8.37	0.99
C-8	9/5/09	9/8/09	14.12	12.55	453	36.11	9.15	5.42	9.04	0.80
C-9	9/24/09	9/28/09	17.71	16.60	363	21.86	11.03	6.63	11.10	1.01
C-10	10/8/09	10/12/09	13.48	13.13	751	57.20	11.17	6.71	11.20	0.98
C-11	10/16/09	10/20/09	11.24	10.61	334	29.70	14.10	8.16	14.34	0.95
C-12	12/1/09	12/4/09	9.96	8.19	530	64.71	12.50	7.21	13.04	0.94
C-13	1/29/10	2/2/10	5.96	4.85	354	72.94	12.51	7.29	13.08	1.04
Santa Ana Samples										
A-1	11/24/09	12/1/09	3.27	1.87	439	138	11.70	6.88	12.98	1.50
A-2	12/18/09	12/22/09	4.84	3.17	471	195	9.32	5.76	8.96	1.47
A-3	12/29/09	1/5/10	4.06	2.42	336	180	8.57	5.26	7.60	1.42
Stratospheric-Tropospheric Exchange Samples										
E-1	3/20/09	3/24/09	26.12	25.43	819	32.20	11.56	6.71	11.60	0.78
E-2	5/22/09	5/26/09	43.02	42.32	820	19.38	9.89	5.69	9.89	0.61
E-3	7/6/09	7/9/09	21.39	20.85	868	41.64	11.59	6.77	11.63	0.82

### 3.7 References

- Alexander, B., R. J. Park, D. J. Jacob, and S. L. Gong (2009), Transition metal-catalyzed oxidation of atmospheric sulfur: Global implications for the sulfur budget, *Journal of Geophysical Research-Atmospheres*, 114.
- Alexander, B., J. Savarino, N. I. Barkov, R. J. Delmas, and M. H. Thiemens (2002), Climate driven changes in the oxidation pathways of atmospheric sulfur, *Geophysical Research Letters*, 29(14).
- Alexander, B., D. J. Allman, H. M. Amos, T. D. Fairlie, J. Dachs, D. A. Hegg, and R. S. Sletten (2012), Isotopic constraints on the formation pathways of sulfate aerosol in the marine boundary layer of the subtropical northeast Atlantic Ocean, *Journal of Geophysical Research-Atmospheres*, 117.
- Alexander, B., R. J. Park, D. J. Jacob, Q. B. Li, R. M. Yantosca, J. Savarino, C. C. W. Lee, and M. H. Thiemens (2005), Sulfate formation in sea-salt aerosols: Constraints from oxygen isotopes, *Journal of Geophysical Research-Atmospheres*, 110(D10).
- Athanasopoulou, E., M. Tombrou, A. G. Russell, A. Karanasiou, K. Eleftheriadis, and A.
- Dandou (2010), Implementation of road and soil dust emission parameterizations in the aerosol model CAMx: Applications over the greater Athens urban area affected by natural sources, *Journal of Geophysical Research-Atmospheres*, 115.
- Black, G., R. L. Sharpless, and T. G. Slanger (1982), Rate Coefficients at 298-K for SO Reactions with O-2, O-3, and NO2, *Chemical Physics Letters*, 90(1), 55-58.
- Brothers, L. A., G. Dominguez, A. Abramian, A. Corbin, B. Bluen, and M. H. Thiemens (2010), Optimized low-level liquid scintillation spectroscopy of S-35 for atmospheric and biogeochemical chemistry applications, *Proceedings of the National Academy of Sciences of the United States of America*, 107(12), 5311-5316.
- Caine, J. M., G. P. Ayers, H. Sievering, R. W. Gillett, and M. A. Hooper (1999), The use of magnesium as a marker for sea salt at Cape Grim, *Baseline Atmospheric Program-1996*.
- Chin, M., D. J. Jacob, G. M. Gardner, M. S. Foreman Fowler, P. A. Spiro, and D. L. Savoie (1996), A global three-dimensional model of tropospheric sulfate, *Journal of Geophysical Research-Atmospheres*, 101(D13), 18667-18690.
- Cho, H. M., Y. L. Hong, and G. Kim (2011), Atmospheric depositional fluxes of cosmogenic S-35 and Be-7: Implications for the turnover rate of sulfur through the biosphere, *Atmospheric Environment*, 45(25), 4230-4234.

- Dominguez, G., T. Jackson, L. Brothers, B. Barnett, B. Nguyen, and M. H. Thiemens (2008), Discovery and measurement of an isotopically distinct source of sulfate in Earth's atmosphere, *Proceedings of the National Academy of Sciences of the United States of America*, 105(35), 12769-12773.
- Draxler, R. R., and G. D. Rolph (2011), HYSPLIT (Hybrid Single-Particle Lagrangian Integrated Trajectory) Model, access via NOAA ARL READY Website. (<http://ready.arl.noaa.gov/HYSPLIT.php>). NOAA Air Resources Laboratory, Silver Springs, Md.
- Faloon, I., S. A. Conley, B. Blomquist, A. D. Clarke, V. Kapustin, S. Howell, D. H. Lenschow, and A. R. Bandy (2009), Sulfur dioxide in the tropical marine boundary layer: dry deposition and heterogeneous oxidation observed during the Pacific Atmospheric Sulfur Experiment, *Journal of Atmospheric Chemistry*, 63(1), 13-32.
- Fosberg, M. A., O'Dell, Clyde, A., and Schroeder, Mark J. (1966), *Some characteristics of the three-dimensional structure of Santa Ana winds*, Berkeley, California.
- Franz, P., and T. Röckmann (2005), High-precision isotope measurements of (H<sub>2</sub>O)-O-16, (H<sub>2</sub>O)-O-17, (H<sub>2</sub>O)-O-18, and the Delta O-17-anomaly of water vapor in the southern lowermost stratosphere, *Atmospheric Chemistry and Physics*, 5, 2949-2959.
- Graustein, W. C., and K. K. Turekian (1996), Be-7 and Pb-210 indicate an upper troposphere source for elevated ozone in the summertime subtropical free troposphere of the eastern North Atlantic., *Geophysical Research Letters*, 23(5), 539-542.
- Guazzotti, S. A., J. R. Whiteaker, D. Suess, K. R. Coffee, and K. A. Prather (2001), Real-time measurements of the chemical composition of size-resolved particles during a Santa Ana wind episode, California USA, *Atmospheric Environment*, 35(19), 3229-3240.
- Holt, B. D., R. Kumar, and P. T. Cunningham (1981), O-18 Study of the Aqueous-Phase Oxidation of Sulfur-Dioxide, *Atmospheric Environment*, 15(4), 557-566.
- Holt, B. D., R. Kumar, and P. T. Cunningham (1982), Primary Sulfates in Atmospheric Sulfates - Estimation by Oxygen Isotope Ratio Measurements, *Science*, 217(4554), 51-53.
- Huang, C. J., Y. L. Lin, M. L. Kaplan, and J. J. Charney (2009), Synoptic-Scale and Mesoscale Environments Conducive to Forest Fires during the October 2003 Extreme Fire Event in Southern California, *Journal of Applied Meteorology and Climatology*, 48(3), 553-579.
- Johnston, J. C., and M. H. Thiemens (1997), The isotopic composition of tropospheric ozone in three environments, *Journal of Geophysical Research-Atmospheres*, 102(D21), 25395-25404.

Krankowsky, D., P. Lämmerzahl, and K. Mauersberger (2000), Isotopic measurements of stratospheric ozone, *Geophysical Research Letters*, 27(17), 2593-2595.

Krankowsky, D., P. Lämmerzahl, K. Mauersberger, C. Janssen, B. Tuzson, and T. Röckmann (2007), Stratospheric ozone isotope fractionations derived from collected samples, *Journal of Geophysical Research-Atmospheres*, 112(D8).

Kulmala, M., U. Pirjola, and J. M. Makela (2000), Stable sulphate clusters as a source of new atmospheric particles, *Nature*, 404(6773), 66-69.

Kunasek, S. A., B. Alexander, E. J. Steig, E. D. Sofen, T. L. Jackson, M. H. Thiemens, J. R. McConnell, D. J. Gleason, and H. M. Amos (2010), Sulfate sources and oxidation chemistry over the past 230 years from sulfur and oxygen isotopes of sulfate in a West Antarctic ice core, *Journal of Geophysical Research-Atmospheres*, 115.

Lal, D., and B. Peters (1968), COSMIC RAY PRODUCED RADIOACTIVITY ON THE EARTH, *Journal Name: pp 551-612 of Handbuch der Physik. Band XLVI/2. Fluegge, S. Sitte, K. (eds.). Berlin, Heidelberg, New York, Springer-Verlag, 1967.; Other Information: Orig. Receipt Date: 31-DEC-68, Medium: X.*

Lal, D., J. R. Arnold, and M. Honda (1960), Cosmic-Ray Production Rates of Be-7 in Oxygen, and P-32, P-33, S-35 in Argon at Mountain Altitudes, *Physical Review*, 118(6), 1626-1632.

Lämmerzahl, P., T. Röckmann, C. A. M. Brenninkmeijer, D. Krankowsky, and K. Mauersberger (2002), Oxygen isotope composition of stratospheric carbon dioxide, *Geophysical Research Letters*, 29(12).

Lee, C. C. W., and M. H. Thiemens (2001), The delta O-17 and delta O-18 measurements of atmospheric sulfate from a coastal and high alpine region: A mass-independent isotopic anomaly, *Journal of Geophysical Research-Atmospheres*, 106(D15), 17359-17373.

Lee, C. C. W., J. Savarino, H. Cachier, and M. H. Thiemens (2002), Sulfur (S-32, S-33, S-34, S-36) and oxygen (O-16, O-17, O-18) isotopic ratios of primary sulfate produced from combustion processes, *Tellus Series B-Chemical and Physical Meteorology*, 54(3), 193-200.

Lyons, J. R. (2001), Transfer of mass-independent fractionation in ozone to other oxygen-containing radicals in the atmosphere, *Geophysical Research Letters*, 28(17), 3231-3234.

Martens, C. S., J. J. Wesolowski, R. C. Harriss, and R. Kaifer (1973), Chlorine Loss from Puerto-Rican and San-Francisco Bay Area Marine Aerosols, *Transactions-American Geophysical Union*, 54(4), 283-283.

Mauersberger, K., P. Lämmerzahl, and D. Krankowsky (2001), Stratospheric ozone isotope enrichments-revisited, *Geophysical Research Letters*, 28(16), 3155-3158.

McCabe, J. R., J. Savarino, B. Alexander, S. L. Gong, and M. H. Thiemens (2006), Isotopic constraints on non-photochemical sulfate production in the Arctic winter, *Geophysical Research Letters*, 33(5).

Michalski, G., Z. Scott, M. Kabling, and M. H. Thiemens (2003), First measurements and modeling of Delta O-17 in atmospheric nitrate, *Geophysical Research Letters*, 30(16).

Miller, N. L., and N. J. Schlegel (2006), Climate change projected fire weather sensitivity: California Santa Ana wind occurrence, *Geophysical Research Letters*, 33(15).

Morin, S., R. Sander, and J. Savarino (2011), Simulation of the diurnal variations of the oxygen isotope anomaly (Delta O-17) of reactive atmospheric species, *Atmospheric Chemistry and Physics*, 11(8), 3653-3671.

Morin, S., J. Savarino, S. Bekki, S. Gong, and J. W. Bottenheim (2007), Signature of Arctic surface ozone depletion events in the isotope anomaly (Delta O-17) of atmospheric nitrate, *Atmospheric Chemistry and Physics*, 7, 1451-1469.

NOAA (2009), National Climatic Data Center, State of the Climate: Wildfires for annual 2009, published online December 2009, retrieved on May 16, 2012 from <http://www.ncdc.noaa.gov/sotc/fire/2009/13>.

Osaki, S., Y. Tagawa, T. Chijiwa, S. Sugihara, and Y. Maeda (1999), Atmospheric deposition of S-35, *Journal of Radioanalytical and Nuclear Chemistry*, 239(3), 543-547.

Patris, N., S. S. Cliff, P. K. Quinn, M. Kasem, and M. H. Thiemens (2007), Isotopic analysis of aerosol sulfate and nitrate during ITCT-2k2: Determination of different formation pathways as a function of particle size, *Journal of Geophysical Research-Atmospheres*, 112(D23).

Priyadarshi, A., G. Dominguez, J. Savarino, and M. Thiemens (2011), Cosmogenic S-35: A unique tracer to Antarctic atmospheric chemistry and the polar vortex, *Geophysical Research Letters*, 38.

Priyadarshi, A., J. Hill-Falkenthal, E. Coupal, G. Dominguez, and M. H. Thiemens (2012), Measurements of S-35 in the marine boundary layer at La Jolla, California: A new technique for tracing air mass mixing during Santa Ana events, *Journal of Geophysical Research-Atmospheres*, 117.

Raphael, M. N. (2003), The Santa Ana Winds of California, *Earth Interactions*, 7.

Rasch, P. J., M. C. Barth, J. T. Kiehl, S. E. Schwartz, and C. M. Benkovitz (2000), A description of the global sulfur cycle and its controlling processes in the National Center for Atmospheric Research Community Climate Model, Version 3 (vol 105, pg 1367, 2000), *Journal of Geophysical Research-Atmospheres*, 105(D5), 6783-6783.

Robertshaw, J. S., and I. W. M. Smith (1980), Rate Data for  $O + OCS \rightarrow SO + CO$  and  $SO + O_3 \rightarrow SO_2 + O_2$  by a New Time-Resolved Technique, *International Journal of Chemical Kinetics*, 12(10), 729-739.

Savarino, J., and M. H. Thiemens (1999), Mass-independent oxygen isotope (O-16, O-17, O-18)

fractionation found in H-x, O-x reactions, *Journal of Physical Chemistry A*, 103(46), 9221-9229.

Savarino, J., C. C. W. Lee, and M. H. Thiemens (2000), Laboratory oxygen isotopic study of sulfur (IV) oxidation: Origin of the mass-independent oxygen isotopic anomaly in atmospheric sulfates and sulfate mineral deposits on Earth, *Journal of Geophysical Research-Atmospheres*, 105(D23), 29079-29088.

Savarino, J., B. Alexander, V. Darmohusodo, and M. H. Thiemens (2001), Sulfur and oxygen isotope analysis of sulfate at micromole levels using a pyrolysis technique in a continuous flow system, *Analytical Chemistry*, 73(18), 4457-4462.

Seinfeld, J. H., and S. N. Pandis (1998), *Atmospheric chemistry and physics : from air pollution to climate change*, xxvii, 1326 p. pp., Wiley, New York.

Sievering, H., J. Cainey, M. Harvey, J. McGregor, S. Nichol, and P. Quinn (2004), Aerosol non-sea-salt sulfate in the remote marine boundary layer under clear-sky and normal cloudiness conditions: Ocean-derived biogenic alkalinity enhances sea-salt sulfate production by ozone oxidation, *Journal of Geophysical Research-Atmospheres*, 109(D19).

Su, J. G., M. Jerrett, B. Beckerman, M. Wilhelm, J. K. Ghosh, and B. Ritz (2009), Predicting traffic-related air pollution in Los Angeles using a distance decay regression selection strategy, *Environmental Research*, 109(6), 657-670.

Tanaka, N., and K. K. Turekian (1991), Use of Cosmogenic S-35 to Determine the Rates of Removal of Atmospheric  $SO_2$ , *Nature*, 352(6332), 226-228.

Tanaka, N., and K. K. Turekian (1995), Determination of the Dry Deposition Flux of  $SO_2$  Using Cosmogenic S-35 and Be-7 Measurements, *Journal of Geophysical Research-Atmospheres*, 100(D2), 2841-2848.

Thiemens, M. H., and J. E. Heidenreich (1983), The Mass-Independent Fractionation of Oxygen - a Novel Isotope Effect and Its Possible Cosmochemical Implications, *Science*, 219(4588), 1073-1075.

Turekian, K. K., and N. Tanaka (1992), The Use of Atmospheric Cosmogenic S-35 and Be-7 in Determining Depositional Fluxes of  $SO_2$ , *Geophysical Research Letters*, 19(17), 1767-1770.

Vicars, W. C., S. K. Bhattacharya, J. Erbland, and J. Savarino (2012), Measurement of the  $^{17}\text{O}$ -excess ( $\Delta^{17}\text{O}$ ) of tropospheric ozone using a nitrite-coated filter, *Rapid Communications in Mass Spectrometry*, 26(10), 1219-1231.

Virkkula, A., K. Teinila, R. Hillamo, V. M. Kerminen, S. Saarikoski, M. Aurela, J. Viidanoja, J. Paatero, I. K. Koponen, and M. Kulmala (2006), Chemical composition of boundary layer aerosol over the Atlantic Ocean and at an Antarctic site, *Atmospheric Chemistry and Physics*, 6, 3407-3421.

Westerling, A. L., D. R. Cayan, T. J. Brown, B. L. Hall, and L. G. Riddle (2004), Climate, Santa Ana Winds and autumn wildfires in southern California, *Eos Trans. AGU*, 85(31).

Zahn, A., P. Franz, C. Bechtel, J. U. Grooss, and T. Röckmann (2006), Modelling the budget of middle atmospheric water vapour isotopes, *Atmospheric Chemistry and Physics*, 6, 2073-2090.

## Chapter 4

### Seasonal Variations in $^{35}\text{S}$ and $\Delta^{17}\text{O}$ of Sulfate Aerosols on the Antarctic Plateau

#### 4.1 Abstract

The first reported seasonal  $\Delta^{17}\text{O}$  anomaly in sulfate aerosols and measurements of radioactive  $^{35}\text{SO}_4^{2-}$  activities collected from Dome C, Antarctica, are reported.  $\Delta^{17}\text{O}$  values exhibit minima during summer (as low as 0.91‰) when tropospheric oxidation patterns are dominated by OH/H<sub>2</sub>O<sub>2</sub> mechanisms. Significant enrichment during autumn and spring is observed (up to 2.40‰) as ozone oxidation increases in the troposphere relative to summer and both stratospheric sources and long range transport become more significant to the total sulfate budget. An unexpected decrease in  $\Delta^{17}\text{O}$  is seen as winter progresses. This decline is concluded to potentially arise due to a reduction in vertical mixing in the troposphere or linked to variations in the long range transport of sulfur species to Antarctica.  $^{35}\text{SO}_4^{2-}$  activities exhibit maxima during summer (up to 1219 atoms  $^{35}\text{S}/\text{m}^3$ ), that correlate with the peak in stratospheric flux, and minima during winter (as low as 146 atoms  $^{35}\text{S}/\text{m}^3$ ) when the lack of solar radiation substantially reduces photochemical activity. It is shown that  $^{35}\text{S}$  offers the potential to be used as an additional tracer to study stratospheric and tropospheric interactions and is used to estimate stratospheric input. Maxima in stratospheric input are produced during summer/autumn with an upper limit of 5.5 ng/m<sup>3</sup> and minima during winter/spring with an upper limit of 1.1 ng/m<sup>3</sup>. From these results, it is concluded that the variation in  $\Delta^{17}\text{O}$  is more reliant upon shifts in tropospheric oxidation mechanisms and long range transport than on changes in the stratospheric flux.

#### 4.2 Introduction

Interest in the sulfur cycle stems from the ability of sulfate aerosols to affect climate through its scattering effect of solar radiation and aptitude in forming cloud condensation nuclei [Arimoto *et al.*, 2001; Kiehl *et al.*, 2000]. Sulfate is predominantly produced by oxidation of SO<sub>2</sub>, which is directly emitted into the atmosphere via fossil fuel combustion, industrial processes, and volcanoes, or secondarily produced in the atmosphere via oxidation of reduced sulfur species such as dimethyl sulfide (DMS) [Bates *et al.*, 1992;



*Chin et al.*, 2000; *Liss et al.*, 1997; *Mather et al.*, 2003; *Smith et al.*, 2001]. Gas phase oxidation of SO<sub>2</sub> to SO<sub>4</sub><sup>2-</sup> via OH radicals nucleates new particles, increasing the extent of cloud condensation nuclei, whereas aqueous oxidation via O<sub>3</sub> or H<sub>2</sub>O<sub>2</sub> does not lead to new particle formation, but may influence cloud properties by increasing particle growth rates within clouds [*Andronache et al.*, 1997; *Kulmala et al.*, 2000; *Stockwell and Calvert*, 1983; *Weber et al.*, 2001]. Increased understanding of the transformation mechanisms of SO<sub>2</sub> to SO<sub>4</sub><sup>2-</sup> can lead to better understanding of how sulfate formation affects cloud and climate properties, thus lowering the uncertainty of aerosol forcing in future climate modeling.

Radioactive <sup>35</sup>S (half-life of 87 days, β decay to <sup>35</sup>Cl) is naturally produced in the atmosphere by cosmic ray spallation of <sup>40</sup>Argon and quickly oxidizes to <sup>35</sup>SO<sub>2</sub> (≈ 1 sec) [*Lal and Peters*, 1967]. <sup>35</sup>SO<sub>2</sub> may be removed from the atmosphere via wet and dry deposition or oxidized to <sup>35</sup>SO<sub>4</sub><sup>2-</sup> via gas (OH) and aqueous phase (O<sub>3</sub>, H<sub>2</sub>O<sub>2</sub>) oxidation and incorporated into aerosol particles. Thus, the chemical properties of <sup>35</sup>SO<sub>2</sub> and <sup>35</sup>SO<sub>4</sub><sup>2-</sup> are expected to be nearly identical to SO<sub>2</sub> and SO<sub>4</sub><sup>2-</sup>, respectively [*Brothers et al.*, 2010]. The stratosphere constitutes the main reservoir of <sup>35</sup>S [*Lal et al.*, 1960], but due to the long residence time of gases and aerosols in the stratosphere (≈1 year), most <sup>35</sup>S decays to <sup>35</sup>Cl before it reaches the troposphere as <sup>35</sup>SO<sub>2</sub> and <sup>35</sup>SO<sub>4</sub><sup>2-</sup>, except during stratospheric-tropospheric exchange (STE) events [*Priyadarshi et al.*, 2011]. With the difference in production rates and atmospheric lifetimes between tropospheric and stratospheric species, it is expected that <sup>35</sup>S activity varies significantly between the stratosphere and troposphere, thus potentially making <sup>35</sup>S an effective tracer for understanding boundary layer chemistry, air mass transfer, and STE [*Brothers et al.*, 2010; *Cho et al.*, 2011; *Lee and Thiemens*, 2001; *Osaki et al.*, 1999; *Priyadarshi et al.*, 2011; *Priyadarshi et al.*, 2012; *Tanaka and Turekian*, 1991; 1995; *Turekian and Tanaka*, 1992].

Along with radioactive tracers, multiple stable oxygen isotopes have long been used to trace atmospheric processes and constrain source and sink budgets in biogeochemical cycles [*Brenninkmeijer et al.*, 2003; *Thiemens*, 2006; *Thiemens et al.*, 2012]. Most chemical reactions in the atmosphere follow a mass dependent fractionation as δ<sup>17</sup>O and δ<sup>18</sup>O vary in relative proportion to their reduced masses, yielding the relation δ<sup>17</sup>O ≈ 0.52δ<sup>18</sup>O, where  $\delta = \left( \frac{R_{\text{sample}}}{R_{\text{standard}}} - 1 \right) * 1000$  and R = <sup>17</sup>O/<sup>16</sup>O or <sup>18</sup>O/<sup>16</sup>O. Any process

deviating from this relationship is termed as mass independent fractionation or a  $^{17}\text{O}$  anomaly ( $\Delta^{17}\text{O}$ ), where  $\Delta^{17}\text{O} = \delta^{17}\text{O} - 0.52 \delta^{18}\text{O}$  quantifies the extent of mass fractionation deviation. Atmospheric  $\text{SO}_2$  rapidly exchanges isotopes with water, erasing any original isotopic characteristics [Holt *et al.*, 1981]. Thus, any  $^{17}\text{O}$  anomaly observed in sulfate is the direct result of oxidation from  $\text{SO}_2$  to  $\text{SO}_4^{2-}$  and reflects the relative importance of different oxidants allowing for quantitative determination of the aqueous and gas phase  $\text{SO}_2$  oxidation pathways [Alexander *et al.*, 2009; Alexander *et al.*, 2012a; Dominguez *et al.*, 2008; Lee and Thiemens, 2001; McCabe *et al.*, 2006; Patris *et al.*, 2007; Savarino *et al.*, 2003]. The main chemical reactions relevant to the sulfate isotopic composition are listed in Table 1. Studies have shown that ozone ( $\Delta^{17}\text{O} \approx 35\text{‰}$ ) and hydrogen peroxide ( $\Delta^{17}\text{O} \approx 1.7\text{‰}$ ) [Lyons, 2001; Savarino and Thiemens, 1999] both possess a  $^{17}\text{O}$  anomaly and transfer a portion of this anomaly to sulfate during aqueous phase  $\text{SO}_2$  oxidation. Gas phase oxidation via hydroxide radicals has been shown to be a mass dependent process even though several processes may transfer a  $^{17}\text{O}$  excess to OH. [Savarino and Thiemens, 1999; Savarino *et al.*, 2000]. Equilibrium isotopic exchange with water at low latitudes has been shown to be faster than all OH net sinks, consequently erasing any  $^{17}\text{O}$  excess originally present in OH radicals [Michalski *et al.*, 2003]. However, the polar latitudes are the only regions where the troposphere is dry and sufficiently cold enough to limit this exchange process [Morin *et al.*, 2007]. Morin *et al.* (2007) calculated that OH chemical sink reactions could outweigh equilibrium isotopic exchange when taking polar temperatures and water vapor content into consideration. Dry conditions and low temperatures observed in the stratosphere have led to predictions of a significant  $^{17}\text{O}$  excess in OH radicals, upwards of 40‰ mainly due to O-exchange with  $\text{NO}_2$  [Lyons, 2001; Zahn *et al.*, 2006]. Consequently, it is possible that OH radicals possess a  $^{17}\text{O}$  anomaly in the Antarctic troposphere, though laboratory experiments have yet to confirm this hypothesis.

The combination of  $^{35}\text{SO}_4^{2-}$  and  $\Delta^{17}\text{O}$  measurements in sulfate potentially allows the ability to constrain how sulfate oxidation mechanisms are affected by a change in atmospheric conditions and properties since both chemical ( $\Delta^{17}\text{O}$ ) and chronological ( $^{35}\text{S}$ ) information is available. The correlation between enhanced levels of  $^{35}\text{SO}_4^{2-}$  and  $\Delta^{17}\text{O}$  was described by Lee and Thiemens, (2001) at White Mountain Research Station, located at the remote site of Mount Barcroft, California (37.5° N, 118.2° W), and suggested a contribution of high altitude air, possibly of stratospheric source, as the cause for the

simultaneous increase. The correlation was again detected during Santa Ana wind events in Southern California caused by the increase of free tropospheric air mixing into the boundary layer due to a high pressure system building over the Great Basin in the Southern Sierra Nevada Mountains in conjunction with a low pressure offshore system [Hill-Falkenthal *et al.*, 2012]. Here, we present a year-long sampling of sulfate aerosols at Dome C, Antarctica, and show the seasonal variation in  $^{35}\text{SO}_4^{2-}$  and  $\Delta^{17}\text{O}$ . Recently, cosmogenic  $^{35}\text{SO}_4^{2-}$  measurements have been reported for Dome C and Dumont D'Urville showing significant seasonal changes [Priyadarshi *et al.*, 2011]. Ice core studies involving oxygen isotopic measurements in Antarctica show distinct changes in the oxidative formation pathways of sulfate over long time scales [Alexander *et al.*, 2003; Kunasek *et al.*, 2010; Sofen *et al.*, 2011]. However, a study of oxygen isotopic compositions in sulfate aerosols remains to be done at an inland Antarctic site such as Dome C, the site of the oldest ice recovered during the EPICA program, observing the seasonal variation of sulfate.

### 4.3 Methods

Bulk aerosol samples were collected at Dome C, Antarctica (75.06° S, 123.23° E, 3233 m) using a Hi-Volume aerosol sampler at weekly intervals from 1/15/2010-1/21/2011. Samples were sent to UC San Diego once the yearlong campaign was completed and measured for  $^{35}\text{SO}_4^{2-}$  activity using a Wallac Quantalus 1220 Ultra Low Level Liquid Scintillation counter following the procedure of Brothers *et al.* (2010). The liquid scintillation technique used here possesses a small background error of less than 5 atoms/m<sup>3</sup>, limiting background noise as a potential error resulting in measurement errors of only about 2%. Activity measurements were corrected for background activity and the decay of  $^{35}\text{S}$  between the sampling and measurement periods. Radioactive decay occurs during the sampling collection period as well. To account for this, the back correction for decay was applied to the midpoint of each collection period. After these corrections, activity measurements were then converted to concentrations of  $^{35}\text{S}$  atoms/m<sup>3</sup>. As samples from early in the campaign were measured over a year after collection, the back corrections for these possess larger errors relative to those collected at the end of the campaign. This becomes apparent while observing the  $^{35}\text{S}$  activity record in Figure 1, where the largest relative errors are seen in January and February of 2010, while in the latter months, data markers are typically larger than the error.

To measure  $\Delta^{17}\text{O}$ , samples were combined into monthly aliquots to acquire sufficient sulfate concentrations for accurate isotopic analysis using an Isotope Ratio Mass Spectrometer (MAT 253). Sulfate was converted to  $\text{AgSO}_4$ , subsequently pyrolyzed in quartz tubes at a temperature of  $1030^\circ\text{C}$  to obtain  $\text{O}_2$  gas, and oxygen isotopic compositions ( $\delta^{18}\text{O}$  and  $\delta^{17}\text{O}$ ) were measured after purification through a gas chromatograph [Savarino *et al.*, 2001]. Analysis of replicate laboratory standards yielded errors of 0.1‰ and 1.0‰ for  $\Delta^{17}\text{O}$  and  $\delta^{18}\text{O}$ , respectively. The use of quartz tubes to convert  $\text{AgSO}_4$  to  $\text{O}_2$  is known to lower the  $\Delta^{17}\text{O}$  anomaly in samples through a non-mass dependent process, whereas gold tubes have shown no such effect [Schauer *et al.*, 2012]. To rectify this, the correction factor determined in Schauer *et al.* (2012), ( $\Delta^{17}\text{O}_{\text{gold}} = \Delta^{17}\text{O}_{\text{quartz}} * 1.14 + 0.06$ ), is applied to the initial isotopic measurements. Isotopic compositions are also corrected for sea salt content in each sample with typical errors of 5% for cation and anion measurements. Sodium is frequently used as a sea salt marker, however, large sodium blanks associated with the filter papers used in this sampling system eliminated sodium as a viable sea salt tracer. Magnesium, conversely, has an undetectable filter blank. Oxygen isotopic compositions are corrected for sea salt content assuming the molar ratio of  $\text{SO}_4^{2-}:\text{Mg}^{2+}$  in sea water to be 0.5369 and sea salt sulfate to have a  $\Delta^{17}\text{O}$  of 0‰ and a  $\delta^{18}\text{O}$  of 10‰. Previous studies at Dome C have shown no fractionation between  $\text{Mg}^{2+}$  concentrations and sea salt sodium concentrations, suggesting that magnesium originates almost exclusively from sea spray and has a negligible crustal contribution [Udisti *et al.*, 2012], therefore making magnesium the most viable proxy for sea salt sulfate.

#### **4.4 Antarctic Meteorology**

Antarctica's unique meteorological conditions and air circulation patterns significantly affect local boundary layer chemistry. Antarctica has a high plateau in its interior and steeply slopes downward towards its perimeter at sea level [Wendler and Kodama, 1984]. Weather conditions differ considerably in summer compared to winter. Sunlight is present 24 hours a day above the polar circle during summer, yet is absent in winter. Large radiative cooling at the ice surface creates a temperature inversion in the lowest few hundred meters of the atmosphere leading to strong katabatic winds moving from inland to coastal Antarctica [Parish and Bromwich, 2007; Roscoe, 2004; Stohl and Sodemann, 2010]. The inversion is strongest in winter due to the lack of sunlight, and exists intermittently during the summer on a much

weaker scale [Van De Berg *et al.*, 2008]. Dome C does not experience strong katabatic winds typical of inland sites as it is located on a regional topographical maximum where local slopes do not exceed 1%, and as a result, experiences one of the lightest winds in Antarctica [Genthon *et al.*, 2010; Wendler and Kodama, 1984].

The chemical environment is completely different during winter than any other time of the year as photochemical reactions and chemical oxidation shut down. This trend is observed from surface ozone mixing ratios, which peak during the polar winter at both coastal and inland Antarctic sites due to the lack of chemical reactivity [Helmig *et al.*, 2007; Legrand *et al.*, 2009]. Solar radiation time frames are equivalent in autumn and spring suggesting these two seasons are relatively similar in atmospheric and chemical conditions. However, the elevated levels of photochemically reactive species that build up during winter initiate when solar radiation returns during spring increasing photochemical activity. This, in turn with the annual occurrence of stratospheric ozone depletion which allows greater amounts of UV flux to reach the troposphere renders an atmosphere with a stronger oxidative capacity in spring relative to autumn.

The polar vortex and ozone hole are annual occurrences over Antarctica. Some coastal Antarctic sites shift in and out of the vortex depending on the distortion of the vortex, however, the Dome C site remains inside the vortex until it dissipates. The 2010 ozone hole was classified as a late-starter, delayed by two significant stratospheric warming events. These events prevented a large ozone hole from forming thereby making the 2010 ozone hole one of the smallest of the past 15-20 years [Krummel and Fraser, 2011].

## **4.5 Sources of Sulfate in Antarctica**

### **4.5.1 Biogenic Sulfate Source**

Sulfate sources into Antarctica may be ascribed to three main components: marine biogenic, stratospheric input, and continental dust sources due to long range transport and volcanic emissions [Legrand and Saigne, 1991; Patris *et al.*, 2000; Priyadarshi *et al.*, 2011; Prospero *et al.*, 1991; Pruett *et*

*al.*, 2004; *Shaw*, 1988]. DMS, formed due to biogenic input from phytoplankton and zooplankton, are the major source of oxidized sulfur compounds at high southern latitudes distant from direct continental SO<sub>2</sub> source emissions [*Gondwe et al.*, 2004; *Liss et al.*, 1997; *Read et al.*, 2008]. During the summer, DMS is considered the only relevant source of sulfur species at coastal Antarctica and accounts for over 90% of the sulfate budget [*Minikin et al.*, 1998; *Preunkert et al.*, 2007]. Due to the lack of sunlight, biogenic secondary sulfate production drastically dips in winter allowing other non-sea salt sulfate sources to become significant contributors to the overall sulfate budget [*Minikin et al.*, 1998]. DMS is rapidly oxidized in the buffer layer, (1.2 days in summer) with SO<sub>2</sub> being the main oxidation byproduct [*Preunkert et al.*, 2008]. *Preunkert et al.* (2008) showed that the seasonal DMS cycle at Dome C is characterized by a summer minimum, opposite of that observed at coastal sites such as Dumont D'Urville, due to the higher transit time relative to the oxidation lifetime of DMS. The typical transit time of air masses between coastal and inland Antarctic sites is estimated to be 9 days [*Swanson et al.*, 2004], whereas the lifetime of SO<sub>2</sub> does not exceed 4 days during the Antarctic summer with respect to its gas phase oxidation to sulfuric acid [*Mauldin et al.*, 2004]. Therefore, most of the summertime biogenic secondary sulfate source present at Dome C is oxidized during transport to inland Antarctica. Photooxidation of DMS is weak during the winter months as DMS concentrations at Dome C show minimal changes relative to coastal sites [*Preunkert et al.*, 2008].

#### 4.5.2 Stratospheric Sulfate Source

Beryllium-7 (<sup>7</sup>Be) isotopes have recently been used to study the influence of stratospheric flux to the troposphere [*Dibb et al.*, 2003; *Kulan et al.*, 2006; *Zanis et al.*, 1999]. Beryllium isotopes chemically attach to aerosol particles upon formation and are thus sensitive to aerosol lifetimes and concentrations. This is problematic in Antarctica due to stark decreases in aerosol concentrations during winter due to the lack of aerosol formation, consequently, deciphering whether decreased <sup>7</sup>Be activity during winter is a component of reduced STE or reduced chemical aerosol attachment is complicated. The use of the isotopic ratio of <sup>10</sup>Be/<sup>7</sup>Be to determine STE flux into the boundary layer normalizes the variation in aerosol concentration as both isotopes are equally affected by the decrease in aerosol concentrations during winter. <sup>10</sup>Be has a half-life of 1.39 million years, whereas <sup>7</sup>Be has a half-life of 53 days. A change in the ratio of <sup>10</sup>Be/<sup>7</sup>Be isotopes thus arises from a variation in STE flux. Measurements of <sup>10</sup>Be/<sup>7</sup>Be ratios taken in

Antarctica suggest a summer/autumn maximum and a winter/spring minimum in STE flux [Elsässer *et al.*, 2011]. Based on neutron fluxes and evaluated cross sections, the production ratio of  $^{10}\text{Be}/^7\text{Be}$  is calculated to be 0.52 [Masarik and Beer, 1999]. With beryllium isotope ratios ranging on average from 1.4 to 1.9, this implies an influx of stratospheric air year-round to the Antarctic boundary layer. Downward stratospheric intrusions into the troposphere have been estimated to be two times larger during summer than winter [Wagenbach, 1996]. Minikin *et al.* (1998) calculated this downward flux only accounts for  $2.0 \text{ ng/m}^3$  sulfate in summer and  $1.0 \text{ ng/m}^3$  in winter and is in reasonable agreement with recent modeling work that estimate the atmospheric transport from the stratosphere to be maximum in late summer/autumn and about 4-5 times stronger than during late winter/spring on the Antarctic plateau [Stohl and Sodemann, 2010].

These findings are unexpected considering the lack of a thermal tropopause during the polar winter due to the absence of radiative heating over Antarctica [Neff, 1999]. The lack of a barrier between the stratosphere and troposphere during winter suggests that STE could occur more frequently in winter than summer [Roscoe, 2004]. However, recent studies show that the thermal criterion is often insufficient for determining the tropopause during the Antarctic winter and spring [Alexander *et al.*, 2012b; Zangl and Hoinka, 2001]. Other than the thermal definition, the tropopause may be defined chemically by sharp increases in the vertical profile of ozone mixing ratios, or by measurement of the dynamical variation of the tropopause [Alexander *et al.*, 2012b]. The dynamical tropopause is located at the position of a surface of constant potential vorticity. Unlike the thermal definition, the dynamical approach considers the stability of the atmosphere, as well as its circulation and density characteristics [Wilcox *et al.*, 2012]. The tropopause is clearly defined during the polar winter and spring seasons when applying the dynamical [Alexander *et al.*, 2012b] and chemical definitions [Tomikawa *et al.*, 2009] of the tropopause suggesting a barrier separating the stratosphere and troposphere remains.

The elevation of the tropopause has been observed to reach a peak height of about 9 km in summer/autumn and increases to a height of 13-14 km during the winter/spring seasons. This has been suggested as resulting from low stratospheric temperatures due to the seasonal temperature minimum in winter and ozone loss in spring [Evtushevsky *et al.*, 2008]. Other studies have found the same trends in tropopause height above Antarctica with summer/autumn heights around 9 km, and winter/spring heights

near 11 km [Pedro *et al.*, 2011]. The shorter distance stratospheric air masses must travel to reach the boundary layer is thought to enhance the probability of surface stratospheric flux during summer. In addition, the subtropical and polar jets strengthen during winter due to the increased temperature gradient between the poles and the equator suppressing the exchange between the upper stratosphere (above the 380K isentropic surface) and lower stratosphere [Dethof *et al.*, 2000; Dethof *et al.*, 1999; Jordan *et al.*, 2003]. As a result, less overworld air penetrates the troposphere during winter. Stohl *et al.* (2010) and Pedro *et al.* (2011) observed that the seasonal cycle of STE transport closely tracks that of tropopause height with summer/autumn maximums and winter/spring minimums.

Polar stratospheric cloud (PSC) deposition is an annual occurrence during late winter and early spring leading to both denitrification and dehydration of the stratosphere [Fahey *et al.*, 1990]. Tritium isotopes are used to study the deposition of PSCs to the troposphere, as the abundance of tritium in stratospheric water is 4 orders of magnitude higher than that of tropospheric water. Observations have shown the largest increases in tritium from August to October [Wagenbach *et al.*, 1998]. Beryllium isotope ratios cannot be used to detect PSC deposition as no substantial air mass exchange across the tropopause is required to detect PSC remnants at the surface of Antarctica [D. Wagenbach, 1996]. These findings are corroborated with observation of the largest  $\Delta^{17}\text{O}$  anomalies in Antarctic nitrate during winter (July through September) [Frey *et al.*, 2009; Savarino *et al.*, 2007]. As PSCs are formed on stratospheric sulfate aerosols, a portion of stratospheric sulfate is assumed to be lost to the troposphere during such events.

#### 4.5.3 Continental Sulfate Source

Past transport and subsequent deposition of continental dust to Antarctica has been studied through ice core measurements, however, a lack of observational studies of current deposition pathways has led to large uncertainties in the origin of present day dust aerosols. Transport models have been used to estimate the impact of long range transport to Antarctica from other continents and have attributed most continental dust deposition to an origin in South America and Australia [Li *et al.*, 2008; Lunt and Valdes, 2002; Luo *et al.*, 2003]. Li *et al.* (2008) estimates that 50% of the continental dust deposited in Antarctica originates in South America, 35% in Australia, while only 10% derives from the northern hemisphere. Ice



core measurements in ice dating back to the late 1700's to 2000 show that continental sources contributed less than 2% of the total sulfate composition based on non-sea salt calcium tracers [Kunasek *et al.*, 2010]. However, these ice core studies are limited by time resolution making it difficult to differentiate month to month variation sometimes masking seasonal changes. Continental sources could play a vital role in background sulfate levels during the polar winter when biogenic secondary sulfate production substantially declines.

Using  $^{210}\text{Pb}$  measurements as a reference for transport from continental sources show maximum activities during summer and minimums in late autumn and winter [Lambert *et al.*, 1990; Savoie *et al.*, 1992]. With the Antarctic continent almost entirely covered in ice, the outgassing of  $^{222}\text{Rn}$  is minimal meaning the measured  $^{210}\text{Pb}$  is thought to be derived almost exclusively from long range transport [Lambert *et al.*, 1990]. We note that these measurements were obtained at coastal sampling sites and might not truly represent the inland site of Dome C. The lack of sampling campaigns at inland Antarctic sites limits the resolution and seasonal pattern evaluation at Dome C. The only campaign which states  $^{210}\text{Pb}$  measurements at an inland site was at South Pole in Savoie *et al.* (1992) and confirms that summer activity levels are greater than winter. Meridional aerosol transport from southern and mid-latitudes operates most effectively in the upper troposphere where the anticipated lifetime of particles is significantly longer than in the marine boundary layer [D. Wagenbach, 1996]. However, transport in the upper troposphere is significantly reduced with the establishment of the circumpolar vortex [Mroz *et al.*, 1989; Schwerdtfeger, 1984], thus resulting in the summer maximum. Therefore, it is expected that the seasonal trends in continental sulfate at inland sites follow the general trends seen at coastal sites.

The continental sulfate contribution has been estimated at about  $22 \text{ ng/m}^3$  in summer and  $11.5 \text{ ng/m}^3$  in winter at coastal Antarctic sites [Minikin *et al.*, 1998]. Non-sea salt sulfate concentrations at the inland site of Kohnen ( $75^\circ \text{ S}$ ,  $0^\circ \text{ E}$ ; roughly 520 km inland of Neumayer Station) were found to be a factor of almost 2 lower than the non-sea salt sulfate concentrations at Neumayer [Weller and Wagenbach, 2007]. Using this data, it is estimated that long range transport from continental sources are depleted by about a factor of two at inland sites suggesting a reasonable upper limit of continental sulfate at Dome C is about  $11 \text{ ng/m}^3$  in summer and  $6 \text{ ng/m}^3$  in winter. Hence, even though the continental source decreases during

winter, the overall contribution of continental sources to the total sulfate budget is actually greater during winter than summer due to the large decline in biogenic activity.

Large volcanic events have historically been shown to alter climate through the rapid emission of  $\text{SO}_2$  into the atmosphere, particularly the stratosphere, and subsequent conversion to  $\text{SO}_4^{2-}$ . All volcanic sulfuric acid aerosols eventually settle to the Earth's surface, including on the polar ice sheets, and are observed to increase sulfate concentrations in Antarctic ice cores [Delmas *et al.*, 1992; Hammer, 1977; Langway Jr *et al.*, 1988]. The data presented here reveals seasonal sulfate concentrations in agreement with previous campaigns from inland Antarctica and show that sulfate from volcanic sources was not of large influence during this campaign.

## 4.6 Results and Discussion

### 4.6.1 Sulfate Concentrations

Sulfate concentrations ( $\text{ng/m}^3$ ), presented in Table 2 and Figure 1a, show maxima in summer with a peak of  $268.4 \text{ ng/m}^3$  on 5 February 2010, and minima in winter with a low of  $12.5 \text{ ng/m}^3$  collected on 18 June 2010. These findings are consistent with previous aerosol campaigns undertaken at inland Antarctic sites [Arimoto *et al.*, 2001; Becagli *et al.*, 2012; Fattori *et al.*, 2005; Udisti *et al.*, 2012; Weller and Wagenbach, 2007]. The large increases in summer are the result of increased biogenic production in the Southern Ocean and subsequent oxidation to sulfate in the boundary and buffer layers. The OH radical is highly correlated with UV solar flux as the primary source of OH is via  $\text{O}(^1\text{D}) + \text{H}_2\text{O} \rightarrow 2\text{OH}$ , with  $\text{O}(^1\text{D})$  formed via photolysis. The major atmospheric loss process for DMS is oxidation via OH radical [Jefferson *et al.*, 1998], thus, the reduction in UV flux results in a reduction in biogenically produced secondary sulfate and sulfate concentrations plummet to attain minimum background levels during winter.

### 4.6.2 Seasonality of $^{35}\text{S}$ Activity

$^{35}\text{SO}_4^{2-}$  activity is displayed in Figure 1b and follows the same seasonal patterns as sulfate concentrations with a maximum in summer and minimum in winter, agreeing with previous samplings at Dome C [Priyadarshi *et al.*, 2011].  $^{35}\text{SO}_4^{2-}$  activities reach a maximum of  $1219 \text{ atoms } ^{35}\text{S} / \text{m}^3$  on 22

January 2010 and a minimum of 146 atoms  $^{35}\text{S}/\text{m}^3$  on 13 August 2010. Although biogenically produced secondary sulfate is the main cause for increased sulfate concentrations during summer, this source is not directly related to the seasonal cycle of  $^{35}\text{SO}_4^{2-}$ . The largest source of  $^{35}\text{S}$  in the ocean is due to the deposition of  $\text{SO}_2$  and  $\text{SO}_4^{2-}$  from the atmosphere onto ocean surfaces, where, following deposition,  $\text{SO}_2$  is oxidized to  $\text{SO}_4^{2-}$  in the ocean. Assuming steady state, the deposition of  $^{35}\text{S}$  is as follows:

$$[^{35}\text{SO}_4^{2-}] = \frac{\tau}{D} \{ [^{35}\text{SO}_2]_{\text{MBL}} * v_{d1} + [^{35}\text{SO}_4^{2-}]_{\text{MBL}} * v_{d2} \} \quad (4.1)$$

where  $v_{d1}$  ( $1.2 * 10^{-2}$  m/sec) and  $v_{d2}$  ( $0.05 * 10^{-2}$  m/sec) are the deposition velocities of  $\text{SO}_2$  and  $\text{SO}_4^{2-}$  over the ocean [Xu and Carmichael, 1998]. Steady state concentrations for  $^{35}\text{SO}_2$  and  $^{35}\text{SO}_4^{2-}$  in the marine boundary layer (MBL) of Antarctica were determined to be 189 atoms/ $\text{m}^3$  and 728 atoms/ $\text{m}^3$ , respectively [Priyadarshi et al., 2011]. Using the mean lifetime ( $\tau$ ) of 126 days for  $^{35}\text{S}$  and assuming a mixing depth (D) of 200 meters for surface ocean water, the concentration of  $^{35}\text{SO}_4^{2-}$  in Antarctic ocean water is determined to be 143 atoms/liter. As these radioactive sulfur species insert into the oceanic nutrient cycle, they are diluted by the large reservoir of nonradioactive sulfur species already present in the ocean. With concentrations of  $\text{SO}_4^{2-}$  in ocean water of 28.9 mmol/liter, an atomic ratio of about  $8.2 * 10^{-21}$  [ $^{35}\text{S}$ ]/[S] is determined for oceanic sulfate. Since the chemical properties of  $^{35}\text{SO}_4^{2-}$  are similar to bulk sulfate, phytoplankton do not differentiate between  $^{35}\text{SO}_4^{2-}$  and  $\text{SO}_4^{2-}$  during sulfate uptake. It is determined that  $1.39 * 10^{-5}$  atoms/ $\text{m}^3$  is obtained from 270 ng/ $\text{m}^3$  of DMS oxidized sulfate showing that biogenic activity from the ocean reservoir has a negligible effect on radioactive  $^{35}\text{S}$  in Antarctic sulfate.

$^{35}\text{SO}_4^{2-}$  trends closely parallel previous studies involving  $^{10}\text{Be}/^7\text{Be}$  ratios [Elsässer et al., 2011] showing the seasonality of  $^{35}\text{SO}_4^{2-}$  is influenced by the STE cycle, which shows maxima in summer and minima during winter. Large increases in  $^{35}\text{SO}_4^{2-}$  activity at mid-latitudes have previously been correlated to stratospheric intrusions [Priyadarshi et al., 2012].  $^{35}\text{S}$  is also influenced by the oxidative capacity of the atmosphere, which increases the production of  $^{35}\text{SO}_4^{2-}$  during summer as increased photochemistry shortens the lifetimes of reduced sulfur species and increases oxidation of  $\text{SO}_2$  to  $\text{SO}_4^{2-}$ .

Variations in air circulation patterns are the most plausible source of variation on week to week time scales. *Priyadarshi et al. (2011)* showed that enhanced STE was able to explain large increases in  $^{35}\text{SO}_4^{2-}$  during both the summer and winter seasons in Antarctica. *Priyadarshi et al. (2012)* also reported increases in  $^{35}\text{SO}_4^{2-}$  in the boundary layer as a result of an enrichment of free tropospheric mixing with the lower troposphere. Therefore, fluctuations in both stratospheric and tropospheric mixing affect  $^{35}\text{SO}_4^{2-}$  activity in the boundary layer.

The  $^{35}\text{S}$  production rate is independent of UV flux or oxidant levels in the atmosphere and is assumed to be constant on a week to month timescale. As discussed,  $^{35}\text{S}$  atoms rapidly react to form  $^{35}\text{SO}_2$  in less than a second, much faster than the oxidation timescales of  $\text{SO}_2$  to  $\text{SO}_4^{2-}$ , which can range from days to months in Antarctica depending on the time of year. Therefore, the concentrations of  $^{35}\text{SO}_2$  in the atmosphere are directly related to its oxidation to  $^{35}\text{SO}_4^{2-}$ .  $\text{SO}_2$  oxidation to  $\text{SO}_4^{2-}$  during winter is basically non-existent in relation to summer oxidation levels resulting in a buildup of  $^{35}\text{SO}_2$  during winter and a seasonal trend opposite of  $^{35}\text{SO}_4^{2-}$ . Although stratospheric input is greater in the summer, which would produce an increase in  $^{35}\text{SO}_2$  during these events, this  $^{35}\text{SO}_2$  is oxidized to  $^{35}\text{SO}_4^{2-}$  relatively quickly once reaching the troposphere, leading to larger buildups of  $^{35}\text{SO}_4^{2-}$  than  $^{35}\text{SO}_2$  in the boundary layer. Unfortunately, due to the difficulty of collecting  $\text{SO}_2$  in the dry Antarctic conditions, this hypothesis has yet to be verified by experimental measurements.

Specific  $^{35}\text{S}$  activity ( $^{35}\text{SO}_4^{2-}$  abundance normalized to the non-sea salt sulfate concentration) displayed in Figure 1c shows the opposite seasonal trends relative to  $^{35}\text{SO}_4^{2-}$  activity, with maximum values attained during winter months and minimums in summer. Specific  $^{35}\text{S}$  activity normalizes the radioactivity count to the sulfate concentration, thus accounting for non-radioactively produced sulfate like biogenic production, which  $^{35}\text{SO}_4^{2-}$  activity does not account for. Specific  $^{35}\text{S}$  activity ranges from 318 atoms  $^{35}\text{S}$  /nmol non-sea salt sulfate on 14 January 2011 to 3744 atoms  $^{35}\text{S}$  /nmol non-sea salt sulfate on 25 June 2010. This trend is directly related to biogenic productivity, which is the main source of sulfate during summer, consequently, resulting in a dilution effect of specific  $^{35}\text{S}$  activity when sulfate concentrations increase during summer, while  $^{35}\text{SO}_4^{2-}$  activity is unaffected.

### 4.6.3 Seasonal Variation of $\Delta^{17}\text{O}$ in Sulfate

Figure 2 shows the seasonality of oxygen isotopes measured from January 2010 to January 2011 at Dome C, Antarctica. Minima can be seen during summer when OH and  $\text{H}_2\text{O}_2$  oxidation dictate sulfate formation and biogenic sources dominate the sulfate budget. The maximum anomaly occurs during early winter as ozone oxidation increases relative to summer and biogenic production is minimal due to the decrease in UV flux. An unexpected decline in  $\Delta^{17}\text{O}$  is seen as winter progresses. It is unlikely that this decline is the result of a shift in  $\text{SO}_2$  oxidation processes within the Antarctic troposphere due to the lack of solar radiation which dramatically slows any photochemical and oxidative processes. As long range transport and STE become larger factors to the overall sulfate budget during winter, a shift in one of these two processes can potentially result in the dramatic decline that is seen in the  $\Delta^{17}\text{O}$  anomaly.

In general, Antarctica may be divided into three distinct time periods, with the transitions from summer to autumn (January 2010-April) and spring to summer (October-January 2011) broken up by the polar winter (June-August). Figure 3 breaks the Antarctic year into these distinct periods and shows strong correlation between  $\Delta^{17}\text{O}$  and specific  $^{35}\text{S}$  activity. The variation in UV flux as the seasons change is the largest factor in the correlation during the summer/autumn and spring/summer periods, however, as solar radiation is non-existent during winter, the correlation between  $\Delta^{17}\text{O}$  and specific  $^{35}\text{S}$  activity must be the result of another mechanism.

#### 4.6.3.1 Summer/Autumn and Spring/Summer

The variation in UV flux throughout the year in Antarctica cause shifts in the pathways of  $\text{SO}_2$  oxidation. As stated earlier, the OH radical is highly correlated with the UV flux and reaches maximum production during the summer.  $\text{H}_2\text{O}_2$  concentrations in the atmosphere track OH radical levels as the major source of the hydrogen peroxide precursor,  $\text{HO}_2$ , is reaction between OH and CO in remote regions where anthropogenic emissions are low [Finlayson-Pitts and Pitts Jr., 2000]. Ozone concentrations rise in autumn and spring relative to summer due to the reduction in the UV flux as photochemical destruction is the main sink for ozone. This, in turn with the subsequent decrease in OH and  $\text{H}_2\text{O}_2$  concentrations, result in more  $\text{O}_3$  oxidation in autumn and spring relative to summer, thus increasing the overall  $\Delta^{17}\text{O}$  seen in sulfate

aerosols.  $\Delta^{17}\text{O}$  values are slightly larger during spring compared to autumn despite rapid ozone depletion events via reaction with halogens that can occur in the atmospheric boundary layer exclusively during springtime in polar regions. This ozone depletion mechanism is most prominent at coastal regions that have greater exposure to marine BrO enriched air masses [Helmig *et al.*, 2007] than at inland sites like Dome C. Activation of deposited nitrate from snowpack during spring leads to increases in surface ozone production, where surface ozone levels have regularly exceeded wintertime maximums. [Crawford *et al.*, 2001; Helmig *et al.*, 2007; Jones and Wolff, 2003; Legrand *et al.*, 2009]. This mechanism likely prompts an increase in the amount of  $\text{SO}_2$  oxidized via ozone during spring relative to autumn resulting in the enhancement of  $\Delta^{17}\text{O}$ .

From Figure 3, specific  $^{35}\text{S}$  activity is evidently enhanced in autumn relative to spring and is likely linked to the decline in vertical mixing that occurs during winter due to the lack of solar radiation. This in turn results in less vertical mixing during the spring season relative to autumn [Bottenheim and Barrie, 1996] as it takes time to reestablish atmospheric equilibrium after the development of a stagnant troposphere during the polar winter. The correlations between specific  $^{35}\text{S}$  activity and  $\Delta^{17}\text{O}$  are likely the result of variations in UV flux and OH radical concentrations from season to season. As stated earlier, OH is the major sink for DMS oxidation, thus resulting in the decrease in specific  $^{35}\text{S}$  activity during periods of enhanced UV flux due to the increase of biogenic secondary sulfate production. At the same time, a reduction in the  $\Delta^{17}\text{O}$  anomaly of sulfate results from the enhanced oxidation of  $\text{SO}_2$  via OH in concurrence with increased photochemical destruction of ozone.

In addition to the shift in oxidation pathways between seasons, the biogenically derived secondary sulfate component dominates the overall sulfate budget during summer. The substantial reduction in the production of biogenic reduced sulfur species during autumn and spring allow sources such as stratospheric and continental sulfate to have a greater impact on the overall sulfate budget. Stratospheric sulfate is expected to contain larger  $\Delta^{17}\text{O}$  anomalies compared to tropospheric sources due to higher ozone contributions. Also, as discussed in Hill-Falkenthal *et al.* (2012), stratospheric  $\text{SO}_2$  and OH contain larger  $\Delta^{17}\text{O}$  anomalies compared to their tropospheric counterparts. Stratospheric water likely possesses a mass independent oxygen isotope composition due to its formation from photochemical substituents [Franz and

Röckmann, 2005]. This anomaly is then exchanged with SO<sub>2</sub> giving sulfur dioxide a mass independent  $\Delta^{17}\text{O}$  anomaly in the stratosphere unlike, and greater than, tropospheric SO<sub>2</sub>. Even if isotope exchange does not completely eliminate the <sup>17</sup>O excess of OH in the polar troposphere as discussed by *Morin et al.* (2007), temperatures and water vapor content are still lower in the polar stratosphere relative to the troposphere resulting in stratospheric OH radicals containing an enhanced <sup>17</sup>O excess relative to its tropospheric counterpart. Furthermore, increased stratospheric NO<sub>x</sub> concentrations result in transfer of the NO<sub>x</sub> mass independent oxygen isotopic signature to OH [*Zahn et al.*, 2006] during gas phase oxidation of SO<sub>2</sub> in the stratosphere. Thus, the stratospheric component can potentially play an important role as well in the seasonality of  $\Delta^{17}\text{O}$  along with the shift in tropospheric oxidation processes as the UV flux declines.

#### 4.6.3.2 Winter

Unlike the periods of summer/autumn and spring/summer where the UV flux is constantly fluctuating, solar radiation is essentially non-existent during winter. This suggests that the mechanisms of tropospheric SO<sub>2</sub> oxidation vary little during winter. In addition, winter has only a small, constant background biogenic source increasing the importance of sulfate transported from the stratosphere and from other continents via long range transport.  $\Delta^{17}\text{O}$  is expected to be enhanced during winter due to the increase in reliance on ozone oxidation in the troposphere. However, a substantial decline in  $\Delta^{17}\text{O}$  is seen as winter progresses from June to August.

A change in tropospheric oxidation pathways is an unlikely source of the decline in  $\Delta^{17}\text{O}$ . Temperatures drop below -60° C resulting in an atmosphere with an extremely low absolute humidity [*Bottenheim and Barrie*, 1996]. SO<sub>2</sub> oxidation via ozone is an aqueous reaction and is thus, affected by changes in absolute humidity. Nevertheless, this drop in absolute humidity is likely of minor importance due to the timescales of oxidation chemistry during the polar winter. The lifetime of ozone is about 100 days and the lifetime of SO<sub>2</sub> is estimated to be 150 days [*Davis et al.*, 1998; *Helmig et al.*, 2007]. Little chemistry occurs during winter, therefore, changes in  $\Delta^{17}\text{O}$  are likely the result of a change in the contribution from either long range transport or stratospheric flux.

As discussed, long range transport is strongly affected by the circumpolar vortex that forms during the Antarctic winter, which greatly reduces transport in the upper troposphere [Mroz *et al.*, 1989; Priyadarshi *et al.*, 2011; Schwerdtfeger, 1984]. However, large cyclonic storm systems increase in occurrence during winter in the Southern Ocean leading to the transport of sea salt laden air from lower latitudes up into the buffer layer and lower free troposphere, where they are subsequently carried to inland Antarctic sites [Bodhaine, 1996]. Sea salt sulfate concentrations have been observed to increase due to winter cyclonic storms and may account for up to 80% of the total inorganic aerosol load at Dome C [Jourdain *et al.*, 2008]. These systems likely carry a portion of non-sea salt sulfate from the Southern Oceans and nearby continents. Unlike Antarctica, the Southern Oceans and surrounding continents outside the Antarctic Circle experience daily sunlight where non-sea salt sulfate production will occur at a greater rate than near the Antarctic continent. However, it is unlikely that the increased occurrence of non-sea salt sulfate transported by winter storms can completely account for the decrease in  $\Delta^{17}\text{O}$ . Sea salt sulfate and non-sea salt sulfate concentrations do not vary sufficiently from June to August to suggest a substantial month to month difference in the concentration of long range transported sulfate carried up the Antarctic plateau. Thus, the drop seen in  $\Delta^{17}\text{O}$  during this period cannot be accounted for by a linear change in the concentration of non-sea salt due to long range transport. However, a shift in the distribution and origin of the sulfate transported to Antarctica can potentially lead to large variations in  $\Delta^{17}\text{O}$ . Although no studies have been reported, the  $\Delta^{17}\text{O}$  in sulfate originating near South America, Africa, and Australia likely differ as each of these locations are affected by their own unique atmospheric circulation patterns along with varying contributions from anthropogenic pollution and biomass burning. At present, it is difficult to resolve the magnitude of this effect, however, future modeling will be instrumental in placing constraints on these mechanisms.

Another potential factor is the stratospheric sulfate component. Stratospheric fluxes have been estimated to exchange only about  $1.0 \text{ ng/m}^3$  of sulfate with the troposphere during winter [Minikin *et al.*, 1998]. However, PSC deposition during late winter could account for an increase in stratospheric sulfate flux leading to a rise in  $\Delta^{17}\text{O}$ . When temperatures in the stratosphere drop below the PSC formation threshold of 196 K, nitric acid and water condense onto sulfate aerosols. As these particles grow in size, the



relative amount of sulfuric acid diminishes to a point where the composition is primarily  $\text{HNO}_3\text{-H}_2\text{O}$  and subsequently deposits to the troposphere. At temperatures corresponding to PSC formation, the composition of these droplets has been estimated to consist of 47%  $\text{HNO}_3$  and 3%  $\text{H}_2\text{SO}_4$  by weight under equilibrium conditions as determined from the use of thermodynamic equilibrium calculations [Koop and Carslaw, 1996]. Using these percentages, it is possible to estimate the flux of additional sulfate from PSC deposition. Nitrate concentrations at both Dumont D'Urville and Dome C increase by about  $40 \text{ ng/m}^3$  during the months of July through September in relation to winter background levels [Frey *et al.*, 2009; Savarino *et al.*, 2007]. This increase in nitrate corresponds to an additional load of about  $2.5 \text{ ng/m}^3$  of sulfate from stratospheric PSC deposition, in agreement with Minikin *et al.* (1998), who calculated that PSC deposition would contribute an absolute maximum of  $5 \text{ ng/m}^3$  to the total sulfate budget during the winter/spring seasons. These calculations suggest that an increase in the total stratospheric flux at the end of winter likely increases the  $\Delta^{17}\text{O}$  anomaly in sulfate as is seen in the nitrate cycle. However, this is in disagreement with the present  $\Delta^{17}\text{O}$  observations. The 2010 ozone hole was one of the smallest in recent record characterized by small amounts of ozone depletion (40-60% less than the 2005-2009 averages) [De Laat and van Weele, 2011]. Stratospheric warming events resulted in a reduced surface area of PSCs compared to long term averages [Krummel and Fraser, 2011], indicating that PSC deposition was also significantly reduced.  $\Delta^{17}\text{O}$  measurements suggest little influence is attributed to PSC deposition during late winter as no enhancement in the  $\Delta^{17}\text{O}$  anomaly is seen. Presently, it is difficult to determine if this lack of enhancement during winter is an abnormality due to reduced ozone destruction in the stratosphere, or whether this is a standard occurrence.

Specific  $^{35}\text{S}$  activity can be used as an additional tool to probe the winter decline in  $\Delta^{17}\text{O}$ . As stated earlier, the mechanism responsible for the decline in specific  $^{35}\text{S}$  activity during winter is not the result of shifts in UV flux like that seen during the summer/autumn and spring/summer periods. Collective increases in both specific  $^{35}\text{S}$  activity and  $\Delta^{17}\text{O}$  have recently been shown to be associated with episodes of increased free tropospheric air circulation with the boundary layer [Hill-Falkenthal *et al.*, 2012]. The same trend is seen in Figure 3 suggesting that the variations in specific  $^{35}\text{S}$  activity and  $\Delta^{17}\text{O}$  during winter are a function of changes in vertical mixing and air mass fluctuations. Since solar radiation and subsequent

emission of thermal radiation from the Earth's surface is required to maintain a well-mixed troposphere, the lack of solar flux produces a more stratified troposphere as winter progresses. This results in less mixing of upper altitude air masses, including that of the upper and mid-troposphere within the boundary layer. This stratification of the troposphere linked with variations in the amplitude and origin of long range transport species is a potential source for the decline in  $\Delta^{17}\text{O}$  seen during winter as no enhancement from PSC deposition is seen.

#### 4.6.4 Constraints on Stratospheric Flux

$^{35}\text{S}$  has previously been used as a diagnostic tool to constrain stratospheric flux [Priyadarshi *et al.*, 2011; 2012].  $^{35}\text{S}$  concentrations for the Antarctic troposphere and stratosphere have been determined by Priyadarshi *et al.* (2011). The model parameters are described in detail in Priyadarshi *et al.* (2011), however, in short, cosmogenic production rates for the  $^{35}\text{S}$  radionuclide were calculated for the stratosphere and troposphere based on latitude and altitude dependency as done in Lal and Peters (1967). Timescales for oxidation and removal rates of both  $^{35}\text{SO}_2$  and  $^{35}\text{SO}_4^{2-}$  were varied in accordance to atmospheric conditions in Antarctica to determine seasonal  $^{35}\text{SO}_2$  and  $^{35}\text{SO}_4^{2-}$  concentrations. Here, we use these modeled values in conjuncture with  $^{35}\text{S}$  activity measurements obtained in this study to estimate upper limits for stratospheric flux.

An upper limit of  $5.5 \text{ ng/m}^3$  for the summer/autumn seasons is determined with the largest limits occurring in February and March,  $5.5 \text{ ng/m}^3$  and  $4.2 \text{ ng/m}^3$ , respectively. Stratospheric deposition during winter/spring is deemed to be far less, with an upper limit of  $1.1 \text{ ng/m}^3$ . Upper limits for August and September were estimated to be  $0.5 \text{ ng/m}^3$  and  $1.1 \text{ ng/m}^3$ , respectively. As suggested earlier, the overall magnitude of STE peaks late summer/early autumn, consistent with models [Stohl *et al.*, 2010] and previous studies using  $^{10}\text{Be}/^7\text{Be}$  ratios [Elsässer *et al.*, 2011]. The upper limits determined here are also in favorable agreement with previous values concluded by Miniken *et al.* (1998), with a slightly larger estimation of STE during summer/autumn. A rise in the stratospheric sulfate component during late winter/early spring linked to PSC deposition is not seen in the  $^{35}\text{S}$  data, complimenting the lack of an increase in winter  $\Delta^{17}\text{O}$  measurements. As stated earlier, it may not be quantitatively concluded at present

whether this is a common feature in the Antarctic sulfate record, however, it is reasonable to state that a large increase in  $\Delta^{17}\text{O}$  due to PSC deposition like that seen in the nitrate cycle is highly unlikely.

Comparing these upper limits to sulfate concentrations in Table 1, it can be seen that stratospheric sulfate constitutes no more than 4% of the total sulfate budget during any one month. Therefore, it is deemed that shifts in tropospheric oxidative pathways and long range transport are likely the major sources responsible for the variation in  $\Delta^{17}\text{O}$  seen at Dome C, Antarctica, with minimal influence from stratospheric sulfate sources. In the future, high resolution oxygen isotope measurements on a weekly timescale can provide more insight into the fluctuations in oxidative chemistry and stratospheric flux in Antarctica sulfate as measurements on a monthly scale likely mask some short term variation.

#### 4.7 Conclusions

Aerosol sampling from January 2010 to January 2011 at Dome C, Antarctica is used to study both the seasonal variation in aerosol cosmogenic  $^{35}\text{SO}_4^{2-}$  activity and  $\Delta^{17}\text{O}$  of sulfate aerosols. The resemblance between the seasonality of  $^{35}\text{S}$  in this data set and  $^{10}\text{Be}/^7\text{Be}$  isotopic ratios from previous works introduces the ability to use  $^{35}\text{S}$  as an additional tracer for stratospheric intrusions and air mass circulation in the troposphere. The  $^{35}\text{SO}_4^{2-}$  cycle is consistent with the seasonality of STE, resulting in a summer maxima. The winter minima in  $^{35}\text{SO}_4^{2-}$  are a direct result of a decrease in STE and less oxidation of  $\text{SO}_2$  to  $\text{SO}_4^{2-}$  when no solar radiation is present to facilitate photochemical reactions. The associated  $\Delta^{17}\text{O}$  anomalies show minima during summer reflecting a strong dependence on the OH and  $\text{H}_2\text{O}_2$  oxidation mechanisms. In addition, biogenic secondary sulfate is the dominant component of the total sulfate budget during summer, constituting over 90%, and dilutes the stratospheric and long range transport sulfate components. In autumn and spring,  $\Delta^{17}\text{O}$  anomalies rise suggesting that tropospheric sulfate production shifts to an increase in ozone oxidation relative to summer as OH and  $\text{H}_2\text{O}_2$  concentrations decrease due to the dip in solar radiation. Biogenic activity also decreases during autumn and spring resulting in an increase in the relative importance of both stratospheric and long range transport components to the overall  $\Delta^{17}\text{O}$  anomalies in sulfate. This suggests that winter should contain the largest  $\Delta^{17}\text{O}$  anomalies due to the lack of biogenic secondary sulfate production and rise in the ozone oxidation mechanism, however, a distinct downward trend is observed as winter progresses. A consistent decrease in both specific  $^{35}\text{S}$  activity and

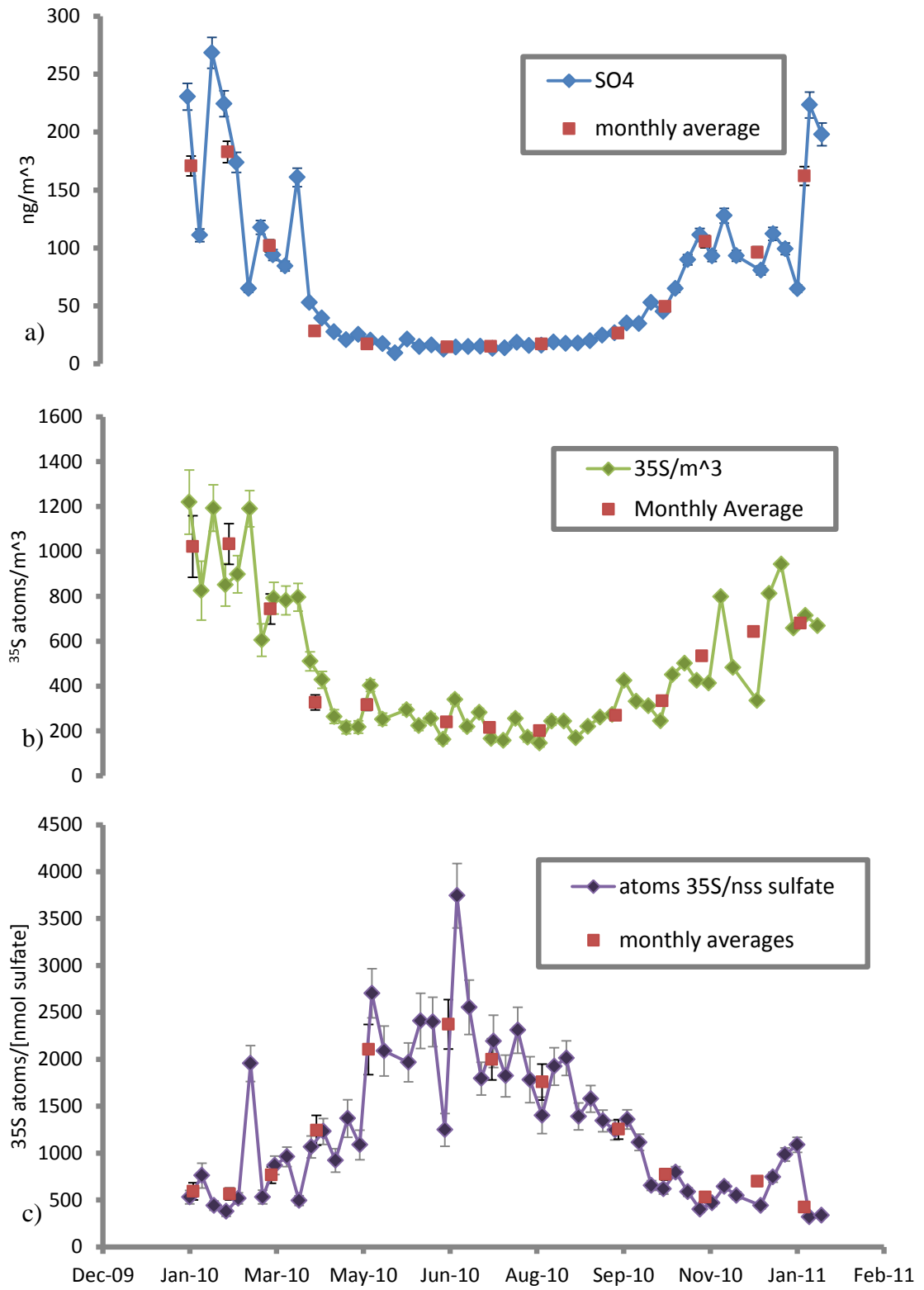
$\Delta^{17}\text{O}$  during winter suggests that a reduction in vertical mixing in the troposphere as a result of the lack of solar radiation plays a role in affecting the oxidative pathways of sulfate. This, in accordance with variation in long range transported sulfate from the Southern Ocean and nearby continents potentially lead to the winter drop in  $\Delta^{17}\text{O}$ . Nevertheless, the cause for the winter decrease in  $\Delta^{17}\text{O}$  is still unresolved, partially because an expanded future data set is needed. To determine the contribution of stratospheric flux to the tropospheric sulfate budget,  $^{35}\text{S}$  measurements were used in conjunction with previous modeling studies to estimate upper limits. An upper limit of  $5.5 \text{ ng/m}^3$  in the summer/autumn months peaking in February and an upper limit of  $1.1 \text{ ng/m}^3$  in the winter/spring seasons peaking in September for the stratospheric flux were determined. No large increase in stratospheric deposition in sulfate was seen during late winter/early spring caused by PSC deposition like that typically seen in the nitrate cycle. It is determined that the variation in  $\Delta^{17}\text{O}$  in sulfate is the result of shifts in tropospheric oxidation processes with minimal perturbation from stratospheric transport. As this is the first attempt to study the seasonal variation of sulfate aerosols using stable oxygen isotopes and radioactive  $^{35}\text{S}$  in Antarctica, continued monitoring can lead to better constraints on sulfate oxidation mechanisms and determine if in fact winter  $\Delta^{17}\text{O}$  anomalies in sulfate consistently decrease each year.

#### **4.8 Acknowledgements**

Chapter 4, in full, is a reprint of material from Journal of Geophysical Research-Atmospheres, Hill-Falkenthal, J., A. Priyadarshi, J. Savarino, and M. Thiemens, Seasonal variations in  $^{35}\text{S}$  and  $\Delta^{17}\text{O}$  of sulfate aerosols on the Antarctic plateau, volume 118, 2013. The dissertation author was the primary author of this paper.

Figure 4.1

- a) Seasonal sulfate concentrations showing maxima in summer and minima in winter. Biogenic productivity increases sulfate concentrations in the summer due to increased DMS oxidation to  $\text{SO}_4^{2-}$ , whereas this process is heavily depleted during winter due to the lack of solar radiation. The red dots represent monthly averages as seen in Table 4.2.
- b) Seasonal variation in  $^{35}\text{SO}_4^{2-}$  activity measurements vary in turn with STE cycles and the oxidative capacity of the atmosphere and show maxima in the summer and minima in the winter. The red dots represent monthly averages as seen in Table 4.2.
- c) Seasonal variation in specific  $^{35}\text{S}$  activity show opposite trends as compared to  $^{35}\text{S}$  activity and sulfate concentrations with maxima in the winter and minima in the summer. Biogenically produced secondary sulfate contains negligible amounts of  $^{35}\text{S}$  activity, which dilutes the specific  $^{35}\text{S}$  activity during periods of increased solar radiation. Red dots represent monthly averages as seen in Table 4.2.



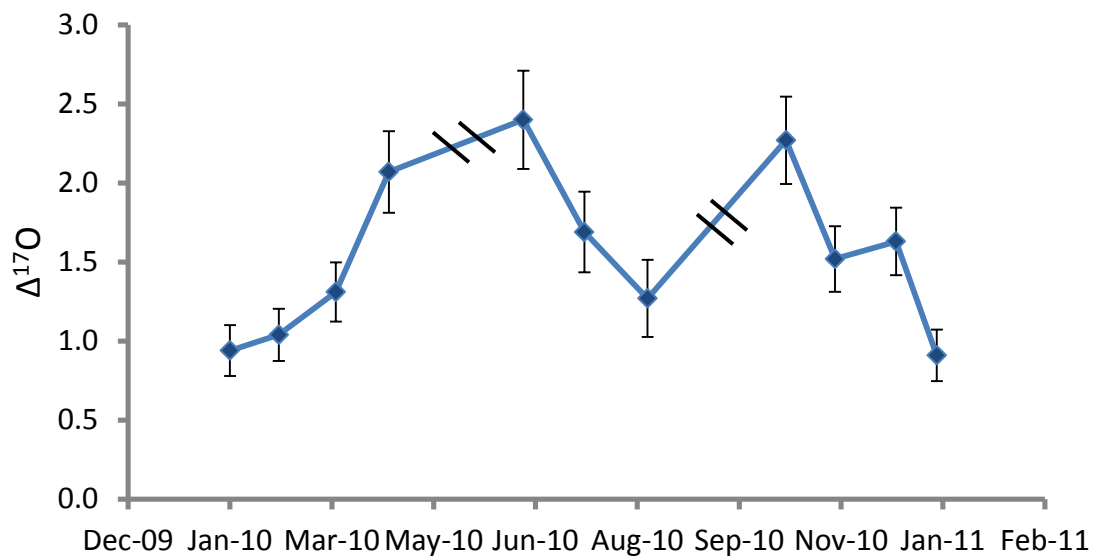


Figure 4.2

$\Delta^{17}\text{O}$  anomalies in sulfate from Dome C are plotted showing the variation between seasons. Samples were combined into monthly allotments to obtain enough sulfate to run isotopic measurements. Double dashes represent months of missing data.  $\Delta^{17}\text{O}$  anomalies exhibit a summer minima with steady increases in autumn and spring as the UV flux drops and ozone oxidation becomes more prominent. A stark decrease in  $\Delta^{17}\text{O}$  is seen during the polar winter linked to a reduction in tropospheric mixing as winter progresses and variations in the amplitude and origin of long range transported sulfate.

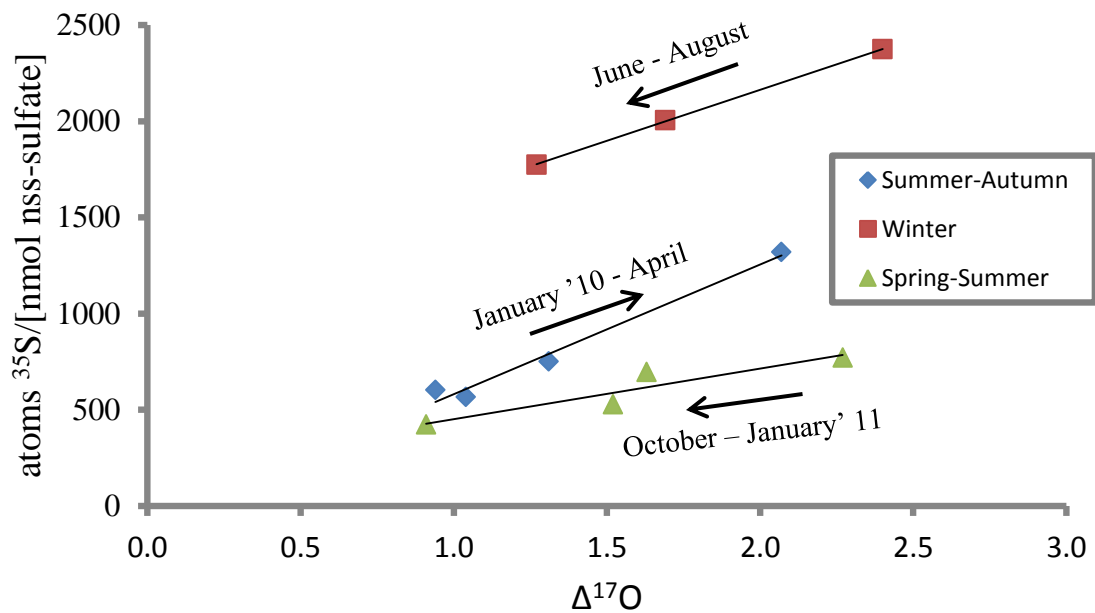


Figure 4.3

Antarctica may be divided into three distinct periods, with the transitions from summer to autumn (January 2010-April) and spring to summer (October-January 2011) broken up by the polar winter (June-August). Correlation between specific  $^{35}\text{S}$  activity and  $\Delta^{17}\text{O}$  is seen when breaking the Antarctic sampling campaign into these three distinct periods with  $R^2$  values for each period of 0.9, 0.9, and 0.8 for the summer/autumn, winter, and spring/summer time periods, respectively. NSS-sulfate represents non-sea salt sulfate.



Table 4.1

$\Delta^{17}\text{O}$  values for the relevant tropospheric sulfate oxidation pathways are listed.  $\Delta^{17}\text{O}$  Sulfate refers to the anomaly transferred to sulfate from the oxidant of choice. Isotopic analysis has shown that two oxygen atoms from  $\text{H}_2\text{O}_2$  are transferred to the product sulfate during oxidation via hydrogen peroxide, whereas only one oxygen atom is transferred from  $\text{O}_3$  during oxidation via ozone [Savarino *et al.*, 2000]. Note that these oxidants have been predicted to contain larger  $\Delta^{17}\text{O}$  anomalies in the stratosphere, thus, resulting in larger  $\Delta^{17}\text{O}$  anomalies in stratospheric sulfate than tropospheric sulfate.

<b>Troposphere</b>			
<b>Oxidation Pathway</b>	<b>Phase</b>	<b><math>\Delta^{17}\text{O}</math> oxidant (‰)</b>	<b><math>\Delta^{17}\text{O}</math> Sulfate (‰)</b>
<b><math>\text{SO}_2 + \text{OH}</math></b>	<b>Gas</b>	<b>0</b>	<b>0</b>
<b><math>\text{S(IV)} + \text{H}_2\text{O}_2</math></b>	<b>Aqueous</b>	<b>1.7</b>	<b>0.9</b>
<b><math>\text{S(IV)} + \text{O}_3</math></b>	<b>Aqueous</b>	<b>35</b>	<b>8.8</b>

Table 4.2

Summary of monthly averages for sulfate concentration,  $^{35}\text{SO}_4^{2-}$  activity measurements, and oxygen isotopic compositions. Oxygen isotopic samples for the months of May and September were lost due to equipment malfunction. NSS- $\text{SO}_4^{2-}$  represents the non-sea salt sulfate component.

Month	$\text{SO}_4^{2-}$ ( $\text{ng}/\text{m}^3$ )	nss- $\text{SO}_4^{2-}$ ( $\text{ng}/\text{m}^3$ )	$^{35}\text{SO}_4^{2-}$ activity (atoms $^{35}\text{S}/\text{m}^3$ )	Specific Activity (atoms $^{35}\text{S}/\text{nmol}$ nss- $\text{SO}_4$ )	$\delta^{18}\text{O}$ (‰)	$\Delta^{17}\text{O}$ (‰)
Jan 2010	170.8±8.5	162.7±11.5	1022±137	603±92	-2.50±1.03	0.94±0.16
Feb 2010	182.9±9.2	175.7±12.4	1033±91	564±64	-3.81±1.08	1.04±0.17
Mar 2010	102.0±5.1	95.1±6.7	744±67	751±86	-3.95±1.08	1.31±0.19
Apr 2010	28.2±1.4	23.8±1.7	327±33	1319±163	-5.63±1.16	2.07±0.26
May 2010	19.6±2.0	13.4±1.0	316±25	2264±243	-	-
Jun 2010	14.6±0.7	9.7±0.7	240±21	2375±264	2.19±1.03	2.40±0.31
Jul 2010	15.1±0.8	10.3±0.7	215±18	2004±221	6.38±1.20	1.69±0.25
Aug 2010	17.2±0.9	10.9±0.8	201±18	1770±199	6.74±1.23	1.27±0.24
Sep 2010	26.5±1.3	20.8±1.5	269±12	1242±105	-	-
Oct 2010	49.5±2.5	41.7±3.0	335±12	771±61	-5.17±1.14	2.27±0.28
Nov 2010	105.5±5.3	97.1±6.9	534±14	528±40	4.82±1.12	1.52±0.21
Dec 2010	96.3±4.8	88.7±6.3	643±13	696±51	-5.08±1.13	1.63±0.21
Jan 2011	162.1±8.1	154.9±11.0	680±11	421±31	2.50±1.03	0.91±0.16

#### 4.9 References

Alexander, B., R. J. Park, D. J. Jacob, and S. Gong (2009), Transition metal-catalyzed oxidation of atmospheric sulfur: Global implications for the sulfur budget, *J. Geophys. Res.*, 114, D02309, doi: 10.1029/2008JD010486.

Alexander, B., M. H. Thiemens, J. Farquhar, A. J. Kaufman, J. Savarino, and R. J. Delmas (2003), East Antarctic ice core sulfur isotope measurements over a complete glacial-interglacial cycle, *J. Geophys. Res.-Atmos.*, 108(D24), 4786, doi: 10.1029/2003JD003513.

Alexander, B., D. J. Allman, H. M. Amos, T. D. Fairlie, J. Dachs, D. A. Hegg, and R. S. Sletten (2012a), Isotopic constraints on the formation pathways of sulfate aerosol in the marine boundary layer of the subtropical northeast Atlantic Ocean, *J. Geophys. Res.-Atmos.*, 117, D06304, doi: 10.1029/2011JD016773.

Alexander, S. P., D. J. Murphy, and A. R. Klekociuk (2012b), High resolution VHF radar measurements of tropopause structure and variability at Davis, Antarctica (69 S, 78 E), *Atmos. Chem. Phys. Discuss*, 12, 26173-26205, doi:10.5194/acpd-12-26173-2012.

Andronache, C., W. Chameides, D. Davis, B. Anderson, R. Pueschel, A. Bandy, D. Thornton, R. Talbot, P. Kasibhatla, and C. Kiang (1997), Gas-to-particle conversion of tropospheric sulfur as estimated from observations in the western North Pacific during PEM-West B, *J Geophys Res*, 102(D23), 28511-28538, doi:10.1029/97JD01969.

Arimoto, R., A. S. Nottingham, J. Webb, C. A. Schloesslin, and D. D. Davis (2001), Non-sea salt sulfate and other aerosol constituents at the South Pole during ISCAT, *Geophys Res Lett*, 28(19), 3645-3648, doi: 10.1029/2000GL012714.

Bates, T., B. Lamb, A. Guenther, J. Dignon, and R. Stoiber (1992), Sulfur emissions to the atmosphere from natural sources, *J Atmos Chem*, 14(1), 315-337, doi: 10.1007/BF00115242.

Becagli, S., et al. (2012), Study of present-day sources and transport processes affecting oxidised sulphur compounds in atmospheric aerosols at Dome C (Antarctica) from year-round sampling campaigns, *Atmos. Environ.*, 52, 98-108, doi: 10.1016/j.atmosenv.2011.07.053.

Bodhaine, B. (1996), *Central Antarctica: Atmospheric Chemical Composition and Atmospheric Transport, in Chemical Exchange Between the Atmosphere and Polar Snow*, eds. E.W. Wolff and R.C. Bales, NATO ASI Series I, 43, 145-172, Springer-Verlag, Berlin.

Bottenheim, J. W., and L. A. Barrie (1996), *Chemical reactions in the polar troposphere relevant to C, S, and N compounds*, in "Chemical Exchange Between the Atmosphere and Polar Snow", eds. E.W. Wolff and R.C. Bales, NATO ASI Series I, 43, 201-224, Springer-Verlag, Berlin.

Brenninkmeijer, C. A. M., C. Janssen, J. Kaiser, T. Rockmann, T. S. Rhee, and S. S. Assonov (2003), Isotope effects in the chemistry of atmospheric trace compounds, *Chemical Reviews*, *103*(12), 5125-5161, doi: 10.1021/cr020644k(12), 5125-5161.

Brothers, L. A., G. Dominguez, A. Abramian, A. Corbin, B. Bluen, and M. H. Thiemens (2010), Optimized low-level liquid scintillation spectroscopy of  $^{35}\text{S}$  for atmospheric and biogeochemical chemistry applications, *P. Natl. Acad. Sci. USA*, *107*(12), 5311-5316, doi: 10.1073/pnas.0901168107

Chin, M., R. B. Rood, S.-J. Lin, J.-F. Müller, and A. M. Thompson (2000), Atmospheric sulfur cycle simulated in the global model GOCART: Model description and global properties, *J. Geophys. Res.*, *105*(D20), 24671-24687, doi: 10.1029/2000JD900384.

Cho, H. M., Y. L. Hong, and G. Kim (2011), Atmospheric depositional fluxes of cosmogenic  $^{35}\text{S}$  and  $^7\text{Be}$ : Implications for the turnover rate of sulfur through the biosphere, *Atmos. Environ.*, *45*(25), 4230-4234, doi:10.1016/j.atmosenv.2011.05.002.

Crawford, J. H., et al. (2001), Evidence for photochemical production of ozone at the South Pole surface, *Geophys. Res. Lett.*, *28*(19), 3641-3644, doi: 10.1029/2001GL013055.

Davis, D., G. Chen, P. Kasibhatla, A. Jefferson, D. Tanner, F. Eisele, D. Lenschow, W. Neff, and H. Berresheim (1998), DMS oxidation in the Antarctic marine boundary layer: Comparison of model simulations and field observations of DMS, DMSO, DMSO<sub>2</sub>, H<sub>2</sub>SO<sub>4</sub>(g), MSA(g), and MSA(p), *J. Geophys. Res.*, *103*(D1), 1657-1678, doi: 10.1029/97JD03452.

De Laat, A. T. J., and M. van Weele (2011), The 2010 Antarctic ozone hole: Observed reduction in ozone destruction by minor sudden stratospheric warmings, *Sci. Rep.*, *1*, 38; doi: 10.1038/srep00038.

Delmas, R. J., S. Kirchner, J. M. Palais, and J. R. PETIT (1992), 1000 years of explosive volcanism recorded at the South Pole, *Tellus B*, *44*(4), 335-350, doi: 10.1034/j.1600-0889.1992.00011.x.

Dethof, A., A. O'Neill, and J. Slingo (2000), Quantification of the isentropic mass transport across the dynamical tropopause, *J. Geophys. Res.*, *105*(D10), 12279-12293, doi: 10.1029/2000JD900127.

Dethof, A., A. O'Neill, J. M. Slingo, and H. G. J. Smit (1999), A mechanism for moistening the lower stratosphere involving the Asian summer monsoon, *Quarterly Journal of the Royal Meteorological Society*, *125*(556), 1079-1106, doi: 10.1002/qj.1999.49712555602.

Dibb, J. E., R. W. Talbot, E. Scheuer, G. Seid, L. DeBell, B. Lefer, and B. Ridley (2003), Stratospheric influence on the northern North American free troposphere during TOPSE:  $^7\text{Be}$  as a stratospheric tracer, *J. Geophys. Res.*, *108*(D4), 8363, doi: 10.1029/2001JD001347.

- Dominguez, G., T. Jackson, L. Brothers, B. Barnett, B. Nguyen, and M. H. Thiemens (2008), Discovery and measurement of an isotopically distinct source of sulfate in Earth's atmosphere, *P. Natl. Acad. Sci. USA*, 105(35), 12769-12773, doi: 10.1073/pnas.0805255105.
- Elsässer, C., D. Wagenbach, R. Weller, M. Auer, A. Wallner, and M. Christl (2011), Continuous 25-yr aerosol records at coastal Antarctica Part 2: variability of the radionuclides  $^7\text{Be}$ ,  $^{10}\text{Be}$  and  $^{210}\text{Pb}$ , *Tellus B*, 63(5), 920-934, doi: 10.1111/j.1600-0889.2011.00543.x.
- Evtushevsky, O. M., A. V. Grytsai, A. R. Klekociuk, and G. P. Milinevsky (2008), Total ozone and tropopause zonal asymmetry during the Antarctic spring, *J Geophys Res*, 113(D7), D00B06, doi: 10.1029/2008/JD009881.
- Fahey, D. W., K. K. Kelly, S. R. Kawa, A. F. Tuck, M. Loewenstein, K. R. Chan, and L. E. Heidt (1990), Observations of denitrification and dehydration in the winter polar stratospheres, *Nature*, 344(6264), 321-324, doi: 10.1038/344321a0.
- Fattori, I., S. Becagli, S. Bellandi, E. Castellano, M. Innocenti, A. Mannini, M. Severi, V. Vitale, and R. Udisti (2005), Chemical composition and physical features of summer aerosol at Terra Nova Bay and Dome C, Antarctica, *J Environ Monitor*, 7(12), 1265-1274, doi: 10.1039/b507327h.
- Finlayson-Pitts, B. J., & Pitts Jr, J. N (2000), *Chemistry of the upper and lower atmosphere: Theory, experiments, and applications*, 969pp., Academic Press, San Diego, Calif.
- Franz, P., and T. Röckmann (2005), High-precision isotope measurements of  $\text{H}_2^{16}\text{O}$ ,  $\text{H}_2^{17}\text{O}$ ,  $\text{H}_2^{18}\text{O}$ , and the  $\Delta^{17}\text{O}$ -anomaly of water vapor in the southern lowermost stratosphere, *Atmos. Chem. Phys.*, 5, 2949-2959, doi: 10.5194/acp-5-2949-2005.
- Frey, M. M., J. Savarino, S. Morin, J. Erbland, and J. M. F. Martins (2009), Photolysis imprint in the nitrate stable isotope signal in snow and atmosphere of East Antarctica and implications for reactive nitrogen cycling, *Atmos Chem Phys*, 9(22), 8681-8696, doi:10.5194/acp-9-8681-2009.
- Genthon, C., M. S. Town, D. Six, V. Favier, S. Argentini, and A. Pellegrini (2010), Meteorological atmospheric boundary layer measurements and ECMWF analyses during summer at Dome C, Antarctica, *J. Geophys. Res. Atmos.*, 115(D5), D05104, doi: 10.1029/2009JD012741.
- Gondwe, M., M. Krol, W. Klaassen, W. Gieskes, and H. de Baar (2004), Comparison of modeled versus measured MSA:nss  $\text{SO}_4^{2-}$  ratios: A global analysis, *Global Biogeochem. Cycles*, 18, GB2006, doi: 10.1029/2003GB002144.
- Hammer, C. U. (1977), Past volcanism revealed by Greenland ice sheet impurities, *Nature*, 270, 482-486, doi: 10.1038/270482a0.

- Helmig, D., S. J. Oltmans, D. Carlson, J.-F. Lamarque, A. Jones, C. Labuschagne, K. Anlauf, and K. Hayden (2007), A review of surface ozone in the polar regions, *Atmos Environ*, *41*(24), 5138-5161, doi: 10.1019/j.atmosenv.2006.09.053.
- Hill-Falkenthal, J., A. Priyadarshi, and M. Thiemens (2012), Differentiating sulfate aerosol oxidation pathways for varying source altitudes using  $^{35}\text{S}$  and  $\Delta^{17}\text{O}$  tracers, *J. Geophys. Res.*, *117*, D18302, doi: 10.1029/2012JD018242.
- Holt, B. D., R. Kumar, and P. T. Cunningham (1981), Oxygen-18 Study of the aqueous-phase oxidation of sulfur dioxide, *Atmos. Environ.*, *15*(4), 557-566, doi: 10.1016/0004-6981(81)90186-4.
- Jefferson, A., D. J. Tanner, F. L. Eisele, D. D. Davis, G. Chen, J. Crawford, J. W. Huey, A. L. Torres, and H. Berresheim (1998), OH photochemistry and methane sulfonic acid formation in the coastal Antarctic boundary layer, *J Geophys Res-Atmos*, *103*(D1), 1647-1656, doi: 10.1029/97JD02376.
- Jones, A.E., Wolff, E.W. (2003), An analysis of the oxidation potential of the South Pole boundary layer and the influence of stratospheric ozone depletion, *J. Geophys. Res.*, *108*(D18), 4565, doi:10.1029/2003JD003379.
- Jordan, C. E., J. E. Dibb, and R. C. Finkel (2003),  $^{10}\text{Be}/^7\text{Be}$  tracer of atmospheric transport and stratosphere-troposphere exchange, *J. Geophys. Res.*, *108*(D8), 4234, doi: 10.1029/2002JD002395.
- Jourdain, B., S. Preunkert, O. Cerri, H. Castebrunet, R. Udisti, and M. Legrand (2008), Year-round record of size-segregated aerosol composition in central Antarctica (Concordia station): Implications for the degree of fractionation of sea-salt particles, *J. Geophys. Res.*, *113*(D14), D14308, doi: 10.0129/2007JD009584.
- Kiehl, J. T., T. L. Schneider, P. J. Rasch, M. C. Barth, and J. Wong (2000), Radiative forcing due to sulfate aerosols from simulations with the National Center for Atmospheric Research Community Climate Model, Version 3, *J Geophys Res-Atmos*, *105*(D1), 1441-1457, doi: 10.1029/1999JD900495.
- Koop, T., and K. S. Carslaw (1996), Melting of  $\text{H}_2\text{SO}_4 \cdot 4\text{H}_2\text{O}$  particles upon cooling: Implications for polar stratospheric clouds, *Science*, *272*(5268), 1638-1641, doi: 10.1126/science.272.5268.1638.
- Krummel, P., and P. Fraser (2011), The 2010 Antarctic Ozone Hole Summary: Tuesday 11 January 2011, *Centre for Australian Weather and Climate Research*; <http://www.environment.gov.au/atmosphere/ozone/publications/pubs/ozone-reports11jan11.pdf>.
- Kulan, A., A. Aldahan, G. Possnert, and I. Vintersved (2006), Distribution of  $^7\text{Be}$  in surface air of Europe, *Atmos Environ*, *40*(21), 3855-3868, doi: 10.1016/j.atmosenv.2006.02.030.

- Kulmala, M., U. Pirjola, and J. M. Makela (2000), Stable sulphate clusters as a source of new atmospheric particles, *Nature*, 404(6773), 66-69.
- Kunasek, S. A., B. Alexander, E. J. Steig, E. D. Sofen, T. L. Jackson, M. H. Thiemens, J. R. McConnell, D. J. Gleason, and H. M. Amos (2010), Sulfate sources and oxidation chemistry over the past 230 years from sulfur and oxygen isotopes of sulfate in a West Antarctic ice core, *J. Geophys. Res.-Atmos.*, 115, D18313, doi: 10.1029/2010JD013846.
- Lal, D., and B. Peters (1967), Cosmic Ray Produced Radioactivity On The Earth, in: *Handbuch der Physik*, Vol. XLVI/2, Springer, Berlin, pp. 551-612
- Lal, D., J. R. Arnold, and M. Honda (1960), Cosmic-Ray Production Rates of  $^7\text{Be}$  in Oxygen, and  $^{32}\text{P}$ ,  $^{33}\text{P}$ ,  $^{35}\text{S}$  in Argon at Mountain Altitudes, *Phys. Rev.*, 118(6), 1626-1632, doi: 10.1103/PhysRev.118.1626.
- Lambert, G., B. Ardouin, and J. Sanak (1990), Atmospheric transport of trace elements toward Antarctica, *Tellus B*, 42(1), 76-82, doi: 10.1034/j.1600-0889.1990.00009.x.
- Langway Jr, C., H. Clausen, and C. Hammer (1988), An inter-hemispheric volcanic time-marker in ice cores from Greenland and Antarctica, *Ann. Glaciol*, 10, 102-108.
- Lee, C. C. W., and M. H. Thiemens (2001), The  $\delta^{17}\text{O}$  and  $\delta^{18}\text{O}$  measurements of atmospheric sulfate from a coastal and high alpine region: A mass-independent isotopic anomaly, *J. Geophys. Res.-Atmos.*, 106(D15), 17359-17373, doi: 10.1029/2000JD900805.
- Legrand, M., and C. F. Saigne (1991), Methanesulfonic acid in south polar snow layers: A record of strong El Nino?, *Geophys. Res. Lett.*, 18(2), 187-190, doi: 10.1029GL02784.
- Legrand, M., S. Preunkert, B. Jourdain, H. Gallée, F. Goutail, R. Weller, and J. Savarino (2009), Year-round record of surface ozone at coastal (Dumont d'Urville) and inland (Concordia) sites in East Antarctica, *J Geophys Res*, 114, D20306, doi: 10.1029/2008JD011667.
- Li, F., P. Ginoux, and V. Ramaswamy (2008), Distribution, transport, and deposition of mineral dust in the Southern Ocean and Antarctica: Contribution of major sources, *J. Geophys. Res.*, 113, D10207, doi: 10.1029/2007JD009190.
- Liss, P. S., A. D. Hatton, G. Malin, P. D. Nightingale, and S. M. Turner (1997), Marine sulphur emissions, *Philosophical Transactions of the Royal Society of London. Series B: Biological Sciences*, 352(1350), 159-169, doi: 10.1098/rstb.1997.0011.
- Lunt, D. J., and P. J. Valdes (2002), Dust deposition and provenance at the Last Glacial Maximum and present day, *Geophys. Res. Lett.*, 29(22), 2085, doi: 10.1029/2002GL015656.

Luo, C., N. M. Mahowald, and J. del Corral (2003), Sensitivity study of meteorological parameters on mineral aerosol mobilization, transport, and distribution, *J. Geophys. Res.*, *108(D15)*, 4447, doi: 10.1029/2003JD003483.

Lyons, J. R. (2001), Transfer of mass-independent fractionation in ozone to other oxygen-containing radicals in the atmosphere, *Geophys. Res. Lett.*, *28(17)*, 3231-3234, doi: 10.1029/2000GL012791.

Masarik, J. and Beer, J. (2009), An updated simulation of particle fluxes and cosmogenic nuclide production in the Earth's atmosphere, *J. Geophys. Res.*, *114*, D11103, doi:10.1029/2008JD010557.

Mather, T. A., D. M. Pyle, and C. Oppenheimer (2003), Tropospheric volcanic aerosol, in *Volcanism and the Earth's Atmosphere*, *Geophys. Monogr. Ser.*, vol 139, edited by A Robock and C. Oppenheimer, pp.189-212, AGU, Washington D.C. doi: 10.1029/139GM112.

Mauldin, R. L., E. Kosciuch, B. Henry, F. L. Eisele, R. Shetter, B. Lefer, G. Chen, D. Davis, G. Huey, and D. Tanner (2004), Measurements of OH, HO<sub>2</sub>+RO<sub>2</sub>, H<sub>2</sub>SO<sub>4</sub>, and MSA at the south pole during ISCAT 2000, *Atmos Environ*, *38(32)*, 5423-5437, doi: 10.1016/j.atmosenv.2004.06.031.

McCabe, J. R., J. Savarino, B. Alexander, S. L. Gong, and M. H. Thiemens (2006), Isotopic constraints on non-photochemical sulfate production in the Arctic winter, *Geophys. Res. Lett.*, *33*, L05810, doi: 10.1029/2005GL025164.

Michalski, G., Z. Scott, M. Kabiling, and M. H. Thiemens (2003), First measurements and modeling of  $\Delta^{17}\text{O}$  in atmospheric nitrate, *Geophys. Res. Lett.*, *30(16)*, 1870, doi: 10.1029/2003GL017015.

Minikin, A., M. Legrand, J. Hall, D. Wagenbach, C. Kleefeld, E. Wolff, E. C. Pasteur, and F. Ducroz (1998), Sulfur-containing species (sulfate and methanesulfonate) in coastal Antarctic aerosol and precipitation, *J. Geophys. Res.*, *103(D9)*, 10975-10990, doi: 10.1029/98JD00249.

Morin, S., J. Savarino, S. Bekki, S. Gong, and J. Bottenheim (2007), Signature of Arctic surface ozone depletion events in the isotope anomaly ( $^{17}\text{O}$ ) of atmospheric nitrate, *Atmos Chem Phys*, *7(5)*.

Mroz, E. J., M. Alei, J. H. Capps, P. R. Guthals, A. S. Mason, and D. J. Rokop (1989), Antarctic Atmospheric Tracer Experiments, *J. Geophys. Res.*, *94(D6)*, 8577-8583, doi: 10.1029/JD094iD06p08577.

Neff, W. D. (1999), Decadal time scale trends and variability in the tropospheric circulation over the South Pole, *J. Geophys. Res.*, *104(D22)*, 27217-27251, doi: 10.1029/1999JD900483.

Osaki, S., Y. Tagawa, T. Chijiwa, S. Sugihara, and Y. Maeda (1999), Atmospheric deposition of S-35, *J. Radioanal. Nucl. Ch.*, *239(3)*, 543-547, doi: 10.1007/BF02349066.



Parish, T. R., and D. H. Bromwich (2007), Reexamination of the near-Surface airflow over the Antarctic continent and implications on atmospheric circulations at high southern latitudes, *Monthly Weather Review*, *135*(5), 1961-1973, doi: 10.1175/MWR3374.1.

Patris, N., R. J. Delmas, and J. Jouzel (2000), Isotopic signatures of sulfur in shallow Antarctic ice cores, *J. Geophys. Res.*, *105*(D6), 7071-7078, doi: 10.1029/1999JD900974.

Patris, N., S. S. Cliff, P. K. Quinn, M. Kasem, and M. H. Thiemens (2007), Isotopic analysis of aerosol sulfate and nitrate during ITCT-2k2: Determination of different formation pathways as a function of particle size, *J. Geophys. Res.-Atmos.*, *112*, D23301, doi: 10.1029/2005JD006214.

Pedro, J., U. Heikkilä, A. Klekociuk, A. Smith, T. van Ommen, and M. Curran (2011), Beryllium-10 transport to Antarctica: Results from seasonally resolved observations and modeling, *J Geophys Res*, *116*, D23120, doi: 10.1029/2011JD016530.

Preunkert, S., B. Jourdain, M. Legrand, R. Udisti, S. Becagli, and O. Cerri (2008), Seasonality of sulfur species (dimethyl sulfide, sulfate, and methanesulfonate) in Antarctica: Inland versus coastal regions, *J. Geophys. Res.*, *113*, D15302, doi: 10.1029/2008JD009937.

Preunkert, S., M. Legrand, B. Jourdain, C. Moulin, S. Belviso, N. Kasamatsu, M. Fukuchi, and T. Hirawake (2007), Interannual variability of dimethylsulfide in air and seawater and its atmospheric oxidation by-products (methanesulfonate and sulfate) at Dumont d'Urville, coastal Antarctica (1999-2003), *J. Geophys. Res.*, *112*, D06306, doi: 10.1029/2006JD007585.

Priyadarshi, A., G. Dominguez, J. Savarino, and M. Thiemens (2011), Cosmogenic  $^{35}\text{S}$ : A unique tracer to Antarctic atmospheric chemistry and the polar vortex, *Geophys. Res. Lett.*, *38*, L13808, doi:10.1029/2011GL047469.

Priyadarshi, A., J. Hill-Falkenthal, E. Coupal, G. Dominguez, and M. H. Thiemens (2012), Measurements of  $^{35}\text{S}$  in the marine boundary layer at La Jolla, California: A new technique for tracing air mass mixing during Santa Ana events, *J. Geophys. Res.-Atmos.*, *117*, D08301, doi: 10.1029/2011JD016878.

Prospero, J. M., D. L. Savoie, E. S. Saltzman, and R. Larsen (1991), Impact of oceanic sources of biogenic sulfur on sulfate aerosol concentrations at Mawson, Antarctica, *Nature*, *350*(6315), 221-223, doi: 10.1038/350221a0.

Pruett, L. E., K. J. Kreutz, M. Wadleigh, P. A. Mayewski, and A. Kurbatov (2004), Sulfur isotopic measurements from a West Antarctic ice core: implications for sulfate source and transport, *Annals of Glaciology*, *39*(1), 161-168, doi: 10.3189/172756404781814339.

Read, K. A., et al. (2008), DMS and MSA measurements in the Antarctic Boundary Layer: Impact of BrO on MSA production, *Atmos Chem Phys*, *8*(11), 2985-2997, doi: 10.5194/acp-8-2985-2008.

Roscoe, H. K. (2004), Possible descent across the “Tropopause” in Antarctic winter, *Advances in Space Research*, 33(7), 1048-1052, doi: 10.1016/s0273-1177(03)00587-8.

Savarino, J., and M. H. Thiemens (1999), Mass-independent oxygen isotope ( $^{16}\text{O}$ ,  $^{17}\text{O}$ ,  $^{18}\text{O}$ ) fractionation found in  $\text{H}_x$ ,  $\text{O}_x$  reactions, *J. Phys. Chem. A.*, 103(46), 9221-9229, doi: 10.1021/jp991221y.

Savarino, J., C. C. W. Lee, and M. H. Thiemens (2000), Laboratory oxygen isotopic study of sulfur (IV) oxidation: Origin of the mass-independent oxygen isotopic anomaly in atmospheric sulfates and sulfate mineral deposits on Earth, *J. Geophys. Res.-Atmos.*, 105(D23), 29079-29088.

Savarino, J., B. Alexander, V. Darmohusodo, and M. H. Thiemens (2001), Sulfur and oxygen isotope analysis of sulfate at micromole levels using a pyrolysis technique in a continuous flow system, *Anal. Chem.*, 73(18), 4457-4462, doi: 10.1021/AC010017f.

Savarino, J., S. Bekki, J. H. Cole-Dai, and M. H. Thiemens (2003), Evidence from sulfate mass independent oxygen isotopic compositions of dramatic changes in atmospheric oxidation following massive volcanic eruptions, *J Geophys Res-Atmos*, 108(D21), 4671, doi: 10.1029/2003JD003737.

Savarino, J., J. Kaiser, S. Morin, D. M. Sigman, and M. H. Thiemens (2007), Nitrogen and oxygen isotopic constraints on the origin of atmospheric nitrate in coastal Antarctica, *Atmos Chem Phys*, 7(8), 1925-1945, doi: 10.5194/acp-7-1925-2007.

Savoie, D. L., J. M. Prospero, R. J. Larsen, and E. S. Saltzman (1992), Nitrogen and Sulfur Species in Aerosols at Mawson, Antarctica, and Their Relationship to Natural Radionuclides, *J Atmos Chem*, 14(1-4), 181-204, doi: 10.1007/BF00115233.

Schauer, A. J., et al. (2012), Oxygen isotope exchange with quartz during pyrolysis of silver sulfate and silver nitrate, *Rapid Commun Mass Sp*, 26(18), 2151-2157, doi: 10.1002/rcm.6332.

Schwerdtfeger, W. (1984), *Weather and Climate of the Antarctic*, Amsterdam, Elsevier, 261 pp.

Shaw, G. E. (1988), Antarctic aerosols: A review, *Reviews of Geophysics*, 26(1), 89-112, doi: 10.1029/RG026i001p00089.

Smith, S. J., H. Pitcher, and T. Wigley (2001), Global and regional anthropogenic sulfur dioxide emissions, *Global and planetary change*, 29, 99-119, doi: 10.1016/S0921-8181(00)00057-6.

Sofen, E. D., B. Alexander, and S. A. Kunasek (2011), The impact of anthropogenic emissions on atmospheric sulfate production pathways, oxidants, and ice core  $\Delta^{17}\text{O}(\text{SO}_4^{2-})$ , *Atmos Chem Phys*, 11(7), 3565-3578, doi: 10.5194/acp-11-3565-2011.

Stockwell, W. R., and J. G. Calvert (1983), The mechanism of the HO-SO<sub>2</sub> reaction, *Atmos Environ*, 17(11), 2231-2235, doi: 10.1016/0004-6981(83)90220-2.

Stohl, A., and H. Sodemann (2010), Characteristics of atmospheric transport into the Antarctic troposphere, *J. Geophys. Res.*, 115, D02305, doi: 10.1029/2009JD012536.

Swanson, A. L., D. D. Davis, R. Arimoto, P. Robert, E. L. Atlas, F. Flocke, S. Meinardi, F. S. Rowland, and D. R. Blake (2004), Organic trace gases of oceanic origin observed at South Pole during ISCAT 2000, *Atmos Environ*, 38(32), 5463-5472, doi: 10.1016/j.atmosenv.2004.03.072.

Tanaka, N., and K. K. Turekian (1991), Use of cosmogenic <sup>35</sup>S to determine the rates of removal of atmospheric SO<sub>2</sub>, *Nature*, 352(6332), 226-228, doi: 10.1038/352226a0.

Tanaka, N., and K. K. Turekian (1995), Determination of the dry deposition flux of SO<sub>2</sub> using cosmogenic <sup>35</sup>S and <sup>7</sup>Be measurements, *J. Geophys. Res.-Atmos.*, 100(D2), 2841-2848, doi: 10.1029/94JD02305.

Thiemens, M. H. (2006), History and applications of mass-independent isotope effects, *Annu Rev Earth Pl Sc*, 34, 217-262, doi: 10.1146/annurev.earth.34.031405.125026.

Thiemens, M. H., S. Chakraborty, and G. Dominguez (2012), The Physical Chemistry of Mass-Independent Isotope Effects and Their Observation in Nature, in *Annual Review of Physical Chemistry*, Vol 63, edited by M. A. Johnson and T. J. Martinez, 155-177, doi: 10.1146/annurev-physchem-032511-143657.

Tomikawa, Y., Y. Nishimura, and T. Yamanouchi (2009), Characteristics of Tropopause and Tropopause Inversion Layer in the Polar Region, *Sola*, 5, 141-144, doi: 10.2151/sola.2009-036.

Turekian, K. K., and N. Tanaka (1992), The use of atmospheric cosmogenic <sup>35</sup>S and <sup>7</sup>Be in determining depositional fluxes of SO<sub>2</sub>, *Geophys. Res. Lett.*, 19(17), 1767-1770, doi: 10.1029/92GL01879.

Udisti, R., et al. (2012), Sea spray aerosol in central Antarctica. Present atmospheric behaviour and implications for paleoclimatic reconstructions, *Atmos Environ*, 52, 109-120, doi: 10.1016/j.atmosenv.2011.10.018.

Van De Berg, W. J., M. R. van den Broeke, and E. van Meijgaard (2008), Spatial structures in the heat budget of the Antarctic atmospheric boundary layer, *Cryosphere*, 2(1), 1-12, doi: 10.5194/tc-2-1-2008.

Wagenbach, D. (1996), *Coastal Antarctica: Atmospheric chemical composition and atmospheric transport, in Chemical exchange between the atmosphere and polar snow*, eds. E. Wolff and R. Bales, NATO ASI Series I, 43: 173-199, Springer-Verlag, Berlin.

- Wagenbach, D., U. Görlach, K. Moser, and K. O. Münnich (1988), Coastal Antarctic aerosol: the seasonal pattern of its chemical composition and radionuclide content, *Tellus B*, 40B(5), 426-436, doi: 10.1111/j.1600-0889.1988.tb00114.x.
- Wagenbach, D., M. Legrand, H. Fischer, F. Pichlmayer, and E. W. Wolff (1998), Atmospheric near-surface nitrate at coastal Antarctic sites, *J. Geophys. Res.*, 103(D9), 1107-11020, doi: 10.1029/97jd03364.
- Weber, R. J., G. Chen, D. D. Davis, R. L. Mauldin, D. J. Tanner, F. L. Eisele, A. D. Clarke, D. C. Thornton, and A. R. Bandy (2001), Measurements of enhanced H<sub>2</sub>SO<sub>4</sub> and 3-4 nm particles near a frontal cloud during the First Aerosol Characterization Experiment (ACE 1), *J Geophys Res-Atmos*, 106(D20), 24107-24117, doi: 10.1029/2000JD000109.
- Weller, R., and D. Wagenbach (2007), Year-round chemical aerosol records in continental Antarctica obtained by automatic samplings, *Tellus B*, 59(4), 755-765, doi: 10.1111/j.1600-0889.2007.00293.x.
- Wendler, G., and Y. Kodama (1984), On the climate of Dome C, Antarctica, in relation to its geographical setting, *Journal of Climatology*, 4(5), 495-508, doi: 10.1002/joc.3370040505.
- Wilcox, L. J., B. J. Hoskins, and K. P. Shine (2012), A global blended tropopause based on ERA data. Part II: Trends and tropical broadening, *Quarterly Journal of the Royal Meteorological Society*, 138(664), 576-584, doi: 10.1002/Qj.910.
- Xu, Y. W., and G. R. Carmichael (1998), Modeling the dry deposition velocity of sulfur dioxide and sulfate in Asia, *J. Appl. Meteorol.*, 37(10), 1084-1099, doi: 10.1175/1520-0450(1998)037<1084:mtddvo>2.0.co;2.
- Zahn, A., P. Franz, C. Bechtel, J. U. Grooss, and T. Röckmann (2006), Modelling the budget of middle atmospheric water vapour isotopes, *Atmos. Chem. Phys.*, 6, 2073-2090, doi: 10.5194/acp-6-2073-2006.
- Zangl, G., and K. P. Hoinka (2001), The tropopause in the polar regions, *Journal of Climate*, 14(14), 3117-3139, doi: 10.1175/1520-0442(2001)014<3117:Ttitpr>2.0.Co;2.
- Zanis, P., E. Schuepbach, H. W. Gäggeler, S. Hübener, and L. Tobler (1999), Factors controlling beryllium-7 at Jungfrauoch in Switzerland, *Tellus B*, 51(4), 789-805, doi: 10.1034/j.1600-0889.1999.t01-3-00004.x.

## Chapter 5

### Detection of Radioactive $^{35}\text{S}$ at Fukushima and other Japanese Sites

#### 5.1 Abstract

The Fukushima nuclear power plant was severely damaged by an earthquake and concomitant tsunami during March 2011. An effect of this disaster was secondary formation of radioactive  $^{35}\text{S}$  via the  $^{35}\text{Cl}(n,p)^{35}\text{S}$  reaction, when neutrons from the partially melted reactor cores activated the coolant sea water. Here we report the first measurements of  $^{35}\text{S}$  in sulfate aerosols and rain water collected at six Japanese sampling sites, Hokkaido, Tsukuba, Kashiwa, Fuchu, Yokohama, and Fukushima, during March-September 2011. The measured  $^{35}\text{SO}_4^{2-}$  concentrations in aerosols vary significantly. The Kashiwa (AORI) site shows the highest  $^{35}\text{SO}_4^{2-}$  concentration ( $6.1 \times 10^4 \pm 200$  atoms/ $\text{m}^3$ ) on 1 April 2011, which is nearly 100 times higher than the natural background activity. Considering the percentage loss of  $^{35}\text{SO}_4^{2-}$  resulting from dry and wet deposition and dilution of the radiation plume in the boundary layer during transport, it was determined that the surface air concentration of  $^{35}\text{SO}_4^{2-}$  at Fukushima would have been  $2.8 \times 10^5$  atoms/ $\text{m}^3$  during the week after the earthquake, which is in agreement with the model prediction [Priyadarshi *et al.*, 2011a].  $^{35}\text{SO}_4^{2-}$  activity in rain water collected during March-May 2011 at Tokyo Tech Yokohama varies from  $1.1 \times 10^5$  to  $9.8 \times 10^5$  atoms/liter, whereas stream water collected near Fukushima was found to have  $1.2 \times 10^5$  atoms/liter during April. Even after 6 months,  $^{35}\text{SO}_4^{2-}$  activity remains very high ( $9.9 \times 10^4 \pm 770$  atoms/ $\text{m}^3$ ) in the marine boundary layer in the Fukushima region, which implies that the reactor core was producing radioactive sulfur.

#### 5.2 Introduction

On 11 March 2011, a magnitude 9.0 earthquake occurred in the western Pacific Ocean, with its epicenter approximately 72 km east of the Oshika peninsula of Tohoku Japan (see <http://earthquake.usgs.gov/earthquakes/eqinthenews/2011/usc0001xgp/>). The earthquake triggered a catastrophic tsunami with severe collateral damage. In addition to a significant loss of life and infrastructure destruction, the tsunami caused damage to the Fukushima Daiichi nuclear power plant (<http://www.iaea.org>). Immediately after the earthquake, the reactors at the Fukushima nuclear power plant were automatically shut down and boron-carbon control rods inserted between the fuel columns to absorb

neutrons and halt the nuclear chain reaction. Even after the shutdown, the reactor core required a prolonged cooling because the uranium fuel continues to decay into radioactive byproducts and release heat. A preliminary computer model by the U.K. National Nuclear Laboratory showed that even after the shutdown of the Fukushima nuclear power plant, the radioactive byproducts of the fission reaction still generated 7 megawatts of heat [Brumfiel, 2011a]. Because both the regular and the emergency backup power supply (diesel generators) that powered the cooling system of the power plant were severely damaged by the tsunami waves, the reactor core became sufficiently hot that it initiated a melt down and released hydrogen gas that eventually ignited and caused explosions. The core damage was estimated to be 55%, 35%, and 30% for Units 1, 2, and 3, respectively (<http://www.iaea.org>). Even after 6 months of continuous cooling, the reactor core was too hot to allow access [Brumfiel, 2011b]. As the result of these events, a significant amount of radioactivity was released into the atmosphere [Chino *et al.*, 2011; Morino *et al.*, 2011]. Potentially dangerous levels of radiation were detected nearly 30-40 km away from the nuclear plant. Approximately  $4 \times 10^{11}$  neutrons/m<sup>2</sup> were emitted during the first week following the earthquake, which led to the formation of radioactive <sup>35</sup>S [Priyadarshi *et al.*, 2011a]. During the first few weeks (13 March to 26 March 2011) after the earthquake and tsunami, several hundred tons of sea water was pumped into the partially melted reactor core as a coolant. Neutrons emitted from the reactor core were absorbed or captured by the constituents of sea water to produce a variety of radioactive isotopes, mainly <sup>24</sup>Na by interaction of neutrons with stable sodium via an (n,γ) reaction and <sup>35</sup>S produced by interaction of neutrons with stable chlorine via an (n,p) reaction [Dyrssen and Nyman, 1955; Love and Sam, 1962]. Since <sup>24</sup>Na has a very short half-life (15 h), the total radioactivity after a week was nearly exclusively due to <sup>35</sup>S [Dyrssen and Nyman, 1955].

Once produced, <sup>35</sup>S was oxidized to <sup>35</sup>SO<sub>2</sub> gas, which was eventually further oxidized to <sup>35</sup>SO<sub>4</sub><sup>2-</sup> aerosol in the atmosphere, similar to the natural atmospheric process [Brothers *et al.*, 2010; Priyadarshi *et al.*, 2011b; Tanaka and Turekian, 1991]. It was subsequently transported in the atmosphere depending on air mass trajectories and removed from the atmosphere by dry/wet deposition and radioactive decay. <sup>35</sup>S is a unique tracer in that it provides information on the number of neutrons emitted from the reactor core and can be used to probe the condition of the reactor core as well as the containment vessel. Because of the

unavailability of samples near the Fukushima power plant, there have been no measurements of  $^{35}\text{S}$  until now. Based on  $^{35}\text{S}$  measurements of atmospheric sulfate and  $\text{SO}_2$  samples collected at La Jolla, California, and concomitant model calculations, the concentration of  $^{35}\text{SO}_4^{2-}$  in surface air was estimated to be  $2 \times 10^5$  atoms/ $\text{m}^3$  at Fukushima during March 2011 [Priyadarshi *et al.*, 2011a]. Here we report the first measurement of radioactive  $^{35}\text{S}$  in sulfate aerosols and rain water collected at different sites in Japan (Figure 1) and compare the data with the model calculation of Priyadarshi *et al.* (2011a).

### 5.3 Methods

Aerosol samples were collected at six different places in close proximity to the Fukushima nuclear power plant (37.25°N, 141.02°E; Figure 1): Tokyo Institute of Technology (Tokyo Tech) Yokohama (35.52°N, 139.48°E); Atmosphere and Ocean Research and Institute (AORI), University of Tokyo, Kashiwa, Chiba Prefecture (35.90°N, 139.94°E); Tokyo University of Agriculture and Technology (TUAT), Fuchu, Tokyo (35.68°N, 139.48°E); National Institute of Environmental Studies (NIES), Tsukuba, Ibaraki Prefecture (36.05°N, 140.12°E); Hokkaido Research Organization, Sapporo (43.08°N, 141.34°E); and Kawamata town, Fukushima prefecture (37.40°N, 140.36°E). These sampling sites, except for Sapporo, are located within a 250 km radius south of the Fukushima nuclear plant. The aerosol samples were collected from March through September 2011 using a high-volume air sampler. Rain water samples were collected only at Tokyo Tech during March-May 2011. In addition, a water sample from a local water stream, situated in Fukushima prefecture, nearly 50 km away from the Fukushima nuclear power plant, was collected in April 2011. The samples were analyzed at the University of California, San Diego. The details of the sample processing for analyzing  $^{35}\text{S}$  activity in sulfate aerosols have been described by Brothers *et al.* (2010). Three or four liters of rainwater were passed through a pre-prepared anion resin column to trap sulfate on the resin surface, and 15 ml of HBr (1 M) was passed through the resin column to elute sulfate ions from the resin. The solution was then neutralized by adding  $\text{Ag}_2\text{O}$  and oven dried. Sulfate was cleaned of organics as discussed by Brothers *et al.* (2010). The  $^{35}\text{S}$  activity was counted in an ultralow-level liquid scintillation spectrometer (Wallac 1220 Quantulus) and was corrected for the background activity (which is 1.07 DPM and probably due to the radioactivity contributed from vial material and the scintillation gel used for counting) and the decay time from the sample collection date. The natural variation in  $^{35}\text{SO}_4^{2-}$

concentration, as reported by *Priyadarshi et al.* (2011b, 2012), is from 130 to 900 atoms/m<sup>3</sup> and from 200 to 1600 atoms/m<sup>3</sup> at Scripps Pier in Southern California and in Antarctica, respectively.

#### 5.4 Results and Discussion

<sup>35</sup>S activities measured in sulfate aerosols collected at Tokyo Tech, AORI, TUAT, NIES, Hokkaido, and Fukushima (different aerosol size fraction) are shown in Figures 2 and 3. Even though the sampling sites are relatively close to each other (southward direction from Fukushima, except for Hokkaido), a large variation in <sup>35</sup>SO<sub>4</sub><sup>2-</sup> activities was observed during March-April 2011. <sup>35</sup>SO<sub>4</sub><sup>2-</sup> concentrations were  $0.26 \times 10^3 - 11.78 \times 10^3$ ,  $0.69 \times 10^3 - 61.4 \times 10^3$ ,  $0.51 \times 10^3 - 1.42 \times 10^3$ ,  $1.41 \times 10^3 - 18.05 \times 10^3$ ,  $0.56 \times 10^3 - 2.63 \times 10^3$  atoms/m<sup>3</sup> at Tokyo Tech, AORI, TUAT, NIES, and Hokkaido, respectively (Table 1). The <sup>35</sup>S activities observed at Tokyo Tech, AORI and NIES are significantly higher than those observed at TUAT, NIES, and Hokkaido sites. At Fukushima, <sup>35</sup>SO<sub>4</sub><sup>2-</sup> varies from  $8.1 \times 10^3$  to  $9.9 \times 10^4$  atoms/m<sup>3</sup> and from 46 to 62 atoms/m<sup>3</sup> in fine and coarse fractions, respectively (Table 2). <sup>35</sup>SO<sub>4</sub><sup>2-</sup> concentrations at AORI ( $6.1 \times 10^4$  atoms/m<sup>3</sup>) and Fukushima ( $1.2 \times 10^5$  atoms/m<sup>3</sup>) are the highest <sup>35</sup>S activities ever measured in any atmospheric sample and are nearly 100 times higher than the natural background. Radioactive <sup>35</sup>S (half-life 87 days) is also produced by the interaction of cosmic rays with <sup>40</sup>Ar in the Earth's atmosphere [*Lal and Peters, 1967*]. The natural background <sup>35</sup>SO<sub>4</sub><sup>2-</sup> concentration in the atmosphere varies from 300 to 900 atoms/m<sup>3</sup> [*Brothers et al., 2010; Priyadarshi et al., 2012*]. Even in Antarctica, where the production rate of <sup>35</sup>S is maximal [*Lal and Peters, 1967*], <sup>35</sup>SO<sub>4</sub><sup>2-</sup> varies from 120 to 1600 atoms/m<sup>3</sup> [*Priyadarshi et al., 2011b*]. Such a high concentration of <sup>35</sup>SO<sub>4</sub><sup>2-</sup> at AORI indicates the presence of another source of <sup>35</sup>S in the marine boundary layer. *Priyadarshi et al.* (2011b) demonstrated that the partially damaged reactor core of the Fukushima nuclear power plant produced radioactive <sup>35</sup>S via <sup>35</sup>Cl(n,p)<sup>35</sup>S reaction during the first few weeks following the earthquake. The Hybrid Single Particle Lagrangian Integrated Trajectory (HYSPPLIT) model developed by NOAA's Air Resources Laboratory (ARL) [*Draxler and Rolph, 2011*] was used to calculate the air mass back-trajectories to determine the origin and pathway of the air masses affecting the sampling sites involved in this study. We considered the air mass mixing and its transport within the boundary layer. The backward air mass trajectories were calculated for 72 h at three different altitudes (10, 500, and 1000 m) over each sampling station. As shown



in Figure 4, surface air masses at AORI arrived from the north near Fukushima on 1 April 2011 and are thus responsible for the observed spike in  $^{35}\text{SO}_4^{2-}$  activity ( $6.1 \times 10^4$  atoms/m<sup>3</sup>). The sampling site at Hokkaido lies north of Fukushima and is thus not affected by the  $^{35}\text{S}$  emission at Fukushima. A possible reason for lower  $^{35}\text{SO}_4^{2-}$  activity at TUAT is its geographical location and the prevailing air mass transport vectors. TUAT is situated in Fuchu city, which has many terraces and hills across it. The Fuchu and Kokobunji hills align from west to east whereas the Sengen-Yama hill is located on the northeastern side, which may affect the air mass trajectories coming from Northeast Fukushima. Fine-scale air mass trajectory analysis is not available, but future modeling efforts could be instrumental in developing this.

Based on  $^{35}\text{S}$  activity measurements in California and a moving box model, the surface air concentration of  $^{35}\text{SO}_4^{2-}$  at Fukushima was predicted to be  $2 \times 10^5$  atoms/m<sup>3</sup> in the week following the earthquake [Priyadarshi *et al.*, 2011a]. The present data show a maximum activity of  $6.1 \times 10^4$  atoms/m<sup>3</sup> at AORI on 1 April 2011, which is about three times lower than the model estimated value. Because the AORI site is nearly 250 km away from the Fukushima nuclear plant, a dilution of the radiation plume in the boundary layer and loss of  $^{35}\text{SO}_4^{2-}$  aerosol particles by dry and wet deposition during the transport are expected to decrease the  $^{35}\text{SO}_4^{2-}$  concentration significantly before reaching the AORI site. Morino *et al.* (2011) used a 3D chemical transport model to simulate the distribution of radioactive  $^{131}\text{I}$  and  $^{137}\text{Cs}$  over Japan (both inland and the surrounding nearby oceanic surface) during 10-30 March 2011. The model considered the emission of radionuclides ( $^{131}\text{I}$  and  $^{137}\text{Cs}$ ) at the Fukushima nuclear power plant, horizontal and vertical advection, diffusion affecting the radiation plume during transport, dry and wet deposition of gas and aerosols, and radioactive decay to determine the percentage loss of radioactive  $^{131}\text{I}$  and  $^{137}\text{Cs}$  over Fukushima and nearby prefectures. Since  $^{137}\text{Cs}$  behaves as an aerosol particle due to its attachment to fine aerosols [Sportisse, 2007], we compare its distribution with  $^{35}\text{SO}_4^{2-}$  aerosols. According to Morino *et al.* (2011), nearly 15% of  $^{137}\text{Cs}$  emitted from the Fukushima nuclear power plant was deposited over the Fukushima prefecture, whereas on average, 22% of emitted  $^{137}\text{Cs}$  was deposited over land in Japan during March. The percentage loss was greater (8-41%) during a transient cyclone that passed over Japan during 15-17 March and 19-23 March [Morino *et al.*, 2011].

Based on the observed  $^{35}\text{SO}_4^{2-}$  concentration peak at AORI on 1 April 2011 (Figure 2) and the model estimation of *Morino et al.* (2011), the surface air concentration of  $^{35}\text{SO}_4^{2-}$  at Fukushima was estimated to be between  $1.1 \times 10^5$  and  $2.8 \times 10^5$  atoms/m<sup>3</sup> during March, whereas the predicted concentration was  $2 \times 10^5$  atoms/m<sup>3</sup> [*Priyadarshi et al.*, 2011a]. This difference may be due partially to uncertainties related to the calculation of depositional rates of radionuclides, because the collection efficiency of dry-deposited aerosols is difficult to quantify precisely [*Morino et al.*, 2011]. In addition, the model used by *Priyadarshi et al.* (2011a) to calculate the concentration of  $^{35}\text{SO}_4^{2-}$  ( $2 \times 10^5$  atoms/m<sup>3</sup>) at Fukushima contains unavoidable uncertainty. The model is particularly sensitive to the dilution rate of the radiation plume during the long-range transport from Fukushima to La Jolla, California. A 10% change in dilution rate in the model would change the model output (surface air concentration of  $^{35}\text{SO}_4^{2-}$ , i.e.,  $2 \times 10^5$  atoms/m<sup>3</sup>) by 20%.

At Fukushima,  $^{35}\text{SO}_4^{2-}$  activity measured in fine sulfate aerosols are higher than in the coarse fraction during August through September 2011 (Figure 3 and Table 3). This is because  $^{35}\text{S}$  produced at the reactor was oxidized to  $^{35}\text{SO}_2$  and subsequently oxidized to  $^{35}\text{SO}_4^{2-}$  in the fine fraction by gas-phase oxidation of  $^{35}\text{SO}_2$ . We note that, even after 6 months,  $^{35}\text{S}$  activity was very high in the marine boundary layer in the Fukushima region, which implies that the reactor core was still active and releasing neutrons. However, the presence of a viable chlorine source is not known. The neutrons might be reacting either with residual evaporated salt deposits or with sea water coming in and out across a crack developed in the containment vessel. The reason for the higher  $^{35}\text{S}$  activity observed during September compared with July-August is not yet clear and warrants extended future sampling.

The  $^{35}\text{SO}_4^{2-}$  concentration in rain water collected during March-May 2011 at Tokyo Tech Yokohama varies from  $1.1 \times 10^5$  to  $9.8 \times 10^5$  atoms/liter, whereas stream water collected near Fukushima was found to have  $1.2 \times 10^5$  atoms/liter during April (Table 3). The concentration in rain water is nearly 10 times higher than the  $^{35}\text{SO}_4^{2-}$  concentration ( $6.2 \times 10^4$  atoms/liter) contained in rain water collected at La Jolla, California, during January 2010. Atmospheric processes such as rainout or washout cleanse the atmosphere by removing aerosol particles and gases. Model simulation dealing with long-range transport of dust and aerosols and deposition on the surface/ocean depends sensitively on the adapted aerosol-

scavenging coefficient. We utilized  $^{35}\text{S}$  measurements in aerosols and rainwater to calculate the aerosol-scavenging coefficient. The scavenging coefficient ( $k$ ) is defined as [Okita *et al.*, 1996]:

$$k = [(C_w/C_a) * 10^6] * (P/h) \quad (5.1)$$

where  $C_w$  and  $C_a$  are the  $^{35}\text{S}$  concentration in rain water (mg/liter) and air ( $\mu\text{g}/\text{m}^3$ ), respectively;  $P$  is the precipitation rate (cm/s); and  $h$  is the height of the cloud top (cm). We do not have measurements of the rate of precipitation of each individual event. The average precipitation rate (varying between 1.4 and 2.6 mm/h) was taken from the Japan Meteorological Agency and is given in Table 3. The height of the cloud top was assumed to be 2 km based on the fact that rainfall rate is more significant below the melting height (2-3 km), where the main wet removal occurs in cloud [Mittermaier and Illingworth, 2003]. After this height, the precipitation rate decreases and becomes less intense [Scott, 1982]. A recent measurement also shows that the mean cloud top height in the Hawaiian region is 2.1 km [Zhang *et al.*, 2012]. For our samples, the value of  $k$  varies from  $6.5 \times 10^{-3}/\text{s}$  to  $1.5 \times 10^{-2}/\text{s}$ , which agrees with other measurements [Andronache, 2004; Chate *et al.*, 2011; Laakso *et al.*, 2003; Maria and Russell, 2005; Okita *et al.*, 1996; Schumann, 1989]. The calculated values from Andronache (2004) vary from  $2.1 \times 10^{-3}/\text{s}$  to  $4.3 \times 10^{-4}/\text{s}$ , for corresponding precipitation rates of 1.5 mm/h and 4.7 mm/h.

It has been demonstrated that  $^{35}\text{S}$  is a unique tracer in understanding air mass mixing and quantifying aerosol dry and wet deposition [Cho *et al.*, 2011; Priyadarshi *et al.*, 2011b; Priyadarshi *et al.*, 2012; Tanaka and Turekian, 1991; Turekian and Tanaka, 1992]. Approximately  $2 \times 10^{11}$  atoms of  $^{35}\text{S}$  were produced from Fukushima within the first 6 months following the earthquake, which is lower by a factor of  $10^{11}$  compared with the total global production of  $2 \times 10^{22}$  atoms of  $^{35}\text{SO}_4^{2-}$  by cosmic rays, of which  $5 \times 10^{20}$  atoms of  $^{35}\text{S}$  are contained in the boundary layer itself. However, because Fukushima is a very localized point source, the released  $^{35}\text{SO}_4^{2-}$  was detected several thousand miles away from the source.

The presence of excess  $^{35}\text{SO}_4^{2-}$  (two orders of magnitude higher than the natural background) provides a unique opportunity to understand the chemical transformation, the air mass transport, and potentially the fate of  $^{35}\text{SO}_4^{2-}$  in soil on short time scales. A yearlong sampling of aerosol, soil, and rain water collected at several sampling sites in Japan for  $^{35}\text{S}$  analysis along with a regional transport model will

further resolve and quantify the distribution rate of regional radiogenic (and by proxy stable) sulfur in the natural environment.

### 5.5 Conclusions

We report the first measurement of radioactive  $^{35}\text{S}$  in sulfate aerosol collected at six different sampling sites close to the Fukushima nuclear power plant during March-September 2011. A very high  $^{35}\text{SO}_4^{2-}$  activity was observed at Fukushima, AORI, NIES, Tsukuba, and Tokyo Tech Yokohama that is nearly 100 times higher than the natural background  $^{35}\text{S}$ . Based on  $^{35}\text{SO}_4^{2-}$  concentrations measured at AORI in April, the surface air concentration of  $^{35}\text{S}$  was estimated to be  $2.8 \times 10^5$  atoms/m<sup>3</sup> at Fukushima during March. Even after 6 months,  $^{35}\text{S}$  activity was very high in the marine boundary layer in the Fukushima region, which implies that the reactor core was still active. The reason for higher  $^{35}\text{SO}_4^{2-}$  during September compared with July-August is probably the periodic use of seawater as a coolant.  $^{35}\text{SO}_4^{2-}$  concentration in rainwater collected at Tokyo Tech Yokohama varies from  $1.1 \times 10^5$  to  $9.8 \times 10^5$  atoms/liter. The  $^{35}\text{SO}_4^{2-}$  concentration measured in air and rainwater was employed to determine the rain-scavenging coefficient, which varies from  $6.5 \times 10^{-3}$  to  $1.5 \times 10^{-2}$  s<sup>-1</sup>.

### 5.6 Acknowledgements

Chapter 5, in full, is a reprint of material from Journal of Geophysical Research-Atmospheres, Priyadarshi, A., J. Hill-Falkenthal, M. Thiemens, N. Yoshida, S. Toyoda, K. Yamada, A. Mukotaka, A. Fujii, M. Uematsu, S. Hatakeyama, I. Noguchi, Y. Nojiri, and H. Tanimoto, Detection of radioactive  $^{35}\text{S}$  at Fukushima and other Japanese sites, volume 118, 2013. The dissertation author was one of two primary investigators and authors of this paper.

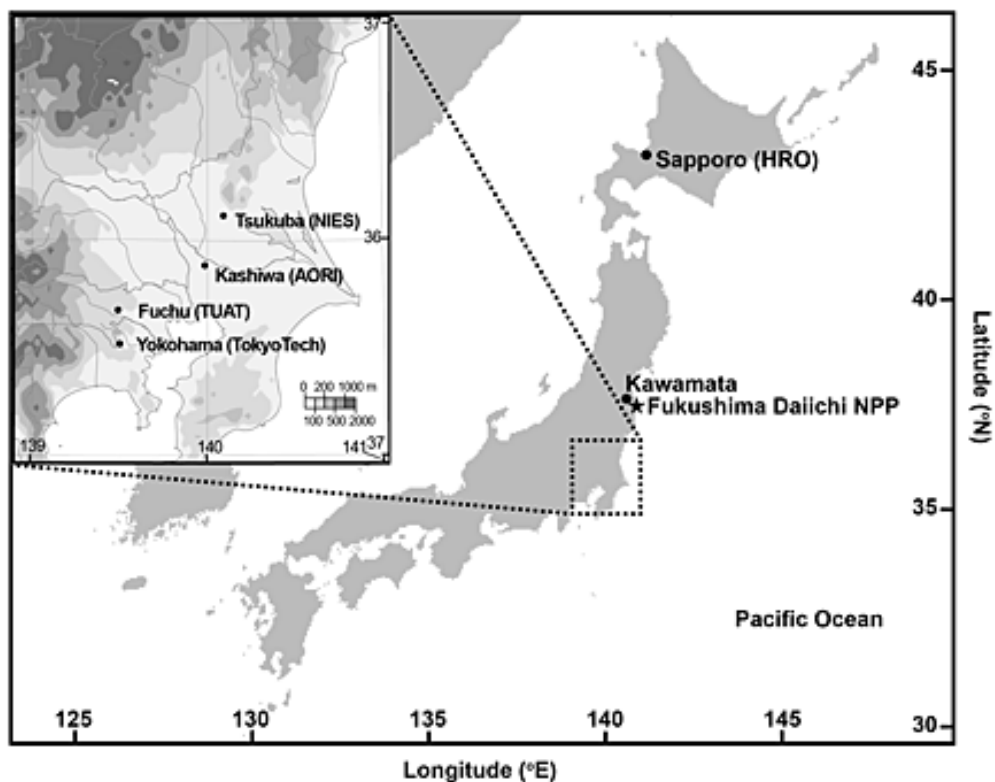


Figure 5.1

Details of the sampling sites. Aerosol samples were collected at six different places in close proximity to the Fukushima nuclear power plant (37.25°N, 141.02°E): Tokyo Institute of technology (Tokyo Tech), Yokohama (35.52°N, 141.02°E); Tokyo University of Agriculture and Technology (TUAT), Fuchu, Tokyo (35.68°N, 139.94°E). These sampling sites except for Sapporo are located within a 250 km radius and south of the Fukushima nuclear plant.

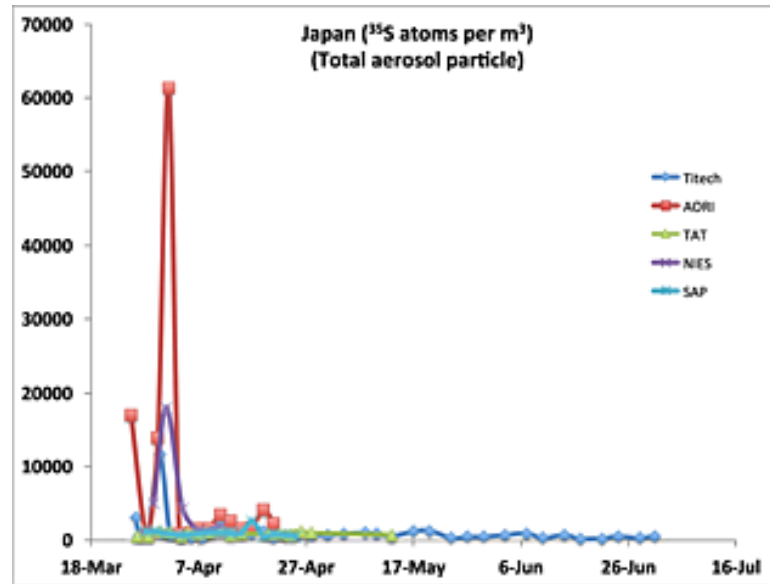


Figure 5.2

$^{35}\text{SO}_4^{2-}$  activity measured at five different samples near Fukushima. The maximum  $^{35}\text{SO}_4^{2-}$  activity ( $6.1 \times 10^4$  atoms/ $\text{m}^3$ ) was observed at AORI on 1 April 2011.

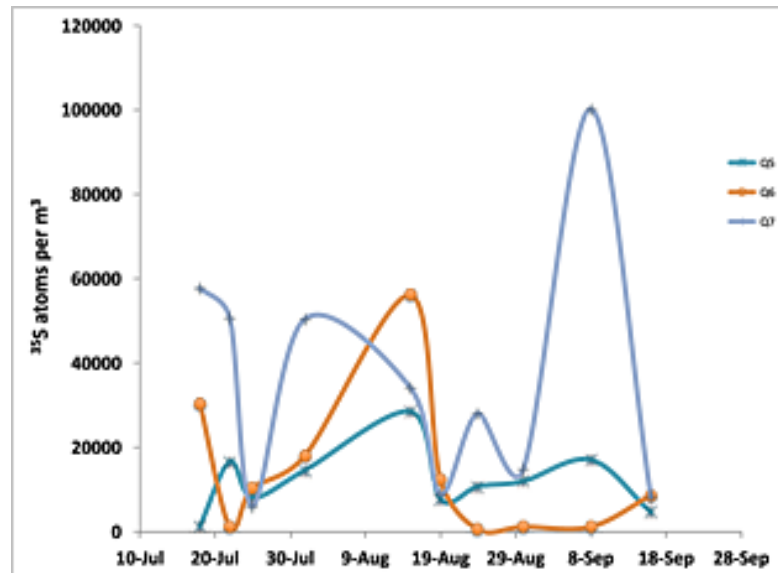


Figure 5.3

$^{35}\text{SO}_4^{2-}$  measured in different aerosol size fractions (Q5, Q6, Q7, representing aerosol size fraction between 0.69 and 1.3  $\mu\text{m}$ , between 0.39 and 0.69  $\mu\text{m}$ , and less than 0.39  $\mu\text{m}$ , respectively) collected at Fukushima prefecture.  $^{35}\text{SO}_4^{2-}$  in fine particles (Q7 < 0.39  $\mu\text{m}$ ) is nearly 100 times higher than the natural background and shows that, even after 6 months after the nuclear disaster, the reactor core was active and producing  $^{35}\text{S}$ .

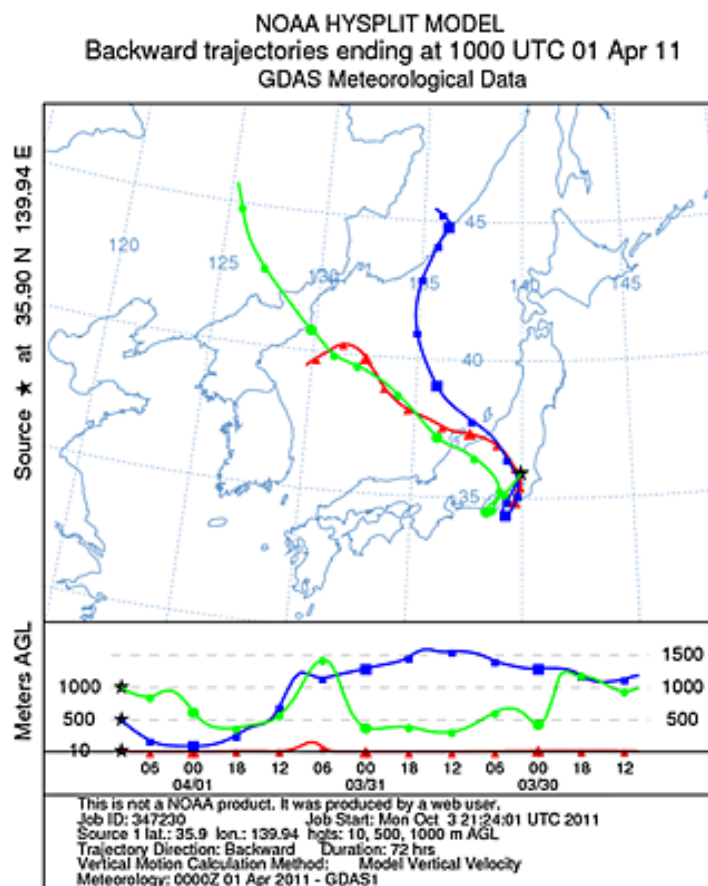


Figure 5.4

HYSPLIT- 3 day air mass back trajectories were calculated over the AORI sampling site at three different altitudes (10, 50, and 1000m). The surface air masses arrive from northern western regions of Japan near Fukushima and are mainly responsible for the spike in  $^{35}\text{SO}_4^{2-}$  activity observed on 1 April 2011.



Table 5.1

Measurement of radioactive  $^{35}\text{S}$  in sulfate aerosol collected at different sampling sites near Fukushima.

Sample ID	Collection Time (m/d/y)		Air Volume ( $\text{m}^3$ )	$^{35}\text{SO}_4^{2-}$ atoms/ $\text{m}^3$ $(10^3)$
	Starting Date	End Date		
Tokyo Institute of Technology (Tokyo Tech), Yokohama				
1	3/25/11	3/26/11	991	$3.06 \pm 0.12$
2	3/26/11	3/26/11	735	$0.56 \pm 0.11$
3	3/26/11	3/27/11	724	$0.72 \pm 0.12$
4	3/27/11	3/28/11	2001	$1.25 \pm 0.04$
5	3/28/11	3/30/11	2945	$11.78 \pm 0.07$
6	3/30/11	4/1/11	2960	$0.73 \pm 0.03$
7	4/1/11	4/3/11	2931	$0.48 \pm 0.03$
8	4/3/11	4/5/11	2980	$0.35 \pm 0.03$
9	4/5/11	4/7/11	2969	$0.41 \pm 0.03$
10	4/7/11	4/9/11	2973	$1.03 \pm 0.07$
11	4/9/11	4/11/11	2962	$1.75 \pm 0.08$
12	4/11/11	4/13/11	2959	$0.94 \pm 0.07$
13	4/13/11	4/15/11	2980	$1.11 \pm 0.07$
14	4/15/11	4/17/11	2984	$0.88 \pm 0.07$
15	4/17/11	4/19/11	2993	$1.25 \pm 0.08$
16	4/19/11	4/21/11	2961	$0.46 \pm 0.07$
17	4/21/11	4/23/11	2980	$0.79 \pm 0.07$
18	4/23/11	4/25/11	2985	$0.77 \pm 0.07$
19	4/25/11	4/28/11	4479	$0.76 \pm 0.05$
20	4/28/11	5/1/11	4413	$0.70 \pm 0.05$
21	5/1/11	5/4/11	4495	$0.93 \pm 0.07$
22	5/4/11	5/8/11	2884	$1.03 \pm 0.09$
23	5/8/11	5/10/11	2980	$0.88 \pm 0.09$
24	5/10/11	5/13/11	4511	$0.62 \pm 0.06$
25	5/13/11	5/17/11	5949	$1.22 \pm 0.05$
26	5/17/11	5/20/11	4467	$1.32 \pm 0.06$
27	5/20/11	5/24/11	5959	$0.35 \pm 0.04$
28	5/24/11	5/27/11	4493	$0.49 \pm 0.05$
29	5/27/11	5/30/11	4138	$0.50 \pm 0.05$
30	5/30/11	6/3/11	6200	$0.74 \pm 0.04$
31	6/3/11	6/7/11	5900	$0.97 \pm 0.04$
32	6/7/11	6/10/11	4415	$0.34 \pm 0.04$
33	6/10/11	6/14/11	5969	$0.73 \pm 0.04$
34	6/14/11	6/17/11	4469	$0.26 \pm 0.04$
35	6/17/11	6/21/11	5887	$0.29 \pm 0.03$
36	6/21/11	6/24/11	4492	$0.55 \pm 0.04$
37	6/24/11	6/28/11	5961	$0.34 \pm 0.03$
38	6/28/11	7/1/11	4451	$0.62 \pm 0.04$
Atmosphere and Ocean Research Institute (AORI), Kashiwa, Chiba Pref.				
39	3/23/11	3/25/11	1303	$17.08 \pm 0.10$

Table 5.1 Continued

Sample ID	Collection Time (m/d/y)		Air Volume (m <sup>3</sup> )	<sup>35</sup> SO <sub>4</sub> <sup>2-</sup> atoms/m <sup>3</sup> *(10 <sup>3</sup> )
	Starting Date	End Date		
40	3/25/11	3/28/11	2353	0.70 ± 0.04
41	3/28/11	3/30/11	1597	13.90 ± 0.11
42	3/30/11	4/1/11	1568	61.40 ± 0.20
43	4/1/11	4/3/11	1553	0.96 ± 0.05
44	4/3/11	4/5/11	1586	1.14 ± 0.05
45	4/5/11	4/7/11	1584	1.65 ± 0.13
46	4/7/11	4/9/11	1541	1.62 ± 0.14
47	4/9/11	4/11/11	1584	3.44 ± 0.15
48	4/11/11	4/13/13	1574	2.58 ± 0.15
49	4/13/11	4/15/11	1558	1.54 ± 0.14
50	4/15/11	4/17/11	1539	1.78 ± 0.15
51	4/17/11	4/19/11	1566	4.11 ± 0.17
52	4/19/11	4/21/11	1579	2.35 ± 0.15
Tokyo University of Agriculture and Technology, Fuchu, Tokyo				
53	3/24/11	3/26/11	2837	0.65 ± 0.03
54	3/26/11	3/28/11	2885	0.52 ± 0.03
55	3/28/11	3/30/11	2855	1.22 ± 0.04
56	3/30/11	4/1/11	2851	1.16 ± 0.03
57	4/1/11	4/3/11	2939	0.52 ± 0.03
58	4/3/11	4/5/11	2779	1.00 ± 0.08
59	4/5/11	4/7/11	2869	0.97 ± 0.08
60	4/7/11	4/9/11	2868	1.05 ± 0.08
61	4/9/11	4/11/11	2885	1.42 ± 0.08
62	4/11/11	4/13/11	2882	0.81 ± 0.08
63	4/13/11	4/15/11	2743	0.93 ± 0.08
64	4/15/11	4/17/11	2899	0.87 ± 0.07
65	4/20/11	4/22/11	2911	0.70 ± 0.07
66	4/22/11	4/24/11	2857	0.97 ± 0.10
67	4/24/11	4/26/11	2857	1.26 ± 0.10
68	4/26/11	4/28/11	2849	1.05 ± 0.10
69	4/28/11	5/1/11	2825	0.78 ± 0.09
National Institute of Environmental Studies (NIES), Tsukuba, Ibaraki Pref.				
70	3/24/11	3/29/11	7065	5.02 ± 0.03
71	3/29/11	4/1/11	4230	18.05 ± 0.14
72	4/1/11	4/4/11	4224	4.39 ± 0.08
73	4/4/11	4/7/11	4284	1.41 ± 0.06
74	4/7/11	4/11/11	5686	1.94 ± 0.05
Hokkaido Research Organization, Sapporo				
75	3/25/11	3/28/11	3953	1.26 ± 0.10
76	3/28/11	3/30/11	2933	1.20 ± 0.08
77	3/30/11	4/1/11	2933	0.96 ± 0.08
78	4/1/11	4/3/11	2918	0.78 ± 0.07
79	4/3/11	4/5/11	2919	0.76 ± 0.07
80	4/5/11	4/7/11	2857	0.95 ± 0.08
81	4/7/11	4/9/11	2919	1.08 ± 0.08
82	4/9/11	4/11/11	2923	1.05 ± 0.08
83	4/11/11	4/13/11	2922	0.96 ± 0.08

Table 5.1 Continued

Sample ID	Collection Date (m/d/y)		Air Volume (m <sup>3</sup> )	<sup>35</sup> SO <sub>4</sub> <sup>2-</sup> atoms/m <sup>3</sup> *(10 <sup>3</sup> )
	Starting Date	End Date		
84	4/13/11	4/15/11	2924	1.04 ± 0.07
85	4/15/11	4/17/11	2929	2.63 ± 0.10
86	4/17/11	4/19/11	2930	0.56 ± 0.07
87	4/19/11	4/21/11	2932	0.83 ± 0.10
88	4/21/11	4/23/11	2931	0.75 ± 0.10
89	4/23/11	4/25/11	2937	0.62 ± 0.09

Table 5.2

$^{35}\text{S}$  measurement in aerosol particles of different size fractions collected from Fukushima Prefecture, about 100 km from the Fukushima Nuclear Power Plant. Higher  $^{35}\text{S}$  activity is associated with fine sulfate particles, which are produced mainly from gas-phase oxidation of  $^{35}\text{SO}_2$ . Q1, Q2, Q3, Q4, Q5, Q6, Q7 represent aerosol size fraction of  $>10.2\ \mu\text{m}$ ,  $4.2\text{-}10.2\ \mu\text{m}$ ,  $2.1\text{-}4.2\ \mu\text{m}$ ,  $1.3\text{-}2.1\ \mu\text{m}$ ,  $0.69\text{-}1.3\ \mu\text{m}$ ,  $0.39\text{-}0.69\ \mu\text{m}$ , and  $<0.39\ \mu\text{m}$ , respectively.

Sample ID	Collection Date (m/d/y)		Air Volume ( $\text{m}^3$ )	$^{35}\text{SO}_4^{2-}$ atoms/ $\text{m}^3$ * ( $10^3$ )
	Start Date	End Date		
Cedar Forrest, Kawamata-cho, Fukushima prefecture				
0718 Q1	7/9/11	7/18/11	6616	$0.34 \pm 0.04$
0718 Q2				$0.65 \pm 0.05$
0718 Q3				$0.52 \pm 0.04$
0718 Q4				$1.41 \pm 0.06$
0718 Q5				$1.34 \pm 0.06$
0718 Q6				$30.41 \pm 0.18$
0718 Q7				$57.53 \pm 0.24$
0725 Q1	7/18/11	7/25/11	5783	$0.20 \pm 0.05$
0725 Q2				$0.15 \pm 0.05$
0725 Q3				$0.13 \pm 0.05$
0725 Q4				$0.56 \pm 0.06$
0725 Q5				$8.12 \pm 0.12$
0725 Q6				$10.31 \pm 0.14$
0725 Q7				$6.02 \pm 0.11$
0801 Q1	7/25/11	8/1/11	5746	$0.27 \pm 0.05$
0801 Q2				$0.43 \pm 0.05$
0801 Q3				$0.46 \pm 0.05$
0801 Q4				$2.06 \pm 0.08$
0801 Q5				$14.56 \pm 0.15$
0801 Q6				$17.97 \pm 0.17$
0801 Q7				$50.38 \pm 0.26$
0815 Q1	8/8/11	8/15/11	5870	$0.20 \pm 0.05$
0815 Q2				$0.48 \pm 0.05$
0815 Q3				$0.50 \pm 0.05$
0815 Q4				$4.55 \pm 0.10$
0815 Q5				$28.39 \pm 0.20$
0815 Q6				$56.0 \pm 0.27$
0815 Q7				$34.12 \pm 0.22$
0824 Q1	8/15/11	8/24/11	7444	$0.16 \pm 0.04$
0824 Q2				$0.19 \pm 0.04$
0824 Q3				$0.25 \pm 0.04$
0824 Q4				$1.64 \pm 0.06$
0824 Q5				$10.72 \pm 0.12$
0824 Q6				$0.52 \pm 0.05$
0824 Q7				$28.03 \pm 0.19$
0830 Q1	8/24/11	8/30/11	4975	$0.21 \pm 0.05$
0830 Q2				$0.18 \pm 0.05$
0830 Q3				$0.22 \pm 0.05$
0830 Q4				$1.60 \pm 0.08$

Table 5.2 Continued

Sample ID	Collection Date (m/d/y)		Air Volume (m <sup>3</sup> )	<sup>35</sup> SO <sub>4</sub> <sup>2-</sup> atoms/m <sup>3</sup> (10 <sup>3</sup> )
	Start Date	End Date		
0830 Q5				11.95 ± 0.15
0830 Q6				16.74 ± 0.17
0830 Q7				14.75 ± 0.16
0916 Q1	8/30/11	9/16/11	12,762	0.05 ± 0.02
0916 Q2				0.04 ± 0.02
0916 Q3				0.05 ± 0.02
0916 Q4				0.43 ± 0.03
0916 Q5				4.59 ± 0.06
0916 Q6				8.58 ± 0.08
0916 Q7				8.14 ± 0.07
School ground, Kawamata-cho, Fukushima prefecture				
0713 Q1	7/9/11	7/13/11	3105	0.63 ± 0.09
0713 Q2				0.48 ± 0.09
0713 Q3				0.77 ± 0.10
0713 Q4				3.96 ± 0.14
0713 Q5				7.24 ± 0.17
0713 Q6				20.74 ± 0.26
0713 Q7				62.32 ± 0.41
Agriculture field, Kawamata-cho, Fukushima prefecture				
0722 Q1	7/9/11	7/22/11	9909	0.12 ± 0.03
0722 Q2				0.15 ± 0.03
0722 Q3				0.21 ± 0.03
0722 Q4				0.68 ± 0.03
0722 Q5				16.52 ± 0.13
0722 Q6				1.14 ± 0.04
0722 Q7				50.64 ± 0.20
0819 Q1	8/17/11	8/19/11	1460	0.56 ± 0.16
0819 Q2				0.44 ± 0.16
0819 Q3				0.41 ± 0.16
0819 Q4				1.35 ± 0.18
0819 Q5				7.74 ± 0.27
0819 Q6				12.39 ± 0.31
0819 Q7				8.84 ± 0.28
0908 Q1	8/27/11	9/8/11	8640	0.56 ± 0.17
0908 Q2				0.50 ± 0.17
0908 Q3				0.49 ± 0.18
0908 Q4				1.21 ± 0.20
0908 Q5				17.02 ± 0.38
0908 Q6				1.17 ± 0.19
0908 Q7				99.98 ± 0.77

Table 5.3

$^{35}\text{S}$  measured in rain water samples collected in Tokyo and Fukushima during March-May 2011 shows that  $^{35}\text{S}$ /liter of rain water was 10 times higher than that in background rain water, as observed in La Jolla, California rain.

Rain Samples	Sampling Date	Average Rainfall Rate (mm/h)	$^{35}\text{SO}_4^{2-}$ (atoms/liter)	$C_a$ (atoms/m <sup>3</sup> ) <sup>b</sup>	$K$ (s <sup>-1</sup> ) <sup>a</sup>
Tokyo Tech #1	3/24/11	1.4	$9.8 \times 10^5$		
#2	4/25/11	2	$2.1 \times 10^5$	770	$7.6 \times 10^{-3}$
#3	5/11/11	2	$1.9 \times 10^5$	616	$8.7 \times 10^{-3}$
#4	5/13/11	2.6	$1.1 \times 10^5$	616	$6.5 \times 10^{-3}$
#5	5/24/11	1.7	$2.2 \times 10^5$	344	$1.5 \times 10^{-2}$
Fukushima stream water <sup>c</sup>	4/28/11		$1.2 \times 10^5$		
La Jolla rain	1/26/10		$6.2 \times 10^4$		

<sup>a</sup>The rain-scavenging coefficient ( $k$ ) was calculated based on the  $^{35}\text{SO}_4^{2-}$  concentration measured in rainwater and air.

<sup>b</sup>The concentration of  $^{35}\text{SO}_4^{2-}$  in air collected at Tokyo Tech, Yokohama.

<sup>c</sup>Water sample collected from a stream situated in Fukushima prefecture, 50 km away from Fukushima nuclear power plant.

## 5.7 References

Andronache, C. (2004), Estimates of sulfate aerosol wet scavenging coefficient for locations in the Eastern United States, *Atmospheric Environment*, 38(6), 795-804.

Brothers, L. A., G. Dominguez, A. Abramian, A. Corbin, B. Bluen, and M. H. Thiemens (2010), Optimized low-level liquid scintillation spectroscopy of  $^{35}\text{S}$  for atmospheric and biogeochemical chemistry applications, *Proceedings of the National Academy of Sciences*, 107(12), 5311-5316.

Brumfiel, G. (2011a), The meltdown that wasn't, *Nature*, 471, (<http://www.nature.com/news/2001/110322/full/471417a.html>), 417-418.

Brumfiel, G. (2011b), Fukushima's reactor cores still too hot to open, *Nature*, (<http://www.nature.com/news/2011/110907/full/news.2011.525.html>).

Chate, D., P. Murugavel, K. Ali, S. Tiwari, and G. Beig (2011), Below-cloud rain scavenging of atmospheric aerosols for aerosol deposition models, *Atmospheric Research*, 99(3), 528-536.

Chino, M., H. Nakayama, H. Nagai, H. Terada, G. Katata, and H. Yamazawa (2011), Preliminary estimation of release amounts of  $^{131}\text{I}$  and  $^{137}\text{Cs}$  accidentally discharged from the Fukushima Daiichi nuclear power plant into the atmosphere, *Journal of nuclear science and technology*, 48(7), 1129-1134.

Cho, H.-M., Y.-L. Hong, and G. Kim (2011), Atmospheric depositional fluxes of cosmogenic  $^{35}\text{S}$  and  $^7\text{Be}$ : Implications for the turnover rate of sulfur through the biosphere, *Atmospheric Environment*, 45(25), 4230-4234.

Draxler, R. R., and G. D. Rolph (2011), HYSPLIT (Hybrid Single-Particle Lagrangian Integrated Trajectory) Model access via NOAA ARL READY Website (<http://ready.arl.noaa.gov/HYSPLIT.php>). NOAA Air Resources Laboratory, Silver Spring, MD.

Dyrssen, D., and P. Nyman (1955), Slow-neutron-induced radioactivity of sea-water, *Acta Radiologica [Old Series]*, 43(5), 421-427.

Laakso, L., T. Grönholm, Ü. Rannik, M. Kosmale, V. Fiedler, H. Vehkamäki, and M. Kulmala (2003), Ultrafine particle scavenging coefficients calculated from 6 years field measurements, *Atmospheric Environment*, 37(25), 3605-3613.

Lal, D., and B. Peters (1967), Cosmic ray produced radioactivity on the earth, *Handb. Phys.*(46), 551-612.

Love, D. L., and D. Sam (1962), Radiochemical Determination of Sodium-24 and Sulfur-35 in Seawater, *Analytical chemistry*, 34(3), 336-340.

Maria, S. F., and L. M. Russell (2005), Organic and Inorganic Aerosol Below-Cloud Scavenging by Suburban New Jersey Precipitation, *Environmental Science & Technology*, 39(13), 4793-4800.

Mittermaier, M. P., and A. J. Illingworth (2003), Comparison of model-derived and radar-observed freezing-level heights: Implications for vertical reflectivity profile-correction schemes, *Quarterly Journal of the Royal Meteorological Society*, 129(587), 83-95.

Morino, Y., T. Ohara, and M. Nishizawa (2011), Atmospheric behavior, deposition, and budget of radioactive materials from the Fukushima Daiichi nuclear power plant in March 2011, *Geophysical Research Letters*, 38(7).

Okita, T., H. Hara, and N. Fukuzaki (1996), Measurements of atmospheric SO<sub>2</sub> and SO<sub>4</sub><sup>2-</sup>, and determination of the wet scavenging coefficient of sulfate aerosols for the winter monsoon season over the Sea of Japan, *Atmospheric Environment*, 30(22), 3733-3739.

Priyadarshi, A., G. Dominguez, and M. H. Thiemens (2011a), Evidence of neutron leakage at the Fukushima nuclear plant from measurements of radioactive <sup>35</sup>S in California, *Proceedings of the National Academy of Sciences*, 108(35), 14422-14425.

Priyadarshi, A., G. Dominguez, J. Savarino, and M. Thiemens (2011b), Cosmogenic <sup>35</sup>S: A unique tracer to Antarctic atmospheric chemistry and the polar vortex, *Geophysical Research Letters*, 38(13), L13808.

Priyadarshi, A., J. Hill-Falkenthal, E. Coupal, G. Dominguez, and M. H. Thiemens (2012), Measurements of <sup>35</sup>S in the marine boundary layer at La Jolla, California: A new technique for tracing air mass mixing during Santa Ana events, *Journal of Geophysical Research: Atmospheres* (1984–2012), 117(D8).

Schumann, T. (1989), Large discrepancies between theoretical and field-determined scavenging coefficients, *Journal of aerosol science*, 20(8), 1159-1162.

Scott, B. (1982), Theoretical estimates of the scavenging coefficient for soluble aerosol particles as a function of precipitation type, rate and altitude, *Atmospheric Environment* (1967), 16(7), 1753-1762.

Sportisse, B. (2007), A review of parameterizations for modelling dry deposition and scavenging of radionuclides, *Atmospheric Environment*, 41(13), 2683-2698.

Tanaka, N., and K. Turekian (1991), Use of cosmogenic <sup>35</sup>S to determine the rates of removal of atmospheric SO<sub>2</sub>.

Turekian, K. K., and N. Tanaka (1992), The use of atmospheric cosmogenic <sup>35</sup>S and <sup>7</sup>Be in determining depositional fluxes of SO<sub>2</sub>, *Geophysical Research Letters*, 19(17), 1767-1770.



Zhang, C., Y. Wang, A. Lauer, K. Hamilton, and F. Xie (2012), Cloud base and top heights in the Hawaiian region determined with satellite and ground-based measurements, *Geophysical Research Letters*, 39(15).

## Chapter 6

### Future Applications to Heterogeneous Chemistry

#### 6.1 Abstract

Throughout this thesis,  $^{35}\text{S}$  and  $\Delta^{17}\text{O}$  have been used as tracers for the atmospheric sulfur cycle, providing detailed information regarding the lifetimes and formation pathways of sulfate aerosols. In the laboratory,  $\Delta^{17}\text{O}$  has prevalently been used to constrain the mechanisms of individual reactions responsible for sulfate formation and the application of this knowledge has led to further understanding of chemistry in the present atmosphere. However, application of  $^{35}\text{S}$  has yet to be fully taken advantage of in the laboratory setting. Here, we preliminarily assess the feasibility of applying  $^{35}\text{S}$  to the study of heterogeneous chemical reactions of  $\text{SO}_2$  through the use of a chemical flow tube. Initial experiments calculating the uptake rate of  $^{35}\text{SO}_2$  on magnesium oxide dust produced values significantly lower than previously published data. Uptake ratios on the order of  $10^{-5}$  and  $10^{-7}$  with large variability were produced, whereas previous literature values suggest uptake ratios on the order of  $10^{-3}$  and  $10^{-4}$ . Although significant developmental work needs to be done to improve on the experimental methodology, these studies suggest that  $^{35}\text{S}$  can become a viable tracer for heterogeneous reaction chemistry with a significantly refined flow chamber. The work does show  $^{35}\text{S}$  measurement via the liquid scintillation technique has a special ability to obtain measurements on significantly low concentration scales which can become an important attribute when attempting to measure reaction kinetics on surfaces of extremely low reactivity.

#### 6.2 Introduction

Mineral dust is an important component of particulate matter (PM) with an estimated annual contribution of 1000-3000 teragrams to the atmosphere [Li *et al.*, 2006]. These particles represent between 1/3 and 1/2 of the total annual primary aerosol emissions by mass [Penner, 2001]. With lifetimes up to several weeks, trans-continental transport of dust particles can occur in the free troposphere where cloud removal processes are weak and transport swift [Husar, 2004]. As dust ages in the atmosphere, its composition is modified through interaction with trace gases, such as  $\text{SO}_2$  and  $\text{NO}_x$ , via adsorption processes and heterogeneous reactions [Adams *et al.*, 2005]. These heterogeneous surface reactions can have a strong

influence on the physical and chemical properties of a particle. This includes light absorption and reflection properties as well as a particle's ability to participate in cloud formation as a CCN particle. Thus, surface chemistry in the atmosphere has the potential to influence future weather patterns and climate.

SO<sub>2</sub> is released to the troposphere via fossil fuel combustion, volcanic emissions, and oxidation of reduced sulfur species predominately from biogenic sources. Modeling studies suggest that mineral aerosols have a significant impact on the chemistry of SO<sub>2</sub> in the troposphere [Song and Carmichael, 1999]. Recent field studies have observed anti-correlations between the concentrations of SO<sub>2</sub> and mineral dust, suggesting that SO<sub>2</sub> binds to mineral dust either through physical adsorption or heterogeneous chemical reaction [Adams *et al.*, 2005; Andreae *et al.*, 2003; Hanke *et al.*, 2003; Tang *et al.*, 2004]. Laboratory studies have shown subsequent oxidation of SO<sub>2</sub> to sulfate once taken up by these particles [Judeikis *et al.*, 1978; Mamane and Gottlieb, 1989] and it is estimated that nearly half of all global SO<sub>2</sub> emissions are converted to particulate sulfate [Adams *et al.*, 2005]. It is well known that SO<sub>2</sub> can be oxidized to sulfate in aqueous layers of aerosols via ozone or hydrogen peroxide and through gas phase oxidation by OH. However, there is limited knowledge about the heterogeneous oxidation processes of SO<sub>2</sub> on dust surfaces and the mechanisms are not completely understood [Dentener *et al.*, 1996; Luria and Sievering, 1991; Usher *et al.*, 2002]. Improved understanding of trace gas uptake and surface oxidation are necessary to improve the constraints for the radiative forcing on mineral dust in the atmosphere.

Measurement techniques, including Knudsen cells [Gebel *et al.*, 2000; Goodman *et al.*, 2001; Usher *et al.*, 2002], Diffuse Reflectance Infrared Fourier Transform Spectroscopy (DRIFTS) [Li *et al.*, 2006; Li *et al.*, 2007; Zhang *et al.*, 2006], and flow tubes coupled to mass spectrometers [Adams *et al.*, 2005] have been used to study SO<sub>2</sub> uptake onto particles. Initial uptake coefficients ( $\gamma_0$ ) for SO<sub>2</sub> span a range of values from 0.1 for uptake on calcium carbonate [Santschi and Rossi, 2006] to less than  $1 \times 10^{-7}$  for uptake onto silicon dioxide [Usher *et al.*, 2002]. Many discrepancies remain in the literature about the true uptake coefficients of SO<sub>2</sub> for various dust particles. For example, the measured initial uptake coefficient on calcium carbonate varies by more than three orders of magnitude, from 0.1 [Santschi and Rossi, 2006] to  $(1.4 \pm 0.7) \times 10^{-4}$  [Usher *et al.*, 2002]. For a comprehensive listing of experimentally measured uptake coefficients for SO<sub>2</sub> gas with mineral dusts, refer to Crowley *et al.*, (2010). Table 6.1 shows a list of several

calculated uptake ratios, including MgO, Al<sub>2</sub>O<sub>3</sub>, CaCO<sub>3</sub>, and SiO<sub>2</sub>. Here, we investigate the feasibility of a new flow tube methodology utilizing the uptake of SO<sub>2</sub> onto mineral dust employing the use of radioactive <sup>35</sup>Sulfur (<sup>35</sup>S) as a tracer for SO<sub>2</sub> to further elucidate the values of laboratory measured uptake coefficients. The use of radiogenic sulfur has never been attempted in a flow tube. These experiments are intended as a preliminary examination of its potential. Previously, <sup>35</sup>S has been used as a sensitive tracer to study sulfate formation pathways, atmospheric circulation patterns, and the variation in atmospheric oxidation lifetimes of SO<sub>2</sub> [Brothers *et al.*, 2010; Priyadarshi *et al.*, 2012; Tanaka and Turekian, 1991]. <sup>35</sup>S offers increased measurement sensitivity over concentration measurements, reducing sample requirements relative to most other measurement techniques. This increased sensitivity may allow the ability to improve on the inherent uncertainties in uptake coefficient data that exists in the current literature.

## 6.3 Experimental

### 6.3.1 Flow Tube Apparatus

Initial experiments were carried out in a flow tube (Figure 6.1) consisting of a horizontally mounted Pyrex glass tube 100 cm in length with a 2.5 cm inner diameter. The walls of the flow tube were coated with halocarbon wax (Series 1500 Inert Wax, Halocarbon Products Corporation) to minimize the adsorption of reactive gases onto the walls of the tube. The flow rate is controlled under laminar flow conditions with a Tylan 260 series mass flow controller using ultra-high purity helium as the carrier gas set at a bulk flow rate of 1500 sccm. The linear flow velocity (LFV) was adjusted by varying the overall pressure inside the tube according to the following equation:

$$\text{LFV (cm/sec)} = F/Ap \quad (6.1)$$

where F is the flow rate (cm<sup>3</sup>/sec) obtained from the mass flow controller, A is the cross sectional area (cm<sup>2</sup>) of the tube ( $\pi r^2$ ), and p, the pressure (torr) inside the tube relative to atmosphere ( $\frac{x}{760 \text{ torr}}$ ) [Yasuda, 1985]. An aliquot of SO<sub>2</sub> is introduced perpendicular to the helium flow from an attached bulb. The perpendicular design improves mixing upon interaction with the carrier gas. The mixing time required for SO<sub>2</sub> with the He carrier flow is given by:

$$\tau_{\text{mix}} = a^2/5D \quad (6.2)$$

where  $a$  is the radius (cm) of the tube and  $D$  is the diffusion coefficient ( $\text{cm}^2/\text{sec}$ ) of the mixing gas defined as:

$$D = D_0 \left(\frac{T}{T_0}\right)^{1.81} \left(\frac{P_0}{P}\right) \quad (6.3)$$

$D_0$ , 0.11  $\text{cm}^2/\text{sec}$  for  $\text{SO}_2$ , is the diffusion coefficient at standard temperature and pressure ( $T_0 = 273\text{K}$  and  $P_0 = 760$  torr). At atmospheric pressure and room temperature (298 K), the mixing time for  $\text{SO}_2$  is 2.42 seconds. For a pressure of 50 torr, the mixing time decreases to 0.16 sec. The distance travelled before reaching diffusive equilibrium, ( $L_{\text{mix}}$ ), is also dependent on the linear flow velocity:

$$L_{\text{mix}} = \tau_{\text{mix}} * \text{LFV} \quad (6.4)$$

$\text{SO}_2$  reached diffusive equilibrium with the helium carrier gas in 12.3 cm, well before interacting with the mineral dust set about 80 cm axially down the flow tube.

### 6.3.2 Determination of Uptake Coefficients

The uptake coefficient (unitless) is calculated from:

$$\gamma = \frac{4kV}{\omega S} \quad (6.5)$$

where  $k$  ( $\text{sec}^{-1}$ ) is the measured first order rate coefficient for the loss of  $\text{SO}_2$  on the mineral dust,  $V$  ( $\text{cm}^3$ ) is the volume of the flow tube,  $\omega$  ( $\text{cm}/\text{sec}$ ) is the average molecular velocity of  $\text{SO}_2$  and  $S$  ( $\text{cm}^2$ ) is the surface area of the mineral dust. The average molecular velocity of  $\text{SO}_2$  at room temperature is determined to be  $3.13 \times 10^4$   $\text{cm}/\text{sec}$ , where:

$$\omega = \frac{\sqrt{8RT}}{\pi M} \quad (6.6)$$

and  $R$  is the gas constant,  $T$  is 298K, and  $M$  is the molar mass of  $\text{SO}_2$ . Brunauer-Emmett-Teller (BET) surface area ( $\text{m}^2/\text{g}$ ) measurements were determined using a Micromeritics ASAP 2020 Adsorption Analyzer. Initial investigations were undertaken using reagent grade magnesium oxide purchased from

Fisher Scientific with a BET surface area of  $23.96 \pm 0.21 \text{ m}^2/\text{g}$ . The pseudo first-order rate constant ( $k$ ) for the loss of  $\text{SO}_2$  onto the mineral dust was calculated according to:

$$[C]_2 = [C]_1 * e^{\frac{-k\Delta z}{v}} \quad (6.7)$$

where  $[C]_2$  is the amount of gas adsorbed onto the dust particle,  $[C]_1$  is the initial amount of gas injected,  $z$  is the length of salt coverage in the flow tube, and  $v$  is the linear velocity (cm/sec) of the reactant gas. In these experiments,  $z$  is equal to 5 cm. Therefore,  $\frac{z}{v}$  represents the gas-surface reaction time.

### 6.3.3 Radioactivity Measurements

The uptake of radioactive  $^{35}\text{S}$  is measured by transferring the mineral dust from the vessel after each experiment to a solution of hydrogen peroxide to convert all  $^{35}\text{S}$  species to sulfuric acid. This solution is then transferred to a scintillation vial and 10 mL of scintillation cocktail is added before measurement in the Wallac 1220 Quantulus Ultra Low Level Liquid Scintillation Spectrometer. Multiple tests were run to determine the measurement blanks for  $\text{H}_2\text{O}_2$  and mineral dust solutions (Table 6.2) and whether a shielding effect was present limiting the counting efficiency of  $^{35}\text{S}$  in the presence of either substance. As observed in Table 6.3, there is no shielding issue related to the chemical protocol. Multiple blank runs using unreacted magnesium oxide followed by the complete chemical procedure showed consistent blanks of  $1.243 \pm 0.054$  CPM which were subtracted from the final measurement values to obtain the amount of  $\text{SO}_2$  taken up by the dust sample.

### 6.3.4 Formation and Calibration of $^{35}\text{SO}_2$ Bulb

Radioactive  $\text{H}_2^{35}\text{SO}_4$  purchased from Perkin Elmer was converted to  $^{35}\text{SO}_2$  for use in the flow experiments. Spiked  $^{35}\text{S}$  sulfuric acid was added to commercially purchased concentrated sulfuric acid to reach the desired radioactivity and concentration level. This  $\text{H}_2\text{SO}_4$  sample was then converted to  $\text{Ag}_2\text{SO}_4$  by reaction with  $\text{Ag}_2\text{O}$  and pyrolyzed at  $1030^\circ\text{C}$  following the technique described by *Savarino et al.*, (2001).  $\text{SO}_2$  was collected in liquid nitrogen and separated from other condensable gases via gas chromatography before transferring to a 3 L bulb with a  $1.6 \text{ cm}^3$  aliquot. The activity released per aliquot

sample (Table 6.4) was standardized by reaction with  $\text{H}_2\text{O}_2$  followed by measurement in the scintillation counter using the conditions described in *Brothers et al.* (2010). Each aliquot contained about  $10^{12}$  molecules of  $\text{SO}_2$  with an activity level of  $60.569 \pm 0.517$  counts per minute  $^{35}\text{S}$  relative to 10/3/13 11:33 am.

## 6.4 Results and Discussion

Figure 6.2 displays the initial results obtained from direct measurements of radioactivity adsorbed onto magnesium oxide at a linear velocity of 81 cm/sec. From replicate experiments, the uptake coefficient is determined to be  $(9.78 \pm 6.82) * 10^{-6}$ . Published values for the uptake of  $\text{SO}_2$  onto magnesium oxide are scarce, yet range between  $10^{-3}$  and  $10^{-4}$  (Table 6.1). The results from this study produce uptake coefficients orders of magnitude lower than previously published values. A large relative error upwards of 70% was obtained using the  $^{35}\text{S}$  tracer method at a linear velocity of 81 cm/sec. Previous measurement techniques have associated errors around 10% [*Goodman et al.*, 2001; *Usher et al.*, 2002]. The larger scatter seen in the  $^{35}\text{S}$  tracer method is a concern and can potentially be linked to the flow tube design. The measurement of  $\text{SO}_2$  uptake works in principle, however, this error must be decreased if the  $^{35}\text{S}$  radioactive tracer method is to become a viable measurement tool in the scientific community. We discuss some of the problems associated with the initial  $^{35}\text{S}$  tracer method and how to address the issues in a full scale arrangement.

Additional experiments were conducted to test whether the flow velocity of the carrier gas had an influence in the large variation. Multiple experiments were undertaken at various linear velocities including 13, 18, 24, 48, and 290 cm/sec. Results are listed as the calculated average with a one sigma standard deviation in Table 6.5 and show similar results to those determined at a linear velocity of 81 cm/sec. Calculated uptake ratios are still well below published values ranging from as low as  $(8.06 \pm 4.22) * 10^{-7}$  to as high as  $(2.67 \pm 1.97) * 10^{-5}$  with relative errors up to 74%. Adjusting the linear flow rate did not result in an improvement in the accuracy or precision of the measurements.

The heterogeneous uptake of  $\text{SO}_2$  is partially reversible. Desorption of  $\text{SO}_2$  can result during the experimental run and while transferring the dust sample from the flow tube to the hydrogen peroxide solution. This process will amplify the low uptake ratios produced in this study or potentially explain them.

The allocation of SO<sub>2</sub> loss is not measureable in our current experimental set-up, however, an in-situ measurement technique can constitute the magnitude of these desorption processes by measuring the SO<sub>2</sub> release after the reactant gas flow is stopped. For example, *Adams et al.*, (2005) assessed the loss of SO<sub>2</sub> from Saharan dust by measuring the desorption peak once surface exposure with SO<sub>2</sub> was completed using a flow system coupled to a mass spectrometer. Results showed a relatively quick desorption peak, on the time scale of a few seconds, with the majority of SO<sub>2</sub> remaining adsorbed onto the dust particles. Calculations show at least 86% of SO<sub>2</sub> was irreversibly bound, suggesting that chemisorption was the main adsorption process involved in the uptake of SO<sub>2</sub>. Physical adsorption is reversible and arises from weak bond interaction characterized by Van der Waals forces and a heat of adsorption generally below 5 kcal/mole. Chemisorption, however, is often irreversible and involves stronger binding with the formation of new chemical bonds at the adsorbent surface and a heat of adsorption typically between 10-100 kcal/mole [*Finlayson-Pitts and Pitts*, 1986]. Similar results were obtained by *Goodman et al.*, (2001) using FTIR spectroscopy, which observed the absorption/desorption behavior of SO<sub>2</sub> in the absence of water with aluminum oxide and magnesium oxide and concluded that only 10% of the absorbed SO<sub>2</sub> was lost when the sample vessel was evacuated.

It should be noted that the composition of Saharan dust is not equivalent to the dust sample used in this experiment. Significant components of Saharan dust consist of oxides of silicon, aluminum, calcium, and iron with only small amounts of magnesium [*Adams et al.*, 2005; *Usher et al.*, 2002]. The nature of chemisorption can vary substantially depending on the chemical nature of the reactant gas and the surface structure/composition of the dust. Therefore, the desorption processes measured by *Goodman et al.*, (2001) are a better representation of the current experiment. Thus, desorption only accounts for about a 10% loss and cannot account for discrepancies between published uptake ratios and those obtained in this study. Future measurement of this desorption using an in-situ measurement technique can reduce some of the variation seen in replicate trials, however, other processes must be associated with the variability in the measurement process.

An additional sample collection method was attempted where the unreacted sample gas was collected after passage through the flow tube using a LN<sub>2</sub> trap in hopes of improving the reproducibility of



the measurement. Trapped SO<sub>2</sub> gas is then transferred to a hydrogen peroxide solution attached after the LN<sub>2</sub> collection trap (Figure 6.1) to convert to sulfate. Sampling time periods were longer than the contact time between SO<sub>2</sub> and the salt sample to allow adequate time for the reactant gas to completely pass through the flow tube. Therefore, in theory, the desorbed SO<sub>2</sub> species caused by weak physical adsorption are collected in the LN<sub>2</sub> trap along with reactant gas that passed over the salt without attachment. One potential remedy to avoid this desorption artifact is the use of a constant stream of radioactive SO<sub>2</sub> from a tank cylinder instead of the use of an aliquot bulb. A valved control between the flow tube and collection trap can be closed at a desired run time and a back calculation made to determine the concentration of gas through the tube. This calculation implies that the SO<sub>2</sub> flow instantly attains the desired flow rate. However, the system needs adequate time to establish a constant flow, thus, corrections must be made to avoid overestimation of the SO<sub>2</sub> concentration released during the experiment. Blank experiments to assess the timescales and concentrations of SO<sub>2</sub> released before an equilibrated stream is attained must be applied.

Efforts to use the LN<sub>2</sub> trap to collect trace amounts of <sup>35</sup>SO<sub>2</sub> in the helium flow could never be obtained with a high efficiency. Large variations in the amount of <sup>35</sup>SO<sub>2</sub> collected were seen in control runs ranging from about 5-63% collection efficiency. The lack of collection efficiency was unexpected as cryogenic trapping is a standard method of sample collection in gas systems. Due to the high pumping speeds, it is possible that the short contact time between the LN<sub>2</sub> collection trap and the helium flow was not adequate to allow the helium gas to sufficiently cool to a temperature where SO<sub>2</sub> would freeze out. In an effort to mediate this problem, the carrier gas was switched to nitrogen, thermal conductivity of 26.0 mW/mK at 300K relative to 156.7 mW/mK for helium [Lide, 2004], in hopes of improving the trapping of SO<sub>2</sub>. No improvement in the collection efficiency was observed upon adjustment of the carrier gas.

Increased contact times should allow the carrier gas to reach a sufficient temperature to trap SO<sub>2</sub>. Multiple traps were connected in succession to increase the cryogenic contact time, however, the efficiency of SO<sub>2</sub> collection was not improved. To test the cryogenic method, SO<sub>2</sub> samples ranging from 10-200 μmol were pumped through the system. The samples were recollected and measured on a calibrated pressure gauge to obtain a trapping yield. Yields ranged from 95-99% collection efficiency proving the cryogenic trapping system works. The lack of collection efficiency in the experimental samples is likely related to the

small sample sizes. Assuming wall adsorption is the primary loss mechanism during the collection process, a 95-99% efficiency on the  $\mu\text{mol}$  scale would result in a loss of about  $10^{15}$  molecules.  $\text{SO}_2$  concentrations during experimental runs approached  $10^{12}$  total molecules. At these concentrations, any wall loss close to  $10^{12}$  molecules would lower the yield. The low concentrations used in these experiments likely make cryogenic trapping difficult due to losses on the walls of the traps.

Future studies that can apply more realistic salt introduction techniques, such as usage of aerosol particles, would better mimic atmospheric conditions than the use of bulk salt surfaces. Dry powdered salts applied onto a flow tube do not give a true representation of atmospheric conditions. Previous experiments measuring the uptake ratio of  $\text{SO}_2$  onto magnesium oxide all used bulk salt surfaces and applied a BET surface area calculation [Adams *et al.*, 2005; Goodman *et al.*, 2001; Usher *et al.*, 2002]. Since these studies were used for comparison purposes, it was deemed suitable to follow a similar salt application method. The BET surface area represents an upper limit for the surface area of the dust particles by including internal pore volume into the total surface area. Some of these internal pores are likely inaccessible for the reactant gas due to the short contact times used in this experiment. The surface area available to a trace gas will be dependent on its desorption lifetime, which limits the rate of diffusion into the interstitial space of a porous sample [Crowley *et al.*, 2010]. A better representation of atmospheric particles can be generated through the use of a constant output atomizer as employed by Bertram and Thornton, (2009) and Thornton *et al.*, (2003). These methods have the advantage of system alteration to a desired humidity by mixing the aerosol particles with a helium or nitrogen flow of a specific humidity before entrance to the flow tube. The particle size distribution of the aerosols can be controlled through the use of a differential mobility analyzer, negating the need to measure the sample via the Brunauer-Emmett-Teller method. These techniques can lead to a more refined apparatus that better approximates atmospheric conditions and should improve the reproducibility of the experiments.

The use of radioactive tracers to study heterogeneous reactions in flow systems is not unprecedented and has shown success. Studies of nitric acid uptake onto mineral dust has been achieved using  $^{13}\text{N}$ -labeled  $\text{HNO}_3$  (half-life of 9.97 minutes) in a flow tube coupled to a gamma detector [Vlasenko *et al.*, 2009; Vlasenko *et al.*, 2006]. Each  $^{35}\text{S}$  sample is measured for multiple 2 hour cycles as the 87.2 day

half-life of  $^{35}\text{S}$  requires longer measurement periods to obtain adequate counts. No instrument can be coupled directly to a flow system to measure  $^{35}\text{S}$  decay in-situ as the only method to accurately measure low-level beta decay is through the use of liquid scintillation techniques. A possible flaw of the  $^{35}\text{S}$  radioactive tracer method is the lack of an in-situ measurement technique to examine heterogeneous reactions. Techniques such as flow systems coupled to mass spectrometers, FTIR, and DRIFTS are likely the best techniques to study  $\text{SO}_2$  heterogeneous chemistry. Using the DRIFTS measurement technique, *Li et al.*, (2006) studied the mechanistic steps involved in the adsorption of  $\text{SO}_2$  onto calcium carbonate in the presence of ozone by differentiating between the concentrations of  $\text{SO}_2$ ,  $\text{SO}_3^{2-}$ , and  $\text{SO}_4^{2-}$  on the surface particles as a function of time. This type of analysis is difficult to obtain without in-situ measurements.

The main advantage radioactive measurements have over traditional flow tube instrumentation is the unrivaled detection limits. Assuming a limit of detection and quantification of  $\pm 3\sigma$  and  $\pm 10\sigma$ , respectively, above blank measurement uncertainties, the sample concentration of  $^{35}\text{SO}_2$  necessary to detect discernable signals is on the range of  $10^6$ - $10^7$  molecules. As an example, *Vlasenko et al.*, (2009) required only a flow of  $10^5$  molecules/ $\text{cm}^3$  of  $\text{H}^{13}\text{NO}_3$  to obtain reliable results using an in-situ gamma radiation detector. A low detection limit will become an important attribute when studying dust of low reactivity. For example, studies attempting to measure the uptake of  $\text{SO}_2$  and  $\text{HNO}_3$  onto  $\text{SiO}_2$  have shown that adsorption is extremely low. *Usher et al.* (2002) could not determine a measurement peak for the adsorption of  $\text{SO}_2$  onto  $\text{SiO}_2$  and estimated that the reaction could not have an uptake ratio above  $10^{-7}$ . *Zhang et al.*, (2006) determined the reactivity of  $\text{SO}_2$  was slowest for  $\text{SiO}_2$  relative to  $\text{Fe}_2\text{O}_3$ ,  $\text{MgO}$ ,  $\text{TiO}_2$ , and  $\text{Al}_2\text{O}_3$ . Although not explicitly stated in the paper, estimation of the uptake ratio from the given data results in a value  $\approx 1 \times 10^{-8}$ . Future experimental development should improve consistency with previously published results and allow  $^{35}\text{S}$  to become a viable tracer for less reactive dusts such as silicates.

Experiments were undertaken to determine the feasibility of using  $^{35}\text{S}$  to measure adsorption onto  $\text{SiO}_2$ . At present, large uncertainties in the count rates exist, however, showed similar counts to those on magnesium oxide were observed. Although not measured in this study, previous publications show that the BET surface area is about a magnitude greater than that of  $\text{MgO}$  [*Usher et al.*, 2002; *Zhang et al.*, 2006] suggesting that the uptake ratio onto  $\text{SiO}_2$  calculated from the current method is on the order of  $10^{-7}$  to  $10^{-8}$ .

These measurements are a proof of principles as to whether adsorption onto  $\text{SiO}_2$  is detectable via  $^{35}\text{S}$  and suggest that with future improvements, the  $^{35}\text{S}$  tracer method can potentially be used to measure slow  $\text{SO}_2$  heterogeneous reactions.

The use of  $^{35}\text{S}$  as a tracer for heterogeneous reactions can also be explored through the use of large environmental reaction chambers. As with flow studies, the uptake ratio can be determined through equation 6.5. The advantage of environmental chambers is the large increase in volume relative to a flow tube experiment which significantly reduces the collision rate resulting in a longer reaction time. In addition, a chamber study can better simulate atmospheric conditions relative to a flow tube. With a sufficiently large vessel where reactant lifetimes are on the order of hours, measurement of adsorbed  $\text{SO}_2$  at different time intervals (several minutes) can be used to calculate observed uptake ratios as a function of time. In addition, the longer lifetimes in the environmental chamber allows  $^{35}\text{S}$  to measure the reaction as it proceeds, and can be used as a comparison to in-situ measurements. This is limited while using a flow tube due to the short contact times associated with the measurements.

## 6.5 Conclusions

Initial tests were run to assess the feasibility of applying  $^{35}\text{S}$  activity measurements to quantify heterogeneous reaction chemistry. Reproducibility was restrictive, and uptake rate measurements differ from published data. Nevertheless, future improvements in methodology will improve reproducibility and accuracy. The low sample concentrations needed to detect  $^{35}\text{S}$  relative to other detector instrumentation is one of the key advantages that permits future research into a fully developed system using  $^{35}\text{S}$  as a tracer for heterogeneous chemistry. This gives  $^{35}\text{S}$  the potential ability to measure slower reactions which can be difficult to distinguish on other measurement systems. The lack of ability to couple an in-situ measurement device to detect the low level beta decays of  $^{35}\text{S}$  is a limitation as it is not possible to probe additional information about the reaction other than kinetics. However, by applying the  $^{35}\text{S}$  application to environmental chamber studies, it is feasible to reduce the reaction speed enough to measure how a reaction proceeds with time, thus providing measurements similar to those of in-situ instrumentation.

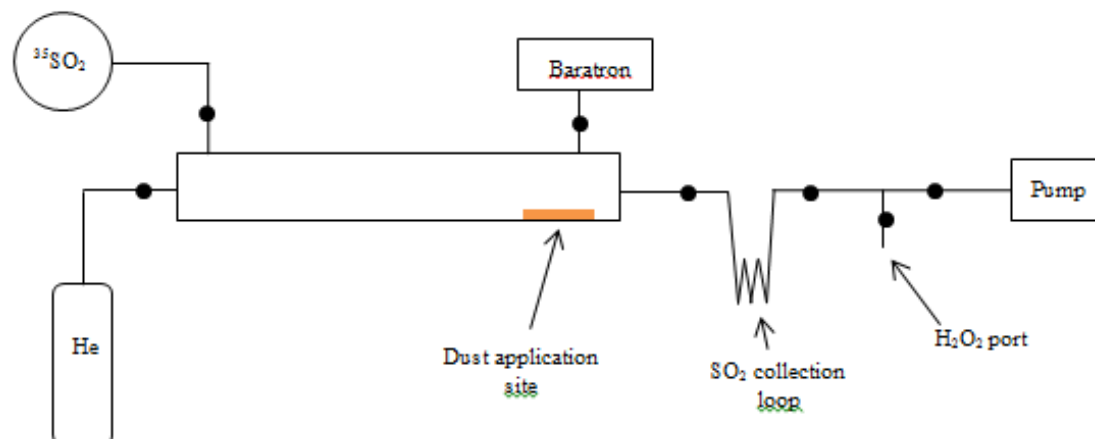


Figure 6.1

Schematic depiction of experimental set-up where the dark circles represent gate and toggle valves. The collection loop and H<sub>2</sub>O<sub>2</sub> port can be added to the system if one wants to collect the unreacted SO<sub>2</sub> for measurement instead of measuring the direct adsorption on the salt particles.

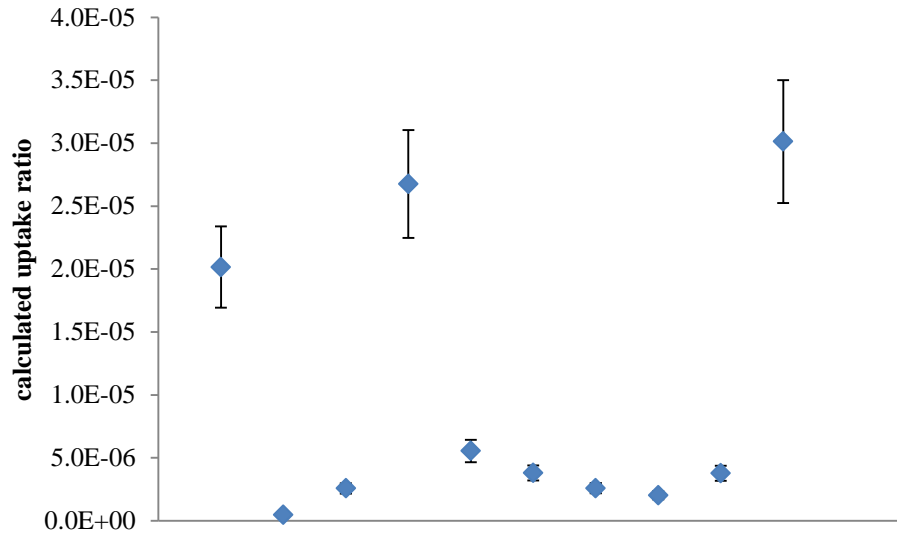


Figure 6.2

Calculated uptake ratios for individual trials at a linear flow velocity of 81 cm/sec. Large variability between the individual trials is apparent with an average uptake ratio of  $(9.78 \pm 6.82) \times 10^{-6}$ , well below published values.

Table 6.1

Published values for SO<sub>2</sub> uptake ratios on various mineral dusts. Previous experiments estimate the uptake ratio of SO<sub>2</sub> onto magnesium oxide to be on the order of 10<sup>-3</sup> to 10<sup>-4</sup>, over a magnitude greater than the calculated ratios obtained with <sup>35</sup>S in this experiment. Uptake ratios for various other mineral dusts are listed, however a complete reference can be found in Crowley et al., (2010). Abbreviations include FT-MS (flow tube coupled to a mass spectrometer), Knudsen-MS/FTIR (Knudsen cell coupled to a mass spectrometer and fourier transform infrared spectrometer), and DRIFTS (Diffuse Reflectance Infrared Fourier Transform Spectrometer).

Mineral Dust	Uptake Ratio	Method Used	Reference
MgO	1 * 10 <sup>-3</sup>	FT-MS	Judeikis et al., (1978)
	(2.6 ± 0.2) * 10 <sup>-4</sup>	Knudsen-MS/FTIR	Goodman et al., (2001)
	(5.1 ± 0.5) * 10 <sup>-4</sup>	Knudsen-MS/FTIR	Usher et al., (2002)
Al <sub>2</sub> O <sub>3</sub>	4 * 10 <sup>-4</sup>	FT-MS	Judeikis et al., (1978)
	(9.5 ± 0.3) * 10 <sup>-5</sup>	Knudsen-MS/FTIR	Goodman et al., (2001)
	(1.6 ± 0.5) * 10 <sup>-4</sup>	Knudsen-MS/FTIR	Usher et al., (2002)
CaCO <sub>3</sub>	0.1	Knudsen-MS	Santschi and Rossi, (2006)
	(7.7 ± 1.6) * 10 <sup>-4</sup>	DRIFTS	Li et al., (2006)
	(1.4 ± 0.7) * 10 <sup>-4</sup>	Knudsen-MS/FTIR	Usher et al., (2002)
SiO <sub>2</sub>	Below 1 * 10 <sup>-7</sup>	Knudsen-MS/FTIR	Usher et al., (2002)

Table 6.2

Measurement blanks for specified samples. Each sample contained 10 mL of scintillation cocktail and dust samples contained 10 mg of magnesium oxide. As the data suggests, there is an inherent increase in the blank due to the presence of magnesium oxide. However, this blank is consistent and can be subtracted off a measured sample.

<b>Work Up Blanks</b>		
H <sub>2</sub> O	H <sub>2</sub> O <sub>2</sub>	MgO + H <sub>2</sub> O <sub>2</sub>
0.835 ± 0.034	0.861 ± 0.043	1.257 ± 0.052
0.837 ± 0.042	0.827 ± 0.042	1.206 ± 0.051
0.818 ± 0.042	0.873 ± 0.061	1.267 ± 0.060
Average		
0.830 ± 0.039	0.854 ± 0.049	1.243 ± 0.054



Table 6.3

Measured samples used a cut of the commercially purchased  $\text{H}_2^{35}\text{SO}_4$  sample purchased from Perkin Elmer. 10 mg of magnesium oxide was used for tests where mineral dust was present. The measured CPM already takes into account the subtracted blanks from table 1. Each sample is corrected back to the measurement time of the first recorded sample ( $\alpha$ ) to account for the decay of  $^{35}\text{S}$ . The measurement regularity seen in this sample set suggested there is no shielding effect due to the presence of  $\text{H}_2\text{O}_2$  or magnesium oxide in the sample vials.

Work Up Shielding Tests			
	Measured CPM	Time	Corrected CPM
$^{35}\text{S}$ STD/ $\text{H}_2\text{O}$	$37.270 \pm 0.238$	5/6/13 18:04 <sup>a</sup>	$37.270 \pm 0.238$
	$35.556 \pm 0.280$	5/13/13 14:40	$37.545 \pm 0.296$
	$34.459 \pm 0.276$	5/15/13 21:05	$37.047 \pm 0.297$
Average	$37.287 \pm 0.277$		
$^{35}\text{S}$ STD/ $\text{H}_2\text{O}_2$	$36.084 \pm 0.234$	5/8/13 12:04	$36.589 \pm 0.237$
	$36.577 \pm 0.286$	5/9/13 5:53	$37.308 \pm 0.292$
	$34.638 \pm 0.279$	5/15/13 9:05	$37.092 \pm 0.299$
Average	$36.996 \pm 0.276$		
$^{35}\text{S}/\text{H}_2\text{O}_2/\text{MgO}$	$36.747 \pm 0.289$	5/9/13 17:53	$37.630 \pm 0.296$
	$36.290 \pm 0.288$	5/10/13 5:53	$37.310 \pm 0.296$
	$36.260 \pm 0.288$	5/10/13 17:53	$37.427 \pm 0.297$
	$35.992 \pm 0.287$	5/11/13 5:53	$37.298 \pm 0.298$
Average	$37.416 \pm 0.297$		

Table 6.4

Initial bulb calibration tests are shown. An aliquot of  $^{35}\text{SO}_2$  was converted back to sulfuric acid by use of  $\text{H}_2\text{O}_2$ . Measured CPM values take into account the measurement blank for hydrogen peroxide in table 1. Samples are corrected back to the measurement time ( $\beta$ ) to account for decay processes. The corrected CPM also takes into account the decrease in bulb concentration that occurs after an aliquot is used, however, this decrease in concentration is negligible for successive trials.

<b>Bulb Calibration</b>		
Measured CPM	Measurement Time	Corrected CPM
$60.722 \pm 0.514$	10/3/13 11:33 <sup>b</sup>	$60.722 \pm 0.514$
$59.896 \pm 0.511$	10/5/13 3:17	$60.721 \pm 0.518$
$59.101 \pm 0.507$	10/5/13 19:17	$60.265 \pm 0.517$
Average	$60.569 \pm 0.517$ on 10/3/13 11:33 am	

Table 6.5

Average uptake ratios calculated at different linear velocities showing similar values as those obtained at 81 cm/sec, still well below published literature values using in situ mass spectroscopic techniques. For samples run at 290 cm/sec, the helium carrier gas flow was dropped below the 1500 sccm values used in other trials in an attempt to test lower pressures in the flow tube.

Linear Velocity (cm/sec)	Contact Time (seconds)	Average Calculated Uptake Ratio
13	0.38	$(8.06 \pm 4.22) * 10^{-7}$
18	0.28	$(4.07 \pm 2.60) * 10^{-6}$
24	0.21	$(6.37 \pm 5.48) * 10^{-6}$
48	0.10	$(2.67 \pm 1.97) * 10^{-5}$
81	0.06	$(9.78 \pm 6.82) * 10^{-6}$
290	0.02	$(1.39 \pm 1.13) * 10^{-5}$

## 6.6 References

- Adams, J., D. Rodriguez, and R. Cox (2005), The uptake of SO<sub>2</sub> on Saharan dust: A flow tube study, *Atmospheric Chemistry and Physics*, 5(10), 2679-2689.
- Andreae, M., T. Andreae, D. Meyerdierks, and C. Thiel (2003), Marine sulfur cycling and the atmospheric aerosol over the springtime North Atlantic, *Chemosphere*, 52(8), 1321-1343.
- Bertram, T., and J. Thornton (2009), Toward a general parameterization of N<sub>2</sub>O<sub>5</sub> reactivity on aqueous particles: the competing effects of particle liquid water, nitrate and chloride, *Atmospheric Chemistry and Physics*, 9(21), 8351-8363.
- Brothers, L. A., G. Dominguez, A. Abramian, A. Corbin, B. Bluen, and M. H. Thiemens (2010), Optimized low-level liquid scintillation spectroscopy of <sup>35</sup>S for atmospheric and biogeochemical chemistry applications, *Proceedings of the National Academy of Sciences*, 107(12), 5311-5316.
- Crowley, J. N., M. Ammann, R. A. Cox, R. G. Hynes, M. E. Jenkin, A. Mellouki, M. J. Rossi, J. Troe, and T. J. Wallington (2010), Evaluated kinetic and photochemical data for atmospheric chemistry: Volume V – heterogeneous reactions on solid substrates, *Atmos. Chem. Phys.*, 10(18), 9059-9223.
- Dentener, F. J., G. R. Carmichael, Y. Zhang, J. Lelieveld, and P. J. Crutzen (1996), Role of mineral aerosol as a reactive surface in the global troposphere, *Journal of geophysical research*, 101(D17), 22869-22889.
- Finlayson-Pitts, B. J., and J. N. Pitts (1986), *Atmospheric chemistry: fundamentals and experimental techniques*, Wiley.
- Gebel, M. E., B. J. Finlayson-Pitts, and J. A. Ganske (2000), The uptake of SO<sub>2</sub> on synthetic sea salt and some of its components, *Geophysical Research Letters*, 27(6), 887-890.
- Goodman, A., P. Li, C. Usher, and V. Grassian (2001), Heterogeneous uptake of sulfur dioxide on aluminum and magnesium oxide particles, *The Journal of Physical Chemistry A*, 105(25), 6109-6120.
- Hanke, M., B. Umann, J. Uecker, F. Arnold, and H. Bunz (2003), Atmospheric measurements of gas-phase HNO<sub>3</sub> and SO<sub>2</sub> using chemical ionization mass spectrometry during the MINATROC field campaign 2000 on Monte Cimone, *Atmospheric Chemistry and Physics*, 3(2), 417-436.
- Husar, R. B. (2004), Intercontinental transport of dust: historical and recent observational evidence, in *Air Pollution*, edited, pp. 277-294, Springer.
- Judeikis, H. S., T. B. Stewart, and A. G. Wren (1978), Laboratory studies of heterogeneous reactions of SO<sub>2</sub>, *Atmospheric Environment*, 12(8), 1633-1641.

Li, L., Z. Chen, Y. Zhang, T. Zhu, J. Li, and J. Ding (2006), Kinetics and mechanism of heterogeneous oxidation of sulfur dioxide by ozone on surface of calcium carbonate, *Atmospheric Chemistry and Physics*, 6(9), 2453-2464.

Li, L., Z. Chen, Y. Zhang, T. Zhu, S. Li, H. Li, L. Zhu, and B. Xu (2007), Heterogeneous oxidation of sulfur dioxide by ozone on the surface of sodium chloride and its mixtures with other components, *Journal of Geophysical Research: Atmospheres (1984–2012)*, 112(D18).

Lide, D. R. (2004), *CRC Handbook of Chemistry and Physics*, CRC press.

Luria, M., and H. Sievering (1991), Heterogeneous and homogeneous oxidation of SO<sub>2</sub> in the remote marine atmosphere, *Atmospheric Environment*, 25(8), 1489-1496.

Mamane, Y., and J. Gottlieb (1989), Heterogeneous reactions of minerals with sulfur and nitrogen oxides, *Journal of aerosol science*, 20(3), 303-311.

Penner, J. E. (2001), Aerosols, their direct and indirect effects, *Climate Change 2001: The Scientific Basis*.

Priyadarshi, A., J. Hill-Falkenthal, E. Coupal, G. Dominguez, and M. H. Thiemens (2012), Measurements of <sup>35</sup>S in the marine boundary layer at La Jolla, California: A new technique for tracing air mass mixing during Santa Ana events, *Journal of Geophysical Research: Atmospheres (1984–2012)*, 117(D8).

Santschi, C., and M. J. Rossi (2006), Uptake of CO<sub>2</sub>, SO<sub>2</sub>, HNO<sub>3</sub> and HCl on Calcite (CaCO<sub>3</sub>) at 300 K: Mechanism and the Role of Adsorbed Water, *The Journal of Physical Chemistry A*, 110(21), 6789-6802.

Savarino, J., B. Alexander, V. Darmohusodo, and M. H. Thiemens (2001), Sulfur and oxygen isotope analysis of sulfate at micromole levels using a pyrolysis technique in a continuous flow system, *Analytical chemistry*, 73(18), 4457-4462.

Song, C. H., and G. R. Carmichael (1999), The aging process of naturally emitted aerosol (sea-salt and mineral aerosol) during long range transport, *Atmospheric Environment*, 33(14), 2203-2218.

Tanaka, N., and K. Turekian (1991), Use of cosmogenic <sup>35</sup>S to determine the rates of removal of atmospheric SO<sub>2</sub>.

Tang, Y., G. R. Carmichael, G. Kurata, I. Uno, R. J. Weber, C.-H. Song, S. K. Guttikunda, J.-H. Woo, D. G. Streets, and C. Wei (2004), Impacts of dust on regional tropospheric chemistry during the ACE-Asia experiment: A model study with observations, *Journal of Geophysical Research: Atmospheres*, 109(D19).

Thornton, J. A., C. F. Braban, and J. P. Abbatt (2003), N<sub>2</sub>O<sub>5</sub> hydrolysis on sub-micron organic aerosols: the effect of relative humidity, particle phase, and particle size, *Physical Chemistry Chemical Physics*, 5(20), 4593-4603.

Usher, C., H. Al-Hosney, S. Carlos-Cuellar, and V. Grassian (2002), A laboratory study of the heterogeneous uptake and oxidation of sulfur dioxide on mineral dust particles, *Journal of Geophysical Research*, 107(D23), 4713.

Vlasenko, A., T. Huthwelker, H. Gäggeler, and M. Ammann (2009), Kinetics of the heterogeneous reaction of nitric acid with mineral dust particles: an aerosol flowtube study, *Physical Chemistry Chemical Physics*, 11(36), 7921-7930.

Vlasenko, A., S. Sjogren, E. Weingartner, K. Stemmler, H. Gäggeler, and M. Ammann (2006), Effect of humidity on nitric acid uptake to mineral dust aerosol particles, *Atmospheric Chemistry and Physics*, 6(8), 2147-2160.

Yasuda, H. (1985), *Plasma polymerization*, Academic Press.

Zhang, X., G. Zhuang, J. Chen, Y. Wang, X. Wang, Z. An, and P. Zhang (2006), Heterogeneous reactions of sulfur dioxide on typical mineral particles, *The Journal of Physical Chemistry B*, 110(25), 12588-12596.